

**AN INTEGRATED APPROACH TO SOUND BEAM FOCUSING
USING PHASED ARRAY AND SAFT FOR
FLAW CHARACTERIZATION**

By

PARITOSH PRABHAKAR NANEKAR

ENGG01200904028

BHABHA ATOMIC RESEARCH CENTRE, MUMBAI

*A thesis submitted to the
Board of Studies in Engineering Sciences*

*In partial fulfillment of requirements
for the Degree of*

DOCTOR OF PHILOSOPHY

of

HOMI BHABHA NATIONAL INSTITUTE



May, 2017

Homi Bhabha National Institute

Recommendations of the Viva Voce Committee

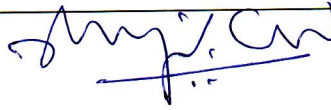
As members of the Viva Voce Committee, we certify that we have read the dissertation prepared by **Paritosh Prabhakar Nanekar** entitled '**An integrated approach to sound beam focusing using phased array and SAFT for flaw characterization**' and recommend that it may be accepted as fulfilling the thesis requirement for the award of Degree of Doctor of Philosophy.

Chairman – Dr. B.K. Dutta



Date: 19-5-17

Guide / Convener – Dr. T. Jayakumar



Date: 19 May 2017

Examiner – Dr. C.V. Krishnamurthy



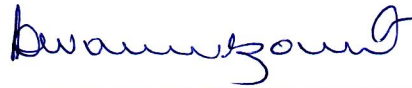
Date: 19/05/2017

Member 1- Dr. R. Balasubramaniam



Date: 19/5/17

Member 2- Dr. T.A. Dwarkanath



Date: 19/05/2017

Member 3- Dr. J. Chattopadhyay



Date: 19/5/17

Final approval and acceptance of this thesis is contingent upon the candidate's submission of the final copies of the thesis to HBNI.

I hereby certify that I have read this thesis prepared under my direction and recommend that it may be accepted as fulfilling the thesis requirement.



(T. Jayakumar)
Guide

Date: May 19, 2017

Place: Mumbai

STATEMENT BY AUTHOR

This dissertation has been submitted in partial fulfillment of requirements for an advanced degree at Homi Bhabha National Institute (HBNI) and is deposited in the Library to be made available to borrowers under rules of the HBNI.

Brief quotations from this dissertation are allowable without special permission, provided that accurate acknowledgement of source is made. Requests for permission for extended quotation from or reproduction of this manuscript in whole or in part may be granted by the Competent Authority of HBNI when in his or her judgment the proposed use of the material is in the interests of scholarship. In all other instances, however, permission must be obtained from the author.

P.P. Nanekar
(Paritosh Nanekar) 25/05/2017

DECLARATION

I, hereby declare that the investigation presented in the thesis has been carried out by me. The work is original and has not been submitted earlier as a whole or in part for a degree / diploma at this or any other Institution / University.

P. P. Nanekar
(Paritosh Nanekar) 25/05/2017

List of Publications arising from the Thesis

A. Journal Publications

1. Ultrasonic phased array examination of circumferential weld joint in reactor pressure vessel of BWR, Nanekar P, Jothilakshmi N, Jayakumar T., Nuclear Engineering and Design, 2013, Vol. 265, 366-374.
2. SAFT-assisted sound beam focusing using phased arrays (PA-SAFT) for non-destructive evaluation, Paritosh Nanekar, Anish Kumar, T. Jayakumar, NDT & E, 2015, Vol. 30, Issue 2, 105-123
3. Characterization of planar flaws by synthetic focusing of sound beam using linear arrays, Paritosh Nanekar, Anish Kumar, T. Jayakumar, Case Studies in Non-destructive Testing and Evaluation, 2015, Vol. 3, 9-14
4. Sound beam focusing using Phased Array-SAFT Technique, Paritosh Nanekar, N Jothilakshmi, Anish Kumar, T Jayakumar, Insight Non-destructive Testing and Condition Monitoring, 2017, Vol. 59, No. 3, 129-137
5. Synthetic Focusing of Sound Beam Using Linear Arrays, Paritosh Nanekar, N Jothilakshmi, Anish Kumar and T Jayakumar, Materials Evaluation, The journal of American Society of Non-destructive testing, 2017, Vol. 75, No. 6, 813-821

P.P. Nanekar
(Paritosh Nanekar) 25/05/2017

B. Papers under review

1. Characterization of planar flaws by Phased Array-SAFT technique, Paritosh Nanekar, N Jothilakshmi, Anish Kumar, T Jayakumar, Measurement
2. SAFT Assisted Sound Beam Focusing using Linear Array for Examination of Circumferential Weld Joint in Pressure Vessel of Boiling Water Reactor, Paritosh Nanekar, N Jothilakshmi, Anish Kumar, T Jayakumar, International Journal on Pressure Vessel and Piping
3. Depth sizing of planar flaws in weld joints by Angle beam PA-SAFT technique, Paritosh Nanekar, N Jothilakshmi, Anish Kumar and T Jayakumar, NDT & E

C. Papers presented at the Conference

1. Comparative Study on Sizing of Fusion-line Defects in Welds using Phased Array and TOFD, 14th Asia Pacific Conference on NDT, Mumbai, Nov. 2013
2. Ultrasonic Phased Array Examination of Circumferential Weld Joint in Reactor Pressure Vessel of BWR, National Conference NDE 2014, Pune, Dec. 2014
3. Sound beam focusing methods using phased array, National Conference NDE 2015, Hyderabad, Nov. 2015

P.P. Nanekar
25/05/2017
(Paritosh Nanekar)

*“If I have seen further than others, it is by
standing upon the shoulders of giants”*

- Isaac Newton

DEDICATIONS

To

My Parents: Smt. Anuradha and Shri Prabhakar Nanekar

and

My Family: Aditi, Eeshan and Smt. Rashmi

ACKNOWLEDGEMENTS

I would first like to thank my Guide Dr. T. Jayakumar (Formerly Director, MMG, IGCAR, Kalpakkam) for providing me innumerable suggestions and ingenuities at every stage of my Ph.D. This work would not have been possible without his guidance. I am indebted to Dr. Anish Kumar, Head UMAS, NDED, IGCAR, for his support and contributions. Not only was he instrumental in shaping the work plan, but his deep understanding of the subject has helped me immensely in the analysis of results. I wish to express my sincere gratitude to Smt. N Jothilakshmi, my colleague at Quality Assurance Division, BARC. Her support in carrying out the simulation studies and the experimental work goes a long way in the successful completion of the Thesis. I take this opportunity to thank my technical advisors Shri. B.K. Shah and Shri. S. Anantaraman (formerly Head, Quality Assurance Division), Chairman, Doctoral Committee Dr. B.K. Dutta, past Chairman, Dr. V.K. Suri, and the current and the past members of the Doctoral Committee for the critical review of the work at every stage and providing me with valuable suggestions. I express my thanks to Shri. Vivek Bhasin, Associate Director, Nuclear Fuels Group and Shri. Dipankar Mukherjee, Head, Quality Assurance Division, for their support. I thank all my colleagues at Quality Assurance Division, BARC, especially Shri. Santosh Salunkhe and Shri. Chandrakant Ninawe, for their help in fabrication of various test samples, which are utilized for the experimental work.

On the personal front, I would like to thank my parents, Smt. Anuradha and Shri. Prabhakar Nanekar and my in-laws, Smt. Lalita and Shri. Uday Parnaik, for their support and blessings. My wife Rashmi has been a source of encouragement all along. She did everything to help me concentrate on my work and never complained about my long absences and little involvement in the household. I owe her a lot of appreciation. My son Eeshan and daughter Aditi have also been immensely helpful. I express my gratitude to my sister Smt. Aparna Luley, my brother Shri. Ashutosh Nanekar, my brother in-law Shri. Gautam Parnaik, and their families for their support. Finally, I wish to place on record my gratitude to all my relatives, friends and well-wishers for their encouragement throughout the course of my Ph.D.

P.P. Nanekar
(Paritosh Nanekar) 25/05/2017

TABLE OF CONTENTS

	Page No.
Abstract	I
List of Figures	IV
List of Tables	XV
Nomenclature	XVII
Chapter 1 Introduction	1
1.1 Focusing of Ultrasonic Beam	1
1.2 Flaw Characterization by Ultrasonic Non-Destructive Evaluation	4
1.3 Background of the Current Research	7
1.4 Structure of the Thesis	10
Chapter 2 Literature Review	13
2.1 Introduction	13
2.2 Sound beam focusing	13
2.2.1 Ancient and Modern Methods	14
2.2.2 Acoustic lenses	16
2.2.3 Piezocomposite Transducers	23
2.2.4 Synthetic Aperture Focusing Technique (SAFT)	26
2.2.5 Phased Array	34
2.2.6 Full Matrix Capture – Total Focusing Method	47
2.2.7 Sampling Phased Array	53
2.2.8 Virtual Array of Sources	56

2.3	Flaw characterization by non-destructive examination	61
2.3.1	Depth sizing of flaws by ultrasonic testing based on the amplitude	64
2.3.1.1	Distance Amplitude Correction (DAC)	64
2.3.1.2	Distance Gain Size (DGS)	65
2.3.1.3	Decibel drop	66
2.3.2	Depth sizing of flaws by ultrasonic testing based on time-of-flight	69
2.3.2.1	Time of Flight Diffraction Technique (TOFD)	69
2.3.2.2	Relative and Absolute Arrival Time Technique	71
2.4	Motivation	73
2.5	Objective	75
Chapter 3	Experimental Details	77
3.1	Introduction	77
3.2	Experimental Set-up	78
3.2.1	Phased Array Instrument	78
3.2.2	Linear Arrays	79
3.2.3	SAFT Algorithm	81
3.3	Evaluation of sound beam divergence for miniature elements of a linear array	85
3.4	Assessment of the effect of array parameters and SAFT processing parameters on sound beam focusing using SFLA	88
3.4.1	Effect of array based parameters	89
3.4.2	Effect of the difference between the true value and the input value of different parameters during SAFT processing	90
3.5	Optimization of the aperture size for PA-SAFT technique	91

3.6 Assessment of the capabilities of SFLA and PA-SAFT techniques for the detection and characterization of volumetric flaws	93
3.6.1 Determination of the sensitivity for the detection of volumetric flaws with a focused sound beam across the depth	95
3.6.2 Determination of the limit of sensitivity for volumetric flaws	96
3.6.3 Determination of lateral coverage achieved by SFLA and PA-SAFT techniques	97
3.6.4 Estimation of the resolving power of SFLA and PA-SAFT techniques	98
3.7 Assessment of the capability of SFLA and PA-SAFT techniques for detection and characterization of planar flaws	99
3.7.1 Characterization of planar flaws in thin section	100
3.7.2 Characterization of planar flaws in thick section	101
3.8 Assessment of the capability of Angle Beam PA-SAFT technique for detection and characterization of flaws	102
3.9 Demonstration of the effectiveness of SFLA and PA-SAFT techniques for characterization of weld flaws	105
3.10 Application of SFLA and PA-SAFT techniques for in-service inspection of circumferential weld joint in reactor pressure vessel of a nuclear boiling water reactor	108
3.11 Summary of the Chapter	111
Chapter 4 SFLA & PA-SAFT - Methodology, Optimization and Variables Affecting Sound Beam Focusing	113
4.1 Introduction	113
4.2 Sound Beam Divergence for Miniature Piezoelectric Crystal	115
4.2.1 Estimation of Beam Divergence for Small Values of D/λ	118
4.2.2 Estimation of Beam Spread Constant k_{dB}	122
4.2.3 Generalized equation for the estimation of sound beam divergence for rectangular piezoelectric elements	124
4.2.4 Validation	126

4.3 SFLA technique	128
4.3.1 Methodology for data acquisition and processing	128
4.3.2 Factors Affecting Focusing	131
4.3.2.1 Linear array based parameters	132
4.3.2.1.1 Aperture Size	132
4.3.2.1.2 Pitch of linear array	135
4.3.2.1.3 Frequency of sound	136
4.3.2.1.4 Total Effective Aperture	138
4.3.2.1.5 Effect of D/λ	139
4.3.2.1.6 Summary of the observations on the effect of array based parameters on sound beam focusing	144
4.3.2.2 SAFT processing parameters	144
4.3.2.2.1 Velocity in the material	145
4.3.2.2.2 Pitch of the linear array	146
4.3.2.2.3 Beam divergence angle	147
4.3.2.2.4 Summary of observations on the effect of SAFT processing based parameters on sound beam focusing	148
4.4 PA-SAFT technique	148
4.4.1 Methodology	149
4.4.2 Selection of Active Aperture	151
4.4.2.1 Sound beam computation using CIVA 11	152
4.4.2.2 Effect of active aperture on acoustic pressure and beam divergence	156
4.4.2.3 Effect of active aperture on the size of the virtual source	162
4.4.2.4 Validation of the optimization studies	164
4.4.3 Effect of Frequency	168

4.5 Angle Beam PA-SAFT technique	170
4.5.1 Methodology	170
4.5.2 Optimization of active aperture size for data acquisition	173
4.6 Comparison of sound beam focusing using SFLA, PA-SAFT and FMC techniques	180
4.7 Summary of the Chapter	183
Chapter 5 Evaluation of the Capabilities of SFLA and PA-SAFT Techniques for Flaw Detection and Characterization	187
5.1 Introduction	187
5.2 Volumetric Flaws	187
5.2.1 Assess the sensitivity and focusing ability for detection of volumetric flaws	189
5.2.1.1 Conventional angle beam phased array using focal laws	190
5.2.1.2 SFLA technique	193
5.2.1.3 PA-SAFT technique	195
5.2.1.4 FMC + TFM technique	196
5.2.1.5 Comparison and analysis of results by different techniques	196
5.2.2 Sensitivity for the detection of volumetric flaws at higher depth	199
5.2.2.1 SFLA technique	200
5.2.2.1 PA-SAFT technique	201
5.2.2.3 FMC + TFM technique	202
5.2.2.4 Comparison of results by various techniques	203
5.2.3 Extent of lateral coverage for detection of volumetric flaws	203
5.2.3.1 Conventional Phased Array	204
5.2.3.2 SFLA technique	206
5.2.3.3 PA-SAFT technique	207

5.2.3.4 FMC + TFM technique	208
5.2.3.5 Comparison and analysis of results by different techniques	208
5.2.4 Resolving power of SFLA and PA-SAFT techniques	211
5.2.4.1 Conventional phased array technique	212
5.2.4.2 SFLA technique	213
5.2.4.3 PA-SAFT technique	214
5.2.4.4 FMC+ TFM technique	215
5.3 Planar Flaws	216
5.3.1 Stainless steel plate of 25 mm thickness with simulated planar flaws	216
5.3.1.1 SFLA technique	217
5.3.1.2 PA-SAFT technique	219
5.3.1.3 FMC + TFM technique	221
5.3.1.4 Evaluation of depth and orientation of inclined slots	221
5.3.1.5 Comparison and analysis of results by different techniques	223
5.3.2 Stainless steel plate of 60 mm thickness with simulated planar flaws	225
5.4 Angle Beam PA-SAFT technique	229
5.5 Uncertainty in depth sizing of planar flaws using SFLA and PA-SAFT Techniques	232
5.6 Summary of the Chapter	236
Chapter 6 Demonstrating the Effectiveness of SFLA and PA-SAFT Techniques for Detection and Characterization of Flaws in Weld Joints	239
6.1 Introduction	239
6.2 Velocity Profiling across the weld	240
6.3 Characterization of volumetric weld flaws	242
6.3.1 Clustered Porosity	243
6.3.2 Slag Inclusion	245

6.3.3 Summary of observations on volumetric flaws	247
6.4 Characterization of planar weld flaws	249
6.4.1 Lack of sidewall fusion	249
6.4.2 Root crack	252
6.4.3 Summary of observations on planar flaws	254
6.5 Characterization of planar weld flaws by Angle beam PA-SAFT technique	255
6.5.1 Root Crack	256
6.5.2 Toe crack	258
6.5.3 Summary of observations on the detection and the characterization of planar flaws by Angle Beam PA-SAFT	259
6.6 Comparison of different techniques for depth sizing of planar flaws	260
6.6.1 Lack of sidewall fusion	260
6.6.2 Root crack	263
6.7 Application of SFLA and PA-SAFT techniques for in-service inspection of a circumferential weld joint in a pressure vessel of a nuclear boiling water reactor	266
6.7.1 Configuration of C1 weld joint and the examination requirements	268
6.7.2 Ultrasonic simulation results	269
6.7.3 Comparison of various techniques for C1 weld examination	276
6.7.4 Experimental Results	277
6.7.4.1 Conventional Phased Array	277
6.7.4.2 SFLA technique	280
6.7.4.3 PA-SAFT technique	282
6.7.4.4 Comparison of various approaches	283
6.8 Summary of the Chapter	286
Chapter 7 Conclusions, Contributions and Suggestions for Future Work	289
7.1 Conclusions	289
7.2 Specific Innovative and Novel Contributions	298
7.3 Suggestions for future work	301
References	303

ABSTRACT

The importance of sound beam focusing in ultrasonic non-destructive evaluation (NDE) cannot be overemphasized. In the past few decades, several approaches for focusing the ultrasound have been developed. The use of acoustic lenses for this purpose dates back to 1920s. Around 1950s, the concept of synthetic aperture for improving the lateral resolution of airborne radar mapping systems came in to existence. This approach was successfully employed using ultrasound for non-destructive examination in 1970s and named as synthetic aperture focusing technique (SAFT). In late 1970s, piezocomposite materials were synthesized, which could be formed in to curved shape to produce a focused sound beam. Around the same time, ultrasonic imaging systems based on the use of linear arrays were developed for medical diagnostics. It was shown that by controlling the sequence of excitation of array elements, the sound beam can be focused at a desired depth and direction. Around 1990s, commercial phased array systems for ultrasonic NDE started finding applications in the industries. These systems became extremely popular for the purpose of focusing ultrasound in order to improve the reliability of inspection, sensitivity for flaw detection and the enhancement in the signal to noise ratio. In the early part of 2000s, sound beam focusing by carrying out the post-processing of the full matrix capture (FMC) data using an algorithm called total focusing method (TFM) was developed. The technique gave very high resolution images of the flaws present within the objects under investigation. In order to overcome the drawbacks of the FMC approach in terms of the sensitivity for the detection of flaws in thick and attenuating materials, techniques based on the concept of virtual array of sources came in to existence.

During the present study, two sound focusing techniques using an integrated approach involving linear array and SAFT have been investigated viz. Synthetic Focusing using Linear Array (SFLA) and Phased Array-SAFT (PA-SAFT). The objective is to derive the benefit of

SAFT and array based inspection and achieve the sound beam focusing, which is comparable or better than what could be achieved by the existing techniques. The integrated approach is based on acquiring the data by a divergent sound beam using a linear array and carry out post-processing of the acquired data by time based SAFT algorithm.

SFLA technique uses a single element for sound beam transmission and reception. Since the size of the piezoelectric element in an array is very small, a well divergent sound beam is generated during the sound beam transmission process, which is used to acquire the raw data. Unlike FMC, which needs a large number of parallel receiver channels to speed up the data acquisition process, with SFLA a single channel system with multiplexing is sufficient for data acquisition. Moreover, unlike FMC, the size of the data acquired by SFLA technique is extremely small. Hence, a real time imaging system based on SFLA can easily be realised. On the other hand, PA-SAFT technique is based on the concept of virtual array of sources. These virtual sources are located very close to the scanning surface so that a divergent sound beam is available in the region of interest during acquisition of the raw data. PA-SAFT technique overcomes the limitations of SFLA and FMC + TFM techniques in terms of the sensitivity for flaw detection in thick and attenuating materials.

Since SFLA technique is based on the use of a single miniature element of a linear array for sound beam transmission, a systematic study has been carried out to evaluate the sound beam divergence for such cases. An empirical relationship has been derived to compute the beam divergence angle for piezoelectric elements with a small size-to-wavelength ratio. A detailed study on the effect of array based and SAFT processing based parameters on the focal spot size using SFLA technique has been carried out. It has been shown that the lateral resolution by SAFT is not independent of the wavelength, as widely reported, while working with the miniature elements in a linear array. An empirical relationship between the focal spot size, and the ratio of the size of the piezoelectric element to the wavelength, has been derived. The

optimum aperture size for the application of PA-SAFT technique under given experimental conditions has been established using simulation and experimental studies. A comparative study has been carried out on the focal spot size achieved by SFLA, PA-SAFT and FMC + TFM techniques.

The capabilities of SFLA and PA-SAFT techniques in terms of the sensitivity for the detection of volumetric flaws, the lateral coverage and the ability to resolve very closely spaced flaws has been studied. The study has also been carried out to assess the capabilities of these techniques on the detection and characterization of planar flaws in thin and thick sections. A variant of PA-SAFT technique using angle beam has been standardized for specific cases, where the application of SFLA, PA-SAFT and FMC techniques may not be possible. The effectiveness of SFLA and PA-SAFT techniques for the characterization of real flaws has been demonstrated on weld samples containing a variety of volumetric and planar flaws. Finally, SFLA and PA-SAFT techniques are used on the mock-up of the weld joint in the pressure vessel of a nuclear boiling water reactor. It is shown that the reference flaws in the mock-up are detected and resolved by SFLA and PA-SAFT techniques using much lesser resources in terms of the instrumentation requirements, as compared to the conventional phased array.

The studies carried out during this Ph.D. work has demonstrated that SFLA and PA-SAFT techniques provide an effective alternative to the conventional phased array and FMC + TFM techniques for sound beam focusing. As compared to the conventional phased array, both these techniques provide a better lateral resolution using much lesser number of elements in an active aperture. As a result, a low configuration phased array instrument can be used for data acquisition. When compared to FMC + TFM technique, the size of the acquired data for post-processing using these techniques is significantly smaller. Hence, a real-time imaging system using these techniques can be realized for industrial use. The results on the detection and characterization of real weld flaws by these techniques have proven that SFLA and PA-SAFT

techniques hold a very good potential for field applications involving ultrasonic non-destructive evaluation.

LIST OF FIGURES

Figure No		Page No
Figure 2.1	Ancient method of sound focusing by a concave surface	15
Figure 2.2	Sound beam focusing by waveguide	15
Figure 2.3	Echo height of a point reflector on the axis of a plane radiator focused by a lens of Perspex in water	18
Figure 2.4	Focal length of a plano concave lens, which includes the correction term for large angle of apertures	18
Figure 2.5	Improvement in the echo height (dB) as a result of focusing for various K values	19
Figure 2.6	(A) Normal plano concave lens, (B) Stepped lens with impermeable zones omitted and (C) Zone lens with zones increasing in thickness by $\lambda/2$	20
Figure 2.7	Characteristics of a focused sound beam	21
Figure 2.8	Sound beam focusing using an acoustic lens and shaped piezocomposite transducers	23
Figure 2.9	Principle of the application of SAFT	28
Figure 2.10	Time delay and averaging scheme during SAFT processing	29
Figure 2.11	(a) Raw B-scan and (b) SAFT processed B-scan for a cast austenitic steel block with side drilled holes	31
Figure 2.12	Conventional B-scan vs. SAFT for the crack on the scanning surface	32
Figure 2.13	Constructive and destructive interference of light waves emitting from two point sources	34
Figure 2.14	Sector scan image of a foetus using phased array ultrasound	35
Figure 2.15	Principle of Beam Steering during a) Transmission and b) Reception	37
Figure 2.16	Sound beam focusing using phased array (a) normal beam and (b) angle beam	38
Figure 2.17	Scanning pattern using phased array: (a) electronic scanning, (b) sectorial scanning and (c) dynamic depth focusing	39
Figure 2.18	Time Delay variation for different focal depth	39

Figure 2.19	A typical directivity plot showing the main lobe, the side lobes and the grating lobe	43
Figure 2.20	Principle of data acquisition (a) Conventional phased array and (b) Full matrix capture	48
Figure 2.21	Fully focused Total Focusing Method	48
Figure 2.22	Total Focusing Method	49
Figure 2.23	B-scan images of a side drilled hole in an aluminum block (a) conventional phased array and (b) FMC + TFM	50
Figure 2.24	Comparison of SPA with conventional phased array technique for the detection of near surface and far surface flaws	54
Figure 2.25	Comparison of SPA with conventional phased array technique for the detection of flaws in carbon fire composite	55
Figure 2.26	Angular response for different excitation schemes using a linear array (a) single element excitation, (b) multi-element simultaneous excitation, (c) multi-element simultaneous excitation with apodization and (d) multi-element simultaneous excitation with de-focusing focal laws	58
Figure 2.27	Beam propagation in transmit focusing. (a) Conventional B-mode, (b) Transmit model for one virtual element located at focal depth in B-mode and (c) Superposition of transmit fields of two virtual sources at imaging points	59
Figure 2.28	Generating DAC curve	65
Figure 2.29	DGS diagram for a normal beam probe B4S	65
Figure 2.30	Decibel drop technique for flaw sizing	67
Figure 2.31	Principle of dB drop technique for depth estimation	67
Figure 2.32	Typical TOFD set-up	69
Figure 2.33	Typical B-scan image obtained using TOFD set-up	70
Figure 2.34	Typical TOFD images for weld defects	71
Figure 2.35	Crack height estimation using RATT	72
Figure 3.1 a	Experimental set-up for data acquisition	79
Figure 3.1 b	Block diagram of data acquisition and processing	79
Figure 3.2	Front Panel of LabView algorithm for SAFT processing of raw B-scan images acquired using SFLA and PA-SAFT techniques	81
Figure 3.3	Aluminum sample with 0.5 mm dia. side drilled holes at various depths from the scanning surface	86

Figure 3.4	Experimental set-up for estimation of beam spread constant for small values of D/λ	87
Figure 3.5	Sound beam computation using CIVA 11 for 10 MHz, 0.3 mm pitch linear array with 8 elements active aperture with no focal law	92
Figure 3.6	Experimental set-up for optimization of aperture size for PA-SAFT technique	93
Figure 3.7	Experimental set-up for data acquisition on carbon steel sample with vertically stacked side drilled holes (a) SFLA, PA-SAFT and FMC techniques, (b) Conventional angle beam phased array using focal laws	96
Figure 3.8	Experimental set-up for data acquisition on an aluminum sample with 0.5 mm dia. side drilled holes	97
Figure 3.9	Experimental arrangement for data acquisition on aluminum sample with laterally separated holes	98
Figure 3.10	Carbon steel Sample with Closely Spaced Side Drilled Holes	99
Figure 3.11	Steel plate with simulated planar flaws	101
Figure 3.12	Placement of linear array for data acquisition on stainless steel plate with simulated planar flaws	101
Figure 3.13	Simulated planar flaws in thick stainless steel block	102
Figure 3.14	Experimental arrangement for data acquisition using Angle Beam PA-SAFT (a) Notch on the back surface and (b) Notch on the scanning surface	103
Figure 3.15	Placement of linear array for data acquisition using Angle Beam PA-SAFT technique on a 60 mm thick stainless steel sample	104
Figure 3.16	Block containing volumetric and planar flaws	105
Figure 3.17	Placement of linear array over the weld for data acquisition by SFLA, PA-SAFT and FMC techniques	106
Figure 3.18	Placement of linear array for data acquisition on weld samples using Angle beam PA-SAFT technique (a) Root crack and (b) Toe crack	107
Figure 3.19	Mock-up block of C1 weld joint in reactor pressure vessel	109
Figure 3.20	Placement of linear array on the top flange of RPV mock-up block for data acquisition using conventional phased array	110
Figure 3.21	Experimental set-up for data acquisition using PA-SAFT on the mock-up block of C1 weld joint in RPV	110
Figure 4.1	Beam spread measurement (a) Experimental set-up and (b) B-scan image from which the 6 dB beam width is determined	119

Figure 4.2	Effect of D on beam divergence for (a) 2 MHz, 64 elements and 0.8 mm pitch, (b) 5 MHz, 64 elements and 0.6 mm pitch and (c) 10 MHz, 128 elements and 0.3 mm pitch linear array	120
Figure 4.3	Variation in beam spread angle with D/λ for linear arrays of different frequencies	121
Figure 4.4	Variation of k_{6dB} value with D/λ for miniature piezoelectric elements	125
Figure 4.5	SFLA methodology (a) Data acquisition (b) Raw A-scans (c) Raw B-scan image (d) A-scans after time shifting and (e) B-scan image after SAFT processing	129
Figure 4.6	(a) Raw and (b) SAFT processed B-scan images for a 0.5 mm dia. side drilled hole at 25 mm depth in an aluminum block using SFLA Technique	131
Figure 4.7	Experimental set-up for data acquisition on side drilled holes in an aluminum block using SFLA technique	131
Figure 4.8	Variation in the focal spot size with the aperture size for a 10 MHz, 0.3 mm pitch linear array	133
Figure 4.9	Variation in the focal spot size with the pitch used for data acquisition for a 10 MHz, 0.3 mm pitch linear array	136
Figure 4.10	Variation in the focal spot size with the frequency for a constant aperture, pitch and total effective aperture	137
Figure 4.11	Variation in the focal spot size with total effective aperture for 10 MHz, 0.3 mm pitch linear array	138
Figure 4.12	Variation in normalized focal spot size with normal element size	141
Figure 4.13	Dependence of beam spread on L_{eff}	142
Figure 4.14	Variation in the focal spot size with the input value of sound velocity during SAFT processing for an aluminum sample (Actual Velocity = 6300 m/s)	145
Figure 4.15	Variation in the focal spot size with the input value of the pitch during SAFT processing (Actual Pitch = 0.3 mm)	146
Figure 4.16	Variation in the focal spot size with the input value of the sound beam divergence angle during SAFT processing (Actual divergence = 25 deg.)	147
Figure 4.17	Data acquisition using PA-SAFT technique	150
Figure 4.18	(a) Raw and (b) SAFT processed B-scan images collected on a 0.5 mm dia. side drilled hole at 25 mm depth in an aluminum block using PA-SAFT technique	150

Figure 4.19	Sound beam computation results for 10 MHz, 0.3 mm pitch linear array with excitation of (a) 1 element (b) 8 elements with no delay law and (c) 8 elements with delay law with focus at 2 mm (Simulation)	153
Figure 4.20	Sound beam computation results for PA-SAFT using (a) 4 el (b) 6 el (c) 8 el (d) 10 el (e) 12 el and (f) 14 elements (Simulation)	154
Figure 4.21	Variation in the sound wave amplitude with the depth for different apertures using 10 MHz, 0.3 mm pitch linear array (Simulation)	157
Figure 4.22	Variation in the sound wave amplitude with the active aperture size at different depths for 10 MHz, 0.3 mm pitch linear array (Simulation)	158
Figure 4.23	Variation in the full beam width for different apertures using 10 MHz, 0.3 mm pitch linear array (Simulation)	159
Figure 4.24	Variation in the sound wave amplitude with depth for different apertures using 5 MHz, 0.6 mm pitch linear array (Simulation)	160
Figure 4.25	Variation in the sound wave amplitude with the active aperture size at different depths for 5 MHz, 0.6 mm pitch linear array (Simulation)	160
Figure 4.26	Variation in the full beam width with the depth for different apertures using 5 MHz, 0.6 mm pitch linear array (Simulation)	161
Figure 4.27	Beam computation results with (a) 3 element (b) 6 element and (c) 8 element using 5 MHz, 0.6 mm phased array (Simulation)	161
Figure 4.28	Variation in 6 dB width of the virtual source at 2 mm depth from the surface for different number of active elements using 10 MHz, 0.3 mm pitch linear array (Simulation)	162
Figure 4.29	Variation in 6 dB width of the virtual source at 2 mm depth from the surface for different number of active elements using 5 MHz, 0.6 mm pitch linear array (Simulation)	163
Figure 4.30	Variation in the focal spot size for various active apertures using 10 MHz, 0.3 mm pitch linear array using PA-SAFT technique	165
Figure 4.31	Variation in focal spot size with various active apertures using 5 MHz, 0.6 mm pitch linear array using PA-SAFT technique	167
Figure 4.32	Beam computation results for an aperture size of 3.6 mm with focusing at 2 mm using (a) 10 MHz, 0.3 mm pitch linear array with 12 active elements and (b) 5 MHz, 0.6 mm pitch linear array with 6 active elements (Simulation)	168
Figure 4.33	Variation in the focal spot size with depth using PA-SAFT technique for 10 MHz, 0.3 mm pitch and 5 MHz, 0.6 mm pitch linear arrays	169

Figure 4.34	Limitation of SFLA, PA-SAFT and FMC techniques for characterization of flaws in unground weld bead	171
Figure 4.35	Placement of linear array on the wedge to generate angle beam	172
Figure 4.36	Methodology for data acquisition by angle beam PA-SAFT	173
Figure 4.37	Data acquisition by AB PA-SAFT technique (a) flaw near the back surface and (b) flaw near the scanning surface	173
Figure 4.38	Sound beam computation results using 5 MHz, 0.6 mm pitch linear array with sound beam steered at 60 deg. for an active aperture comprising of (a) 3 elements (b) 4 elements (c) 6 elements and (d) 10 elements (Simulation)	175
Figure 4.39	Variation in the beam spread angle and the grating lobe amplitude with number of elements in an active aperture using 5 MHz, 0.6 mm pitch linear array (Simulation)	176
Figure 4.40	Variation in the beam spread angle and the grating lobe amplitude with number of elements in an active aperture using 10 MHz 0.3 mm pitch linear array (Simulation)	177
Figure 4.41	Experimental set-up for data acquisition on a 0.5 mm dia. side drilled hole in an aluminum block using Angle Beam PA-SAFT	178
Figure 4.42	(a) Raw and (b) SAFT processed B-scan images of a 0.5 mm dia. side drilled hole in an aluminum block using angle beam PA-SAFT technique	179
Figure 4.43	Variation in focal spot size with depth by SFLA, PA-SAFT and FMC+TFM techniques using 10 MHz, 0.3 mm pitch linear array	181
Figure 4.44	Variation in focal spot size with depth by SFLA, PA-SAFT and FMC+TFM techniques using 5 MHz, 0.6 mm pitch linear array	182
Figure 5.1	Experimental set-up for detection and characterization of vertically stacked holes in carbon steel sample (a) SFLA, PA-SAFT and FMC techniques (b) Conventional angle beam phased array using focal laws (Scale in mm)	189
Figure 5.2	Sector scan images using (a) 16 (b) 32 (c) 48 and (d) 64 active elements for a carbon steel block with vertically stacked side drilled holes	190
Figure 5.3	(a) Raw B-scan images for carbon steel block with vertically stacked side drilled holes acquired using SFLA technique (a) lower gain and (b) higher gain	193
Figure 5.4	SAFT processed B-scan images for carbon steel block with vertically stacked side drilled holes acquired using SFLA technique (a) lower gain and (b) higher gain	195

Figure 5.5	(a) Raw B-scan and (b) SAFT processed B-scan images for carbon steel block with vertically stacked side drilled holes acquired using PA-SAFT technique	195
Figure 5.6	B-scan images for carbon steel block with vertically stacked side drilled holes using FMC + TFM technique (a) lower gain and (b) higher gain	196
Figure 5.7	Experimental set-up to determine the sensitivity for SFLA and PA-SAFT techniques for detection of volumetric flaws	199
Figure 5.8	SAFT processed B-scan images for aluminum block with 0.5 mm dia. side drilled holes using SFLA technique (a) lower gain and (b) higher gain	200
Figure 5.9	SAFT processed B-scan image for aluminum block with 0.5 mm dia. side drilled holes using PA-SAFT technique	201
Figure 5.10	FMC + TFM images for aluminum block with 0.5 mm dia. side drilled hole (a) 25 mm to 140 mm and (b) 140 mm to 250 mm	202
Figure 5.11	Experimental set-up for data acquisition on aluminum block with laterally separated side drilled holes	203
Figure 5.12	B-scan images using conventional phased array multi-point focusing on aluminum block with laterally separated side drilled holes (a) 16 el, (b)32 el, (c) 48 el and (d) 64 el	204
Figure 5.13	(a) Raw B-scan and (b) SAFT processed B-scan image of an aluminum sample with laterally separated side drilled holes using SFLA technique	206
Figure 5.14	(a) Raw B-scan and (b) SAFT processed B-scan image of an aluminum sample with laterally separated side drilled holes using PA-SAFT technique	208
Figure 5.15	FMC + TFM image of an aluminum sample with laterally separated side drilled holes	208
Figure 5.16	Variation in the sound wave amplitude at 25 mm depth in the lateral direction by SFLA and PA-SAFT technique using 10 MHz, 0.3 mm pitch linear array (Simulation)	210
Figure 5.17	Carbon steel sample with closely spaced side drilled holes for determining the resolving power of SFLA and PA-SAFT techniques (a) Placement of linear array and (b) Magnified view of holes (Scale in mm)	212
Figure 5.18	B-scan image and echodynamic plot of a carbon steel block with closely spaced side drilled holes using conventional phased array (a) 16 el aperture and (b) 64 el aperture (Scale in mm)	213

Figure 5.19	B-scan image and echodynamic plot of a carbon steel block with closely spaced side drilled holes using SFLA technique	213
Figure 5.20	B-scan image and echodynamic plot of a carbon steel block with closely spaced side drilled holes using PA-SAFT technique	214
Figure 5.21	FMC + TFM image of a carbon steel block with closely spaced side drilled holes	215
Figure 5.22	Experimental set-up for data acquisition on a planar flaw in 24 mm thick stainless steel plate using SFLA, PA-SAFT and FMC techniques	217
Figure 5.23	(a) Raw B-scan and (b) SAFT processed B-scan image of a 16° inclined slot in stainless steel plate by SFLA technique	218
Figure 5.24	(a) Raw B-scan and (b) SAFT processed B-scan image of a 51° inclined slot in stainless steel plate by SFLA technique	219
Figure 5.25	(a) Raw B-scan and (b) SAFT processed B-scan image of a 16° inclined slot in stainless steel plate by PA-SAFT technique	220
Figure 5.26	(a) Raw B-scan and (b) SAFT processed B-scan image of a 51° inclined slot in stainless steel plate by PA-SAFT technique	220
Figure 5.27	FMC + TFM B-scan images for inclined slots in stainless steel plate (a) 16° oriented slot and (b) 51° oriented slot	221
Figure 5.28	Methodology for assessment of depth and orientation of inclined slots from echodynamic plots (a) Processed B-scan image (b) Echodynamic in the depth direction for the upper tip (c) Echodynamic in the lateral direction for the upper tip (d) Echodynamic in the depth direction for the lower tip and (e) Echodynamic in the lateral direction for the lower tip	223
Figure 5.29	Experimental set-up for detection and characterization of planar flaw in 60 mm thick stainless steel plate (a) SFLA, PA-SAFT and FMC, (b) Angle Beam PA-SAFT	225
Figure 5.30	Processed B-scan images for a 0 deg. oriented planar flaw in 60 mm thick stainless steel plate (a) SFLA, (b) FMC+TFM, (c) PA-SAFT normal and (d) Angle Beam PA-SAFT	226
Figure 5.31	Processed B-scan images for a 20 deg. oriented planar flaw in 60 mm thick stainless steel plate (a) SFLA, (b) FMC+TFM, (c) PA-SAFT normal and (d) Angle Beam PA-SAFT	227
Figure 5.32	Experimental set-up for detection of surface planar flaw by Angle Beam PA-SAFT technique (a) Flaw on the back surface and (b) Flaw on the scanning surface	229

Figure 5.33	(a) Raw B-scan and (b) SAFT processed B-scan image for the notch on the back surface by Angle Beam PA-SAFT	230
Figure 5.34	(a) Raw B-scan and (b) Simulation result and (c) SAFT processed B-scan image for the notch on the scanning surface by Angle Beam PA-SAFT	232
Figure 5.35	SAFT processed B-scan images of a notch on the back surface in aluminum plate (actual sound velocity = 6300 m/s) by SFLA technique processed with (a) Sound velocity 6300 m/s and (b) Sound velocity 6200 m/s	234
Figure 6.1	Experimental set-up for data acquisition on weld samples by SFLA, PA-SAFT and FMC techniques	241
Figure 6.2	Sound velocity profile across the weld and base metal region	241
Figure 6.3	Clustered porosity in the weld sample (Scale in mm)	243
Figure 6.4	(a) Raw B-Scan (b) SAFT processed B-scan image showing multiple spot indications from clustered porosity in the weld sample by SFLA technique	243
Figure 6.5	(a) Raw B-Scan (b) SAFT processed B-scan image showing multiple spot indications from clustered porosity in the weld sample by PA-SAFT technique	244
Figure 6.6	B-scan image showing multiple spot indications from clustered porosity in the weld sample by FMC + TFM technique	244
Figure 6.7	Slag inclusion in the weld sample (Scale in mm)	245
Figure 6.8	(a) Raw B-Scan (b) SAFT processed B-scan image showing the upper and the lower tip signals from the slag inclusion in the weld sample by SFLA technique	246
Figure 6.9	(a) Raw B-Scan (b) SAFT processed B-scan images showing the upper and the lower tip signals from the slag inclusion in the weld sample by PA-SAFT technique	247
Figure 6.10	B-scan image showing the upper and the lower tip signals from the slag inclusion in the weld sample by FMC + TFM technique	247
Figure 6.11	Lack of sidewall fusion in the weld sample (Scale in mm)	249
Figure 6.12	(a) Raw B-Scan (b) SAFT processed B-scan image showing the upper and the lower tip signals from the lack of fusion in the weld sample by SFLA technique	250
Figure 6.13	(a) Raw B-Scan (b) SAFT processed B-scan image showing the upper and the lower tip signals from the lack of fusion in the weld sample by PA-SAFT technique	251
Figure 6.14	B-scan image showing the upper and the lower tip signals from the lack of fusion in the weld sample by FMC + TFM technique	251
Figure 6.15	Root crack in the weld sample (Scale in mm)	252

Figure 6.16	(a) Raw B-Scan (b) SAFT processed B-scan image showing the crack tip signal of the root crack in the weld sample by SFLA technique	252
Figure 6.17	(a) Raw B-Scan (b) SAFT processed B-scan image showing the crack tip signal of the root crack in the weld sample by PA-SAFT technique	253
Figure 6.18	B-scan image showing the crack tip signal of the root crack in the weld sample by FMC + TFM technique	253
Figure 6.19	Experimental arrangement for data acquisition by Angle beam PA-SAFT technique (a) Root crack and (b) Toe crack (Scale in mm)	256
Figure 6.20	Photograph of the root crack in the austenitic stainless steel weld joint (Scale in mm)	256
Figure 6.21	(a) Raw B-Scan (b) SAFT processed B-scan image showing the crack tip signal and the corner trap signal from the root crack in the weld sample by Angle beam PA-SAFT technique	257
Figure 6.22	Photograph of the toe crack in austenitic stainless steel weld joint (Scale in mm)	258
Figure 6.23	(a) Raw B-Scan (b) SAFT processed B-scan image showing the crack tip signal and the corner trap signal from the toe-crack in the weld sample by Angle beam PA-SAFT technique	259
Figure 6.24	Photograph of carbon steel weld sample with lack of sidewall fusion (Scale in mm)	261
Figure 6.25	SAFT processed B-scan images by (a) SFLA (b) PA-SAFT and (c) Angle Beam PA-SAFT (d) FMC + TFM techniques showing the upper and lower tip signals from the lack of sidewall fusion in the carbon steel weld joint	262
Figure 6.26	B-scan images for the root crack in austenitic stainless steel weld joints(a) Raw B-scan image by normal beam PA-SAFT, (b) SAFT processed image by normal beam PA-SAFT, (c) SAFT processed SFLA image (d) FMC+TFM and (e) SAFT processed image by Angle beam PA-SAFT showing the crack-tip and corner trap signal	264
Figure 6.27	Longitudinal and circumferential welds in TAPS RPV	267
Figure 6.28	Schematic of C1 weld joint and its distance from the top flange	268
Figure 6.29	Location of the bolt penetrations on the flange surface with respect to the clad on RPV ID surface	269
Figure 6.30	Beam Computation result at the C1 weld location using 2 MHz, 25 mm dia. single crystal normal beam transducer (Simulation)	270
Figure 6.31	Beam Computation result at the C1 weld location with beam focusing and steering using 5 MHz, 1 mm pitch, 64 active elements linear array (Simulation)	271
Figure 6.32	Beam Computation result at C1 weld location with single element excitation (SFLA) using 2 MHz, 0.8 mm pitch, 64 elements linear array (Simulation)	272

Figure 6.33	Variation in sound wave amplitude at C1 weld location for various active apertures of 2 MHz, 0.8 mm pitch linear array using PA-SAFT technique (Simulation)	275
Figure 6.34	Beam computation results at C1 weld location with 16 active elements of 2 MHz, 0.8 mm pitch, 64 elements linear array using PA-SAFT technique (Simulation)	275
Figure 6.35	Variation in sound beam amplitude profile from ID to OD at C1 weld location using single crystal normal beam transducer (2 MHz, 25 mm dia.), Conventional phased array with steering and focusing, SFLA and PA-SAFT technique using 2 MHz, 0.8 mm pitch, 64 elements linear array (Simulation)	276
Figure 6.36	B-scan image using 2 MHz, 0.8 mm pitch, 64 elements linear array with steering and focusing at C1 weld location using an active aperture of (a) 16, (b) 32, (c) 48 and (d) 64 active elements	278
Figure 6.37	B-scan image using 5 MHz, 1 mm pitch, 64 elements linear array with steering and focusing at C1 weld location (a) side drilled holes and (b) ID and OD notches	280
Figure 6.38	Raw B-scan image using 2 MHz, 0.8 mm pitch, 64 elements linear array with SFLA technique for the detection of (a) side drilled holes and (b) notches	281
Figure 6.39	SAFT processed B-scan images with 2 MHz, 0.8 mm pitch, 64 elements linear array using SFLA technique showing signals from (a) side drilled holes and (b) notches	281
Figure 6.40	Raw B-scan image with 2 MHz, 0.8 mm pitch, 64 elements linear array using PA-SAFT for the detection of (a) side drilled holes and (b) notches	282
Figure 6.41	SAFT processed B-scan images with 2 MHz, 0.8 mm pitch, 64 elements linear array using PA-SAFT technique showing signals from (a) side drilled holes and (b) notches	283

LIST OF TABLES

Table No		Page No
Table 3.1	Details of linear arrays used for the experimental work	80
Table 3.2	Details of parametric study carried out to evaluate the effect of array based parameters on the sound beam focusing by SFLA technique	89
Table 3.3	Details of weld samples with volumetric and planar flaws used for the experimental work	106
Table 4.1(a)	k_{6dB} values for 2 MHz, 0.8 mm pitch, 64 elements linear array	122
Table 4.1(b)	k_{6dB} values for 5 MHz, 0.6 mm pitch, 64 elements linear array	123
Table 4.1(c)	k_{6dB} values for 10 MHz, 0.3 mm pitch, 128 elements linear array	124
Table 4.2(a)	Experimental and calculated θ_{6dB} using 10 MHz, 0.5 mm pitch linear array	126
Table 4.2(b)	Experimental and calculated θ_{6dB} using 8 MHz, 0.5 mm pitch linear array	126
Table 4.2(c)	Effect on orthogonal dimensions on beam spread using 5 MHz, linear array	127
Table 4.3	Variation in δ_{6dB} with D/λ	140
Table 5.1	Results on carbon steel sample with vertically stacked holes using conventional angle beam phased array technique	191
Table 5.2	Comparison of SDR, GR, 6 dB spread and the amplitude variation for carbon steel sample with volumetric flaws by various techniques	197
Table 5.3	Comparison of results on aluminum block with laterally separated side drilled holes using conventional phased array	205
Table 5.4	Comparison of 6 dB spread, lateral coverage and amplitude variation for the laterally separated holes using conventional phased array, SFLA, PA-SAFT and FMC techniques in an aluminum block	209
Table 5.5	Results of depth and orientation assessment of inclined slots in the stainless steel plate by SFLA, PA-SAFT and FMC+TFM approaches	224
Table 5.6	Comparison of results obtained on assessment of depth and orientation on thick SS block with simulated planar flaws by various techniques	228
Table 6.1	Results of depth sizing of volumetric flaws by various techniques	248
Table 6.2	Assessment of flaw height and orientation of planar flaws in the weld samples by SFLA, PA-SAFT and FMC techniques	254

Table 6.3	Assessment of the depth of the cracks in the weld samples by Angle Beam PA-SAFT technique	259
Table 6.4	Near field length and the focusing depth using various apertures	274
Table 6.5	Near field for various active apertures	279
Table 6.6	6 dB spread of side drilled holes and notches obtained by various techniques	284

NOMENCLATURE

b	Orthogonal Dimension of the Linear Array
c	Sound Velocity
d	Inter-Element Spacing
D	Diameter of the Piezoelectric Crystal or Size of Active Aperture
E	Error
f	Focal Length
G_p	Gain in the Acoustic Pressure
h	Defect Height
$H(\theta)$	Beam Directivity or Directivity Function
I	Intensity Value for Pixel Location
k	Beam Divergence Constant
K	Focus Factor
L_f	Length of the Focal Zone
L_{eff}	Effective Aperture Length
N	Total Number of Elements in an Array
N_o	Near Field Length
p	Acoustic Pressure
p'	Pitch
R	Radius of Curvature of acoustic lens
R_c	Reflection Coefficient
t	Thickness
T_c	Transmission Coefficient
V_L	Velocity of Longitudinal Wave
w	Element Width
Z	Acoustic Impedance
Z_{TR}	Transition Range
λ	Wavelength
ρ	Density
δ	Diameter of the Focal Spot
τ	Time Delay
θ	Beam Divergence Angle

θ_s	Steering Angle
β	Beam Angle
ν	Frequency of sound wave
μm	Micrometer
ns	Nanosecond
MHz	Mega-Hertz
dB	Decibel
SAFT	Synthetic Aperture Focusing Technique
SNR	Signal to Noise Ratio
PAUT	Phased Array Ultrasonic Testing
FMC	Full Matrix Capture
TFM	Total Focusing Method
ROI	Region of Interest
NDE	Non-Destructive Examination
SFLA	Synthetic Focusing using Linear Array
PA-SAFT	Phased Array – SAFT
EDM	Electrode Discharge Machining
OD	Outside Diameter
ID	Inside Diameter
CPSM	Cylindrical Phase Shift Migration
<i>API</i>	Array Performance Indicator
SPA	Sampling Phased Array
M-SAF	Multi-Element Synthetic Aperture Focusing
M-SPA	Multi-Element Synthetic Phased Array
BiPBF	Bi-directional Pixel-Based Focusing
TIVAS	Technique to Image using Virtual Array Sources
FDTD	Finite Difference Time Domain
SASB	Synthetic Aperture Sequential Beamforming
DAC	Distance Amplitude Correction
PRL	Primary Reference Level
DGS	Distance Gain Size
<i>SP</i>	Sound Path
TOFD	Time of Flight Diffraction

<i>PCS</i>	Probe Centre Separation
RATT	Relative Arrival Time Technique
AATT	Absolute Arrival Time Technique
ΔUT	Path Difference
TEA	Total Effective Aperture
RPV	Reactor Pressure Vessel
BWR	Boiling Water Reactor
SDR	Size to Distance Ratio
GR	Gain Reserve
POD	Probability of Detection

INTRODUCTION

1.1 Focusing of Ultrasonic Beam

Sound beam focusing has always been a subject of interest in ultrasonic non-destructive evaluation. Focusing not only helps to achieve higher sensitivity, good lateral resolution and improved signal to noise ratio, but also in precisely locating the flaw extremities. This in turn helps to characterize the flaw accurately in terms of its depth (also referred as height or through-wall dimension) and orientation [1-4]. Many ‘hardware’ and ‘software’ based approaches aimed at focusing ultrasound have been developed over the last few decades and have been successfully used during ultrasonic examination of engineering components in industries [4-6]. While the hardware based approaches lead to the ‘direct’ focusing of sound beam within the material, the software based approaches rely on the post processing of the data acquired using a divergent sound beam to achieve sound beam focusing in the region of interest.

The traditional way of sound beam focusing is through the use of an acoustic lens, which is fitted to the front of the crystal. Such transducers are used in immersion testing and several automated systems using spherically or cylindrically focused ultrasonic transducers are used in various industries [7-10]. The use of a lens makes the beam more collimated, but at the same time there is a considerable loss in the transmitted signal. Moreover, transducers with lens can be used only for immersion test, which may not be practical for all component geometries. The lens based focusing transducer gives focusing at a fixed distance or in a fixed zone. As a result, if it is required to carry out the inspection of a thick component with a focused sound beam, then either one needs multiple transducers with different focal lengths or one needs to carry out multiple inspections with the same transducer with varying water path.

Another way of focusing the sound beam is by the post-processing reconstruction technique named Synthetic Aperture Focusing Technique (SAFT). SAFT is typically applied on the B-scan data collected using the conventional pulse-echo technique or the time-of-flight diffraction technique [11-13]. In the conventional SAFT, for each transducer position, the raw data containing a sound beam scattered by a flaw is collected using a divergent ultrasonic beam. During the reconstruction process, the sound beams are time-shifted or back propagated to the scattering source and averaged out using wave propagation formulae. The signal amplitude at the flaw location is highly improved as a result of constructive interference of the sound beam from various locations. At locations other than the flaw, poor correlation of the signal phase causes the destructive interference of the sound beam, which leads to a considerable drop in the signal amplitude. SAFT technique offers high lateral resolution and improves the signal to noise ratio (SNR) of ultrasonic images by eliminating the background noise [14,15]. The effectiveness of SAFT depends on the use of a divergent sound beam and the step size at which the data is acquired for processing. For SAFT processing to be effective, the flaw must be located beyond the near field length, which, for a given material is determined by the crystal diameter and the frequency. Smaller crystal diameter and lower frequency result in a smaller near field and a larger beam divergence. The main advantage of the SAFT is that the focusing capability is independent of the length of the sound path. The lateral resolution that can be theoretically achieved with the SAFT is $D/2$, where D is the diameter of the piezoelectric crystal [16-17]. However, one needs to consider two aspects while using a very small size piezoelectric crystal. The first one is the required sensitivity, which deteriorates as D decreases, and the second one is the availability of the smallest size piezoelectric crystal for a given frequency from the manufacturing and handling point of view. These two aspects determine the practically achievable focusing using SAFT while using a conventional single crystal transducer.

The use of linear arrays to focus the sound beam has gained significant popularity in the last few years. One of the ways of using linear arrays to achieve the sound beam focusing is by phased array ultrasonic testing (PAUT). With PAUT, one can manipulate the sound beam profile within the component by controlling the sequence in which the elements of an array are excited and the time-delay in their excitation and reception. PAUT offers several advantages over the acoustic lens based sound beam focusing. One of these is the possibility of sound beam focusing using contact transducers [18,19]. The other advantage is that the focusing depth and the direction can be varied using a single linear array transducer by the use of appropriate focal laws [20-26]. As a result, one can avoid multiple inspections of a component with a focused transducer and save on the inspection time. Also the fact that the sound beam can be translated electronically from one end of the array to the other, the mechanical design of the manipulator also becomes much simpler. PAUT offers better sensitivity, lateral resolution, good probability of detection and faster inspection as compared to the conventional single crystal based inspection systems. The capability of sound beam focusing using phased array has been successfully utilized for flaw detection and characterization in numerous industries [27-36].

Another way of focusing the sound beam using linear arrays is by a technique known as Full Matrix Capture – Total Focusing Method (FMC + TFM). In FMC, the raw B-Scan data is collected element by element [37,38]. Initially, the first element acts as a transmitter and all elements act as receivers. Subsequently, the second element acts as a transmitter and all as receivers. This goes on till the last element is excited. This process collects the time domain signals for all the transmitter and receiver combinations and generates N^2 A-scan signals for a linear array transducer containing N elements. Once the data is acquired using FMC, the imaging of the region of interest (ROI) is done using Total Focusing Method (TFM). With TFM, the ROI is discretized into grids and the

sound beam is focused at every point in the grid by summing up the signals from all the elements in an array. For each possible transmitter-receiver combination, the summation process is carried out to yield focusing at every point in the image [39,40]. FMC approach leads to a high resolution imaging for the enhanced detection and sizing of flaws. In order to realize the real-time FMC+TFM system for industrial use, it is required that the phased array instrument, which is used to acquire the full matrix data, has the same number of parallel receiver channels as the number of elements in the array. This requirement adds to the cost of instrumentation. At the same time, the data size for TFM processing becomes enormously large, especially while dealing with an array with large number of elements. Also the fact that a single element in an array is used for the sound beam transmission may be a drawback in terms of the sensitivity for flaw detection in thick and attenuating materials. To overcome the drawback of FMC + TFM technique in terms of the sensitivity, a new set of techniques based on the concept of virtual source have been developed in recent years [41-43].

1.2 Flaw Characterization by Ultrasonic Non-Destructive Evaluation

Ultrasonic non-destructive evaluation carried out in industries typically involves detection of flaws that may affect the integrity of component under test. Once detected, the flaw is sized for its critical dimensions and if required, characterized in terms of its metallurgical nature such as crack, slag, porosity, lack-of-fusion etc. More often than not, the detection of a flaw in the component by ultrasonic test is based on the principle of echo or reflection. Once the echo from a flaw is received, there are several approaches for analyzing the reflected signal so that more and accurate information is obtained on the flaw characteristics. These analysis techniques are aimed at: (i) differentiating the real signals from the spurious ones, (ii) determining the flaw location, (iii) evaluating flaw dimensions in terms of length and depth and (iv) classifying the flaw in to crack-

like or non-crack-like. The reliability of flaw detection and the accuracy of its characterization depend to a great extent on the property of material under investigation and the sound beam profile generated within the material by the piezoelectric crystal. Sound waves, while travelling within the material, not only interact with the flaw, but also with the microstructural features such as grain boundaries. These interactions lead to sound beam scattering, which in extreme cases, such as while dealing with coarse and anisotropic grain structure, may lead to poor sensitivity in flaw detection and in-accurate estimation of flaw characteristics [44-46].

Non-destructive examination (NDE) is an integral part during the fabrication of equipments and components for various industries such as nuclear, petrochemical, power, transportation etc. The manufacturing codes and standards dealing with these industries demand that various product forms such as castings, forgings, rolled/extruded products, and weld joints should undergo rigorous inspection by NDE techniques to ensure that the required quality standard, as stipulated by the designer, is met [47-51]. Moreover, these industries also have in-service inspection codes, which necessitate periodic inspection of components, including the weld joints, by NDE to detect and characterize the flaws so that the fitness-for-service assessment of the flawed component can be carried out [52,53]. Ultrasonic NDE plays a crucial role, both during manufacturing stage inspection and in-service inspection, for detection and characterization of flaws. While dealing with weld joints, typical flaws that are required to be detected by ultrasonic NDE are slag, porosity, lack-of-fusion, lack of penetration and cracks [54-56]. The volumetric flaws such as slag and porosity have relaxed acceptance standards in terms of their dimensions. But the planar flaws such as lack-of-fusion, lack of penetration and cracks, which pose a serious threat to the integrity of pressurized components, are required to be detected reliably and characterized accurately [57-59]. One of the crucial parameters governing the acceptance of a component with planar flaws is the

flaw height (depth or through-wall dimension). The conventional ultrasonic testing involves flaw sizing based on the amplitude of the reflected signal [60-62]. The approach for flaw height assessment can be either by comparing the signal amplitude from the flaw with that from a known reference defect or by using amplitude drop techniques (6 dB or 20 dB drop). The amplitude comparison based approach is prone to errors. The real flaws may not be as good reflectors of sound waves as the reference flaws and hence any comparison of reflected signal amplitude from a real flaw with that from a reference flaw leads to underestimation of the flaw height. The dB drop methods for flaw height estimation are also not accurate as errors are introduced due to the sound beam divergence and non-perpendicular incidence of sound beam on the flaw surface [63,64]. Although these approaches are continued to be used in the industry, an approach based on the time-of-flight of the diffracted signals from the flaw extremities has proven to be more accurate for the estimation of the flaw height [65,66].

Modern day ultrasonic testing relies to a great deal on imaging techniques. Typically, ultrasonic imaging involves acquiring the raw A-scan data (time vs amplitude), sampling it using high speed digitizers and then processing the digitized data to create an image. The acquired data can be presented either in the form of a cross-sectional view called a B-scan, or a plan view called a C-scan [67-70]. The raw data and the images can be subjected to several signal processing and image processing algorithms for a variety of purposes, which may include: improving the signal to noise ratio, SAFT, TFM etc. In many automated ultrasonic systems that are used in the industries, ultrasonic imaging has become a standard practice of acquiring the test data during inspection of a product or a component. The reliability of flaw detection and the accuracy of its characterization from the ultrasonic image depend to a great deal on the signal to noise ratio and the resolution (lateral and depth) at which the image has been generated. When an ultrasonic image is used for

depth sizing of flaws based on the time-of-flight, then the accuracy that can be achieved depends on the uncertainty in locating the flaw extremities. To that effect, if one can obtain ‘sharp’ or ‘point-like’ images of the flaw extremities, the accuracy in depth sizing would be very high. This can be realized by focusing the sound beam at the crack extremities using: (a) focused transducer, (b) phased array, (c) SAFT or (d) approaches that are based on the combination of these.

1.3 Background of the Current Research

During the current research work, an integrated approach combining ‘phased array’ and ‘Synthetic Aperture Focusing Technique (SAFT)’ has been investigated for sound beam focusing. The usefulness of this approach for characterization of flaws has been studied by extensive experimental work. The methodology for data acquisition and an algorithm for data processing by SAFT have been developed for the experimental set-up employed, to detect and characterize a variety of simulated and real flaws in plates and weld joints. The objective of this work is to derive the benefits of both, array based inspection and SAFT processing, so as to achieve the sound beam focusing, which is comparable to, or even better than that can be achieved using conventional phased array or SAFT alone. Since the focusing within the material is achieved by SAFT, the raw B-scan data is acquired by a divergent sound beam. Also the fact that a linear array is used, the B-scan data is acquired by electronic scanning.

Two separate techniques have been studied, standardized and validated viz. Synthetic Focusing using Linear Array (SFLA) and Phased Array – SAFT (PA-SAFT). With both the techniques the raw data is acquired by a divergent sound beam, which is subsequently processed by SAFT to achieve sound beam focusing. SFLA uses a single element for sound beam transmission and reception. Unlike FMC, where all the elements of an array receive the sound beam for all the

transmissions, with SFLA, the reception is by the same element in the array, which has transmitted the sound beam. This approach has two specific advantages. Firstly, since the transmission and reception at any given point of time is by a single element of an array, the data acquisition is extremely fast without the need of large number of parallel receiver channels that are required with FMC approach. Secondly, the data size for the post processing using SFLA technique is much smaller than what is encountered using FMC. For example, if a linear array with 128 elements is used for data acquisition using SFLA and FMC, and the data is acquired for 10000 points (1 byte) each, then while using FMC, the data size would be of the order of 164 MB ($128 * 128 * 10000 * 1$). With SFLA, the data size under identical conditions would be of the order of 1.4 MB, which is significantly less than what is required for FMC. One of the drawbacks of SFLA and FMC techniques is the low acoustic power of the transmitted sound beam in the material, since a single element is used for the sound beam transmission. This could pose a major limitation to the detection and characterization of flaws in thick and highly attenuating materials. To overcome this, a technique named Phased Array-SAFT (PA-SAFT), which is based on the concept of virtual array of sources, has been investigated. This technique uses a group of elements for the sound beam transmission. The group has much lesser number of elements than what would be required using a ‘focal law’ based conventional phased array. The use of more number of elements for the sound beam transmission ensures higher acoustic power, leading to better sensitivity and deeper penetration than SFLA and FMC techniques. With PA-SAFT technique, a virtual array of sources is created very close to the scanning surface. A divergent sound beam emanating from these virtual sources is used to acquire the data. The data is subsequently processed by SAFT.

The ability of the sound beam focusing by any technique can be evaluated in terms of the size of the focal spot. With SFLA and PA-SAFT techniques, the array based factors, which affect the

sound beam divergence and the quality of the raw B-scan data, such as the element size (SFLA) or aperture size (PA-SAFT), the pitch at which the elements are arranged in the array, the frequency of sound and the total effective aperture, is likely to influence the focal spot size achieved. Similarly, during SAFT processing if the input values of the sound velocity in the material, the element pitch and the beam divergence angle is different than the actual values, it is also likely to affect the focal spot size.

Since both SFLA and PA-SAFT techniques use a divergent sound beam for acquiring the raw B-scan data, a systematic study has been carried out as part of this research work to evaluate the ‘beam spread’ for piezoelectric crystals having a sub-millimeter dimensions that are typically encountered with linear arrays. The actual beam spread from the miniature elements in an array varies significantly from the beam spread predicted by the mathematical equation given in the literature for the conventional single crystal piezoelectric elements [1]. The effects of various factors, both array based and the SAFT processing based, on the focal spot size that can be achieved by SFLA and PA-SAFT techniques have been analyzed and studied in details. Additionally, for PA-SAFT technique, the aperture size or the number of active elements to be used for sound beam transmission during data acquisition, are optimized by simulation and experimental studies. A variant of PA-SAFT technique using an angle beam for specific cases (called as Angle Beam PA-SAFT), where SFLA, PA-SAFT and FMC techniques cannot be used, has been studied. The capabilities of SFLA and PA-SAFT techniques for the detection and characterization of volumetric and planar flaws have been explored. The resolving power of SFLA and PA-SAFT techniques under given experimental conditions have been determined. These studies are carried out on the samples with artificial flaws in the form of side drilled holes (simulating volumetric flaws) and angular slots (simulating planar flaws), made by electrode

discharge machining (EDM). The effectiveness of these techniques for the characterization of real flaws has been demonstrated on weld samples containing a variety of volumetric and planar flaws. Finally, the methodology for data acquisition and processing using SFLA and PA-SAFT techniques is developed for the in-service inspection of a weld joint in a reactor pressure vessel of a nuclear boiling water reactor.

1.4 Structure of the Thesis

Chapter 1 gives the background of the work carried out as part of the current research. Various techniques, both conventional and advanced, that are used for sound beam focusing are discussed. The importance of flaw characterization by NDE in general and the ultrasonic techniques in particular, which are currently being used for this purpose are mentioned. The highlights of the work carried out as part of this research has been brought out.

Chapter 2 deals with the literature review on the subject of sound beam focusing. A brief account on the evolution of the sound beam focusing methods from ancient to modern times has been given. The current state of array based techniques used for sound beam focusing along with their limitations has been described. The Chapter also gives a brief review of the amplitude based and the time-of-flight based ultrasonic techniques for depth sizing of flaws. Finally, the motivation and the objective of the current research have been brought out.

Chapter 3 deals with the experimental programme. Various objectives of the current research and the details of the samples used for the experimental work to meet these objectives have been described. The experimental set-up, including the details of the phased array instrumentation and the linear arrays used, for this research work has been described. A brief description of the SAFT algorithm used for the processing of the raw B-scan images is given in this Chapter. The

experimental details regarding the placement of linear arrays on the samples and the process of data acquisition using various techniques have been explained.

Chapter 4 deals with the investigation of SFLA and PA-SAFT techniques for sound beam focusing. To begin with, the Chapter describes the results of the experimental work carried out to derive the empirical relationship for arriving at the divergence of the sound beam emanating from a miniature piezoelectric element, which is typically used in a linear array. The methodology adopted for the acquisition and the processing of the B-scan data using SFLA and PA-SAFT techniques has been described. Results on the study of various factors (array based and SAFT processing based) affecting the sound beam focusing using SFLA and PA-SAFT techniques have been brought out. The simulation and experimental work carried out for the optimization of the aperture size for PA-SAFT technique has been described in details.

Chapter 5 deals with exploring the capabilities of SFLA and PA-SAFT techniques for the detection and characterization of volumetric and planar flaws. The Chapter also brings out the sensitivity, the lateral coverage and the limit of resolution that can be achieved using SFLA and PA-SAFT techniques under given experimental conditions. The results of the experimental work carried out on various samples containing artificial flaws are described in details. The comparison of the results on flaw detection and sizing by SFLA, PA-SAFT and FMC+TFM techniques has been brought out in this Chapter. The Chapter also brings out the uncertainty associated with the depth sizing of planar flaws by SFLA and PA-SAFT techniques.

Chapter 6 deals with the application of SFLA and PA-SAFT techniques for the evaluation of welds. The results on the characterization of real weld flaws, both volumetric and planar, by SFLA and PA-SAFT techniques are discussed in this Chapter. The Chapter also describes the application

of SFLA and PA-SAFT techniques for in-service inspection of a circumferential weld joint in a reactor pressure vessel of a nuclear boiling water reactor.

Chapter 7 summarizes the results, conclusions drawn, the contributions of the current research and the suggestions for future work.

2.1 Introduction

The primary objective of this research work is to investigate the sound beam focusing techniques based on an integrated approach involving the use of linear arrays and synthetic aperture focusing technique (SAFT). Subsequently, the effectiveness of these techniques for the detection and characterization of flaws in engineering components have been studied. This Chapter describes the evolution of sound beam focusing techniques from ancient to modern times. A brief account of the advanced techniques based on the use of linear arrays, which are developed in the last couple of decades, for sound beam focusing are discussed. The advantages and the limitations of these techniques have been brought out. The Chapter also briefly describes the conventional and the advanced ultrasonic techniques for the characterization of flaws, more specifically the depth sizing, in engineering components. Finally, the objective and the motivation of this research work have been brought out.

2.2 Sound beam focusing

Like the beam of light, the sound beam can also be focused at a given distance from the source. However, there are some fundamental differences between the light and the sound wave, which must be considered during their focusing. One important basic difference is between the wavelengths (λ) that we generally deal with while using a light wave and a sound wave. With light, a mean wavelength of 0.6 μm is very common and the thickness of the lenses that are typically used for focusing are between a few millimetres to a few centimetres. This works out to be almost 10^4 to 10^5 times the wavelength. With ultrasound, the wavelength in majority of metals is typically of the order of few millimetres while using a 1 MHz frequency. The average thickness of the lens is of the same order of few centimetres, which is about the same or 10

times the wavelength of sound. The second difference is related to the interference phenomenon. In geometrical optics, interference phenomena cannot be assumed as characteristic. There are path differences of the order of 100λ between the elements of a light beam a few millimetres apart on the surface of a lens. Faults in the surface may reach dimensions of half a wavelength and not cause destructive interference at the focus. By way of comparison, the sound waves with opposite phases are emitted from the surface of an ultrasonic lens in concentric rings several millimetres apart and these waves interfere. The other basic difference between the light and the sound wave is the coherence. Wave packets of light, apart from those emitted from strictly monochromatic sources, are not generally coherent. In acoustics, the electrical excitation of an un-damped piezoelectric crystal gives almost monochromatic waves and coherence is always assured.

2.2.1 Ancient and modern methods

Tarnoczy [71] has given an excellent review on the evolution of the sound beam focusing methods from ancient to modern times. The oldest method of sound beam focusing is based on the use of reflection. The sound reinforcing effect of the curved surfaces has been known since early times. Athanasius Kircher dealt with the acoustic beaming based on the reflection in a geometrically correct way in his book *Phonurgia Nova* (1673) (Figure 2.1). Reflection systems include concave reflectors (spherical, parabolic etc.), conical and twin-cone concentrators, and combinations of these types. Important theoretical and experimental work on the concentrators of this kind has been carried out by Griffing and Fox [72].

Acoustic prisms and lenses using the principle of refraction for sound beam focusing also have a long history. In 1852, Sondhaus made sonic lenses of collodium skin filled with carbon dioxide. Since the speed of sound in carbon dioxide is less than in air, a convex lens delays the centre of the sound beam more than the periphery and focusses the sound. A few years later, in 1856, Hajeck made lenses and prisms from other gaseous materials and demonstrated the

focussing effect with concave lenses, if the speed of sound in the lens material is larger than in the ambient medium (air). In ultrasonics, Hopwood [73-75] was the first to deal with the application of lenses. He was followed by Ernst [76-79] and several Soviet investigators who dealt with the theory and construction of acoustic lenses.

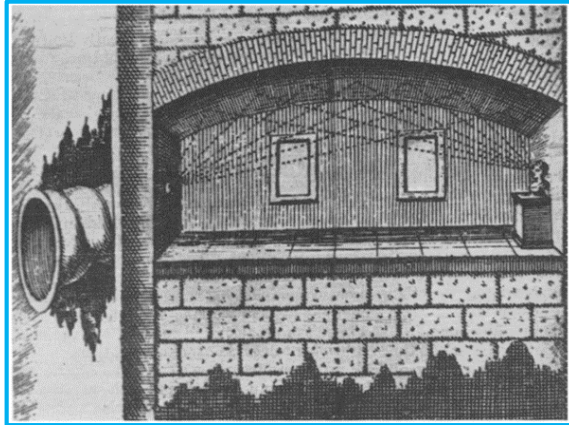


Figure 2.1: Ancient method of sound beam focusing using concave surface [71]

Sound beam focusing based on the interference has also been studied by many researchers. Rayleigh used zone plates for the acoustic purposes as early as 1888. Tarnogzy [71] used waveguides for focusing of sound wave based on the interference phenomenon. Waveguides produce equality in phase with certain path or velocity differences and this results in the concentration of energy. Figure 2.2 shows the principle of sound beam focusing using waveguides. A plane wave incident on A_1 , A_2 travels different paths and interferes constructively at B.

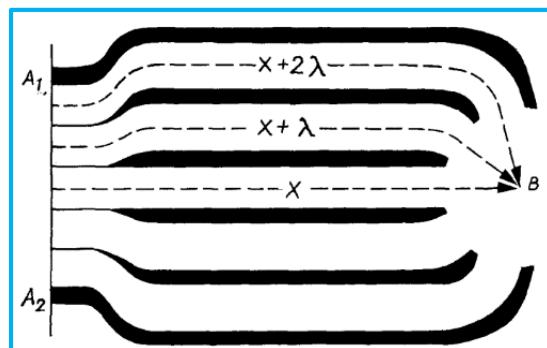


Figure 2.2: Sound beam focusing by waveguide [71]

The most natural acoustic focussing system is provided by a concave emitter, which has no conventional optical analogy. If every point on the surface of a piezoelectric or magnetostrictive emitter emits in the same phase, the shape of the emitted wavefront corresponds, near the surface, to the shape of the surface. If the surface is concave, spherical waves are formed which are focussed at the centre of curvature. In other words, the focussing can be produced by the radiator itself with the focal length equal to the radius of curvature. The invention of ferroelectric substances that could be cast to the shape of lenses made possible the production of widely different concave radiators [80].

2.2.2 Acoustic lenses

Acoustic lenses provide a better alternative to the focusing of the sound beam as compared to the reflectors. These lenses are generally made from solids. If the medium where the sound is required to be focused is a liquid (water, oil) and the lens is made of a solid (Plexiglas, Polystyrene), then the velocity of sound in the lens is higher than the surrounding medium. This is the exact reverse of what happens in optics, where the velocity of light in the surrounding medium (air) is more than the velocity in the lens (glass). Under these conditions, the sound beam exiting from the lens will get focused in the surrounding medium only if the curvature of the lens is concave.

Several aspects must be taken into account in the construction of acoustic lenses. The first one is the acoustic impedance ($Z = \rho c$, where ρ is the density and c is the sound velocity) of the lens material with respect to the acoustic impedance of the surrounding medium. At the interface between the lens and water, the reflection coefficient is given by [1]:

$$R_c = (Z_2 - Z_1)/(Z_2 + Z_1) \quad [1]$$

where, Z_1 and Z_2 are the acoustic impedances of the lens material and water.

Equation 1 indicates that for better transmission of sound in water, the Z value of the lens material should not differ too much from that of water.

Another consideration that needs to be given while selecting the material for the construction of acoustic lenses is the velocity of sound. For a plano-concave lens, the focal length can be given as:

$$f = \frac{R}{(1 - \frac{c_2}{c_1})} \quad [2]$$

where, f is the focal length, R is the radius of curvature of the lens and c_2 and c_1 are velocities of sound in water and the lens material.

Equation 2 suggests that for better refraction and hence the focusing, the velocity of the lens material must be significantly different from that of water. However, this in turn would increase the mismatch in the acoustic impedances and violate the requirements for better transmission.

Considering the above two aspects, the acoustic lenses are generally made from plastics.

The focal distance that can be achieved by the use of acoustic lens can never be larger than the near field length (N_o), which is given by [1]:

$$N_o = D^2/4\lambda \quad [3]$$

where, D is the diameter of the piezoelectric element and λ is the wavelength of sound.

The ratio of focal distance to the near N_o is called as the focus factor K . For K greater than 0.6, the degree of focusing is considered small, while for K less than 0.3, it is considered strong.

For a plane radiator focused by an added lens, the axial pressure distribution is given by [1]:

$$p = p_0 \frac{2}{1 - \frac{z}{z_0}} \sin\left[\frac{\pi}{\lambda} \left(\sqrt{(z - h)^2 + \frac{D^2}{4}} - (z - \frac{c_2}{c_1} h) \right)\right]$$

where, [4]

$$h = R - \sqrt{R^2 - \frac{D^2}{4}} \quad z_0 = \frac{h^2[1 - (c_2/c_1)^2] + a^2}{2h[1 - (c_2/c_1)]}$$

p is the acoustic pressure, z is the distance from the lens in water, D is the diameter of the piezoelectric crystal, R is the radius of curvature of lens and c_2 and c_1 are the sound velocities in water and lens material respectively.

Figure 2.3 shows the variation in the echo amplitude from a point reflector, derived from Equation 4 for a typical case of $D = 10$ mm, $\lambda = 0.5$ mm and $R = 33$ mm.

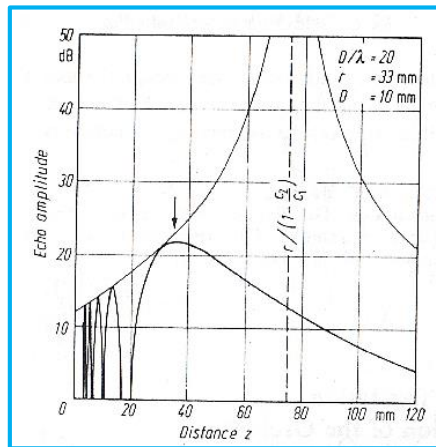


Figure 2.3: Echo height of a point reflector on the axis of a plane radiator focussed by a lens of Perspex in water [1]

The figure indicates that focal distance is much shorter than the geometrically calculated one as given by equation 2.

Figure 2.4 shows a plano-concave lens in which the gain in the focus is a function of the angle of aperture [71].

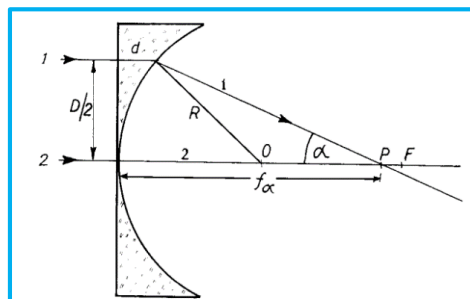


Figure 2.4: Focal length of a plano concave lens, which includes the correction term for large angle of apertures [71]

The condition of the phase equality of the rays 1 and 2 at point P is:

$$\frac{f}{c_1} = \frac{d}{c_2} + \frac{\lambda}{c_1} \sqrt{(f - d)^2 + 2Rd - d^2} \quad [5]$$

The above equation gives focal length, which can be written as:

$$f = \frac{R}{1 - \left(\frac{c_1}{c_2}\right)} - d/2 \frac{\left(\frac{c_1}{c_2}\right)}{\left[\left(\frac{c_2}{c_1}\right) - 1\right]} \quad [6]$$

The first term in the above equation deals with the geometry of the lens while the second term is related to the refraction. Equation 6 is thus the correct lens formula using a plano concave lens for the focusing of sound beam. With increasing angle of aperture, the focus moves towards the lens.

One of the major benefits of the sound beam focusing is the improvement in the sensitivity as a result of concentration of the sound energy in a very small zone. Figure 2.5 [1] shows the variation in echo height of a point reflector at a focus of a circular-disc radiator relative to the average value in front of a plane radiator as a function of focussing factor K calculated for D/λ of 20.

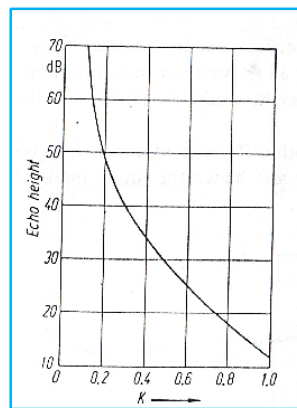


Figure 2.5: Improvement in the echo height (dB) as a result of focusing for various K values [1]

The figure indicates that the gain in sensitivity is significant for the lower value of K . This means that stronger the focusing, better is the sensitivity for flaw detection in the focal zone. As the K value increases (weak focusing), the gain in echo height comes down. At $K=1$, which corresponds to the near-field distance, the gain in echo height is approximately 12 dB.

In addition to the above, the gain due to use of an acoustic lens is also affected by the attenuation in the material, which is a function of the thickness of the lens. Using a mean value, Rosenberg [81] arrived at the following formula to evaluate the gain in the acoustic pressure G_p as a result of focusing using an acoustic lens:

$$G_p = \frac{\pi D^2}{2\lambda f} * \frac{2Z_1 Z_2}{(Z_1 + Z_2)^2} \quad [7]$$

Another factor which affects the efficiency of sound beam focusing using an acoustic lens is the effect of layer thickness on the transmission of sound wave. The amount of energy passing through a plane parallel plate of thickness t immersed in a medium does not depend on the ratio of the acoustic impedance of the two media R_{12} ($R_{12} = Z_1/Z_2$) alone, but also on the ratio of thickness to wavelength (t/λ). The transmission coefficient Tc is given by [1]:

$$Tc = \frac{1}{\sqrt{1 + \frac{1}{4} \left(R_{12} - \frac{1}{R_{12}} \right)^2 \sin^2 \frac{2\pi t}{\lambda}}} \quad [8]$$

The above equation states that the sonic energy passes through the plate without loss if the thickness $t = 2n\lambda/4$. However, if the thickness $t = (2n - 1)\lambda/4$ then the incident sonic energy is largely reflected.

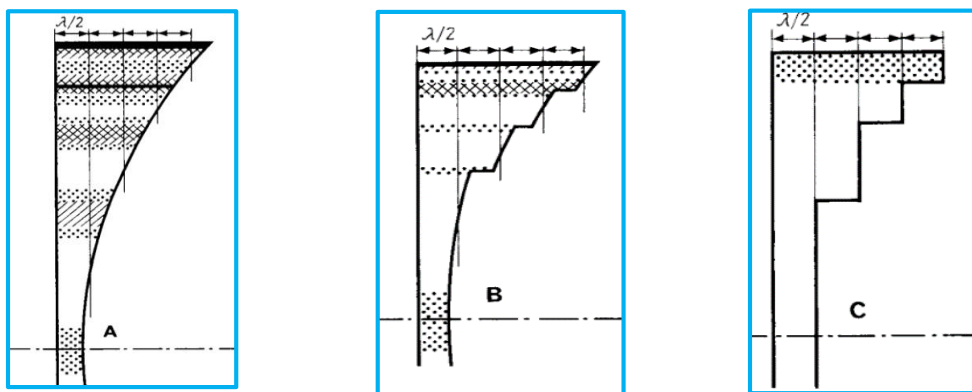


Figure 2.6: (A) Normal plano concave lens, (B) Stepped lens with impermeable zones omitted and (C) Zone lens with zones increasing in thickness by $\lambda/2$ [71]

With the plano concave lens, the value of t differs from the centre of the lens to the periphery and so does the transmission of sound wave across the lens in to the water as per equation 8. One way of overcoming this problem and achieve the maximum transmission is to avoid the thicknesses, which makes the lens opaque to the incident sound. This led to the development of stepped lenses and zone lenses. Figure 2.6 shows the above concept.

In addition to the gain in the sensitivity that is achieved as a result of focusing, there are two more important parameters of the focused sound beam viz. the focal spot size and the length of the focal zone. These two are illustrated in Figure 2.7 [2].

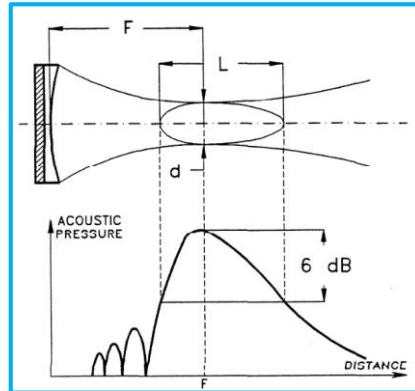


Figure 2.7: Characteristics of a focused sound beam [2]

The diameter of the focal spot (δ) and the length of the focal zone (L_f) can be given as:

$$\delta = \lambda \frac{f}{D} \quad [9]$$

$$L_f = 4\lambda \left(\frac{f}{D}\right)^2 \quad [10]$$

where, λ is the wavelength, f is the focal length and D is the diameter of piezoelectric crystal.

The use of focused ultrasonic transducers for industrial applications dates back to several decades. Even now, the focused ultrasonic transducers using acoustic lenses are very popular and are predominantly used in the automated inspection systems in tube manufacturing industries. J Rooney, et. al, [8] used the focused ultrasonic transducers for the detection of very shallow flaws in small diameter (5 to 12 mm) and small thickness (0.3 to 0.7 mm) tubes to be used as cladding in nuclear fuel. Focusing helped to achieve very good sensitivity for the detection of 5% to 10% wall thickness deep flaws. Focusing also helps to examine materials like austenitic stainless steel welds, because of the improvement in the signal to noise ratio [82-84]. The focused ultrasonic transducers have also been used during in-service inspection. Dombret P. et. al. [85], used large diameter focused transducers for in-service inspection of weld joints in main coolant pump casing. The casing is typically manufactured by the casting

process and hence it is expected to have a large grain size. The use of focused ultrasonic transducers helps to reduce the background noise due to the scattered signals for carrying out meaningful ultrasonic examination. It was also shown that in the cast structure, focusing improved the signal to noise ratio for the enhanced detection of the crack-tip signals so that an accurate estimate of the crack depth can be made [86].

The following rules apply when focusing the sound beam by acoustic lenses [1]:

- A plane radiator can be focused only to distances shorter than its near-field
- The complete near-field of a plane radiator is effectively compressed by focusing in to the space between the radiator and the new focus
- The far-field is also compressed in to a range lying nearer to the new focus
- In the far-field range, beyond the focus, there may also appear some new zones of interference as in the near-field
- The size of the focal spot is determined by the focal length, the wavelength and the diameter of the piezoelectric element

The use of lens for sound beam focusing suffers from two distinct drawbacks viz. the attenuation in the lens material and difficulty in coupling, especially for large aperture. One way to overcome these difficulties is by using shaped piezoelectric transducers. The most common piezoelectric material used for transmitting and receiving ultrasound is lead zirconate titanate (PZT), which is a ceramic. This material cannot be shaped to produce a focused ultrasonic beam. In the past few decades, extensive work has been carried out towards the development of piezocomposite materials, which are flexible and can be made in to desired shapes to produce focussed ultrasonic beam. These materials have found wide applications, both in engineering and medical field.

2.2.3 Piezocomposite Transducers

Piezocomposite elements refer to the class of piezoelectric materials, which are composite in nature. These composites are typically made from ceramic and polymer, to achieve the required flexibility in the piezoelectric material so that it can be shaped to produce focused ultrasonic beam. Figure 2.8 schematically shows difference between the sound beam focusing using ceramic piezoelectric element coupled to an acoustic lens and a shaped piezocomposite element.

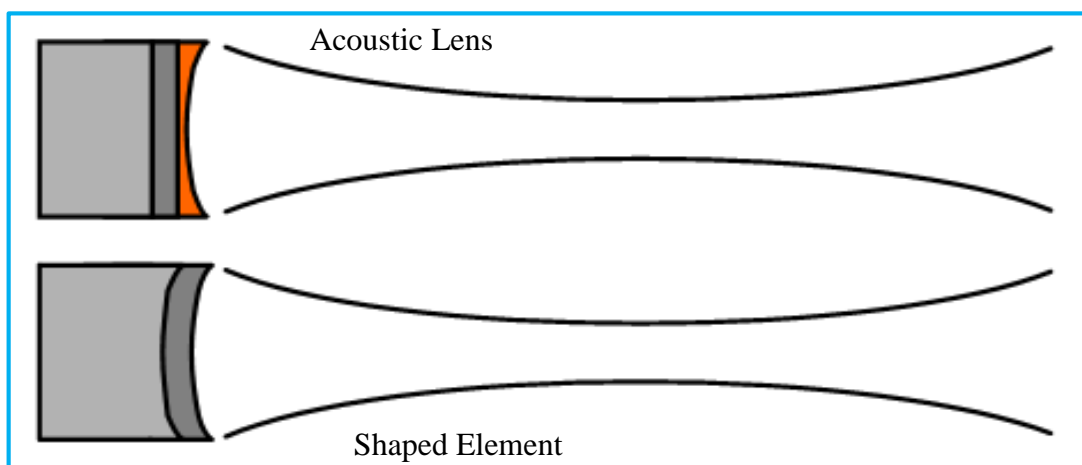


Figure 2.8: Sound beam focusing using an acoustic lens and shaped piezocomposite transducers [91]

The shaped piezoelectric element can be realized by using a flexible material such as polymer. H. Kawai discovered piezoelectric effect in elongated and polarized films of polymers, particularly in Poly Vinylidene Flouride (PVF₂) [87]. Such polymer can be made in to required shape to produce a focused sound beam. The flexibility of PVF₂ is high and the density is low compared to conventional ceramic piezoelectric materials. PVF₂ has low acoustic impedance, which means it has a better acoustic matching as compared to ceramics, with water or a human body. It also has a reasonable piezoelectric coupling, a high piezoelectric coefficient and a wideband frequency response. However, there were problems associated with the use of PVF₂

for engineering and medical applications. The low piezoelectric strain coefficient means that the polymer material cannot be used as an active device for transmitting ultrasound. To overcome this limitation, D.P. Skinner, et.al, [88] developed piezocomposite material. The objective was to take the advantage of both, the ceramic piezoelectric (PZT) and the flexible polymer. The polymer phase lowers the density and increases the elastic compliance, while the piezoelectric PZT imparts large piezoelectric strain coefficients to the composite. R.E. Newnham, et.al. [89] carried out extensive work on processing of piezocomposite materials and studied the effect of various processing routes on piezoelectric properties required for medical and engineering applications. Since their inception, the piezoceramic polymer composites have been widely used in areas such as medical imaging, non-destructive evaluation of materials, underwater vision etc.

One of the most common forms of piezocomposite ultrasonic transducers is the 1-3 piezoelectric ceramic polymer composite. In this, the piezoelectric ceramic phase is linked only in one direction whereas the polymer phase is connected in all the three directions. These are manufactured by inserting the piezoelectric ceramic rods in a polymer material. The ceramic and the polymer resin are chosen according to the characteristics required for the composite material. The height of the ceramic rods is large compared to their lateral dimensions, which favours their vibration in the thickness mode as compared to the radial mode. This results in improved electro-acoustic efficiency that gives these transducers a high level of sensitivity and a high signal to noise ratio (SNR). In addition, the natural damping of composite materials allows a relative bandwidth of 60% to 90% to be obtained while retaining a very good level of sensitivity. Chen et. al. [90] carried out experimental analysis of 1-3 piezocomposite transducers for high intensity applications using a focused sound beam. The analysis involved the evaluation of the coupling factor, bandwidth, acoustic impedance and electro-acoustic efficiency. The experimental analyses demonstrated that although the coupling factor of

composite transducers was higher than that of the ceramic transducer, the composite transducers had a lower efficiency due to the high dielectric loss. The bandwidth and the acoustic impedance of composite transducers were superior to the ceramic transducer. For the composite transducers, the efficiency and acoustic impedance were inversely proportional to the aspect ratio and linearly proportional to the volume fraction. The coupling of inter pillars that are too close to each other could cause a significant decrease in the efficiency of the composite transducer. With an appropriate design in terms of the aspect ratio, volume fraction and PZT-pillar spacing, a high-efficiency, high-intensity focused ultrasound transducer can be achieved. P. Dumas, et. al. [91] compared the performance of focused ultrasonic transducers, one produced with a piezoelectric ceramic having an acoustic lens and the other made of 1-3 piezocomposite, in terms of SNR and lateral resolution. They observed that the piezocomposite transducer exhibited much better SNR and lateral resolution as compared to the piezoelectric transducer with lens. J. Pogue et. al. [92] developed a circular phased array piezocomposite transducer for inspection of steam generator tubes. Delay laws are applied to the elements to focus the sound beam into the radial plane of the tubes, while the curved piezocomposite elements are used to focus the beam in the axial plane.

One of the major limitations of the sound beam focusing using an acoustic lens or a shaped piezocomposite material is that the focal point in the material under investigation is at a fixed distance from the scanning surface. Moreover, it is not possible to focus the sound beyond the near field, which in turn is determined by the size of the piezoelectric crystal and the wavelength. With these limitations, if one has to examine a thick component with a given focused sound beam, then multiple inspections at varying water paths would be required. Also the fact that the focused transducers use a plano-concave lens, one can employ an acoustic lens based transducers only during immersion testing. This may not be practical for all the

applications, especially while dealing with large components or the ones with complicated geometry.

The limitations of the acoustic lens based and shaped piezocomposite focused transducers can be overcome to a large extent by acquiring the data using a plane unfocused transducer and then carry out the signal processing of the acquired data to create the focusing effect at the desired locations within the component. This forms the basis of the sound beam focusing using Synthetic Aperture Focusing Technique (SAFT).

2.2.3 Synthetic Aperture Focusing Technique (SAFT)

The use of synthetic aperture for improving the resolution has been studied since early 1950s. The initial work on this concept was primarily aimed at the improvement in the lateral resolution of airborne radar mapping systems. In 1952, Sherwin [93] reported that a synthetic antenna could be made to focus at any selected range simply by producing the proper systematic phase shifts in the stored signals from that range as they were read-out for processing. Upon read-out, the phases of the stored signals were to be shifted at just the rate that would have occurred if the aircraft had been flying in a circle with its centre at the target. Since the coherent signals from each range interval were to be separately stored and processed, the synthetic antenna could be made to focus at all the ranges simultaneously, a feat which was impossible with geometrical antennas. The feasibility of the technique was demonstrated experimentally for the first time in 1953 by generating the maps of a section of Key West, Florida. The same basic equipment was used to study sea "clutter," during which distinctive properties of radar echoes from the sea surface were observed. [94, 95]. The use of synthetic focusing for combat-surveillance system was extensively studied by Cutrona [96]. The radar research was part of a Project MICHIGAN, which was sponsored by the U. S. Army Combat Surveillance Agency. The major shortcoming of radars at that time was the angular resolution.

Cutrona, et. al., [97] derived the expression of the azimuth resolution that can be achieved using radars for three different cases, viz. conventional, unfocused synthetic antenna and focused synthetic antenna. Their work indicated that the resolution capabilities of conventional, unfocussed and focussed antenna systems differ markedly in their characteristics. It was shown that the resolution, other parameters being fixed, varies directly as the wavelength λ for the conventional case, as the $\sqrt{\lambda}$ for the unfocussed case, and is independent of λ for the focussed case. The dependence of the resolution on the antenna size was shown to improve for the larger apertures in the conventional case, to be independent of the aperture in the unfocussed case, and to improve with the smaller apertures for the focussed case. The dependence of the resolution on the range was shown to deteriorate directly as the range in the conventional case, as \sqrt{R} in the unfocussed case, and to be independent of the range for the focussed case.

The synthetic aperture focusing technique (SAFT) using ultrasound for the detection and characterization of defects was developed by University of Michigan in 1970s [98, 99]. An important advantage of the synthetic focus approach was that the transverse resolution obtained was twice as good as the equivalent system in which parallel beam is transmitted and the system is focused to receive. The one dimensional version of the Synthetic Aperture Focussing Technique (LSAFT) was developed at the IZFP in 1980s [100-102]. Extensive round robin trials on the critical nuclear power plant components were carried out to assess the effectiveness of this technique for flaw detection and characterization. Flaws in very thick (up to nearly 1 m) as well as in quite thin components (down to 12 mm) could be imaged by LSAFT. Reconstructions for the curved surfaces (like OD and ID) during the inspections of vessels, ID inspections of vessel nozzles, and OD inspections of pipes were performed with very good results.

SAFT is the post processing reconstruction technique, which is based on the geometrical reflection or ray acoustic model. With the use of this technique, an improvement in the lateral resolution can be obtained, without using the traditional ultrasonic lenses. The synthetic focus is efficient and does not introduce transmission losses. However, this technique can be employed only in the digital signal acquisition system [11-13]. In SAFT, for each transducer position, the raw data containing a sound beam scattered by a defect is collected using a divergent sound beam. During the reconstruction process, the sound beams are time shifted or back propagated to the scattering source and averaged out using the wave propagation formulae. The signal amplitude at the defect location is highly improved during the averaging due to the constructive interference. Whereas, at other locations, poor correlation of the signal phase causes the destructive interference of the sound beam and leads to a significant drop in the signal amplitude. The principle of SAFT can be explained with a simple system model shown in Figure 2.9 [103].

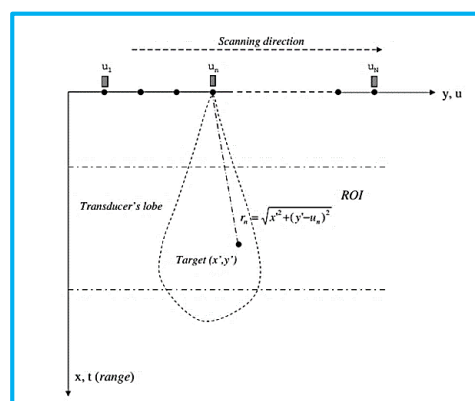


Figure 2.9: Principle of the application of SAFT [103]

The figure indicates that a single crystal transducer is moved in the scanning direction and in the processes acquires the data at discrete locations from u_1 to u_N . The flaw is located in the far-field region of the transducer, which is shown in the figure as the region of interest (ROI). The ROI contains a number of reflecting targets (flaws) in the spatial (x, y) domain, where x is the range while y is the cross-range. The transducer element moves along the u axis, which is parallel to the y axis of the target area, and transmits a broadband pulse. Assuming that the

transducer's radiation pattern is omni-directional, the measured reflected signal at the transducer position u_n is given by:

$$e(t, u_n) \approx \int_x \int_y f(x, y) \cdot b(t, x, y - u_n) *_t p \left(t - \frac{2}{c} \sqrt{x^2 + (y - u_n)^2} \right) dx dy \quad [11]$$

where $b(t, x, y)$ is the spatial-temporal response of the combined transmitter and receiver apertures and the symbol $*_t$ represents the convolution in the time domain. To achieve focus at an observation point (x, y) in the ROI, the SAFT algorithm time-shifts and performs a summation of the received signals $e(t, u_n)$ measured at transducer positions u_n for all n in the synthetic aperture. The delay and averaging scheme of a time domain SAFT is illustrated by the block diagram shown in Figure 2.10.

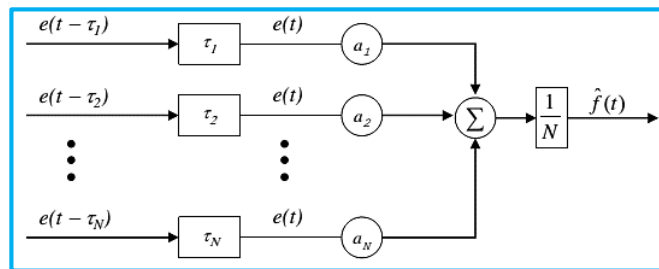


Figure 2.10: Time delay and averaging scheme during SAFT processing [103]

The time delays, denoted by τ_n , aiming to compensate for different pulse traveling time, can be expressed as:

$$\tau_n = \frac{2}{c}(r_n - x') = \frac{2}{c}(\sqrt{x'^2 + (y' - u_n)^2} - x') \quad [12]$$

for $n = 1, 2, \dots, N$, where N is the number of element positions and r_n is the distance from the element at the position u_n to the observation point. After time shifts and summation, the final image is:

$$i(x', y') = \sum_{n=0}^{L-1} \frac{a_n e(t - \frac{x'}{c}, u_n) \delta(t - \tau_n)}{r_n} \quad [13]$$

The number of A-scans that should be included in the synthetic aperture is based on the effective aperture length [103]. All the transducers have some form of a beam pattern that takes the form of a main lobe accompanied by number of side lobes. The main lobe width is an important parameter that defines the transducer's cross-range resolution. The parameter L_{eff} is defined as the largest aperture length corresponding to the wavelength λ that contributes to the SAFT performance in terms of its lateral resolution. For a circular transducer with diameter D , L_{eff} at a distance X is given by:

$$L_{eff} \cong \frac{X\lambda}{D} \quad [14]$$

Thus for a fixed D and λ , the longer the range, the longer is the L_{eff} . On the other hand, for a fixed range, smaller transducer diameter or lower transducer centre frequency results in longer L_{eff} . The SAFT cross range resolution is given by [101]:

$$\delta_{y3dB} \cong \frac{\lambda X}{2L_{eff}} \quad [15]$$

Where L_{eff} is the effective synthetic aperture length, defined as the largest aperture length corresponding to the ultrasonic frequency that contributes to the SAFT performance in terms of its lateral resolution, and R is the focusing range. From equations 14 and 15, the cross-range or lateral resolution by SAFT can be given as:

$$\delta_{y3dB} \cong \frac{D}{2} \quad [16]$$

The above equation indicates that the cross-range resolution of the SAFT system is independent of the ultrasonic frequency and the range, if the effective aperture defined by equation 16 is used for the shortest wavelength in the ultrasonic signal. The smaller the transducer, the better is the resolution. However, the minimal transducer size is limited by the signal to noise ratio required for a given depth in the material under investigation.

The main advantage of SAFT is that the focusing possibility is independent on the length of the sound path. Synthetic focusing increase the lateral resolution, which becomes theoretically

constant along the material depth. Because of the inherent averaging associated with it, the signal-to-noise ratio (SNR) is significantly improved on SAFT processing [102]. Stepinski T. [103] carried out the work on cast austenitic stainless steel block to assess this benefit. The raw and the SAFT processed B-scan images for the side drilled holes in the block are shown in Figure 2.11(a) and (b) respectively. The results clearly indicate the improvements in the signal to noise ratio on SAFT processing.

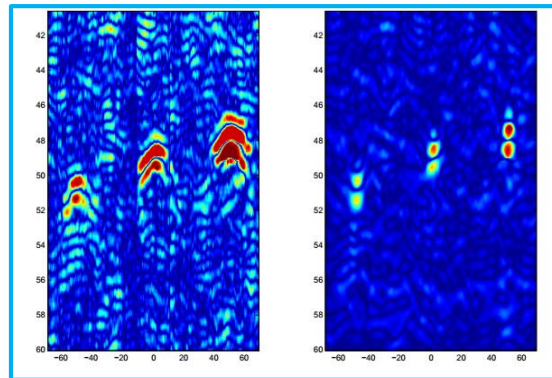


Figure 2.11: (a) Raw B-scan and (b) SAFT processed B-scan for a cast austenitic steel block with side drilled holes [103]

Schmitz et. al. [15] studied the benefits derived from SAFT with respect to better sensitivity for the detection and sizing of cracks. Their study on the detection of crack tips in the austenitic stainless steel weld showed an improvement of close to 10 dB on using SAFT on the raw B-scan data. The authors also compared the raw and the SAFT processed B-scan images on side drilled holes and real cracks. It was observed that SAFT produced better images in terms of resolving two closely spaced holes. Figure 2.12 shows the raw and the SAFT B-scan images acquired on the sample with real vertical crack on the scanning surface.

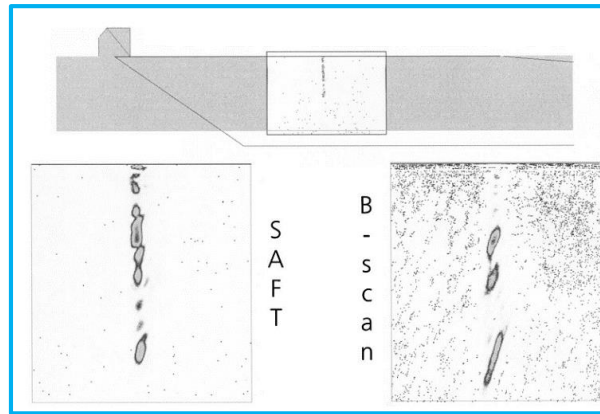


Figure 2.12: Conventional B-scan vs. SAFT for the crack on the scanning surface [15]

While the image from the crack face using SAFT is quite sharp through-out the depth, with the conventional B-scan image, there is a significant increase in the spread of the signal at higher depth. The interpretation with the SAFT data is better than the conventional B-scan image.

Skjelvareid et. al employed the Cylindrical Phase Shift Migration (CPSM) algorithm to perform the synthetic aperture focusing. The imaging algorithm is applied to scan the corroded pipe surface, and it was demonstrated that a high lateral resolution can be obtained even when the pipe wall is several focal lengths away from the transducer [104]. W. Muller et. al. developed ultrasonic imaging techniques based on SAFT for turbine shaft inspection. They successfully re-constructed the two-dimensional image of defect distribution inside the specimen. Even defects oriented radial and having high eccentricity, showed correct results [13]. Ganguli et. al. employed SAFT for the detection of air void defects at various locations inside a reinforced concrete medium. The study showed that SAFT is able to detect air voids (especially those which are linear in shape, such as long straight cracks) embedded at various locations within the subsurface of the concrete along with the steel reinforcement bars. The imaging of air voids in the concrete medium is performed by SAFT using the cross correlation function between the scattered waveforms acquired on the surface and a reference point scatterer response. Scenarios involving a serious loss of structural integrity, where the reinforcement steel bars are

surrounded by multiple air voids, were investigated. It was demonstrated that SAFT is able to identify the location of the damage [105].

SAFT has been successfully applied to isotropic materials over the years for the determination of location, shape, size and orientation of defects [106-110]. However, in anisotropic medium, its application suffers from phenomena such as the direction dependence of the ultrasonic velocities, the beam skewing effect etc. Martin Spies et. al. developed SAFT algorithm, which fully accounts for the nature of wave radiation and propagation within anisotropic materials. For three-dimensional defect reconstruction, the spatial dependence of the ultrasonic group velocities as well as the radiation characteristics of the transducer are exploited and respective algorithms are implemented to obtain quantitative information on the defect parameters in anisotropic unidirectional carbon epoxy composites [111].

Since its development in the early 1950s, SAFT has been extensively employed for a variety of applications involving ultrasonic non-destructive examination. While the major objective is to achieve fine lateral resolution, the additional benefit of improvement in the signal to noise ratio and thereby the image quality has been utilized by many researchers, as described above, to overcome the problems in the industry related to accurate ultrasonic characterization of flaws. Moreover, unlike the acoustic lens based approach, where the focal point is at a fixed distance, with SAFT, the focusing can be achieved through-out the thickness of the component (for the region that lies in the far-field of the transducer used). It is well known, that the lateral resolution that can be achieved by SAFT, is directly proportional to the diameter of the piezoelectric crystal. A very small piezoelectric element will give very good lateral resolution. For a given frequency, there is a lower limit on the minimum size of a piezoelectric crystal, both from the manufacturing considerations as well as from the point of view of the required

sensitivity. This in turn determines the practically achievable lateral resolution by SAFT using the conventional single crystal piezoelectric transducers.

2.2.4 Phased Array

Sound beam focusing by phased array at a given depth and in a given direction is based on the principle of interference of sound waves emanating from the adjacent sources. The principle of constructive and destructive interference of light waves is known since the dawn of 18th century. In 1801, English scientist Thomas Young utilized two point sources of light to create interference patterns. Waves that interfere constructively in phase reinforce each other, while the ones that interfere out-of-phase cancel each other. This is schematically shown in Figure 2.13 [112].

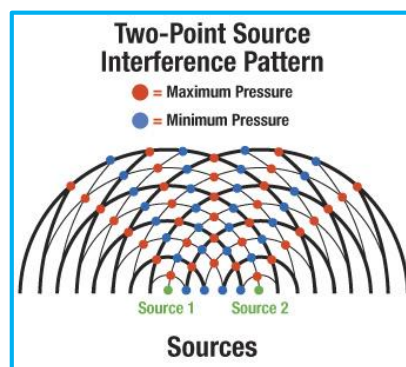


Figure 2.13: Constructive and destructive interference of light waves emitting from two point sources [112]

The term phasing or phase shifting means a way of controlling interactions by time-shifting wave fronts that originate from two or more sources. It can be used to bend, steer, or focus the energy of a wave front. In antenna theory, a phased array is an array of antennas in which the relative phases of the respective signals feeding the antennas are set in such a way that the effective radiation pattern of the array is reinforced in a desired direction and suppressed in undesired directions. Phased array transmission was originally shown in 1905 by Nobel laureate Karl Ferdinand Braun who demonstrated enhanced transmission of radio waves in one

direction. During World War II, Nobel laureate Luis Alvarez used phased array transmission in a rapidly steerable radar system to aid in the landing of the aircrafts [113].

The use of ultrasound in general and phased array in particular in the medical field has a long history [114]. Ultrasonic scanning and imaging system for clinical investigations was developed by obstetrician Ian Donald in late 1950s [115]. Jan C Somer published the paper in 1968 on the electronic sector scanning using an array transducer for ultrasonic diagnosis [116]. Few years later, Thurstone and Olaf von Ramm at the Duke University published a paper on the more advanced version of the electronically steered arrays [117]. The array was capable of generating ten different receive foci. The work was considered to be a pioneering and very important phased-array design at that time.

In the early 1970s, commercial phased array systems for medical diagnostic use first appeared, using steered beams to create cross-sectional images of the human body [118]. Initially, the use of ultrasonic phased array systems was largely confined to the medical field, because of the fact that the predictable composition and structure of the human body make instrument design and image interpretation relatively straightforward. Figure 2.14 shows the typical sector scan image of a foetus using a phased array system [119].



Figure 2.14: Sector scan image of a foetus using phased array ultrasound [119]

Industrial applications of phased array represent a much greater challenge than the medical field because of the widely varying acoustic properties of materials that one encounters such as metals, composites, ceramics, plastics etc. Also, one has to deal with variety of thicknesses

and geometries. The first industrial phased array system, introduced in the 1980s, were extremely large, and required data transfer to a computer in order to do the processing and image presentation. These systems were most typically used for in-service inspection in power industries. The major thrust for the use of phased array came from the nuclear industry as this technology promised better probability of detection and more accurate characterization of flaws. Portable, battery-powered phased array instruments for the industrial use appeared in the 1990s. The transition from the analog to the digital world and the rapid development of inexpensive embedded microprocessors enabled more rapid development of the next generation phased array equipments. In addition, the availability of low power electronic components, better power-saving architectures, and the use of surface mount board design led to miniaturization of this advanced technology. This resulted in phased array tools which allowed electronic setup, data processing, display and analysis, all within a portable device. All this led to the widespread application of phased array technology across the industrial sector.

Phased array differs from the conventional ultrasonic techniques in many ways. First and foremost is the fact that it uses an array of sensors instead of just one or two as in the conventional ultrasonic techniques. Secondly, the hardware and the software of the phased array system allows the user to excite the individual elements or a group of elements in a programmed manner i.e. the user can decide the sequence in which the elements are fired and also the delay in the firing. Another striking feature of the phased array technology is that the data is presented in the form of images so that the user gets the global picture of the inspection process for better and accurate interpretation. The ability to fire the sensors in a programmed manner helps the user to manipulate the sound beam inside the component in real time. As a result of this, the user can perform multiple angle inspections using just one phased array transducer instead of multiple inspections using a conventional single element transducer. At the heart of phased array lies the focal law. Focal law is the sequence and the time delay at

which the individual elements in the array are fired. The focal laws are generated mathematically depending on the way the user wants to manipulate the sound beam [120-123].

The main feature of the phased array ultrasonic technology is the computer-controlled excitation (amplitude and delay) of individual elements in a multi-element transducer. The excitation of piezoelectric elements can generate an ultrasonic focused beam with the possibility of modifying the beam parameters such as angle, focal distance and focal spot size. To generate a sound beam in phase and with constructive interference, various active elements of an array are pulsed at slightly different times.

The principle of sound beam focusing using phased array is shown in Figure 2.15 [6]. The figure indicates that during the transmission process, the elements in an array are fired with the time-delay. The return signals from the flaw are applied variable delay on the reception, summed and averaged before they are stored and displayed.

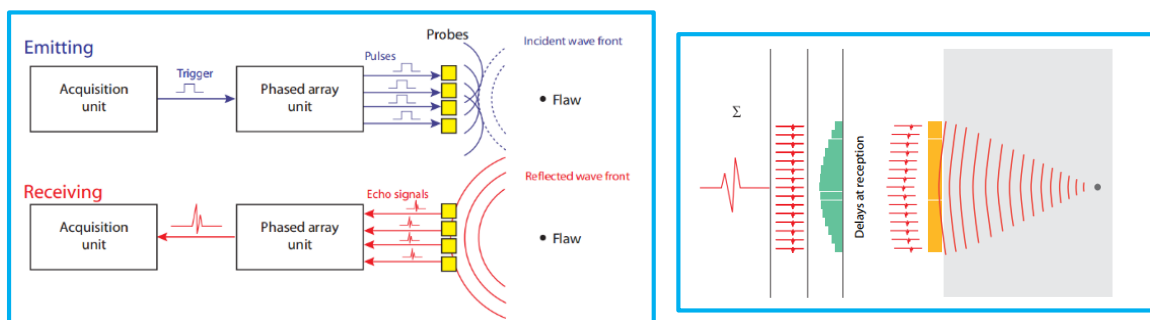


Figure 2.15: Principle of Beam Steering during a) Transmission and b) Reception [6]

One of the major problems associated with the conventional single crystal based ultrasonic testing is the poor detectability of flaws that are not oriented in favourable direction to the incident ultrasonic beam. With phased array, the focused sweeping beam has a better probability of detection for such flaws. Moreover, with focusing one can achieve better resolution to distinguish flaws located close to each other and also produce high resolution ultrasonic images with a good signal to noise ratio. The beam focusing principle for normal and angled incidences is illustrated in Figures 2.16(a) and (b) respectively:

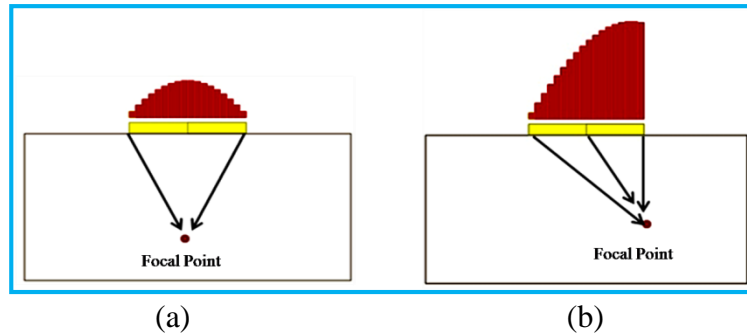


Figure 2.16: Sound beam focusing using phased array (a) normal beam and (b) angle beam

There are three major computer-controlled beam scanning patterns viz. electronic scanning, sectorial scanning and dynamic depth focusing [6]. In the electronic scanning, the same focal law is repeated across a group of active element with a pre-decided element step size. Since, the focal laws remain same, scanning is performed at a constant angle and along the array length. This is equivalent to a conventional single crystal transducer performing inspection while moving in a given scanning direction. If an angled wedge is used, the focal laws compensate for the different time delays inside the wedge. The principle of electronic scanning is schematically shown in Figure 2.17(a). In the sectorial scanning, instead of performing inspection at one particular angle, the sound beam is swept over a range of angles. Unlike the electronic scanning, the active aperture in this case is kept same and the focal laws are varied so that the sound beam is swept over the range of angles. The principle of sectorial scanning is shown schematically in Figure 2.17(b). With the dynamic depth focusing, the sound beam is focused at different depths using the selected aperture. The focal law during the transmission corresponds to the focusing at maximum depth, while during the reception, the focal laws are varied corresponding to the depth at which the sound beam is required to be focused. The principle of dynamic depth focusing is shown schematically in Figure 2.17(c).

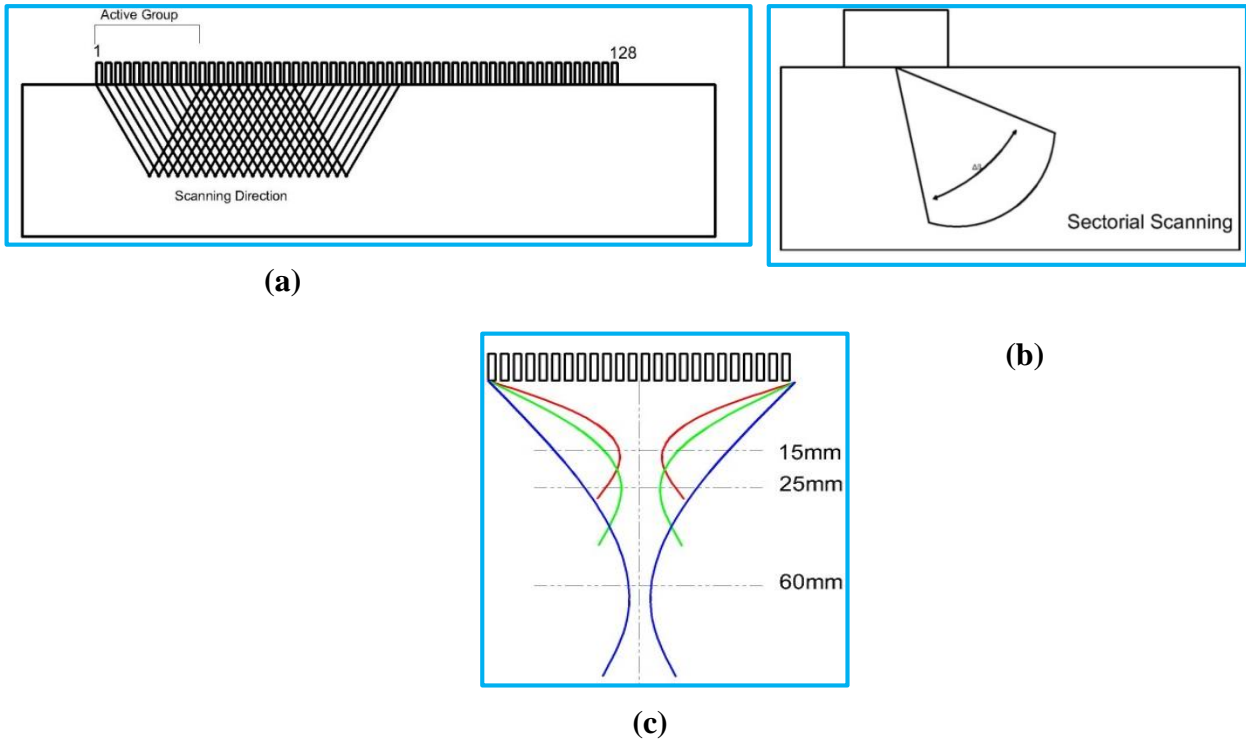


Figure 2.17: Scanning pattern using phased array: (a) electronic scanning, (b) sectorial scanning and (c) dynamic depth focusing [6]

For a contact type linear array without wedge or with a zero-degree wedge, the focal laws for generating longitudinal waves, focused at certain depth, have parabolic variation, with delay increasing from the edges of the array towards the centre. If the focal distance is increased by twice, the required delay for each particular element is reduced to half (Figure 2.18). For a given number of active elements, if the element pitch is increased, the delay for individual element increases linearly.

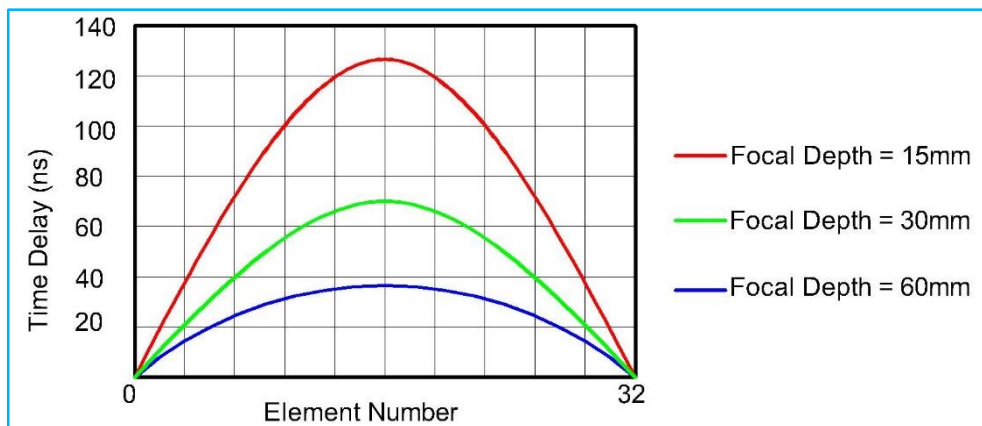


Figure 2.18: Time Delay variation for different focal depth [6]

For arrays without or with a zero-degree wedge, the delay value for an individual element for generating ultrasonic beam at an angle, depend on the position of individual element in an active aperture and on the generated angle. As the beam angle is increased, the delay value for each element increases. For arrays on an angled wedge, the delay laws have a parabolic shape for generating beam at an angle given by Snell's law. For angles smaller than the one given by Snell's law, the delay on the elements increases from the back towards the front of the probe. For greater angles, the delay is higher for the back elements, because the beam generated by the front elements follows a longer path in the wedge, and thus they need to be excited first. In all the cases, the delay value on each element must be accurately controlled.

L Azar, et. al derived a generalized expression for the time delay to achieve the focused sound beam at any given angle using an odd or even number of elements [124]. The sound beam steering is accomplished by sequentially firing the array elements. For a homogeneous and isotropic acoustic medium, the constant inter-element delay for steering the ultrasonic beam can be calculated by [124]:

$$\Delta\tau = p' \frac{\sin\theta_s}{c} \quad [17]$$

where $\Delta\tau$ is the time delay between adjacent elements, p' is the pitch, θ_s the required steering angle, and c is the wave speed in the medium.

Focusing of the transmitted beam is accomplished by combining a spherical timing relationship with a linear one to produce a beam, which is focused at a given range and propagated at a specific azimuth angle. The focusing delays can be calculated by the following formula [124,125]:

$$t_n = \frac{F}{c} \left\{ \left[1 + \left(\frac{\bar{N}d}{F} \right)^2 + \frac{2\bar{N}d}{F} \sin \theta_s \right]^{1/2} - \left[1 + \left(\frac{(n - \bar{N})d}{F} \right)^2 - \frac{2(n - \bar{N})d}{F} \sin \theta_s \right]^{1/2} \right\} \quad [18]$$

for any number of elements N , where t_n is the required time delay for element $n = 0, \dots, N - 1$, $N = (N - 1)/2$, d is the pitch, F is the focal length from the center of the array, θ_s is the steering angle from the center of array, and c is the wave speed. This generalized focusing time-delay formula is valid for any number of array elements (even or odd) for $0^\circ \leq \theta_s \leq 90^\circ$.

Ramm et. al [126] stated that little image improvement would result by sound beam focusing using focal laws if the focal point is beyond the transition range Z_{TR} of the array given by:

$$Z_{TR} = \frac{D^2}{4\lambda} \quad [19]$$

where, D is the overall dimension of the active aperture, which is given by the product of the pitch and the number of elements in an active aperture, and λ is the wavelength in the material.

If targets within the near field of the array aperture are imaged; that is, at distances less than Z_{TR} , then focusing may be employed to increase the system resolution. However, such focusing only improves the system resolution in the restricted region about the focal point. This region of improved focus or depth of field is given by:

$$\Delta Z = 8.15\lambda_0 \left(\frac{F}{D} \right)^2, \quad \left(\frac{2F}{D} \right) > 1 \quad [20]$$

on either side of the focal point for a 20 percent decrease in amplitude. Here F is the focal distance as measured from the centre of the array. It is evident from this equation that the depth of field is inversely proportional to the square of the array aperture at a given focal distance. Hence, for small apertures or weakly focused systems, the depth of field may be adequate to include all the targets of interest. For more strongly focused systems, which provide higher azimuthal resolution, the depth of field may be inadequate. L. Azhar [124] studied the beam focusing behaviour of linear arrays in terms of the directivity pattern. The study shows that when the focusing is done within the near field, the directivity pattern for steering is quite poor

as compared to the focusing. When the focal point changes from within the near field to the far field, the focusing effect converges to pure steering one. The study also showed that the maximum pressure does not necessarily occur at the focal point. However, the best directivity is obtained at a distance corresponding to the focal length.

One of the most important aspects in the design of phased array transducer and the optimization of focal laws is the beam directivity at the desired steering angle [127,128]. The beam directivity or directivity function $H(\theta)$ is defined as the pressure $p(r, \theta, t)$ at any arbitrary angle θ normalized by the pressure $p(r, \theta_s, t)$ at steering angle θ_s .

$$H(\theta) = \left| \frac{\sin [(\pi d(\sin \theta_s - \sin \theta))/\lambda]N}{N \sin [(\pi d(\sin \theta_s - \sin \theta))/\lambda]} \right|. \quad [21]$$

where, d is the inter element spacing, θ_s is the steering angle, λ is the wavelength, D is the size of the piezoelectric element and N is the number of elements.

Woo et. al studied the directivity patterns of the sound beam emanating from the linear array under various conditions [127-129]. A typical directivity plot is shown in Figure 2.19 using the values of $\nu = 2.3$ MHz, $\theta_s = 30^\circ$, $N = 16$, $d = 2\lambda/(1 + \sqrt{3})$, and $D = \lambda/100$, for steel ($c = 5850$ m/s). The maximum pressure occurs in the steering direction. The main lobe is surrounded by many smaller lobes appearing at multiple locations along the θ axis. These lobes are called as the side lobes. This means that the ultrasonic energy “leaks” in to the directions other than the steering direction. There is a lobe appearing at the angle $\theta = -60^\circ$, whose amplitude is the same as that of the main lobe but is much wider. Such a lobe is called as the grating lobe. If the grating lobe exists, a strong secondary signal appears in the directions other than the steering angle, resulting in spurious and confusing signals in the acquired data. If the amplitudes of the side lobes are much smaller than that of the main lobe, the beam is said to be well directed and the steering effect is pronounced. Furthermore, if the main lobe width is small or the shape of

the main lobe is sharp, it means that the acoustic energy is primarily directed in the steering direction.

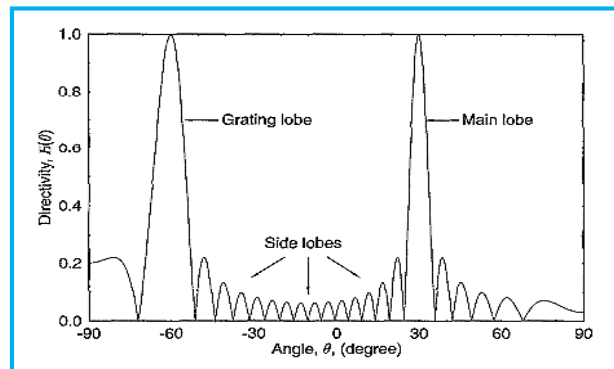


Figure 2.19: A typical directivity plot showing the main lobe, the side lobes and the grating lobe [127-129]

While performing phased array inspection it is required to achieve a good beam directivity and also the required steering ability. It is always desirable to minimize the main lobe width and eliminate the grating lobes. Transducer parameters, which are important for these considerations include, the number of elements in an array N , inter-element spacing d , element size D , and the wavelength in the medium λ . Among these design parameters, the wavelength λ is somewhat fixed to a certain extent since the frequency is generally pre-selected for specific needs of inspection such as material, sensitivity required, thickness of the job etc. The effect of D is negligible, particularly when it is reasonably smaller than the wavelength. The total number of elements is also restricted, since a large number of elements generally pose limitations on the control circuitry. It is of interest to find out the optimum inter-element spacing d to attain the required directivity. The width of the main lobe is given by:

$$\Delta\theta_m = \sin^{-1} \left(\sin \theta_s + \frac{\lambda}{Nd} \right) - \sin^{-1} \left(\sin \theta_s - \frac{\lambda}{Nd} \right), \quad [22]$$

As θ_s increases, main lobe width increases. This means that the directivity of acoustic beams steered at smaller angles are better than those steered at higher angles. One can observe that

$\Delta\theta_m$ approaches zero for infinitely large number of elements ($N \rightarrow \infty$). This condition is impossible to achieve from a practical point of view. The beam directivity improves with an increasing d/λ value or larger d since λ cannot be reduced below a particular limit from material attenuation point of view. In other words, beam directivity can be improved by increasing the spacing between the elements.

The critical inter-element spacing to avoid grating lobes is given as:

$$d_{cr} = \frac{\lambda}{1 + \sin(\theta_s)_{max}}, \quad [23]$$

where $(\theta_s)_{max}$ is the desired maximum operating steering angle of the transducer without producing grating lobes.

Although the inter-element spacing is chosen slightly smaller than the critical value ($d < d_{cr}$), some portions of the grating lobe may still appear in the directivity pattern. The maximum allowable inter-element spacing that completely eliminates grating lobes can be determined from the relationship

$$d_{max} = \frac{\lambda}{1 + \sin(\theta_s)_{max}} \frac{N - 1}{N}. \quad [24]$$

In other words, grating lobes can be completely eliminated by choosing an inter-element spacing that is less than d_{max} . If the inter-element spacing is already given for a transducer, then the maximum steerable angle as a function of d can be given as:

$$(\theta_s)_{max} = \sin^{-1} \left(\frac{\lambda(N - 1)}{dN} - 1 \right). \quad [25]$$

E Kuhnicke studied the effect of steering angle and array parameters on the generation of grating lobes under immersion testing conditions [130]. The study concluded that for the

constant element spacing, the magnitude of grating lobes increases with an increase in the steering angle. If the element width is smaller than $\lambda/2$, no grating lobes appear, even for large steering angles. Pompei et.al. carried out the work on the suppression of the grating lobes by carefully shaping the array elements [131].

Over the years, the ultrasonic phased array technology has been used across several industries [132-144]. In addition to the standard applications involving the use of focal laws for beam steering and focusing, many researchers have used modelling and simulation to improve upon the results obtained by the conventional phased array systems. Jing Ye, et. al [145] carried out model based simulation of the focused sound beam fields produced by a phased array transducer for the examination of dissimilar weld joint. The sound beam undergoes skewing and distortion during its travel through the dissimilar weld joints. If these effects are not considered, the focusing will not be efficient. The study proposed an approach that included modelling the grain orientation of the welds with buttering, calculating the ray path for determination of focal laws, and applying the linear phasing multi-Gaussian beam model in order to focus the sound beam using phased array at a given location in the weld. Hun-Hee Kim, et. al [146], explored the possibility of focusing the ultrasound by linear array using an adaptive focusing technique and the time reversal technique. The effectiveness of focusing by these techniques was compared with that from the conventional phased array, based on the signal amplitude from a side drilled hole in a dissimilar metal weld joint. It was observed that the time reversal technique showed better focusing performance followed by the adaptive focusing technique and then the focal law based phased array. Mahaut, et. al. [147] developed the phased array based dynamic adaptive focusing system called FAUST: Focusing Adaptive Ultrasonic Tomography, for defect characterization using ultrasound. To keep high performance focusing, with a good lateral resolution without array lobes, with a reasonable number of elements, the study optimized the size and the geometry of the elements. Using a

model for field computations called Champ-Sons, applied to phased array transducers, several types of optimized array transducers were studied. Circular arrays were used to focus at normal incidence, whereas elliptical arrays were to generate inclined longitudinal waves without the degradation of the sound beam.

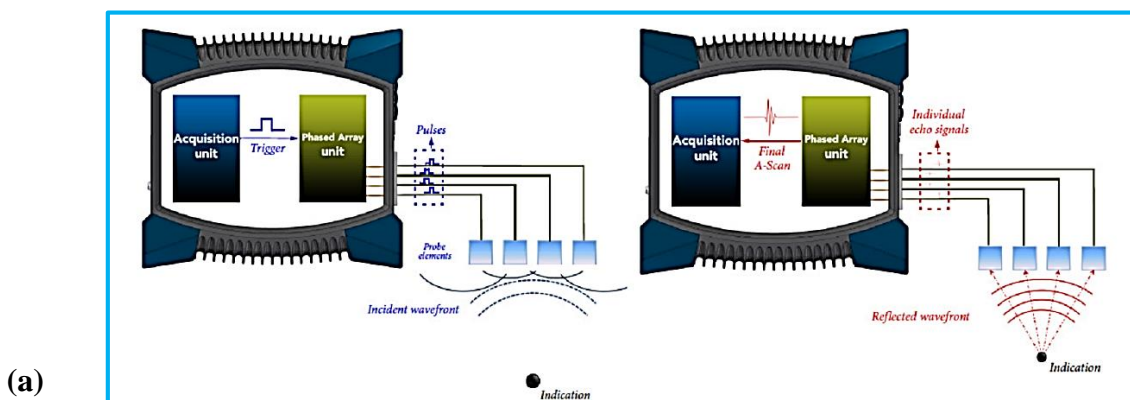
The growth of phased array technology and its acceptance across several industrial sectors in the past couple of decades has been phenomenal. The primary reasons for this are the advantages it offers over the conventional ultrasonic techniques in terms of the reliability of flaw detection, accuracy in the flaw characterization, speed of inspection, inherent imaging capabilities and so on. With regard to the sound beam focusing, phased array technology makes it possible to use the focused sound beam using contact transducers, which was impossible with the conventional acoustic lens based approach. Also the fact that the sound beam can be steered and focused at different depths, allows one to examine the full thickness of the component at one go, rather than carrying out multiple inspections. However, just like the acoustic lens based approach, with phased array too, one can focus the sound beam within the near field, which for a given material and frequency is determined by the active aperture size. The dimension of the focal spot size at any given distance is also determined by this parameter. Focusing at higher depth or achieving a very fine focal spot size requires a large dimension of an active aperture. This means that one needs to transmit and receive signals more number of elements parallelly using a given focal law. This requirement leads to a costlier phased array instrumentation.

The conventional phased array technology uses multiple independent transmitting-receiving channels. During the transmission process, the systems apply time delays to the individual elements of an array in order to generate a physical ultrasonic beam with specific acoustic characteristics through constructive interference of the individual wavefronts. During reception, these standard systems also apply time delays to the signals received by the individual elements in order to put them in phase for the hardware summation process. The

summed and digitized A-Scan signal is then transferred to the computer for display and recording. During the standard phased array acquisition process, the raw elementary signals are processed at the hardware level and are therefore not available for off-line software processing [148]. The need for carrying out the post processing of the raw data acquired during the phased array inspection led to the development of an advanced technique called Full Matrix Capture (FMC). The FMC technique involves capturing and recording all the possible time-domain signals (A-Scans) from every transmitter-receiver pair of elements in the array. These signals can then be processed in various ways to get the effect of beam steering and focusing.

2.2.5 Full Matrix Capture – Total Focusing Method

Full matrix capture (FMC) refers to the technique, which utilizes complete set of time domain data (A-scans) from all the combinations of the transmitting and receiving elements in an array. The data is acquired using a ‘transmit on one and receive on all’ data capture approach, with the first element of an array initially acting as transmitter and every element acting as receiver. The process repeats until all the elements have transmitted; generating a complete set of time domain signals containing N^2 A-scans for an array with N elements. C Holmes et. al. was the first one to use an algorithm named Total Focusing Method (TFM) on the FMC data acquired using a linear array to achieve the sound beam focusing for ultrasonic non-destructive evaluation [37,39,149].



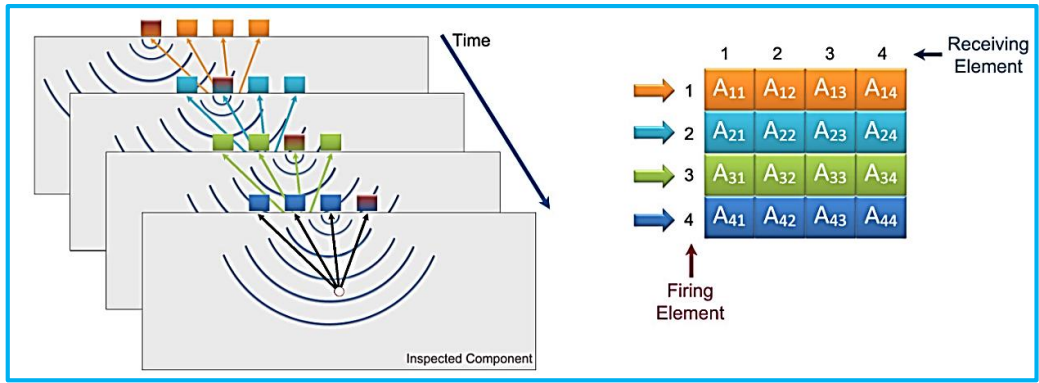


Figure 2.20: Principle of data acquisition (a) Conventional phased array and (b) Full matrix capture [148]

Figures 2.20 (a) and (b) shows the fundamental difference in the data acquisition by conventional phased array and FMC approaches [148].

Figure 2.20(a) indicates that with the conventional phased array, the individual array elements are excited at different times depending on the depth at which the focusing is desired. The signals received from the flaw are delayed, summed and averaged before they are stored and displayed on to the monitor of the phased array instrument. Contrary to this, the FMC technique consists of capturing and recording all the possible time domain signals (A-Scans) from every transmitter-receiver pair of elements in an array.

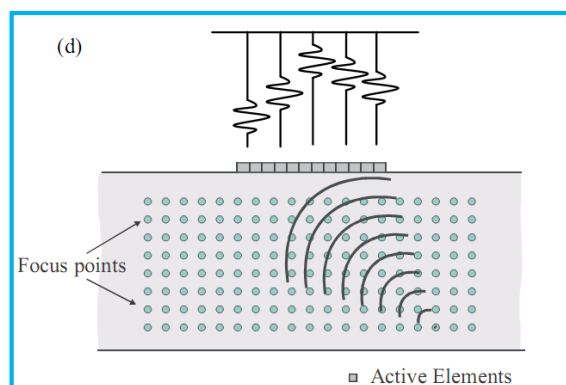


Figure 2.21: Fully focused Total Focusing Method (TFM) [149]

In order to achieve the focusing of the sound beam, imaging of the FMC data is commonly achieved through an algorithm called Total Focusing Method (TFM). In TFM, the sound beam is focused at every point in the target region as shown in Figure 2.21 [149]. The TFM post-processing algorithm proceeds by first discretizing the target region (in the x, z plane) into a grid (Figure 2.21). The signals from all the elements in the array are then summed to synthesize a focus at every point in the grid.

Figure 2.22 shows an array placed over the surface of the sample, which has a point reflector located in the (x, z) plane. The data is first acquired by FMC, during which each element acts as a transmitter and all the elements act as receivers.

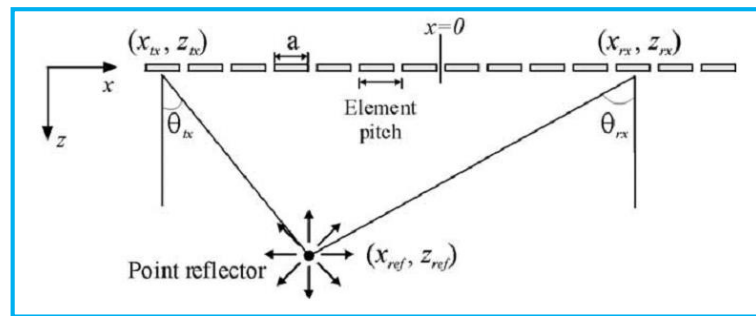


Figure 2.22: Total Focusing Method [149]

The TFM algorithm used to image this data is generated through a standard sum and beam-forming approach given in Equation 26.

$$I(x, z) = \left| \sum h_{tx, rx} \left(\frac{\sqrt{(x_{tx} - x)^2 + z^2} + \sqrt{(x_{rx} - x)^2 + z^2}}{c} \right) \right| \quad [26]$$

where, I is the intensity value for pixel location (x, z) which is determined from the time-of-flight calculations from each transmit (t_x) and receive (r_x) pair to the pixel region of interest (x, z) with c being the velocity in the medium (Figure 2.17). A Hilbert transform (h) is used to convert the real time domain signal into complex form allowing the signal magnitude

(envelope) to be found. This summation is carried out for each possible transmitter–receiver pair. As a result, the maximum amount of information is available for each point.

FMC+TFM approach gives high resolution images of flaws, enhanced detection and sizing capabilities and greater inspection coverage. Although the time required to capture these signals appears to be large, if the array controller has independent parallel reception channels, then the data acquisition by FMC can be performed in approximately the same time as the conventional phased array [39]. However, in that case, one needs a high end phased array instrumentation, which adds to the cost. At the same time, while using the FMC approach for data acquisition, the size of the data file becomes enormously large while dealing with an array with large number of elements.

C Holmes et. al. [39], carried out extensive studies to evaluate the performance of FMC + TFM technique by post-processing of the simulated data on an aluminium block with a side drilled hole. The results obtained by FMC + TFM are compared with the ones obtained by using conventional phased array. Figure 2.23(a) and (b) shows the B-scan images of a side drilled hole using focal law based approach and by FMC + TFM technique.

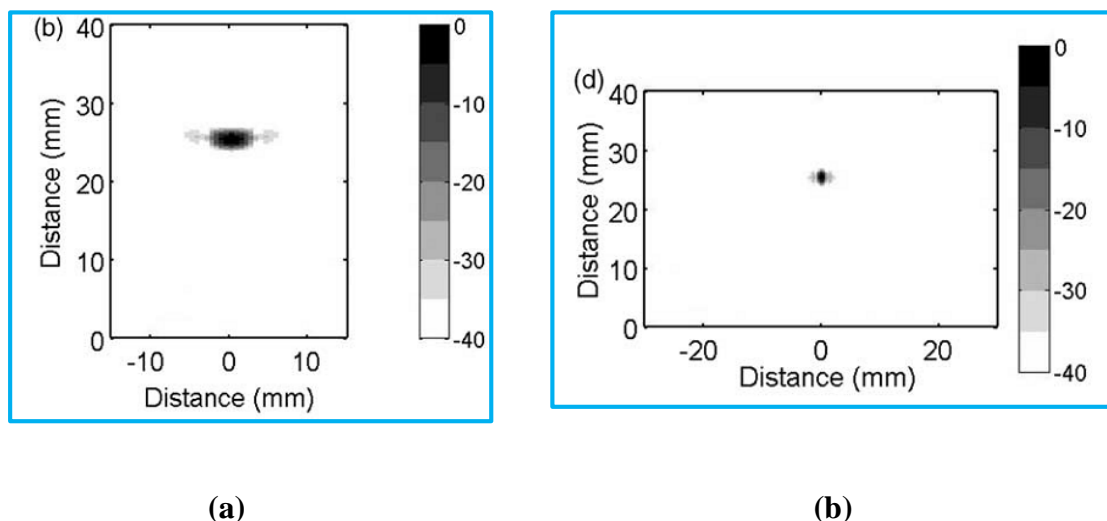


Figure 2.23: B-scan images of a side drilled hole in an aluminium block (a) conventional phased array and (b) FMC + TFM [39]

One thing, which is evident from the above results is that the size of the side drilled hole in the FMC + TFM image is much smaller than the one seen with the conventional phased array. This indicates that the focal spot size using FMC + TFM is smaller, which helps in achieving a better lateral resolution. Another thing which can be inferred from the results is that the lateral coverage by FMC + TFM is significantly higher than the one achieved using conventional phased array. The authors also defined a parameter called array performance indicator (*API*) for the quantitative assessment of the benefit that one can derive with the FMC+TFM technique. The *API* is a dimensionless measure of the spatial size of a point spread function. It is defined as the area, A_{-6dB} , within which the point spread function is greater than - 6 dB down from its maximum value, normalized to the square of the wavelength. *API* is mathematically expressed as:

$$API = \frac{A_{-6dB}}{\lambda^2} \quad [27]$$

A small value of *API* is an indication of better focusing and so a very good lateral resolution.

The authors carried out the experimental validation on an aluminium block with 0.3 mm wide EDM notch machined on the back surface of the sample. A linear array of 5 MHz, 64 elements was placed on the sample to acquire the signal from the tip of the notch. The results indicated that the *API* value using FMC+TFM was almost half the value obtained by the conventional phased array using 32 elements. Also, the signal to noise ratio by FMC+TFM was found to almost 8 dB higher [39].

In addition to the TFM methodology described above, several other approaches were studied by various researchers for sound beam focusing using the FMC data. J Zhang et. al. [150] developed a multi-mode total focusing methodology in which any combination of modes and reflections can be used to produce an image of the test structure. The approach was implemented on the full matrix capture data to achieve synthetic focus at every pixel in the

image. A hybrid model was used to predict the array data and demonstrate the performance of multi-mode imaging concept. The hybrid model combines far-field scattering coefficient matrices with a ray-based wave propagation model. The study showed that with the prior knowledge of the likely scatterer location and orientation, the mode combination and array location can be optimized to maximize the performance of an array inspection. C. Fan et. al. [151] compared the imaging performance using TFM with time reversal MUSIC technique in terms of its ability to resolve closely spaced scatterers in a solid. The performance of the algorithms is evaluated in terms of the lateral resolution and the sensitivity to noise. It was shown that for the weak noise situation ($\text{SNR} > 20 \text{ dB}$), time-reversal MUSIC approach provides significantly enhanced lateral resolution when compared to the total focusing method. However, for higher noise levels, the total focusing method is shown to be robust. N. Quaegebeur, et. al. [152] developed a novel post-processing method for the data captured by FMC. The technique is based on the correlation of measured signals with the theoretical propagated signals computed over a given grid of points. The advantage of this approach is to take into account the transducer directivity, dynamics and complex propagation patterns, such that the number of required array elements for a given imaging performance can be greatly reduced. A Hunter, et. al. [153] developed a Fourier-domain approach to the full-matrix imaging based on the wave number algorithm used in the synthetic aperture radar and sonar. The wave number algorithm provides a mathematically rigorous solution to the inverse problem for the assumed forward wave propagation model, whereas the TFM employs heuristic delay-and-sum beam forming. Consequently, the wave number algorithm has an improved point-spread function and provides better imaging. However, the major advantage of the wave number algorithm is its superior computational performance. For large arrays and images, the wave number algorithm is several orders of magnitude faster than the TFM. On the other hand, the key advantage of the TFM is its flexibility. The wave number algorithm requires a regularly

sampled linear array, while the TFM can handle arbitrary imaging geometries. J Zhang et. al. [154] studied the effect of inconsistencies in the linear arrays on the imaging performance achieved by TFM. The study was carried out for the inter-element variability in the array in terms of the amplitude, phase and delay in-consistencies. The peak amplitude and the measure of the size of the point spread function were used to assess the quality of TFM images simulated for a 1 mm dia. side drilled hole. The study indicated that the imaging performance is most sensitive to the variability in the time-delay rather than phase and amplitude.

To overcome the constraints of the off-line processing, extensive work has been done in recent years to build a real time FMC + TFM systems [155]. M. Sutcliffe, et. al. [156] investigated the optimization of TFM algorithm on the FMC data to obtain images in real time. This approach is combined with several other software engineering optimization techniques including threaded data- capture, the use of look-up tables and half-matrix implementation. D. Lines et. al., [157] used flexible and scalable PC-based hardware modules for on-line data acquisition and display using FMC + TFM. This new architecture was able to achieve acquisition and processing at 20 Hz and higher, meeting the requirements for the interactive scanning and so enabling FMC + TFM technique to transfer from the laboratory into the field. With the advancement in the computer hardware and the data handling and processing technologies, the real-time FMC+TFM technique is now available in many commercial instruments [158,159].

2.2.6 Sampling phased array

A technique involving similar approach as FMC + TFM was developed at IZfP for sound beam focusing. This technique is named as the Sampling Phased Array (SPA) [160]. The conventional phased array requires several shots at different angles to cover an entire cross section. In contrast, in sampling phased array, the same can be achieved with an excitation of a single element in an array. The returning ultrasonic echo signals are captured by every one

of the transducer elements, similar to what is done during FMC. The received signals are used to reconstruct for one or more arbitrary angles and/or focus depths. The reconstruction is greatly enhanced through the use of an algorithm called SynFo, which eliminates the noise and enhances the sensitivity. The benefits of sampling phased array are three fold. Firstly, there is a substantial increase in the testing speed. Secondly, one can reconstruct the matrix for any number of insonification angles, which improves the probability of detection. Thirdly, the complete volume of the material can be imaged through the use of an appropriate reconstruction algorithms without the need to generate the individual A-scan pictures. An additional advantage is provided by the fact that the SPA technique principally employs the transmitter-receiver mode, where the dead-zone (or near-surface) in the test material is significantly reduced.

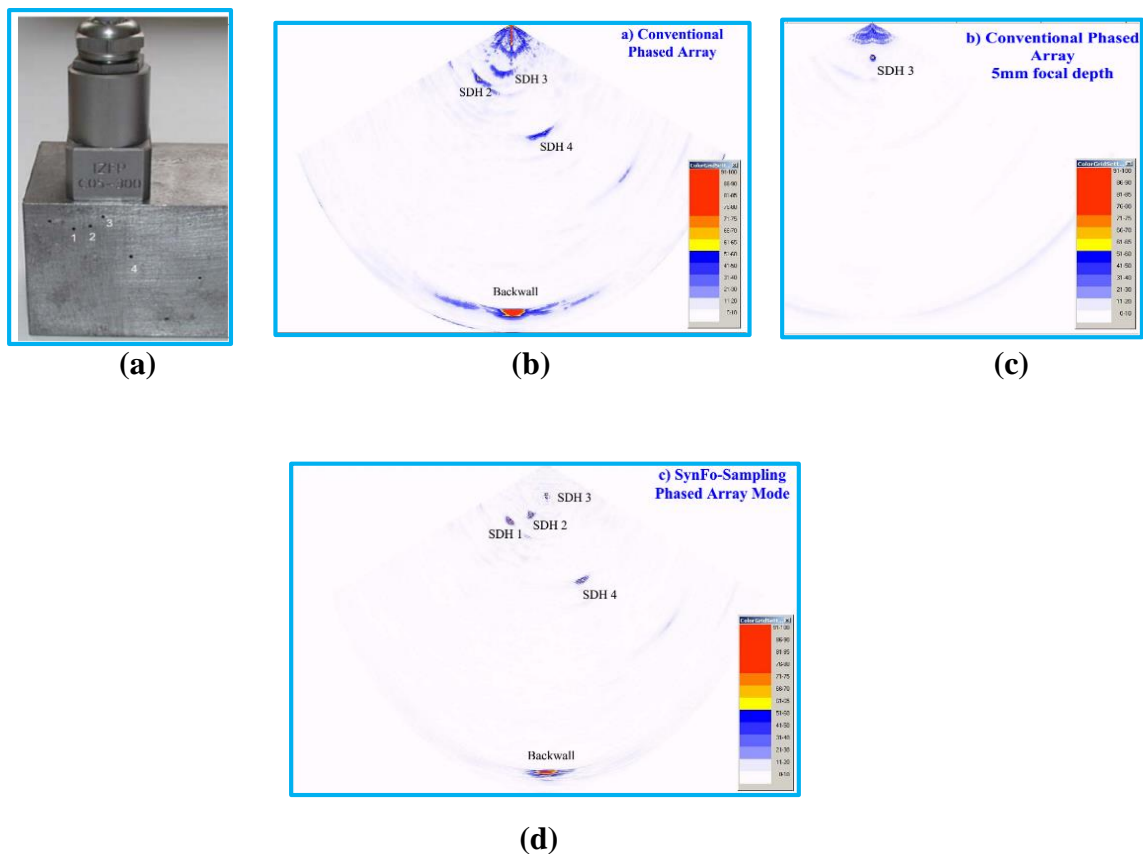


Figure 2.24: Comparison of SPA with conventional phased array technique for the detection of near surface and far surface flaws [161]

Extensive validation trials were carried out at IZfP to assess the benefits of SPA as compared to conventional phased array technique [161]. Figure 2.24 shows the results obtained on a steel sample using various approaches.

Figure 2.24(a) shows a steel block with side drilled holes located close to the scanning surface. With beam steering using the conventional phased array, all the holes are detected but the spread in the signals is significant (Figure 2.24 (b)). With the focusing at a given depth, the side drilled hole no. 3 is well detected with the reduced spread (Figure 2.24 (c)). However, other side drilled holes show a much lower signal amplitude. The best results are achieved by SPA (Figure 2.24 (d)), which detects all the holes with a very low spread in the signals.

Figure 2.25 shows the results on the carbon fibre composite block, which is highly an-isotropic in nature.

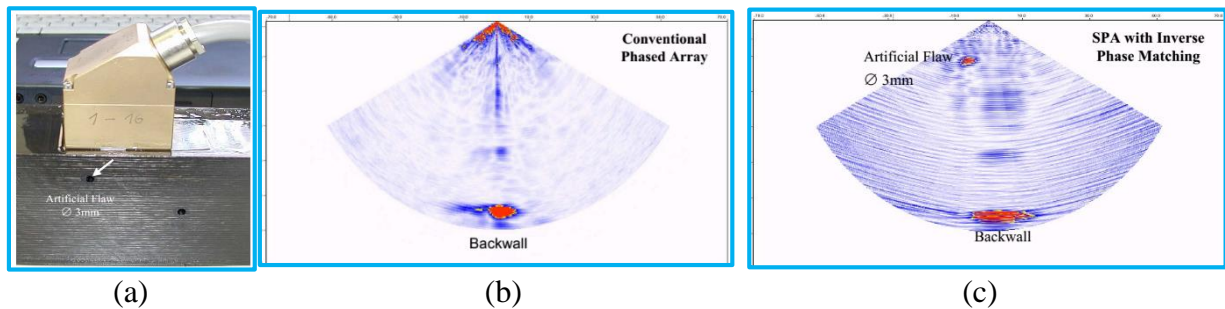


Figure 2.25: Comparison of SPA with conventional phased array technique for the detection of flaws in carbon fibre composite [161]

Figure 2.25(a) shows the linear array placed on a carbon fibre composite block with two side drilled holes. The conventional phased array could not detect these holes reliably (Figure 2.25(b)). With SPA, the detection capability is greatly enhanced (Figure 2.25(c)).

Similar work using SPA was carried out for several industrial components [162]. It was demonstrated that the SPA technique leads to a high resolution imaging of flaws with improved signal to noise ratio and high probability of detection.

The advantages offered by FMC+TFM or SPA over the conventional phased array technique in terms of resolution, signal-to-noise ratio and lateral coverage has attracted the interest of many researchers towards these techniques in the last few years. One of the major reasons for achieving a very high resolution with these techniques is that a single miniature element in an array is used for the sound beam transmission, which gives a very large beam spread. However, the acoustic power of the incident sound beam in the material as a result of a single element excitation is going to be very low. This can be a severe drawback in achieving the required sensitivity for the detection of flaws located at a higher depth or during the examination of materials which are highly attenuating to the sound beam. To overcome this problem, array based techniques based on the concept of virtual array of sources have been developed in recent times.

2.2.7 Virtual Array of Sources

It is well known that the resolution at the focal spot is determined by the size of the piezoelectric element used for the sound beam transmission. When the hardware based approaches are used for the sound beam focusing such as acoustic lens or phased array, the focal spot size reduces (and the resolution improves) with the increase in the size of the piezoelectric element or the effective aperture as the case may be. However, this improvement is at the cost of the reduced focal depth. Contrary to this, when the post processing based approaches are used for the sound beam focusing such as SAFT or TFM, the focal spot size is directly proportional to the size of the piezoelectric element. Smaller dimension elements give large beam spread, which helps in achieving a fine synthetic focus throughout the thickness of the sample under investigation. However, one major limitation of using a miniature piezoelectric element is the loss in the sensitivity for flaw detection, especially at higher depth.

C Frazier, et. al. developed a technique that combines the conventional B-scan with SAFT to achieve focusing beyond the focal point of the transducer. The technique was named as Synthetic Aperture Focusing with Virtual Source Element [163]. M. Skjelvareid, et. al. used this technique for the internal imaging of pipelines [104]. The technique was employed using a single crystal focused ultrasonic transducer. The focused transducers yield a high lateral resolution as long as the distance between the pipe wall and the transducer corresponds to the transducer focal length. If the distance to the wall changes, due to increasing pipe diameter or de-centering of the inspection robot, the lateral resolution is decreased. The authors used synthetic aperture focusing with the virtual source method to extend the effective range of the focused transducer.

The use of linear arrays for imaging using the concept of a virtual source has been reported since early 1990s [164]. The primary objective of these developments was to improve the signal to noise ratio and the sensitivity, which may not be possible with the single element excitation. Karaman et. al., developed two techniques viz. multi-element synthetic aperture focusing (M-SAF) and multi-element synthetic phased array (M-SPA) [165] for imaging using linear arrays and synthetic aperture focusing (SAF). The acoustic power transmitted from a single array element limits the electronic signal to noise ratio (SNR) of SAF. Although beam forming from multiple transmissions increases SNR, it is not acceptable for many applications, especially for medical imaging. To improve SNR, multiple elements can be fired simultaneously with or without aperture apodization. Figure 2.26 shows the angular response that can be obtained by using a linear array under different excitation schemes [165].

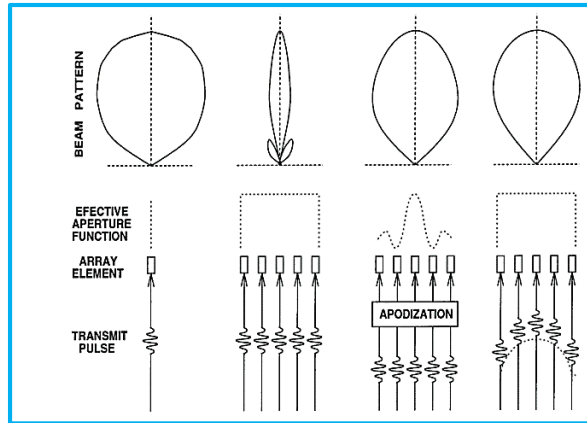


Figure 2.26: Angular response for different excitation schemes using a linear array
(a) single element excitation, (b) multi-element simultaneous excitation, (c) multi-
element simultaneous excitation with apodization and (d) multi-element simultaneous
excitation with de-focusing focal laws [165]

The figure indicates that the simultaneous excitation of multiple elements limits the angular response and can be efficiently used only for linear scanning and imaging with circular arrays. The aperture apodization, such as with a “sinc” type window, results in a transmit beam similar to a single element response. However, the acoustic power capacity of each firing element is not fully utilized and the total transmitted power is very close to that of a single element. The authors [165] synthesized a single element response with a relatively high acoustic power by properly phasing the active transmit elements without introducing any amplitude scaling. This phasing forms a defocusing lens on the sub-aperture consisting of the active elements. A parabolic defocusing lens can be realized using the following delay law:

$$\tau_n = \frac{1}{c} \frac{x_n^2}{2z_d} \quad [28]$$

where x_n is the distance of the n^{th} element from the sub-aperture centre, z_d is the distance of the “defocal” point from the sub-aperture and c is the sound velocity in the medium. To produce a transmit beam as wide as the full sector image, the value of z_d must be chosen properly. With

the use of this approach, one can achieve higher penetration and improved signal to noise ratio as compared to the case when only element excitation is used for acquiring the data.

Moo Ho-Bae et. al. [166], developed an all point transmit-and-receive focusing technique based on the transmit synthetic focusing, combined with the receive dynamic focusing in a linear array transducer. The technique was named as bi-directional pixel-based focusing (BiPBF) technique. In the technique, on transmit, a virtual source element is assumed to be located at the transmit focal depth of a conventional B-mode imaging system. The transmit synthetic focusing is used in two half planes, one before and the other after the transmit focal depth, using the RF data of each scanline, together with all the other relevant RF scanline data previously stored. The principle of this technique is shown in Figure 2.27.

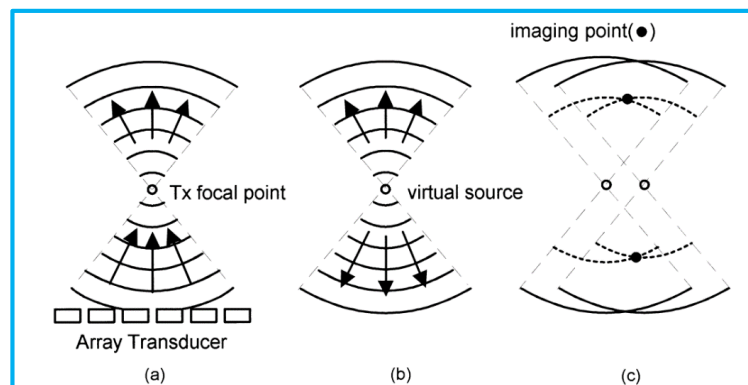


Figure 2.27: Beam propagation in transmit focusing. (a) Conventional B-mode, (b) Transmit model for one virtual element located at focal depth in B-mode and (c) Superposition of transmit fields of two virtual sources at imaging points [166]

In the conventional transmit focusing at one depth, the elements located at the outer edges are fired earlier than the centre element to arrive at the focal point at the same time as the centre one. Thus, the transmitted beam width becomes minimum at the focal depth, and the amplitude becomes maximum. This focused beam is reflected back from an imaging target. On receive, focusing is performed using the same scheme as transmit focusing. In Figure 2.27(a), the transmit field radiated from a transducer, converges toward the focal depth, and thereafter

diverges in the form of a circular wave within a limited angular extent. It appears as if one virtual element is located at the transmit focal depth, generating the circular wave back and forth with respect to itself, as shown in Figure 2.27(b). If a linear array is used, the wavefront in a two-dimensional plane looks like a dipole radiation in which most of the energy is transmitted in the forward and backward directions in a two-dimensional plane. Therefore, the transmit synthetic focusing is possible in two half planes as shown in Figure 2.27(c), one before and the other after the focal depth corresponding to the centre of symmetry of the circular field. The technique improves upon the lateral resolution at all the imaging depths. Also, it increases the transmit power and the signal-to-noise ratio (SNR) of the image.

Another technique based on the concept of a virtual source using linear arrays was developed by Alavuddin et. al. [41]. The technique is named as TIVAS: Technique to Image using Virtual Array Sources. The objective was to achieve the sound beam focusing for the purpose of imaging of defects at larger depth with a good lateral resolution. The technique is based on acquiring the raw B-scan by electronic scanning using a linear array. The raw B-scan data is processed by the synthetic focusing approach for image reconstruction. The authors carried out extensive studies to establish the role of the depth of focus and the focal spot size on the performance of TIVAS semi-analytically and through finite difference time domain (FDTD) simulations. J. Kortbek et. al. developed a novel technique on the concept of virtual array of sources named Synthetic Aperture Sequential Beamforming (SASB) [42]. SASB is a two-stage procedure using two separate beamformers. The initial step is to construct and store a set of B-mode image lines using a single focal point in both transmit and receive. The focal points are considered virtual sources and virtual receivers making up a virtual array. The second stage applies the focused image lines from the first stage as input data, and takes advantage of the virtual array in the delay and sum beamforming. The size of the virtual array is dynamically

expanded and the image is dynamically focused in both transmit and receive and a range independent lateral resolution is obtained.

Another approach, which has been recently reported to improve the data acquisition rate and increase the acoustic power sent into the medium as compared to FMC + TFM, is the technique combining Plane Wave Imaging (PWI) and TFM [167]. In this technique, plane waves are emitted at different angles in transmission and the backscattered signals are recorded by the elements. This is of significance when the region of interest is not directly under the transducer. With less transmissions and a simplified post-processing algorithm, images free of artefacts and with a higher SNR are obtained.

2.3 Flaw characterization by non-destructive examination

Non-destructive examination (NDE) techniques are commonly employed in various industries for the detection and characterization of flaws. These techniques are used at various stages during the manufacturing of the component, while it is in service and in some cases even after the component is retired from the service. During the manufacturing stage, NDE serves as one of the most important quality control tools. Based on the results of NDE, the fabricator makes a decision whether or not the intermediate stage product form such as casting, forging etc. can be further processed. After the component is ready for the shipment, NDE is performed to ensure that component is free from any undesirable flaw stipulated by the designers. NDE during manufacturing stage is carried out as per various codes and standards [46-51]. The standards specify specific NDE technique(s) to be employed for a given product form, the reference defect standard to be used for calibration of test instruments, the criteria for recording of flaw indications, the methodologies for evaluation of flaw indications and the acceptance standard. During in-service inspection, NDE provides vital inputs to the designers, plant operators and the regulatory bodies for carrying out fitness-for-service assessment. These

examinations are carried out as per the established codes and standards [52,53]. Post retirement, NDE is carried out in some cases as an aid to the failure analysis [168].

There are variety of NDE techniques employed on a regular basis for the detection and characterization of flaws in engineering components. These can be broadly classified in to surface examination techniques, volumetric examination techniques and the performance tests [169,170]. The surface examination techniques include visual testing, liquid penetrant testing, eddy current testing and magnetic particle testing. While visual and liquid penetrant tests can only detect those flaws that are open to the examination surface, the magnetic particle and eddy current tests can detect slightly sub-surface flaws depending on the material and the testing parameters. The volumetric examination techniques like radiography and ultrasonic testing can inspect the entire thickness of the component and are capable of detecting surface, sub-surface and the embedded flaws. The performance tests such as helium leak test or acoustic emission are employed to check the integrity of the component [171].

One of the most important tasks during NDE of any component at the manufacturing stage or while in service, is to characterize the flaws that have been detected. Flaw characterization typically involves locating the flaw with respect to some reference, finding its dimensions in terms of length and depth and classifying it in to volumetric (non-crack like), planar (crack-like) or laminar. These inputs are vital in carrying out the structural integrity assessment of a flawed component [172-175]. One of the most critical parameters in deciding the acceptance of a flawed component for continued service is the flaw depth (height or through wall dimensions). Hence, it is of utmost importance that the NDE techniques employed for flaw detection must also accurately size the flaw in terms of its depth [176 -177]. The most effective way of finding the depth of the flaw is to locate its extremities in the thickness direction. From these coordinates, one can find out the depth of the flaw as well as its orientation. Many NDE techniques are handicapped in the estimation of the depth of the flaw, primarily because of

their very principle of operation. For example, one cannot get the information on the depth of a surface flaw by visual examination unless the flaw has a wide opening. Similarly, with liquid penetrant test or magnetic participle test, the depth of the flaw cannot be estimated accurately. Although, radiography is a very popular volumetric NDE technique, estimating the depth of a crack or a lack of fusion observed in the radiograph is seldom done because of the uncertainty associated with it. There are some radiography techniques like Tangential Radiography, which can be used to determine the depth of a corrosion damage in pipelines [178]. However, its application is limited to some specific cases. Eddy current testing has the capability to assess the depth of the flaw found during examination. The depth estimation is based on the phase-analysis of the flaw signals acquired during the inspection [179-181]. There are several advanced electromagnetic NDE techniques such potential drop, magnetic flux leakage, remote field eddy current testing, pulsed-eddy current testing etc. which have been developed over the years and used for field applications for the detection and sizing of flaws in various components [182-184].

Ultrasonic testing is one of the most effective NDE techniques for the characterization of flaws. Being volumetric in nature, it can examine the entire thickness of the component. Also, the fact that it needs access to only one surface, makes it very popular for in-service inspection [185]. The depth sizing of flaws by ultrasonic testing is based on locating the extremities of the flaw with respect to the scanning surface. Several approaches based on the amplitude, the time-of-flight and the spectral analysis of the reflected or diffracted signals from the flaw (or its extremities) have been developed over the past few decades and used in the field for depth sizing of flaws in engineering components [186-191]. A brief account of the ultrasonic based flaw sizing techniques based on the amplitude of the reflected signal from the flaw and on the time-of-flight of the diffracted signals from the flaw extremities are described below.

2.3.1 Depth sizing of flaws by ultrasonic testing based on the amplitude

Ultrasonic testing relies on the reflected signal from the surface of the flaw for its detection. The amplitude of the reflected signal depends on several factors, including the size of the flaw. As a thumb rule, higher signal amplitude corresponds to a large flaw size. There are several methodologies which are employed to interpret the signal amplitude of the reflected signal from the flaw for the assessment of the flaw size. The most common ones are described below.

2.3.1.1 Distance Amplitude Correction (DAC)

A reference block of the same material and geometry of the object to be tested is prepared. Artificial reflectors, also referred as the calibration standard, in the form of holes and notches are introduced in the reference block. Generally, side drilled holes are used for the detection of embedded flaws, notches for the detection of surface breaking flaws and flat bottom holes for the detection of laminar flaws. The size of these reflectors is based on the standard or the procedure, which is being referred for carrying out the ultrasonic test. The transducer, normal beam or angle beam, is positioned over the surface of the sample and the response from these artificial reflectors located at various sound path. From these responses, a calibration curve called as Distance Amplitude Correction (DAC) curve is plotted [60,61]. A typical DAC curve for angle beam examination using side drilled holes is shown in Figure 2.28. This curve is called as the primary reference level (PRL). If any flaw indication is observed during the scanning, an assessment on whether the flaw signal exceeds the PRL is made. The quantitative assessment of flaw size is based on how much dB above or below the PRL, the flaw signal is. The DAC method takes in to account the sound beam attenuation in the material and the beam

spread effect. The size of the flaw obtained by DAC method is never the exact size, but the equivalent size in terms of the calibration standard used.

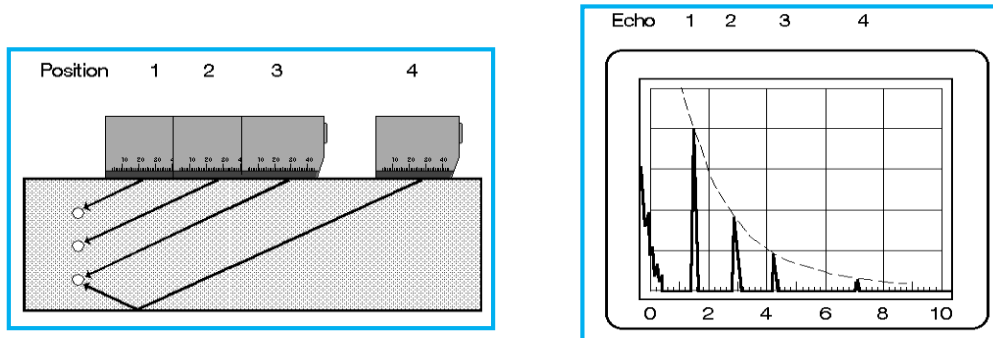


Figure 2.28: Generating DAC curve [62]

2.3.1.2 Distance Gain Size (DGS)

The DGS method is based on the principle that in the far-field of the sound beam, the signal height from a circular disc shaped reflector (flat bottom hole) is directly proportional to the area of the reflector (square of the diameter) and inversely proportional to the square of the distance of the reflector. The DGS method is typically used along with the DGS scales or DGS diagrams, which are available from the transducer manufacturers. A typical DS diagram for a normal beam transducer (B4S) is shown in Figure 2.29 [62].

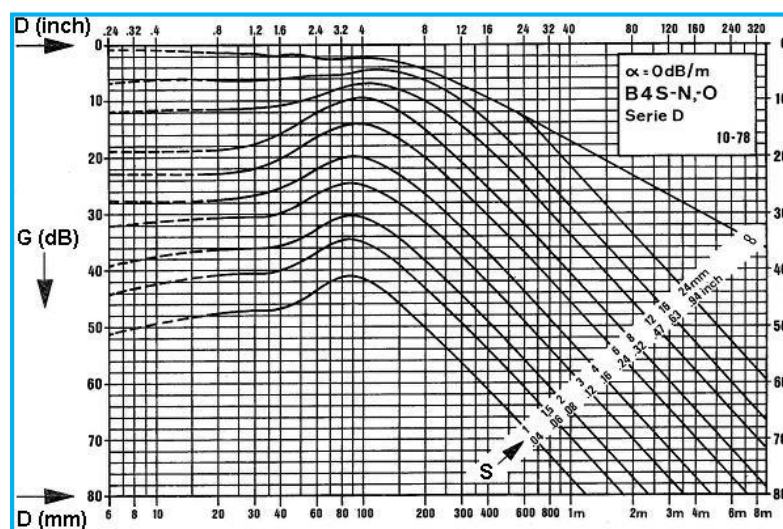


Figure 2.29: DGS diagram for a normal beam probe B4S [62]

The X-axis in figure 2.29 (D) is the distance of the flaw from the scanning surface or the sound path, while the Y-axis (G) is the difference in the amplitude (in terms of dB) between the flaw

and the flat bottom hole. The DGS diagram shown above shows multiple curves for different S values. Each of these corresponds to the DAC curve for a particular size of the flaw bottom hole. These diagrams are generated for the materials with negligible sound attenuation. If the flaw signal is observed during the examination of a component using the DGS method, its size is reported in terms of the diameter of the flat bottom hole. When DGS method is used for the examination of materials with significant sound attenuation, suitable corrections for this has to be made before the assessment of the flaw size. Similarly, when the DGS method is used for the examination of components with curved surfaces such as vessel or pipe, curvature correction has to be applied. The major advantage of DGS method over DAC is that one doesn't need to have a separate reference block. However, the interpretation of the flaw signal to arrive at the equivalent size of the flat bottom hole needs a good understanding of DGS diagrams and their interpretation.

2.3.1.3 Decibel drop

The decibel drop technique is employed for the length and depth sizing of flaws, which are larger than the dimension of the sound beam. In this technique, the transducer is positioned over the component to obtain the maximum response from the flaw. The transducer is then moved until the signal drops to a predetermined level. The position of the transducer and the sound beam paths are noted down and the size of the flaw is evaluated. Two common levels while using decibel drop technique are 6 dB and 20 dB. The principle of dB drop technique is schematically in Figure 2.30 [192].

Figure 2.31 shows an angle beam transducer being scanned over the surface of the sample with a flaw. The figure shows three scan positions (1, 2 and 3) and the corresponding signals (A1, A2 and A3) from the flaw. The maximum response (A2) is obtained when the transducer is at position 2. The transducer is then moved towards the flaw and away from it and the positions (1 and 3) at which the response drops to 50% of the maximum response (A1 and A3) for 6 dB drop method are found out. At these positions, the sound path of the flaw signal is noted. From these sound paths, the depth of the flaw is calculated by the following formula:

$$d = (SP_3 - SP_1) \cos \theta \quad [29]$$

where d is the depth, SP_1 and SP_3 are the sound paths corresponding to positions 1 and 3 respectively, and θ is the beam angle.

Unlike the DAC or DGS method, where the flaw size is reported in terms of the equivalent size of the reference flaw, with dB drop technique, the flaw size obtained is the absolute one. However, this technique is useful only when the flaw size is large as compared to the dimension of the sound beam. If it is not the case, then the flaw size estimated by dB drop technique will have significant errors due to the effect of sound beam divergence [193, 194].

The amplitude comparison based methods for the depth sizing of flaws are prone to significant errors. The real flaws are not as good reflectors of the sound waves as the reference flaws and hence any comparison of reflected signal amplitude from a real flaw with that from a reference flaw leads to underestimation of flaw height [195]. The dB drop methods for flaw height estimation are also not accurate as errors are introduced due to the sound beam divergence and non-perpendicular incidence of sound beam on the flaw surface [196].

2.3.2 Depth sizing of flaws by ultrasonic testing based on time-of-flight

The time-of-flight based approach provides a more accurate assessment of the flaw depth as compared to amplitude based approach [197]. The time-of-flight based approach is not prone to the depth sizing errors due to the factors such as the reflectivity of the flaw to the incident sound beam, unfavorable orientation, branching, transparency, coupling efficiency etc. [198-200]. The depth sizing by the time-of-flight based approach is based on recording the diffracted signals from the crack extremities. Since the time-of-flight of these signals from and to the transducer is dependent of the flaw depth alone, this approach gives a more realistic assessment of the flaw depth. Some of the commonly employed time-of-flight based techniques for depth sizing of flaws are described below.

2.3.2.1. Time of Flight Diffraction Technique (TOFD)

TOFD technique utilizes two ultrasonic angle beam transducers, one acting as a transmitter and the other acting as a receiver [201,202]. The transducers are placed symmetrically over the crack as shown in Figure 2.32 [203].

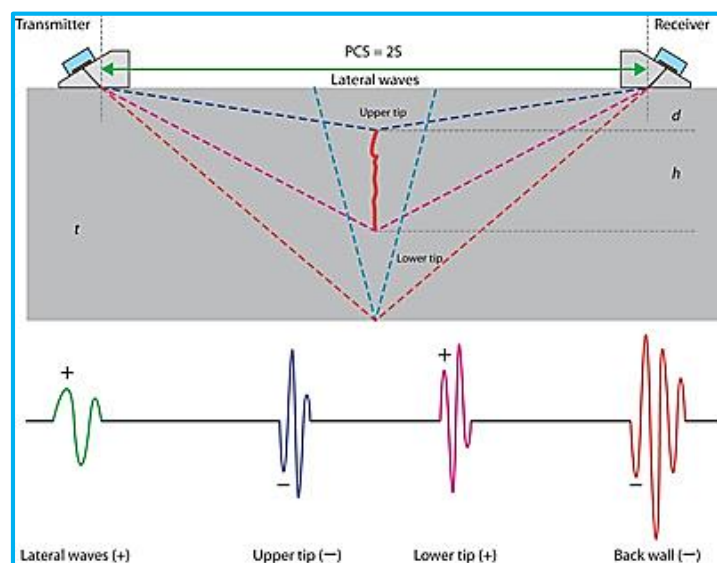


Figure 2.32: Typical TOFD set-up [203]

The transmitter sends the ultrasonic waves, which travel inside the component and interacts with the backwall, the crack face and the crack extremities. There is also a surface wave called as lateral wave that travels from the transmitter to the receiver. The wave reaching the backwall is reflected back and reaches the receiver. The wave incident on the crack face is also reflected back, but doesn't reach the receiver. However, the waves incident on the crack tips undergo diffraction. The diffracted waves travel in all the direction and some of these reach the receiver. The typical A-scan display is shown in Figure 2.32. Since the lateral wave travels the shortest path, it appears first on the A-scan. Contrary to this, the travel path for the backwall signal is the longest and hence it appears last on the A-scan display. In between the signals due to lateral wave and the backwall, there are two additional signals. These signals are the diffracted signals from the upper tip and lower tip of the crack. By accurately measuring the time-of-flight of these signals, one can estimate the depth or through-wall dimension of the crack.

Figure 2.33 shows the typical B-scan image obtained during the TOFD for the configuration shown in Figure 2.32 [204]. The image is acquired by moving the transmitter-receiver assembly along the length of the crack. The X-axis represents the scan direction, while the Y-axis represents the time-of-flight or depth. The image shows the lateral wave, which is practically undisturbed through-out the scan length, followed by the signals from the crack extremities and the backwall.

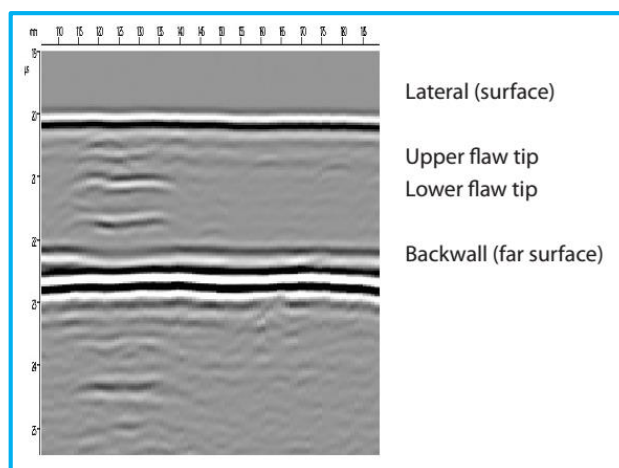


Figure 2.33: Typical B-scan image obtained using TOFD set-up [204]

Assuming that the defect is placed symmetrically between the transducers, the following formulas are used to measure defect height h and the upper ligament d (Figure 2.27)

$$TOF_{lateral} = \frac{PCS}{V_L} \quad [30]$$

$$TOF_{upper\ tip} = [2 ((PCS/2)^2 + d^2)^{0.5}] / V_L \quad [31]$$

$$TOF_{lower\ tip} = [2 ((PCS/2)^2 + (d+h)^2)^{0.5}] / V_L \quad [32]$$

$$TOF_{backwall} = [2 ((PCS/2)^2 + t^2)^{0.5}] / V_L \quad [33]$$

The TOFD technique has been extensively used in the industry for accurate depth sizing of flaws [205-209]. Typical TOFD images for the weld defects are shown in Figure 2.34 [5].

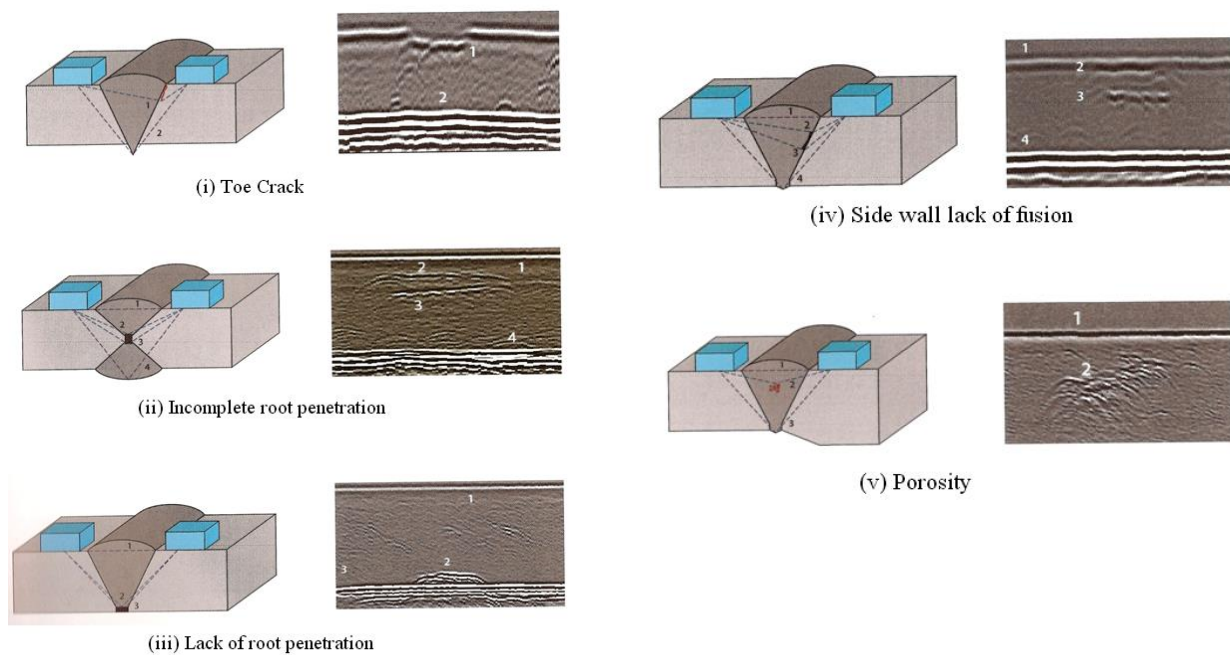


Figure 2.34: Typical TOFD images for weld defects [5]

2.3.2.2 Relative and Absolute Arrival Time Technique

While TOFD uses two transducers for data acquisition, two techniques using a single angle beam transducers are also employed for the depth estimation of crack-like flaws based on the time-of-flight. These are named as: Relative Arrival Time Technique (RATT) and Absolute

Arrival Time Technique (AATT) [210]. RATT is used where the size of the defect is smaller than the beam divergence. For the depth sizing of the defect, the transducer is kept at a fixed position and the ‘crack tip’ and ‘crack corner trap’ are detected at same transducer position as shown in Figure 2.35. The crack height h is then determined as:

$$h = \frac{\Delta UT}{\cos\beta} \quad [34]$$

where, ΔUT is the path difference between the corner signal and the tip signal.

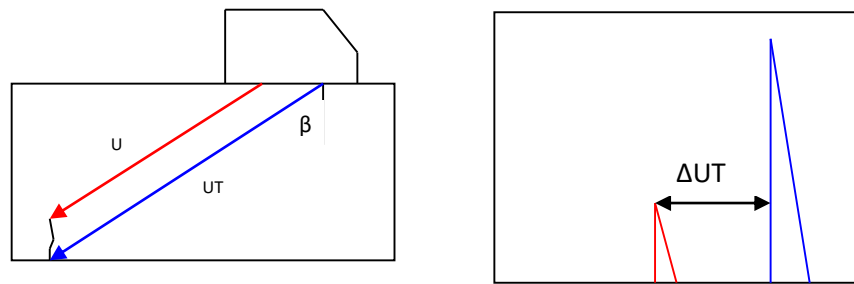


Figure 2.35: Crack height estimation using RATT

AATT is used for flaws that are deeper than the beam size. Under such circumstances, it may not be possible to get the crack tip and the crack corner signal simultaneously. With AATT, the transducer is moved over the scanning surface and the sound path corresponding to the maximum signal amplitude from the crack tip is found out. The depth of the crack h is the given by:

$$h = t - (UT_{path} \cdot \cos\beta) \quad [35]$$

where, t is thickness, and β is the beam angle.

The tip diffraction techniques have proven to be more accurate than the amplitude based techniques for the depth sizing of flaws. These techniques are now routinely used in the industries for the depth sizing of flaws in various components [211, 212].

2.4. Motivation

The review of the literature has revealed that numerous methods for focusing the sound beam for the purpose of ultrasonic non-destructive evaluation have been developed in the past few decades. While the traditional methods based on the use of acoustic lenses or shaped piezocomposite elements are continued to be used in the industries, many advanced methods such as phased arrays are increasingly replacing these for focusing ultrasound. In the current scenario, the emphasis is more on the use of an integrated approach, where the data is acquired by a linear array, either using a single element excitation or an aperture comprising of a few elements, and then achieve sound beam focusing by post-processing of the acquired data using various algorithms such as total focusing method. These integrated approaches have proven to be more effective in terms of lateral resolution, signal to noise ratio and lateral coverage.

One of the major reasons for the success of the integrated approaches like FMC + TFM, Sampling Phased Array and Virtual Array of Sources is that the raw data is acquired using a divergent sound beam. A very small dimension of the piezoelectric element in a linear array, which is seldom available with the conventional single crystal transducer, helps this cause. It has been reported in the literature that the sound beam divergence is a linear function of the ratio λ/D , where λ is the wavelength and D is the size of the piezoelectric element. While this hypothesis holds good for large values of D/λ , with the use of miniature elements in a linear array (where D/λ value is small), it may not be the case. Hence, it is essential to carry out a systematic study using miniature piezoelectric elements and establish a relationship between the element size and the sound beam divergence. This will provide a better insight into the propagation of sound beam in the material and also during the post-processing of the raw data acquired using the divergent sound beam.

One of the standard post-processing algorithms used for the sound beam focusing is the synthetic aperture focusing technique (SAFT). While the lateral resolution that can be achieved

by SAFT depends only on D and is independent of λ , as reported by many researchers, it may not be the case, when SAFT or a similar algorithm is employed for the post-processing of the data acquired by miniature elements in a linear array. One of the reasons for this could be the non-linearity in the dependence of beam divergence angle on the ratio λ/D . Hence, it is worthwhile to explore this aspect and if it is indeed the case, then a relationship on the dependence of the focal spot size (or the lateral resolution) with both D and λ can be established.

The FMC + TFM technique has attracted the attention of many researchers since its development a decade ago for the purpose of ultrasonic non-destructive evaluation. At the same time, it is realized that, to adapt this technique for industrial use it has to be made real-time. To achieve this, one needs to have the same number of parallel receiver channels as the number of elements in the array and also the capability of on-line post-processing. When an array with large number of elements is used with FMC, both these requirements add a significant cost to the phased array instrumentation. In view of this, an alternate technique, which uses a single element for sound beam transmission and reception can be explored. Not only the cost of the instrumentation will be significantly reduced, but the small data size will also help to achieve post-processing in real time. There could be a penalty on the image quality, since the full matrix data is not captured, but the extent of this penalty can only be established after extensive study and experimentation. Moreover, a systematic study on the effect of array parameters and the parameters related to the post-processing algorithm on the focal spot size is always desired, so that the available resources can be optimized to achieve the desired sound beam focusing.

To overcome the drawbacks of FMC + TFM, techniques based on the concept of virtual array of sources have been developed in the past few years. However, no detailed study has been reported in the literature on the optimization of the active aperture size for the purpose of data acquisition. Also, not much published data is available on the performance of these techniques in terms of the detection and characterization of real flaws in engineering components.

It is also realized that, in order to have the maximum data from the flaw for better reconstruction in the final image using FMC + TFM technique or others based on the concept of virtual array, the linear array is required to be placed symmetrically over the flaw. While this condition can be achieved in a majority of the cases, there can be a few instances, where it may not be possible to achieve this. One such case is the detection and characterization of flaws in the weld with an unground bead or crown. A systematic study for such cases using these techniques and if required, development of a new technique using a similar approach is desired.

2.5 Objective

The primary objective of this work is to investigate sound beam focusing techniques using an integrated approach involving linear array and SAFT to overcome the limitations described in the above paragraphs, and then study their usefulness for the purpose of flaw characterization in engineering components. To achieve this, the following work has been carried out:

- ✓ Develop a methodology for data acquisition and processing with a single element transmission and reception using a linear array and SAFT for the purpose of sound beam focusing. This technique is named as Synthetic Focusing using Linear Array (SFLA).
- ✓ Carry out a systematic study to evaluate the sound beam divergence for a miniature element of a linear array and establish an empirical relationship to evaluate the same from its size and the wavelength.
- ✓ Study the effect of array based parameters and SAFT processing based parameters on the size of the focal spot achieved by SFLA and establish the relationship between the focal spot size and the array parameters.
- ✓ Develop a methodology for data acquisition and processing using the concept of virtual array of sources to overcome the drawbacks of SFLA and FMC + TFM techniques with

respect to sensitivity and limited penetration. This technique is named as Phased Array-SAFT (PA-SAFT).

- ✓ Carry out detailed study on the optimization of effective aperture during the application of PA-SAFT technique.
- ✓ Carry out systematic study to assess the performance of SFLA and PA-SAFT techniques in terms of sensitivity, resolution and lateral coverage, and then compare the results obtained by these with the ones obtained by FMC + TFM technique.
- ✓ Evaluate the capabilities of SFLA and PA-SAFT techniques for the detection and characterization of volumetric and planar flaws, both simulated and real.
- ✓ Standardize the PA-SAFT technique using an angle beam for detection and characterization of flaws in weld joints with an unground weld bead, where the application of SFLA, normal beam PA-SAFT and FMC + TFM may be difficult.
- ✓ Develop a methodology for data acquisition and processing by SFLA and PA-SAFT techniques for a real-life application, such as in-service inspection of a weld joint in a pressure vessel of a nuclear boiling water reactor.

EXPERIMENTAL DETAILS

3.1 Introduction

One of the primary objectives of this research work is to investigate sound beam focusing techniques using linear array and SAFT viz. SFLA and PA-SAFT, for sound beam focusing and employ these techniques for the detection and characterization of flaws. Since both these techniques are based on the divergence of sound beam emanating from the miniature elements of a linear array, a systematic study has been carried out to evaluate the sound beam divergence from a sub-millimeter dimension piezoelectric elements, which are typically used in linear arrays. Also, the effect of various parameters related to the linear array and SAFT processing on the focal spot size achieved using SFLA is studied and analyzed in details. A comprehensive study involving simulation and experimental work has been carried out to optimize the active aperture size to be used for acquiring the data using PA-SAFT technique. The effectiveness of SFLA and PA-SAFT techniques on flaw detection and characterization for volumetric and planar flaws has been assessed on separate set of samples. Finally, the usefulness of these techniques for field applications is demonstrated on the weld samples with ‘real’ volumetric and planar flaws and on the mock-up block of a circumferential weld joint in a pressure vessel of a nuclear boiling water reactor.

This Chapter gives the details of experiments carried out to meet the above objectives of the research work. Various samples, which are prepared and used for the experimental work, have been described in terms of their geometry, material and the flaws present in them. The Chapter also gives the details of the experimental set-up comprising of phased array instrumentation, the linear arrays used and how the raw data is acquired on various samples using conventional phased

array, SFLA, PA-SAFT and FMC techniques. A brief description of the algorithm used for SAFT processing using LabView[®] has also been included.

3.2 Experimental Set-up

3.2.1 Phased Array Instrument

During the experimental work, M2M make Multi 2000 phased array system has been used. The instrument has a phased array configuration of 64 x 256. This means that with this instrument one can use an array having up to 256 elements in the multiplexed mode. However, one can use only 64 elements simultaneously to create a focal law. For FMC, the instrument can support an array having up to 64 elements. The instrument has Analog to Digital Converter that samples the data at the frequency of 100 MHz, which corresponds to the time resolution of 10 ns (equivalent to 0.06 mm in steel using longitudinal waves). The sampled data is written to the data file, which can be read and processed using the SAFT algorithm.

The data acquisition software of the instrument allows the user to select the number of elements to be used as an active aperture, the pitch at which the electronic B-scan is to be acquired and the focal laws to be used for acquisition (beam steering, sectorial scanning, single and multi-point focusing etc.). During data acquisition using SFLA and FMC techniques, no focal laws are used. During PA-SAFT, the focal laws are used to focus the sound at a distance very close to the scanning surface. Figures 3.1(a) and (b) show the experimental set-up employed for data acquisition.

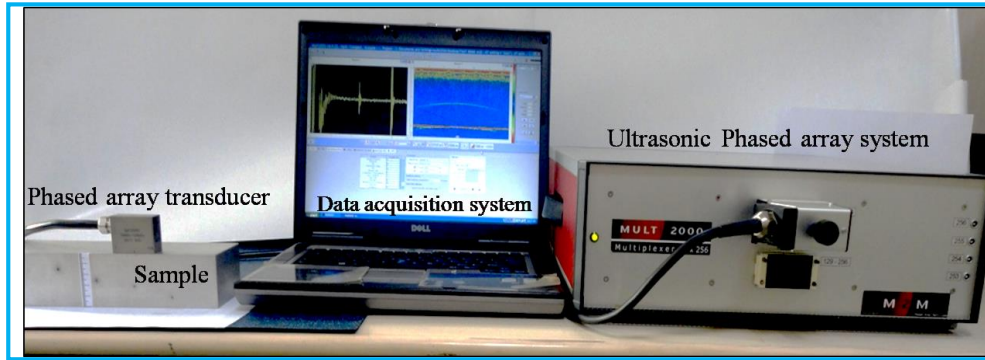


Figure 3.1 a: Experimental set-up for data acquisition

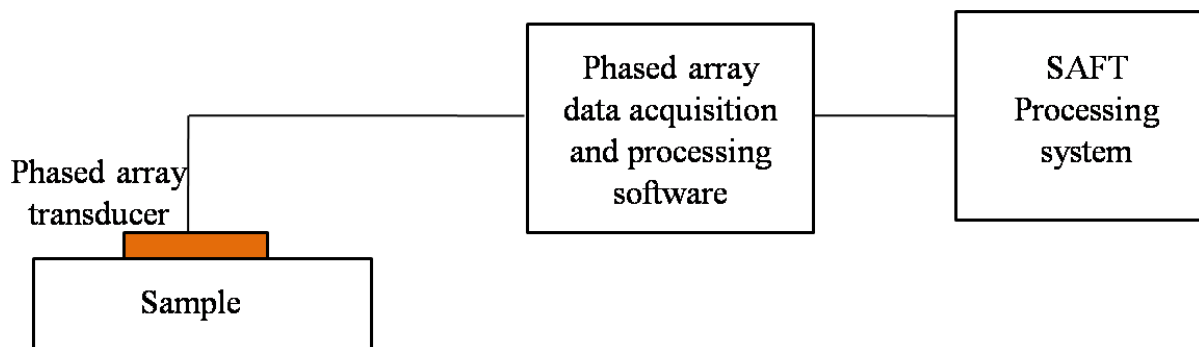


Figure 3.1 b: Block diagram of data acquisition and processing

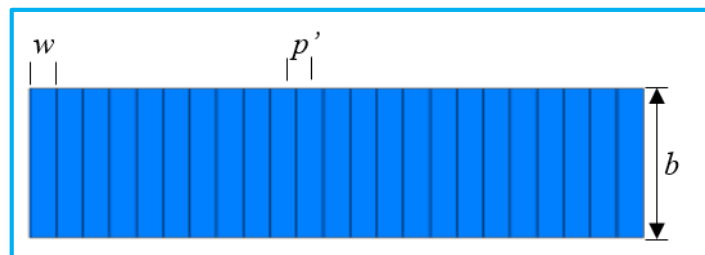
3.2.2 Linear Arrays

During the experimental work, linear arrays of various configurations (frequency, element size, pitch, number of elements) are used. These are given in Table 3.1. The 2 MHz 64 elements 0.8 mm pitch, 5 MHz 64 elements 0.6 mm pitch and 10 MHz 128 elements 0.3 mm pitch arrays are used to study the effect of the size of the miniature piezoelectric elements on the sound beam divergence. These arrays are also used to study the effect of various factors on the focal spot size achieved using SFLA and PA-SAFT techniques. The validation of the outcome of the study carried out to assess the beam divergence from a miniature piezoelectric element is performed using 5 MHz 1 mm pitch 64 elements and 8 MHz 64 element 0.5 mm pitch linear arrays. The study on the

characterization of volumetric and planar flaws (artificial flaws in plates and real flaws in welds) by SFLA and PA-SAFT techniques is carried out using 5 MHz 64 elements 0.6 mm pitch and 10 MHz 0.3 mm pitch 128 elements linear arrays. The study on the mock-up block of circumferential weld joint in the pressure vessel of nuclear boiling water reactor is carried out using 2 MHz 64 elements 0.8 mm pitch and 5 MHz 64 elements 1mm pitch linear arrays.

Table 3.1: Details of linear arrays used for the experimental work

Sr. No.	Frequency (MHz)	Total number of elements (N)	Element Width w (mm)	Element Pitch p' (mm)	Orthogonal Dimension b (mm)	$p'/\lambda_{\text{steel}}$
1	2	64	0.55	0.8	18	0.26
2	5	64	0.5	0.6	10	0.50
3	5	64	0.75	1	7	0.63
4	8	64	0.4	0.5	5	0.67
5	10	128	0.25	0.3	5	0.50



3.2.3 SAFT algorithm

The raw B-scan data acquired using SFLA and PA-SAFT techniques are processed using a time based SAFT algorithm written in LabView. The front panel of the LabView algorithm for SAFT processing is shown in Figure 3.2.

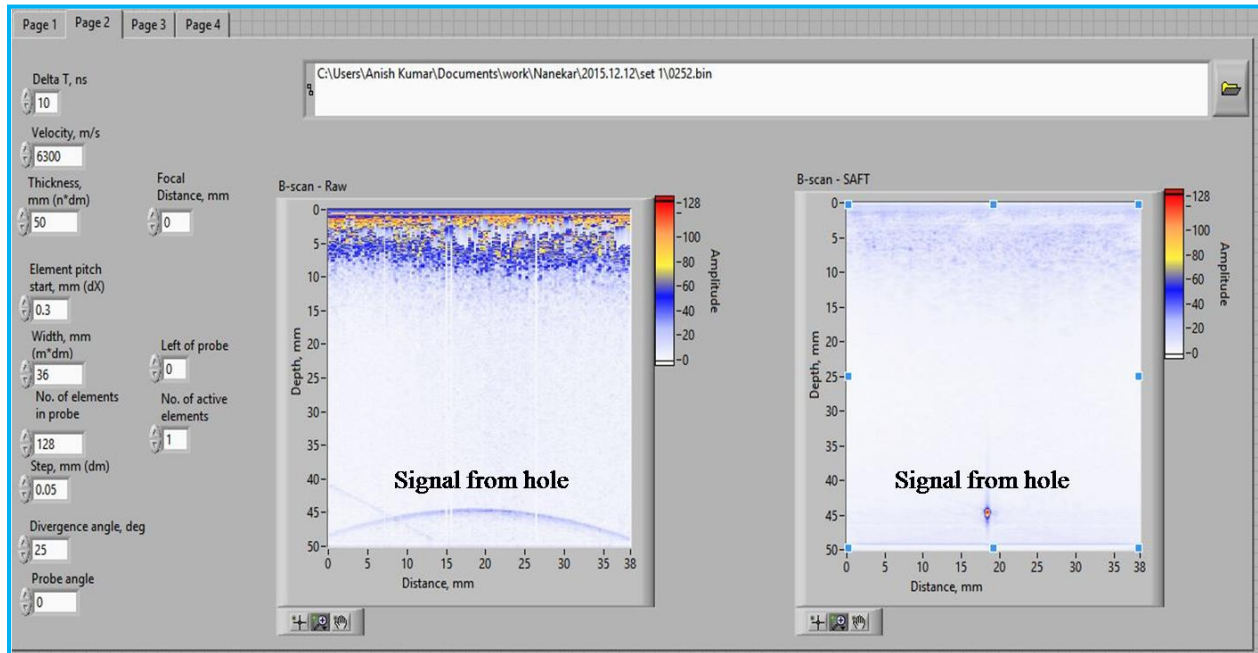


Figure 3.2: Front Panel of LabView algorithm for SAFT processing of raw B-scan images acquired using SFLA and PA-SAFT techniques

Following is the brief description of the input fields that are seen in the front panel:

- File path:** The file path of the raw B-scan appears in this field. The program loads the data file from the corresponding location on the hard drive or external drive for further processing
- Delta T:** This represents the sampling rate or the time interval between the two samples in the A-scan. Since the raw B-scan image is acquired using the sampling (or digitization) rate of 100 MHz, the time interval between the two samples is 10 ns.

- c) **Velocity:** The user needs to input the velocity of the sound in the sample on which the raw data is acquired.
- d) **Thickness:** The maximum thickness for which the data has to be processed and the image should be displayed is specified by the user and entered in this field.
- e) **Focal distance:** This represents the distance from the surface at which the sound beam is focused during the acquisition of the raw B-scan. While using SFLA, this distance is 0 mm. With PA-SAFT, the distance at which the sound beam is focused is entered here. During the experimental work carried out as part of this research work, the focal distance for majority of the samples using PA-SAFT technique is 2 mm.
- f) **Element Pitch:** The user enters the pitch of the linear array used for data acquisition.
- g) **Width:** This represents the width of the linear array used. This is equal to the pitch x total number of elements used for data acquisition.
- h) **Left of the probe:** During SAFT processing, one achieve sound beam focusing at locations, not just below the linear array but even on the left and right side of the array, since the data from this region is available in the raw B-scan because of beam divergence. User can specify this region by entering the appropriate value in this field.
- i) **Number of elements:** The total number of elements in a linear array is specified here.
- j) **Number of active elements:** The total number of elements used in an active aperture during data acquisition are specified here. For SFLA technique, this value is 1, while for PA-SAFT technique, this value depends on the linear array used and the focal distance. The total number of elements in an array, the number of active elements and the pitch at which the data is acquired decides the total number of A-scans for data processing. For example, with SFLA, if a linear array with 128 elements is used and the data is acquired using each element, then the

total number of A-scans is 128. With PA-SAFT technique, if 8 number of active elements are used using the same array, then the total number of A-scans is 121 ($128 - 8 + 1$).

- k) **Step Size:** User needs to specify the lateral spacing between the focal points in this field. Smaller step size gives better results but at the cost of increased processing time.
- l) **Divergence Angle:** User needs to specify the extreme limits of the divergence angle to be considered for processing. Only those A-scans that lie between these limits are used for SAFT processing. A very low value of this parameter results in lesser number of A-scans for SAFT processing, leading to inferior focusing. A very high value of this parameters, leads to a condition wherein there are large number of A-scans for SAFT processing with no useful information from the flaw. This results in a very low amplitude of the flaw signals in the processed image and also an increase in the processing time.
- m) **Probe angle:** The user needs to enter the angle of primary sound beam used for data acquisition. For SFLA, this figure is 0 deg. While for PA-SAFT, this figure will be 0 deg. when normal beam is used for data acquisition. When Angle Beam PA-SAFT is used, then the user needs to input the primary beam angle used during data acquisition.

Once the above fields are entered and the program is executed, the SAFT processed image is displayed next to the raw B-scan image. The colour scale corresponding to the amplitude of the signals is also displayed alongside.

Bandpass filter is used during data processing. For 5 MHz linear array, the frequency band is set from 3 MHz to 7 MHz, while for 10 MHz linear array, it is set from 6 MHz to 14 MHz. During data acquisition by SFLA and PA-SAFT techniques on various samples, a strong backwall signal is obtained in the raw B-scan image. To avoid this signal from creating undesirable artifacts in the processed B-scan image, the backwall signal is eliminated from SAFT processing.

Figure 3.2 shows the raw and the processed B-scan images acquired from a 0.5 mm dia. side drilled hole located at a depth of 45 mm from the surface in a 50 mm thick aluminum block. The image has been acquired using a 10 MHz, 0.3 mm pitch, 128 elements linear array. The raw B-scan image shows that the signal from the hole is fairly wide and has a shape of a hyperbola. The signal is present for the full width of the image, which indicates that the signal from the hole is present in all the A-scans (128 nos. in this case). On the left side of the image, an additional signal (part hyperbola) is also seen. This signal is from the adjacent hole located at a different depth in the sample. The image shows that initial ringing (dead zone) under the given conditions is approximately 7 mm. Also, the amplitude of the signal from the hole is much smaller than the amplitude of the initial pulse. The raw B-scan image shows some breaks in the hole signal at 7 mm, 15 mm and 27 mm distance. These breaks are because of the dead elements in the linear array used. This is confirmed separately by acquiring the electronic B-scan of a backwall using a single element excitation. The B-scan showed loss of backwall signal at these locations. Since the number of dead elements are very small as compared to the number of elements for which useful data is available, there is no significant deterioration in the result obtained on SAFT processing.

The SAFT processed B-scan image shows that the wide spread-out signal from the hole has been reduced to a spot. During SAFT processing, the lateral spacing between the focal points is kept as 0.05 mm and the divergence angle used is 25 deg. Since the data is acquired using SFLA, the probe angle is 0 deg. From the normalized amplitude scale of the raw and the processed B-scan images, one can make out that there is drastic improvement in the amplitude of the signal from the hole in the processed B-scan image (red) as compared to the raw B-scan image (light blue). This is because of the summation of the signals from the hole in large number of A-scans during SAFT processing. The processed image also exhibits significant reduction in the amplitude of the initial ringing and

the background noise as compared to the raw B-scan image. This is because of the inherent averaging associated with the SAFT processing. In effect one can say that, during SAFT processing there is a significant improvement in the signal to noise ratio (SNR). From the processed B-scan image, the following information can be obtained:

- Amplitude of the signal
- The location of the signal from the scanning surface
- Lateral distance of the signal from a reference point (e.g. first element of an array)
- The lateral spread of the signal (6 dB or 20 dB)

The amplitude of the signal is an indication of the effectiveness or the sensitivity for the detection of a flaw (or its extremities). The location of the flaw extremities from the scanning surface gives the information on the height or through-wall dimension of the flaw (also referred as depth). From the lateral position of the flaw extremities one can estimate the orientation of the flaw with respect to the normal to the scanning surface. The lateral spread of the signal is an indication of focal spot size. Smaller spread leads to lesser un-certainty in locating the flaw extremities, both laterally and depth wise.

During this study, raw B-scan data on several samples are acquired by full matrix capture (FMC). These data are subsequently processed by an algorithm called total focusing method (TFM) using ultrasonic simulation package CIVA 11. No bandpass filtering is employed during processing.

3.3. Evaluation of sound beam divergence for miniature elements of a linear array

In order to evaluate the divergence of the sound beam emanating from a miniature element of a linear array, experiments are conducted on a 50 mm thick aluminum block containing 0.5 mm dia., 20 mm deep side drilled holes. Side drilled holes are drilled from one of the faces at a distance of

10 mm, 20 mm, 25 mm, 35 mm and 45 mm from one of the scanning surfaces. This ensures that when the linear array is placed on the two opposite scanning surfaces for data acquisition, the data is available for the sound beam path of 5 mm to 45 mm at every 5 mm interval. The side drilled holes are made by EDM and act as point reflectors to the incident ultrasonic beam. The holes are separated laterally by a distance of 40 mm, so that there is no interference from the adjacent holes when the data is acquired for any specific hole using SFLA and PA-SAFT techniques. The sketch of the sample is shown in Figure 3.3.

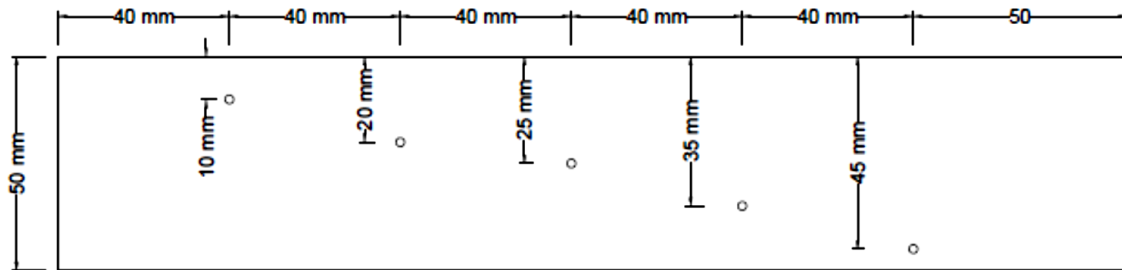


Figure 3.3: Aluminum sample with 0.5 mm dia. side drilled holes at various depths from the scanning surface

In order to evaluate the beam divergence constant for small values of D/λ that are encountered using linear arrays, data is acquired from the hole located at 35 mm depth from the surface. This is done to ensure that the hole is located at a distance, which is at least three times the near-field for the aperture selected. A linear array is placed symmetrically over the hole such that the central element of an array is approximately located over the hole. With this arrangement, B-scan images are acquired by electronic scanning using active aperture varying from a single element to a group of up to 16 elements. Figure 3.4 schematically shows the experimental set-up for data acquisition using 1, 2, 4 and 8 active elements.

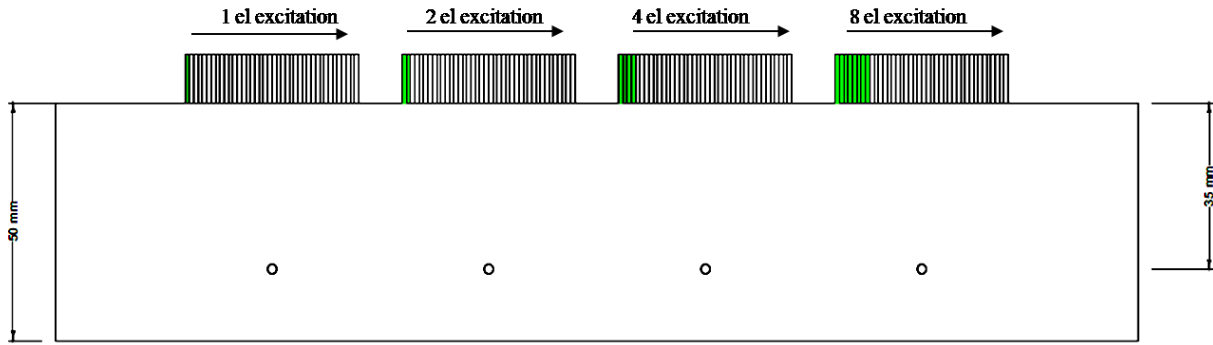


Figure 3.4: Experimental set-up for estimation of beam spread constant for small values of D/λ

With a single linear array, B-scan images are acquired using varying active apertures so that the beam divergence can be evaluated for different values of D/λ . For example, while using a 10 MHz, 0.3 mm pitch linear array (element width 0.25 mm and gap between elements 0.05 mm) on Aluminum ($V_L = 6300$ m/s), the value of λ comes to 0.63 mm. When the electronic B-scan is acquired using a single element excitation, the value of D is 0.25 mm, with two element excitation it becomes 0.55 mm, with four element excitation it becomes 1.15 mm and so on. The corresponding D/λ values for these three cases are 0.39, 0.87 and 1.82 respectively.

Prior to data acquisition from the side drilled hole, the response from the individual elements of an array is equalized by taking the backwall signals from each element of an array and adjusting the amplifier gain on each element. Once this is done, the linear array is placed over the side drilled hole and the B-scan image is acquired electronically by selecting the aperture size as described above. From the B-scan image, the lateral positions of two points on either side of the maximum in the scan direction at which the amplitude from the hole is 6 dB lower than the maximum amplitude are found out. The linear distance between these two points represents the 6 dB beam width at 35 mm depth from the surface. From this width, the half beam spread angle is

mathematically calculated. This exercise is carried out for three different linear arrays: (i) 2MHz, 0.8 mm pitch, 64 elements, (ii) 5 MHz, 0.6 mm pitch, 64 elements and (iii) 10 MHz, 0.3 mm pitch, 128 elements. Based on the results, a mathematical relation to evaluate the beam spread for the sound beam emanating from miniature elements of a linear array is derived. The above linear arrays are chosen so that one gets different values of D as well as different values of λ while acquiring the data with different arrays.

To validate the beam spread equation, the data acquisition, as described above, is carried out on two separate linear arrays viz. 5 MHz, 64 elements, 1 mm pitch and 8 MHz, 64 elements, 0.5 mm pitch. The beam spread found out experimentally is compared with one evaluated using the mathematical relationship.

3.4 Assessment of the effect of array parameters and SAFT processing parameters on sound beam focusing using SFLA

The sound beam focusing using SFLA depends on several factors related to the linear array used and the difference in the input value and the true value of various parameters during SAFT processing of the acquired data. A systematic study is carried out to evaluate the effect of these parameters on the focusing achieved by SFLA. Experiments are conducted on an aluminum block, described in Section 3.3, containing side drilled holes of 0.5 mm diameter located at different depths from the scanning surface (Figure 3.3). The raw data is processed by SAFT algorithm and the 6 dB size of the holes is determined from the processed image. The 6 dB size is taken as a measure of the focal spot size.

3.4.1 Effect of array based parameters

The effect of array based parameters on the sound beam focusing over a depth range of 5 mm to 40 mm is studied for: (i) the aperture size, (ii) the pitch, (iii) the frequency of sound wave and (iv) the total effective aperture (TEA). TEA is the total number of elements used, or the length of the array on the scanning surface for data acquisition.

Table 3.2: Details of parametric study carried out to evaluate the effect of array based parameters on the sound beam focusing by SFLA technique

Array based parameters	Data Sets			
	Set 1	Set 2	Set 3	Set 4
Aperture size (el)	1 to 12	1	1 el	See
Pitch (mm)	0.3 mm	0.3, 0.6, 0.9 and 1.2	0.3 mm	Footnote ¹
TEA (el)	128	128	64, 80, 100, 128	
Frequency (MHz)	10	10	10	2, 5 and 10

el = Total number of elements

¹ While using the 10 MHz linear array, the data is acquired using two active elements, so that the aperture size is 0.55 mm, which is equal or very close to the aperture size while using a single element excitation using 2 MHz (0.55 mm) and 5 MHz (0.5 mm) linear array. The data using 10 MHz linear array is acquired for every alternate element so that a pitch of 0.6 mm can be achieved. This ensures that the pitch using all the three linear arrays is more or less similar (0.6 mm for 5 MHz and 10 MHz and 0.8 mm for 2 MHz). Similarly, using 2 MHz array, the data is acquired for 48 of the total 64 elements, so that the total effective aperture of approximately 38 mm on the scanning surface is similar for all the three cases.

During this study, four sets of raw data are acquired. In each set, one of the above parameters is varied and the others are kept constant. The effect of aperture size is studied by acquiring the data for active apertures comprising of different number of elements. The effect of pitch is studied by acquiring the data for every second, third or fourth element in the array. To study the effect of TEA, the data is acquired for different number of elements in the array. The effect of frequency is studied by acquiring the data using linear array of different frequencies. The details are given in Table 3.2.

3.4.2 Effect of the difference between the true value and the input value of different parameters during SAFT processing

The input value given to the SAFT processing algorithm for the sound velocity in the material, the element pitch of the linear array used and the sound beam divergence angle, may be different than the true value. The effect on the focal spot size as a result of this difference has been studied. For this purpose, the raw B-scan image is acquired on the side drilled hole located at a distance of 35 mm from the surface in the aluminum block shown in Figure 3.3 using 10 MHz, 0.3 mm pitch, 128 elements linear array. The data are acquired using a single element excitation with a pitch of 0.3 mm and the TEA of 128 elements. During SAFT processing, one of the above three parameters is changed while the other two are kept constant. The effect of the difference in the sound velocity on the focal spot size is studied by varying it from 6100 m/s to 6500 m/s at 100 m/s interval (actual velocity is 6300 m/s). The effect of the difference in the pitch on the focal spot size is studied by varying it from 0.28 mm to 0.32 mm with 0.01 mm interval (actual pitch is 0.30 mm). The effect of the difference in the beam divergence angle on the focal spot size is studied by varying it from 10 deg. to 45 deg. with 5 deg. interval (actual beam divergence is approximately 25 deg.).

The true values of sound velocity, element pitch and the beam divergence angle are 6300 m/s, 0.3 mm and 25 deg. respectively. The details are given in Table 3.3.

3.5 Optimization of the aperture size for PA-SAFT technique

The PA-SAFT technique uses a group of active elements for sound beam transmission. The number of active elements to be chosen for the acquisition of the raw B-scan data depends on the linear array used and the depth range for which the focusing is desired. The aperture size for PA-SAFT technique using 5 MHz, 0.6 mm pitch linear array and 10 MHz, 0.3 mm pitch linear array for focusing up to a depth of 40 mm is optimized using detailed simulation studies. This is subsequently validated by experimental work.

The simulation studies are carried out using CIVA 11 [213-216]. CIVA 11 is a semi-analytical package developed by CEA, France. The ultrasonic simulation using CIVA 11, has two modules: the beam computation and the defect response. The beam computation gives the sound beam profile, including the wave amplitude distribution, inside the component for a given experimental arrangement. The user needs to define the material (density, velocity, attenuation coefficient, anisotropy etc.), the transducer details (single crystal or array, geometry of the crystal, wedge details etc.) and the wave modes (longitudinal or shear), which needs to be computed. The transducer is positioned at the desired location over the surface of the sample. The aperture size, sequencing of excitation and the required focal laws are selected. The region of interest within the material is defined and the sound beam profile in this region is computed. Figure 3.5 shows the typical sound beam computation result in a steel sample obtained using CIVA 11 for an active aperture comprising of 8 elements of a 10 MHz, 0.3 mm pitch linear array without the application of focal law. The magnitude of the sound wave amplitude in the computation zone is colour coded,

blue representing the maximum, pink representing the intermediate and green representing the minimum sound pressure.

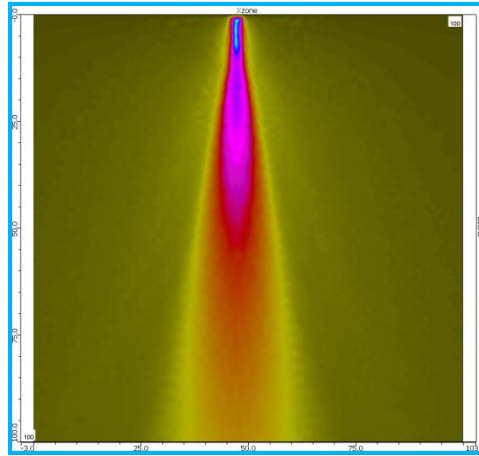


Figure 3.5: Sound beam computation using CIVI 11 for 10 MHz, 0.3 mm pitch linear array with 8 elements active aperture and no focal law

The simulation studies for the optimization of an active aperture for PA-SAFT technique involved the following: (i) variation in the sound wave amplitude with depth, (ii) variation in the beam width with depth, (iii) the overall sound beam profile and (iv) the size of the virtual source that is created at the focal point. These studies are carried out for 5 MHz, 0.6 mm pitch and 10 MHz, 0.3 mm pitch linear arrays. Based on the simulation studies, the optimum size of the active aperture to be employed with PA-SAFT technique while using the above two arrays is arrived at.

In order to validate the outcome of the simulation studies, experiments are carried out on the aluminum sample containing 0.5 mm dia. side drilled holes shown in Figure 3.3. The linear array (5 MHz and 10 MHz) is kept over the surface such that the central elements are approximately over the hole from which the data is being acquired. B-scan images are acquired using active aperture varying from 3 to 12 elements with 5 MHz, 0.6 mm pitch and 4 to 14 elements with 10 MHz, 0.3 mm pitch linear arrays. In each case, the sound beam is focused at a depth of 2 mm from

the surface using focal law. The B-scan images are processed by SAFT algorithm. Figure 3.6 schematically shows the experimental arrangement for acquiring the data by using PA-SAFT technique with different active apertures, for the side drilled hole located at 35 mm depth from the scanning surface. From the processed B-scan image, the 6 dB width of the signal from the holes is found out. This is taken as a measure of the focal spot size.

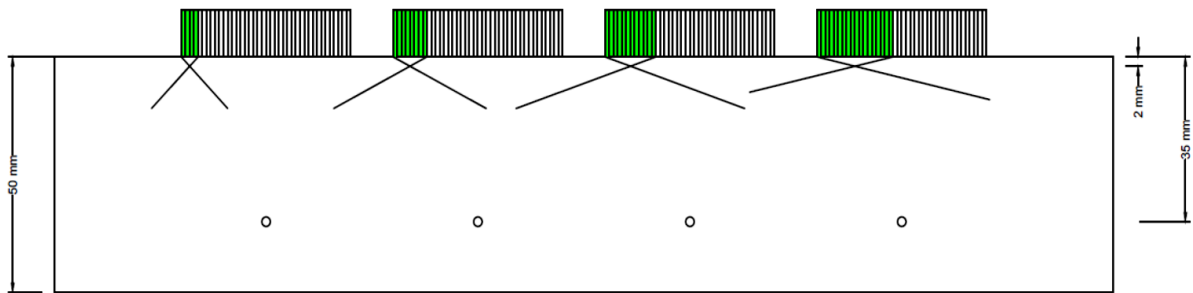


Figure 3.6: Experimental set-up for optimization of aperture size for PA-SAFT technique

3.6 Assessment of the capabilities of SFLA and PA-SAFT techniques for the detection and characterization of volumetric flaws

Volumetric flaws are three-dimensional and are required to be detected and characterized in terms of their dimensions by ultrasonic examination so that their acceptance as per the given specification or standard can be determined. The ability of SFLA and PA-SAFT techniques for the detection and characterization of volumetric flaws is carried out by experimental work on carbon steel and aluminum samples. The volumetric flaws are simulated by side drilled holes machined from one of the faces of the samples. The study is carried out to meet the following objectives:

- Determine the sensitivity for the detection of volumetric flaws with a focused sound beam across the depth

- Determine the limit of sensitivity of these techniques for the detection of volumetric flaws for a given experimental set-up
- Determine the lateral coverage achieved by these techniques
- Determine the limit of resolution of these techniques

To meet the first objective, experiments are carried out on a carbon steel plate sample with 1 mm dia. side drilled holes located one below the other. For meeting the second objective, experiments are performed on an aluminum sample with 0.5 mm dia. side drilled holes at different depths from the scanning surface. The third objective is met by carrying out experiments on aluminum sample with 2 mm dia. side drilled holes located at the same depth from the scanning surface but separated laterally. For meeting the fourth objective, experiments are carried out on a carbon steel plate sample with 0.5 mm side drilled holes at the same depth but separated laterally by a very small distance.

Experimental data on all the samples are acquired using 10 MHz, 0.3 mm pitch, 128 elements linear array. A single element excitation is used during data acquisition with SFLA technique. With PA-SAFT technique, an active aperture comprising 8 elements is used and the sound beam is focused at the depth of 2 mm from the surface. The selection of this aperture size is based on the outcome of the optimization studies carried out by simulation and experimental work. The raw B-scan images acquired using SFLA and PA-SAFT techniques are processed by time based SAFT algorithm. Additionally, experiments are also carried out using the conventional phased array based on focal laws and FMC+TFM technique. Due to the limitations of the phased array instrumentation in terms of the number of parallel receiver channels, only 64 of the 128 elements of 10 MHz linear array are used for the data acquisition using FMC. The use of lesser number of elements for FMC corresponds to lower total effective aperture on the scanning surface, when

compared to the data acquisition using SFLA and PA-SAFT techniques. This may have an adverse effect on the focal spot size achieved.

3.6.1 Determination of the sensitivity for the detection of volumetric flaws with a focused sound beam across the depth

In order to assess the ability of SFLA and PA-SAFT techniques for the detection of volumetric flaws with a focused sound beam across the depth, experiments are conducted on a carbon steel sample with 1 mm dia. side drilled holes. The experimental set-up for data acquisition is shown in Figure 3.7. The sample has eight side drilled holes, located at a depth of 10 mm to 45 mm from the scanning surface. The holes are present one below the other in a straight line and are separated by a distance of 5 mm. Figures 3.7(a) shows the transducer position relative to the holes for acquiring the data using the SFLA, PA-SAFT and FMC techniques. Since a divergent sound beam is used for data acquisition, this kind of the placement of an array ensures that the useful data from all the holes is obtained from majority of the elements (or apertures). However, this arrangement is not suitable for the conventional phased array using focal laws, where a focused sound beam is used for acquiring the data. This is because of the fact that the topmost hole prevents the sound beam from reaching the bottom holes. To facilitate the detection of all the holes by a focused sound beam using focal law based approach, the linear array is placed over the sample not directly over the holes but slightly shifted as shown in Figure 3.7(b). With this arrangement, the sound beam emanating from the active apertures comprising of 16, 32, 48 and 64 active elements is focused across the depth of the sample using focal laws. The selected aperture does not move electronically, but the sound beam is steered and focused to generate the S-scan image.

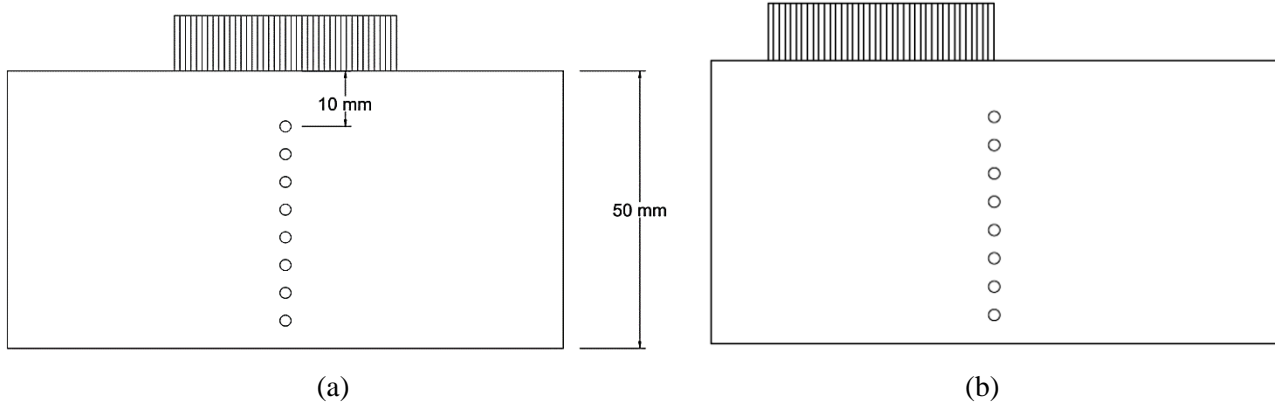


Figure 3.7: Experimental set-up for data acquisition on carbon steel sample with vertically stacked side drilled holes (a) SFLA, PA-SAFT and FMC techniques, (b) Conventional angle beam phased array using focal laws

The following information is extracted from the processed B-scan images:

- The total number of holes detected using a given test set-up
- The maximum amplitude difference between the signals from the holes
- The variation in the 6 dB spread of the signals from the holes

The results obtained by SFLA and PA-SAFT techniques are compared with the ones obtained by conventional phased array and FMC.

3.6.2 Determination of the limit of sensitivity for volumetric flaws

To determine the limit of sensitivity of SFLA and PA-SAFT techniques for the detection of volumetric flaws, experiments are carried out on an aluminum sample containing 0.5 mm side drilled holes located at a distance of 40 mm to 200 mm from the surface. The experimental set-up for data acquisition is shown in Figure 3.8. The figure shows that side drilled holes are located one below the other but separated laterally. As a result, there is no masking effect from the topmost hole for the bottom holes, which is encountered in the carbon steel block described in Section

3.6.1. The raw B-scan data are acquired using 10 MHz, 0.3 mm pitch, 128 elements linear array and are subsequently processed by SAFT or TFM as applicable. From the processed B-scan images, the deepest side drilled hole that is detected is found out. The results obtained by SFLA and PA-SAFT techniques are compared with the ones obtained by FMC + TFM.

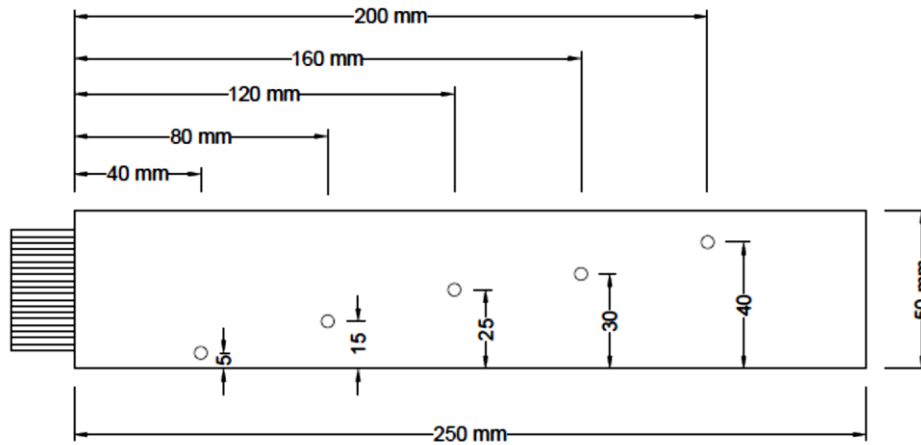


Figure 3.8: Experimental set-up for data acquisition on an aluminum sample with 0.5 mm dia. side drilled holes

3.6.3 Determination of the lateral coverage achieved by SFLA and PA-SAFT techniques

In order to assess the lateral coverage achieved by SFLA and PA-SAFT techniques, experiments are conducted on an aluminum sample having fifteen, 2 mm dia. side drilled holes, located at the depth of 25 mm from the scanning surface. The experimental set-up for data acquisition is shown in Figure 3.9. The central seven holes lie below the array and the remaining eight holes, four of both sides, lie in the region away from it. The data for this sample is acquired using 10 MHz, 0.3 mm pitch, 128 elements linear array. Using the conventional phased array, the sound beam is steered and focused at the depth where the holes are located using the selected aperture (16 to 48 elements). The aperture is not moved electronically. With SFLA, PA-SAFT and FMC techniques, the selected aperture is moved electronically from one end of the array to other and a raw B-scan

image is acquired. During SAFT and TFM processing, it is ensured that the processing range not only includes the material beneath the linear array, but also the material on either side of the array up to a distance of approximately 30 mm. From the processed images, the lateral coverage obtained, the amplitude variation between the signals from the holes and the 6 dB spread of the holes is found out.

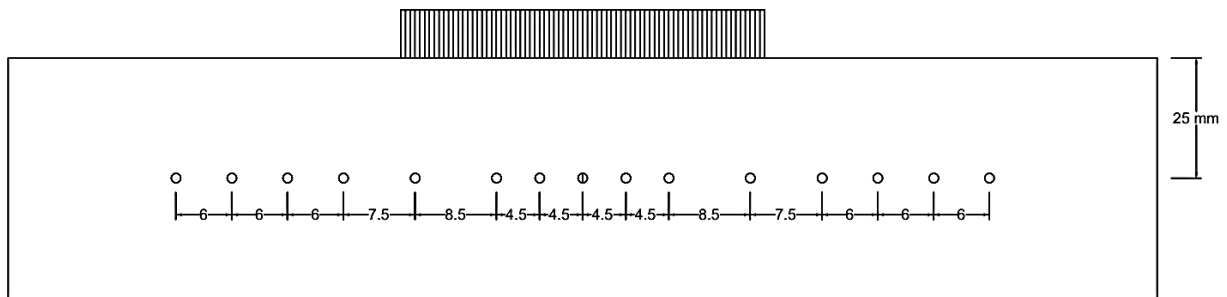


Figure 3.9: Experimental arrangement for data acquisition on aluminum sample with laterally separated holes

3.6.4 Estimation of the resolving power of SFLA and PA-SAFT techniques

Both SFLA and PA-SAFT techniques have a good potential to focus the sound beam within the material. This ability is useful in resolving the two very closely spaced volumetric flaws. In order to quantitatively assess the resolving power of SFLA and PA-SAFT techniques, experiments are conducted on a steel block containing very closely spaced, 0.5 mm diameter side drilled holes. Figure 3.16 shows the sketch of this sample. The sample has six side drilled holes, all located at the depth of 20 mm from the scanning surface. The holes are separated centre-to-centre by a distance of 0.6 mm to 1.5 mm as shown in Figure 3.10.

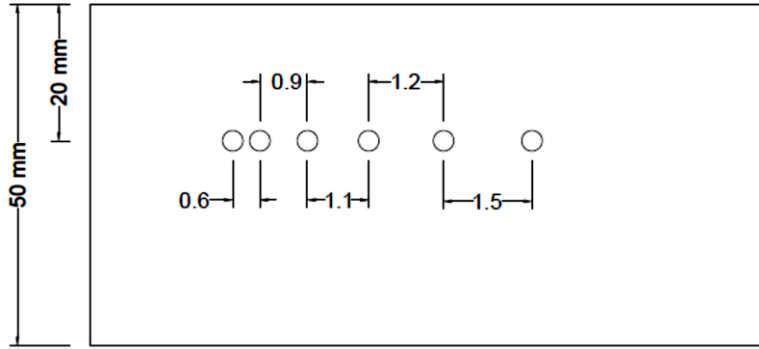


Figure 3.10: Carbon steel Sample with Closely Spaced Side Drilled Holes

A 10 MHz, 0.3 mm pitch, 128 elements linear array is used for data acquisition. The linear array is placed on the sample such that the holes are located below the central elements of the array. For conventional phased array, active apertures comprising of 16 and 64 elements is used to achieve focused sound beam at a depth of 20 mm from the surface using focal laws. B-scan image is acquired by electronic scanning. With SFLA and PA-SAFT techniques, the raw B-scan image is acquired and processed by SAFT algorithm. From the B-scan images, the quantitative assessment of the resolving power of SFLA and PA-SAFT techniques is made. The data is also acquired using the FMC technique for comparison of the results obtained by SFLA and PA-SAFT techniques.

3.7 Assessment of the capability of SFLA and PA-SAFT techniques for the detection and characterization of planar flaws

Planar flaws are two-dimensional and pose a threat to the integrity of the pressurized components. Characterization of planar flaws by NDE is central to the fitness-for-service assessment of a flawed component. The characterization of a planar flaw involves: (i) locating the flaw with respect to the surface, (ii) sizing for its length, (iii) sizing for its depth (height or through-wall dimension) and (iv) estimating its orientation with respect to the principal stresses. While the location and the length of the planar flaw can be assessed accurately by conventional ultrasonic techniques, it is the

accurate estimation of the depth and the orientation, which is a challenging task. The accuracy depends on the uncertainty with which the flaw extremities can be located within the component. Since both SFLA and PA-SAFT techniques are capable of focusing the sound beam through-out the thickness of the component, it is expected that these techniques can precisely locate the flaw extremities, and thus can be employed for accurate characterization of planar flaws in terms of their depth and orientation. In order to assess the capability of SFLA and PA-SAFT techniques for this purpose, experiments are carried out on two stainless steel plate samples, 25 mm and 60 mm thick. The planar flaws in these plates are simulated by inclined slots machined from one of the faces by EDM. The data on these samples are acquired by SFLA, PA-SAFT and FMC techniques using 5 MHz, 0.6 mm pitch, 64 elements linear array. The frequency of 5 MHz is found to be optimum for both the thicknesses. The lower frequency array (2 MHz) may not be able to clearly distinguish the upper tip signal in the 25 mm thick plate sample due to dead zone, while the higher frequency array (10 MHz) may not be suitable for the detection of flaw tips in the 60 mm thick plate due to sound beam attenuation.

3.7.1 Characterization of planar flaws in thin section

The stainless steel plate of 25 mm thickness has six simulated planar flaws oriented from 0 deg. to 51 deg. These are 8.5 mm long, 2 mm wide and 15 mm deep, machined on one of the faces. The sketch of this plate sample is shown in Figure 3.11. The upper tip of the flaws is located at approximately 8 mm from the scanning surface, while the location of bottom tip varies depending on the orientation. In effect, the steel plate has simulated planar flaws of different through-wall dimensions and orientations.

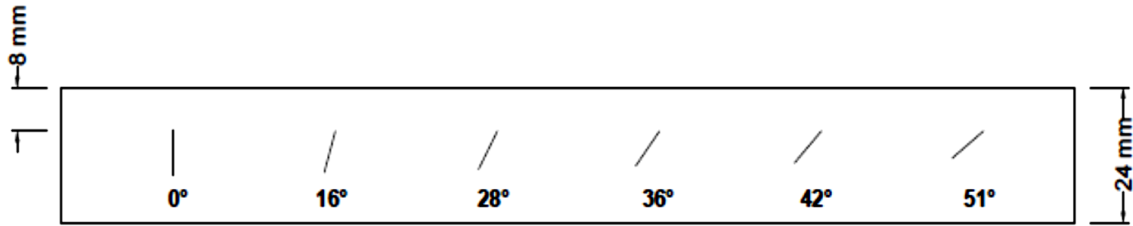


Figure 3.11: Steel plate with simulated planar flaws

The linear array is placed over the sample as shown in Figure 3.12. The raw B-scan is acquired by electronic scanning, which is subsequently processed by SAFT (SFLA and PA-SAFT) and TFM (FMC) algorithms. From the processed image, the extremities of the flaw are located with respect to the scanning surface. From these coordinates, the depth and the orientation of planar flaw is estimated. These are compared with the true values.

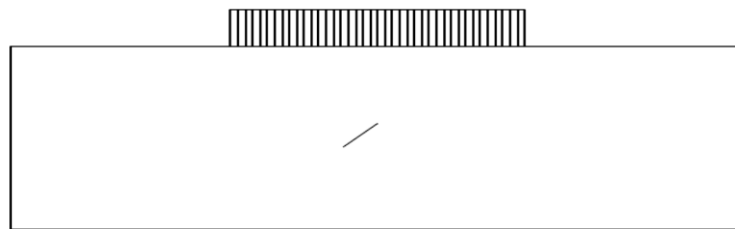


Figure 3.12: Placement of linear array for data acquisition on stainless steel plate with simulated planar flaws

3.7.2 Characterization of planar flaws in thick section

One of the major advantages of SFLA and PA-SAFT techniques is that they use much lesser number of active elements for sound beam focusing as compared to the conventional ‘focal law’ based phased array techniques. One of the limitations of using smaller aperture for sound beam transmission could be lower acoustic power and as a result the inability to detect flaws (or their extremities) that are located deeper. In order to assess the effectiveness of SFLA and PA-SAFT

techniques for the characterization of planar flaws in thick sections, experiments are conducted on a stainless steel sample of 60 mm thickness having 0 deg. and 20 deg. inclined slots. These slots are 10 mm long, 0.5 mm wide and 15 mm deep machined by EDM from one of the faces. The upper tip of these slots is located at a depth of 30 mm from the surface, unlike the previous case where it is much closer. The sketch of this sample is shown in Figure 3.13.

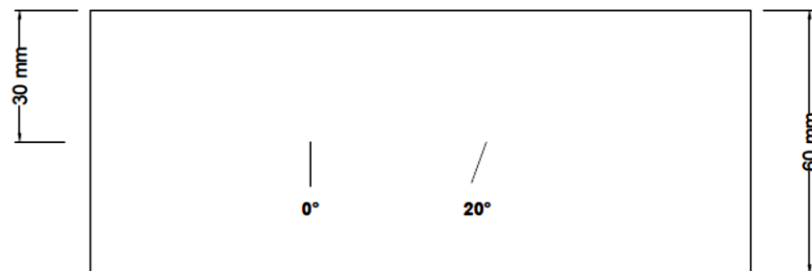


Figure 3.13: Simulated planar flaws in thick stainless steel block

For data acquisition by SFLA, PA-SAFT and FMC techniques, the linear array is placed symmetrically across the flaw on the surface of the sample as shown in Figure 3.12. The raw B-scan data is acquired and is processed by SAFT and TFM, as applicable. From the processed image, the coordinates of the upper and the lower tip signals are found out and the depth and orientation of the flaws are calculated. Additionally, the amplitude difference between the upper and the lower tip signals is also found out. Lower amplitude difference is an indication of reliable detection of the flaw extremities. The depth and the orientation values obtained by various techniques are compared with the true values.

3.8 Assessment of the capability of Angle Beam PA-SAFT technique for detection and characterization of flaws

During the acquisition of raw B-scan data by SFLA, PA-SAFT and FMC techniques, the linear array is kept over the surface of the sample in such a manner that some elements of the array lie

on one side of the flaw while the remaining ones are on the other side. This arrangement ensures that in the raw B-scan, there is useful information from the flaw for majority of the elements or aperture. There can be instances in real life applications, where this requirement cannot be met. One such case is the detection and characterization of flaws in the weld joint with an unground weld bead. Under such circumstances, the linear array cannot be placed over the flaw, but significantly away from it. With this placement, the A-scans from majority of the elements (or aperture) may not have a signal from the flaw. This will lead to poor focusing of sound beam on SAFT processing. In extreme cases, depending on the location of the flaw in the weld joint, it may happen that both the flaw extremities may not be detected by the sound beam emanating from any of the elements or apertures. Under such circumstances, the flaw may go undetected.

One way of overcoming this problem is to use Angle Beam PA-SAFT that is based on acquiring the B-scan data using divergent angle beam. The effectiveness of Angle Beam PA-SAFT for flaw detection and characterization is studied on a 25 mm thick aluminum plate with a 2.2 mm deep surface notch. The B-scan data for this sample is acquired in two ways: (i) placing the linear array on the surface opposite to the one where the notch is present and (ii) placing the linear array on the same surface as the notch.

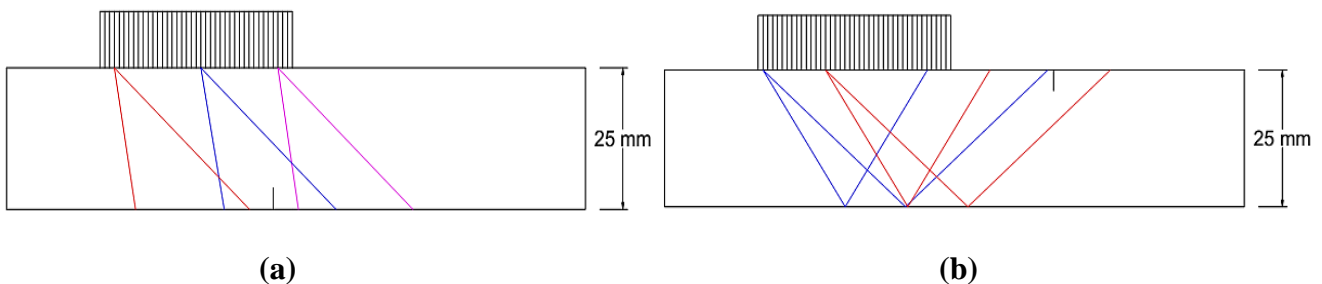


Figure 3.14: Experimental arrangement for data acquisition using Angle Beam PA-SAFT

(a) Notch on the back surface and (b) Notch on the scanning surface

In both the cases, it is ensured that the linear array is not placed over the notch to simulate the real-life condition of an un-ground weld bead. Figure 3.14 shows the experimental arrangement.

The raw B-scan data is acquired using 5 MHz, 0.6 mm pitch, 64 elements linear array. An active aperture of 6 elements is used to steer the sound beam at an angle of 45 deg. When the notch is on the opposite surface where the linear array is placed, the data is acquired for a distance corresponding to more than $\frac{1}{2}$ V path. When the notch is on the same surface, the data is acquired for a distance corresponding to more than 1 V path. The raw B-scan is processed by SAFT algorithm. From the processed B-scan image, the tip of the notch from the scanning surface is located and its depth is found out. This is compared with the true value to assess the effectiveness of Angle Beam PA-SAFT technique for the characterization of flaws.

The effectiveness of Angle Beam PA-SAFT technique for the characterization of the sub-surface planar flaws is studied using a 60 mm thick stainless steel plate described in Section 3.7.2. For the purpose of data acquisition, the linear array of 5 MHz, 0.6 mm pitch, 64 elements is placed on the surface of the sample such that that it is not directly above the flaw but laterally shifted. This is schematically shown in Figure 3.15.

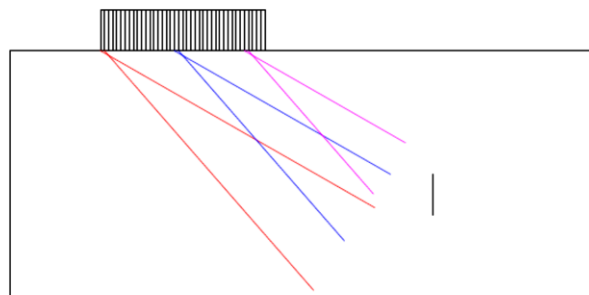


Figure 3.15: Placement of linear array for data acquisition using Angle Beam PA-SAFT technique on a 60 mm thick stainless steel sample

A divergent sound beam traveling at 45 deg. is generated by steering the sound beam. An active

aperture comprising of 6 elements is found to be optimum. From the processed B-scan image, the flaw tips are located. Based on this, the orientation and the depth of the flaws are estimated.

3.9 Demonstration of the effectiveness of SFLA and PA-SAFT techniques for characterization of weld flaws

One of the major objectives of this research work is to demonstrate the effectiveness of SFLA and PA-SAFT techniques for the characterization of real flaws. To meet this objective, experiments are conducted on weld samples made of carbon steel and stainless steel containing volumetric and planar flaws. The locations of these flaws in the weld joint are schematically shown in Figure 3.16. Table 3.3 gives the details of the weld samples used for carrying out the experimental work.

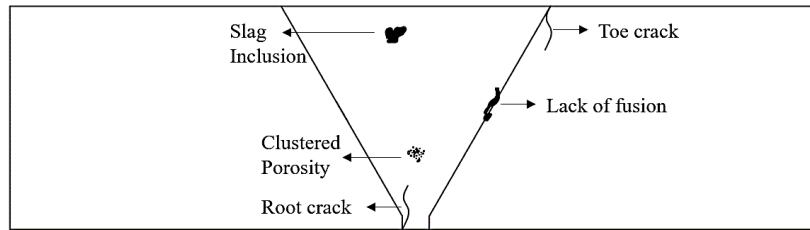


Figure 3.16: Weld samples containing volumetric and planar flaws

Table 3.3: Details of weld samples with volumetric and planar flaws used for the experimental work

Sr. No.	Material	Thickness (mm)	Type of weld flaw	Nature of flaw*
1	Carbon steel	15	Clustered porosity	Volumetric, Sub-surface
2	Carbon steel	15	Slag inclusion	Volumetric, Sub-surface
3	Carbon steel	10	Root crack	Planar, Surface
4	Carbon steel	15	Lack-of-fusion	Planar, Sub-surface
5	Carbon steel	22	Lack-of-fusion	Planar, Sub-surface
6	Stainless steel	25	Root crack	Planar, Surface
7	Stainless steel	25	Toe crack	Planar, Surface

**The above flaws envelope all the flaws that are typically observed in the weld joints*

For sample no. 1 to 5, the weld bead is flushed. Hence using SFLA, PA-SAFT and FMC techniques, the data on these samples are acquired by placing the linear array across the weld as shown in Figure 3.17.

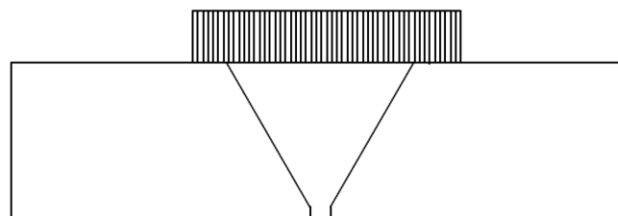


Figure 3.17: Placement of linear array over the weld for data acquisition by SFLA, PA-SAFT and FMC techniques

The stainless steel weld samples (6 and 7), has an unground weld bead. Hence using Angle beam PA-SAFT technique, the data on these samples are acquired as shown in Figures 3.18(a) and (b).

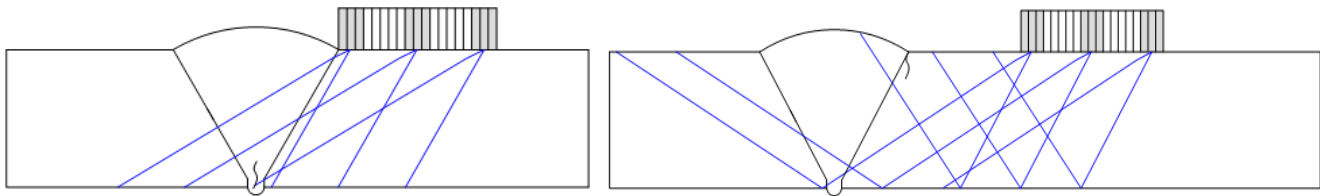


Figure 3.18: Placement of linear array for data acquisition on weld samples using Angle beam PA-SAFT technique (a) Root crack and (b) Toe crack

Sample no. 1 to 4 are used to demonstrate the effectiveness of SFLA and PA-SAFT techniques for the characterization of real volumetric and planar flaws. Sample no. 5 is used to compare the results obtained by SFLA, normal beam PA-SAFT and Angle beam PA-SAFT techniques under identical test conditions. Sample no. 6 and 7 are used to demonstrate the effectiveness of Angle beam PA-SAFT technique for the characterization of real planar flaws on the scanning surface and the back surface of the sample. Sample no. 6 is also used to acquire the data by SFLA and PA-SAFT techniques after the removal of weld bead.

The difference between the actual and the input value of sound velocity during SAFT processing adversely affects the quality of SAFT processed image. During the SAFT processing of the data acquired on the carbon steel weld samples, it is assumed that the sound velocity in the base metal and the weld metal is same. To validate this assumption, a raw B-scan data is acquired on weld sample no. 4 made of carbon steel using a 10 MHz 0.3 mm pitch 128 elements linear array. The array is placed across the weld as shown in Figure 3.17. A single element is used for sound beam transmission and an electronic B-scan is generated containing the first and the second backwall signals. From the time-of-flight difference between the two backwall signals and the actual thickness measured by a micrometer, the sound velocity profile across the weld is generated.

For sample no. 1 to 4 in Table 3.3, the B-scan data are acquired using 10 MHz, 0.3 mm pitch, 128 elements linear array. For the remaining three samples, 5 MHz, 0.6 mm pitch, 64 elements array is used because of higher thickness and stainless steel material. For data acquisition using PA-SAFT technique, an active aperture comprising of 6 and 8 elements is used for 5 MHz and 10 MHz linear array respectively. With FMC, only 64 out of 128 elements of 10 MHz are used for data acquisition. The raw data acquired by SFLA, PA-SAFT (normal beam and angle beam) and FMC techniques is processed by SAFT or TFM, as applicable. From the processed B-scan images, the through-wall dimensions of the weld flaws are found out. The weld samples are then sectioned at the flaw locations and the true depth of these flaws is determined by metallography.

3.10 Application of SFLA and PA-SAFT techniques for in-service inspection of circumferential weld joint in reactor pressure vessel of a nuclear boiling water reactor

As part of this research work, a detailed study is carried out to on a mock-up to establish the feasibility of utilizing the focusing ability of SFLA and PA-SAFT techniques for detection and characterization of flaws in the circumferential weld joint (C1) of reactor pressure vessel (RPV) in a nuclear boiling water reactor (BWR). The weld joint is located at a distance of 425 mm from the top flange, where the linear array can be placed during examination. The study involved simulation using CIVA 11 and experiments on the mock-up block simulating the geometry of the weld joint. The mock-up block is 120 mm thick and is made of carbon steel. Since the acoustic properties (velocity and attenuation) of the carbon steel weld and the carbon steel wrought product are similar, the mock-up does not contain the weld. The mock-up has three side drilled holes of 6 mm dia. at a distance of approximately 32 mm, 63 mm and 94 mm from one of the surfaces (called as OD surface). The mock-up also contains 6 mm deep notches on both the surfaces simulating

ID and OD cracks. The holes and the notches are located at a distance of 425 mm from the flange top face. The sketch of the mock-up block is shown in Figure 3.19. The data on the mock-up block is acquired using conventional phased array, SFLA and PA-SAFT techniques.

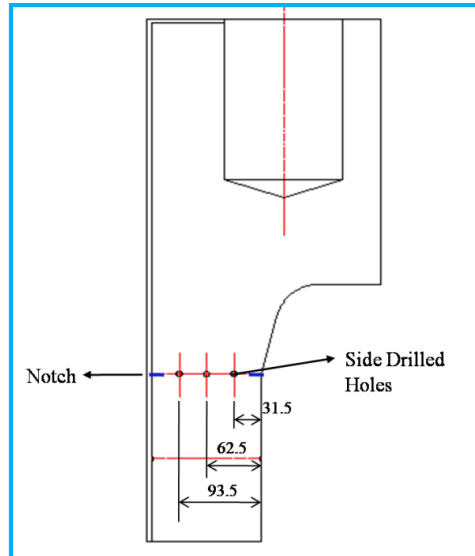


Figure 3.19: Mock-up block of C1 weld joint in reactor pressure vessel

For the conventional phased array, the linear array is placed on the top flange surface and the sound beam is focused at a distance of 425 mm from the top surface. At the same time, the focused sound beam is steered from ID to OD surface using focal laws, so that at any given location, the entire thickness of the weld joint gets inspected from a single position of the linear array by the focused sound beam.

Linear arrays of 2 MHz, 0.8 mm pitch, 64 elements and 5 MHz, 1 mm pitch, 64 elements are used for this purpose. Active apertures varying from 16 to 64 elements are used to create the focal laws corresponding to multi-point focusing. Figure 3.20 shows the experimental arrangement.

For SFLA technique, the data is acquired using 2 MHz, 0.8 mm pitch, 64 elements linear array. The array is placed over the top flange as shown in Figure 3.19. The acquired B-scan image is processed by SAFT algorithm.

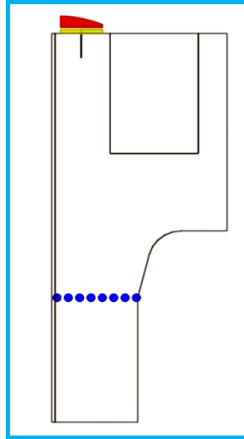


Figure 3.20: Placement of linear array on the top flange of RPV mock-up block for data acquisition using conventional phased array

For PA-SAFT technique, the data is acquired using 2 MHz, 0.8 mm pitch, 64 elements linear array. Simulation studies for the optimization of active aperture are carried out using CIVA 11. For the experimental work, the linear array is placed on the top flange surface and using the optimized active aperture, the sound beam is focused at a depth of 10 mm from the surface. This is schematically shown in Figure 3.21. The B-scan image is acquired by electronic scanning, which is subsequently processed by SAFT algorithm.

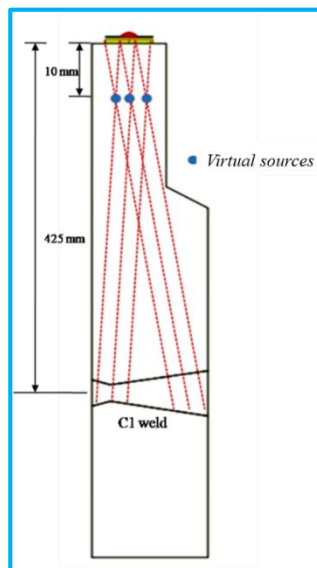


Figure 3.21: Experimental set-up for data acquisition using PA-SAFT on the mock-up block of C1 weld joint in RPV

The results obtained by the conventional phased array, SFLA and PA-SAFT techniques are analyzed in terms of the following parameters:

- Coverage of the weld joint from ID to OD surface
- Detection and resolution of side drilled holes
- Detection of ID and OD notches
- Amplitude variation in the signals from side drilled holes and notches
- 6 dB size of the side drilled holes and the notches from the processed B-scan images

3.11 Summary of the Chapter

The experimental procedures employed for this research work comprising of phased array instrumentation, linear arrays, SAFT processing algorithm and the samples have been described in this Chapter. The Chapter discussed in details the experimental work carried out to address the following aspects:

- ✓ Methodology for estimating the sound beam divergence from miniature piezoelectric elements that are used in linear arrays
- ✓ Study the effect of array based parameters and SAFT processing parameters on sound beam focusing using SFLA technique
- ✓ The simulation studies and the experimental work carried out to optimize the aperture size for PA-SAFT technique
- ✓ Assessment of the effectiveness of SFLA and PA-SAFT techniques for detection and characterization of volumetric and planar flaws, both simulated and real
- ✓ Application of SFLA and PA-SAFT techniques for in-service inspection of weld joint in a pressure vessel of a nuclear boiling water reactor

4.1 Introduction

An integrated approach using linear array and SAFT to achieve sound beam focusing has been investigated during this research work. Two techniques using this approach have been studied and standardized viz. Synthetic Focusing using Linear Array (SFLA) and Phased Array-SAFT (PA-SAFT). Both the techniques involve acquiring the B-scan image using a divergent sound beam emanating from a linear array and then processing this data by time based SAFT algorithm to achieve sound beam focusing, both laterally and across the depth of the component. This integrated approach is advantageous in many ways over the other approaches for sound beam focusing employing: (i) SAFT on the B-scan data acquired using a single crystal transducer, (ii) conventional phased array using focal laws and (iii) Full Matrix Capture-Total Focusing Method. Some of these advantages are listed below:

- ✓ A small source size in a linear array for sound beam transmission, as compared to the conventional single crystal transducer, gives large sound beam divergence. This leads to better focusing during SAFT.
- ✓ As the elements in an array are arranged very close to each other, the raw B-scan data is acquired at very small intervals during electronic scanning. This leads to enhancement in the SAFT processing.
- ✓ With a single crystal transducer, the near field extends to a considerable distance because of higher dimensions of the piezoelectric element. Focusing by SAFT cannot be achieved in the near field. On the other hand, very small size of a piezoelectric element in a linear array limits

the near field to a very shallower depth. This ensures that the sound beam focusing using linear array and SAFT is achieved almost throughout the thickness of the component.

- ✓ Using conventional phased array, the sound beam focusing is limited to the near field distance, which in turn is determined by the number of elements in an active aperture. Focusing at larger depth needs large number of elements. Since the focusing using the integrated approach is based on SAFT, focusing can be achieved over a very large depth by using lesser number of elements.
- ✓ The SAFT based approach is inherently associated with the signal averaging. As a result, there is significant improvement in signal to noise ratio, which enhances the reliability of flaw detection and characterization.
- ✓ Use of a divergent sound beam for data acquisition coupled with SAFT processing, helps to achieve larger lateral coverage and improved resolution.
- ✓ The hardware requirements for the phased array instrument, in terms of parallel receiver channels, are substantially less using an integrated approach as compared to the conventional phased array and FMC + TFM technique. This means a low cost and compact instrumentation for data acquisition.
- ✓ Enormous reduction in the size of the raw data for post-processing as compared to FMC, especially while using linear array with large number of elements. This aspect is crucial in building up a real-time system for industrial applications.

Both SFLA and PA-SAFT techniques derive their strength from the use of a divergent sound beam emanating from a single or a group of elements in a linear array during data acquisition. For the

conventional single crystal transducers with large D/λ ratio, the sound beam divergence angle is a linear function of the ratio λ/D [1]. For the miniature piezoelectric elements in a linear array, the D/λ ratio is small. Hence the mathematical relationship given in the literature to evaluate the sound beam divergence while dealing with linear array, may not remain valid. In this Chapter, an empirical relationship to evaluate the beam divergence for sub-millimeter size piezoelectric elements, which are used in linear arrays, has been derived. A detailed methodology for data acquisition and processing using SFLA and PA-SAFT techniques has been described. The array based and the SAFT processing based factors, which affect the sound beam focusing, have been studied by extensive experimental work. The results have been analyzed and discussed in details. Contrary to what is reported in the literature [16,17,101] that the focal spot size achieved by SAFT depends on the dimension of the piezoelectric crystal alone, it has been observed that this does not hold true when SAFT is applied on the data acquired using linear array. The primary reason for this could be the non-linearity in the dependence of sound beam divergence angle on the ratio λ/D . An empirical relationship showing the dependence of the focal spot size on the dimension of piezoelectric element in the array and the wavelength of sound, has been derived. The optimization of aperture size for PA-SAFT technique has been dealt with in details and the results of simulation studies and experimental validation for this purpose have been brought out. The results of the comparative study carried out on the focusing ability of SFLA, PA-SAFT and FMC + TFM techniques have been discussed.

4.2 Sound Beam Divergence for Miniature Piezoelectric Crystal

The sound beam focusing using SAFT is primarily dependent on three factors: the beam divergence, the number of A-scans with useful data and the interval at which the A-scan data has been acquired. Large beam divergence, more number of A-scans and small data interval lead to

effective focusing using SAFT. For a given material, the sound beam divergence is inversely proportional to the piezoelectric crystal size D and the frequency of sound ν .

SAFT based sound beam focusing using linear array offers several benefits as compared to the conventional single crystal transducer. While using single crystal piezoelectric transducers, the crystal dimension D is of the order of a few millimeters, which limits the beam divergence to a lower value. While using a linear array, each individual element is typically of the order of a fraction of a millimeter. As a result, the sound beam divergence achieved is significantly higher than what could be achieved using conventional signal crystal piezoelectric transducer. Since the elements in an array are typically arranged at a pitch of the order of a fraction of a millimeter, a large number of A-scan data acquired at a very small interval are available for SAFT processing. These factors help to achieve more effective sound beam focusing by SAFT using linear arrays as compared to a single crystal transducer. The lateral resolution that can be theoretically achieved using SAFT is of the order of $D/2$ [16,17,98,217]. Since very small values of D can be realized using linear array, sound beam focusing using linear array and SAFT can be very effective.

Mathematically, the sound beam divergence in the far-field is directly proportional to the ratio λ/D , where λ is the wavelength in the material.

For large values of D/λ , the half beam divergence angle for a rectangular shaped piezoelectric crystal is given by the following equation [1]:

$$\sin \theta = k \cdot \frac{\lambda}{D} \quad [36]$$

where, θ is the half beam divergence angle, λ is the wavelength of sound in the material and k is the beam divergence constant ($k_{6dB} = 0.44$ for 6 dB beam divergence).

While dealing with a conventional single crystal piezoelectric element, the value of D is of the order of a few millimeters, and λ of the order of a fraction of a millimeter to few millimeters depending on the frequency of sound used. As a result, the value of D/λ is fairly large and hence the above equation can be used to arrive at the sound beam divergence. On the other hand, while dealing with linear arrays, the value of D is typically of the order of a fraction of a millimeter. As a result, the value of D/λ is very small and could even be less than 1, depending on the array used. In such cases, the sound beam divergence estimated by the above equation, may not match with the actual value. For example, when a single element of a linear array of 10 MHz frequency and 0.3 mm pitch (each element is 0.25 mm wide) is excited, then as per equation 36 the 6 dB beam divergence in steel should be approximately ± 90 deg. However, in reality the beam divergence observed for this case is much less. This shows that equation 36, and more specifically the value of $k = 0.44$ is not valid for small values of D/λ that are typically encountered with miniature piezoelectric elements in linear arrays. For sub-millimeter dimension piezoelectric elements, one needs to derive 'new' values for the constant k , so that the theoretically calculated value of sound beam divergence matches closely with the observed ones.

One of the crucial inputs for SAFT processing of the raw data acquired using linear arrays is the sound beam divergence. If the input value to the SAFT algorithm is less than the actual sound beam divergence, then less number of A-scans will be used for summation and averaging during SAFT processing. This will lead to inferior focusing. On the other hand, if the input value is too large as compared to the actual beam divergence, then there will be a number of A-scans with no useful information. During summation and averaging, this will lead to a lower amplitude of the flaw signal in the processed image. Also, more number of A-scans than the optimum will lead to an increase in the processing time. This has an adverse effect while building-up 'real-time'

systems. Hence, it is desirable to know the actual value of the sound beam divergence for the data that has been acquired using linear array during this research work. Based on the experimental work, an empirical relationship to calculate the sound beam divergence for miniature piezoelectric elements has been derived. The results are described in details in the following section.

4.2.1 Estimation of Beam Divergence for Small Values of D/λ

A linear array is placed on an aluminum block containing 0.5 mm dia. side drilled hole located at a distance of 35 mm from the scanning surface. Figure 4.1(a) shows the photograph of the experimental set-up. The experimental details are given in Chapter 3, Section 3.3. Figure 4.1(b) shows the B-scan image obtained for the side drilled hole. The side drilled hole, which is like a point reflector is imaged as a wide hyperbola. The image is colour coded in terms of the amplitude. The central region of the image shows high amplitude, which gradually reduces as one move towards the left and the right side. The decrease in the amplitude is because of two reasons: (i) the beam divergence effect and (ii) the attenuation. The attenuation co-efficient for three frequencies, 2 MHz, 5 MHz and 10 MHz, which are used for data acquisition, is measured on this block and is found to be negligible for the distances involved.

For the central elements, the distance to the hole is shortest and the hole is seen by the central beam emanating from this element. As a result, the beam path of the side drilled hole signal is shortest and the amplitude, strongest. As one moves away from the central element, the beam path of the hole signal increase. Also the hole is not seen by the central, but the adjacent beam. As a result, the signal from the hole appears at a higher beam path and with a lesser amplitude. As one moves away further, the beam path continues to increase and the amplitude continues to fall as the hole is detected by the peripheral sound beam, which is weaker than the central beam.

From the B-scan image, the two points (x_1 and x_2) on either side of the central element(s) where the amplitude of the signal from the hole drops to 6 dB of the maximum amplitude is found out. The linear distance between the two points gives the 6 dB width of the sound beam at a depth where the side drilled hole is located from the scanning surface. If y is the depth of the side drilled hole from the surface and w' is the half width of the sound beam, then the half beam spread angle θ is calculated as:

$$\tan \theta = \frac{w'}{y} \quad [37]$$

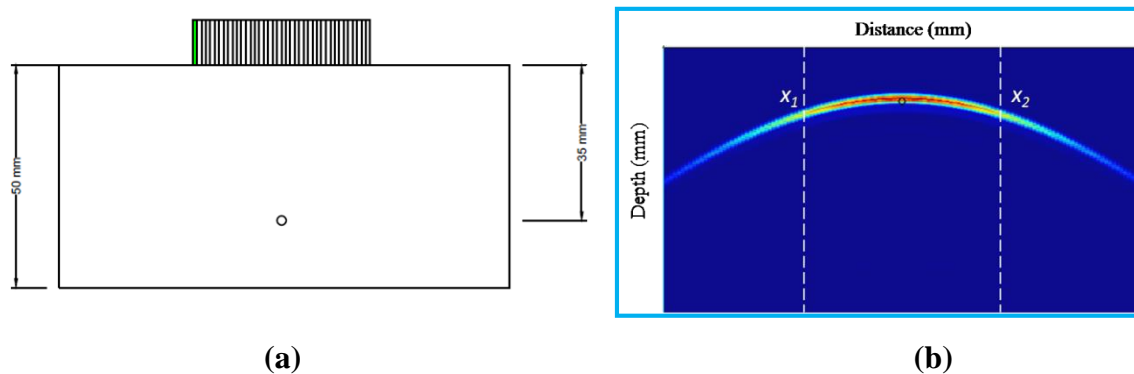


Figure 4.1: Beam spread measurement (a) Experimental set-up and (b) B-scan image from which the 6 dB beam width is determined

The above exercise is carried out for three different linear arrays: (i) 2MHz, 0.8 mm pitch 64 elements, (ii) 5MHz, 0.6 mm pitch, 64 elements and (iii) 10 MHz, 0.3 mm pitch, 128 elements. For each case, B-scan image is acquired using different number of elements as active apertures, so that the data is available for different D values. The value of half beam divergence angle θ is calculated from equation 37. Figure 4.2 shows the effect of aperture size (D) on θ_{6dB} for the above three linear arrays. In each case, the curve corresponding to equation 36, where k_{6dB} is taken as 0.44, is also shown.

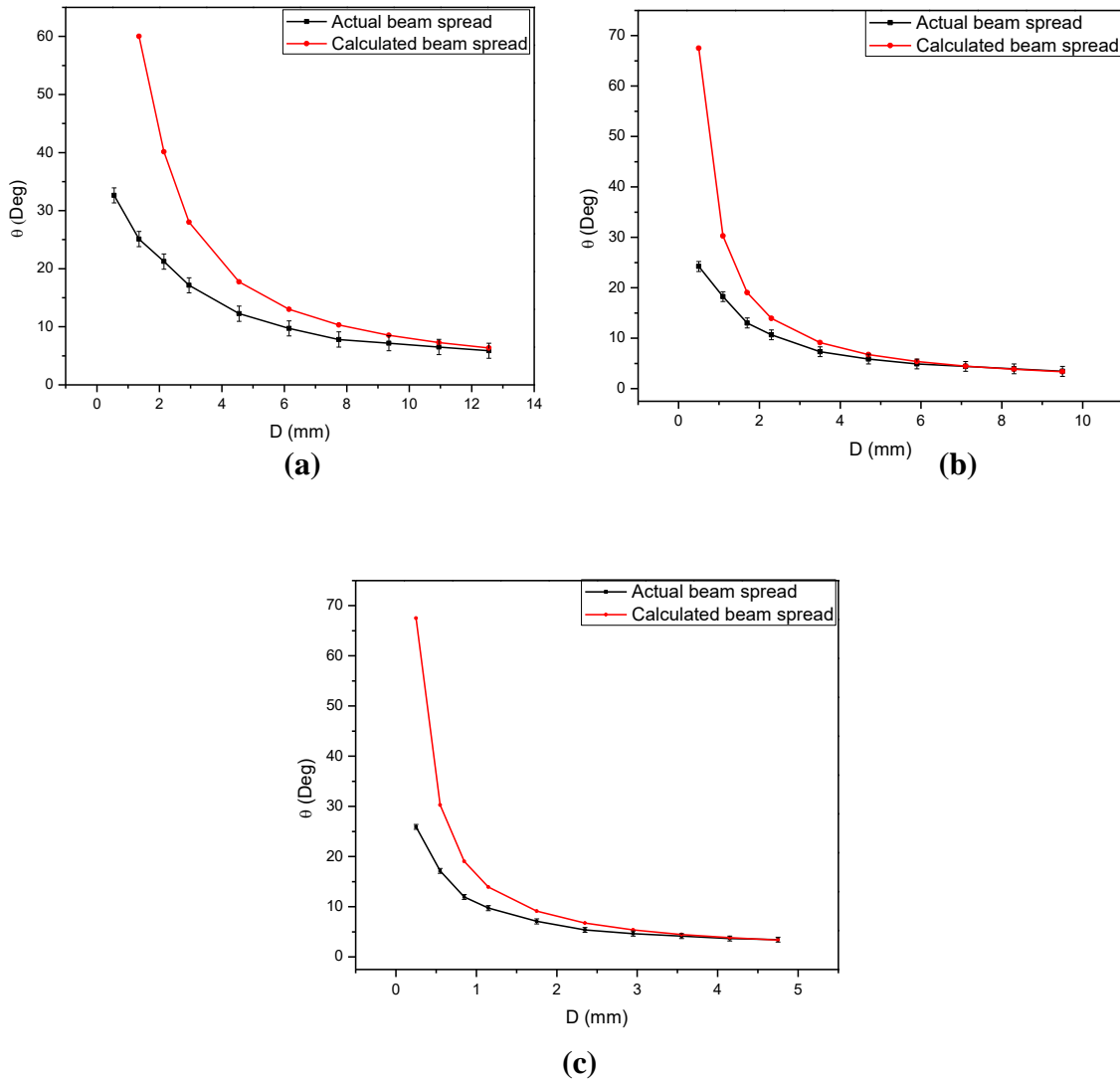


Figure 4.2: Effect of D on beam divergence for (a) 2 MHz, 64 elements and 0.8 mm pitch, (b) 5 MHz, 64 elements and 0.6 mm pitch and (c) 10 MHz, 128 elements and 0.3 mm pitch linear array

The results indicate the following:

- For low values of D , the observed beam spread is much smaller than what is estimated by equation 36

- As D increases, the value of beam spread angle θ decreases, which is in line with equation 36
- For large values of D , the observed half beam spread angle approaches the one estimated by equation 36
- Similar values of D (from different frequency linear arrays) do not show similar half beam spread angle. For example, for the D value of 2.2 mm using 10 MHz, 5 MHz and 2 MHz linear array, the value of θ is found to 5.4°, 10.7° and 21.2° respectively. This indicates that the beam spread angle is not the function of D alone.

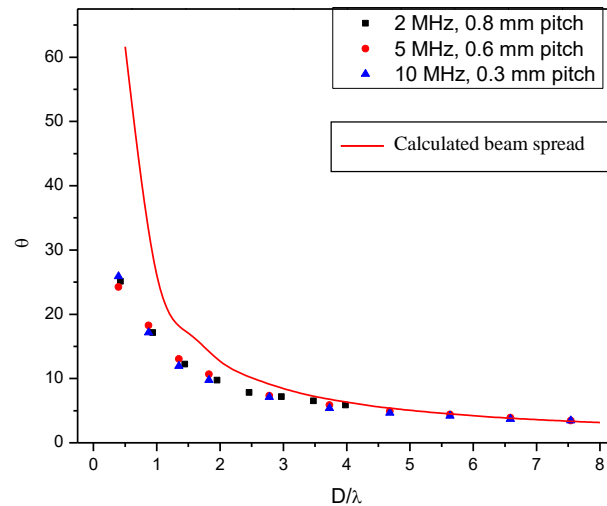


Figure 4.3: Variation in beam spread angle with D/λ for linear arrays of different frequencies

Figure 4.3 shows the variation in the observed half beam spread angle with D/λ for the above three linear arrays. The curve corresponding to equation 36 is also plotted. Figure 4.3 indicates that similar values of D/λ corresponding to different linear arrays, give similar beam spread angles. From this, it can be inferred that the half beam spread angle depends on D/λ .

4.2.2 Estimation of Beam Spread Constant k_{6dB}

From the observed data, it is clear that the value of $k_{6dB} = 0.44$ is valid only for large D/λ values and is much smaller while dealing with the excitation of a single element or few elements using a linear array. It can be inferred that for small values of D/λ where equation 36 is not valid, not only the value of k_{6dB} is less than 0.44, but it varies with D/λ before attaining a constant value.

From the observed beam spread angle θ for various D/λ values, using the above three linear arrays, the values of constant k_{6dB} are calculated using the following equation:

$$k_{6dB} = \sin \theta * \frac{D}{\lambda} \quad [38]$$

Tables 4.1(a), 4.1(b) and 4.1(c) gives the k_{6dB} values obtained for various D/λ values.

Table 4.1(a): k_{6dB} values for 2 MHz, 0.8 mm pitch, 64 elements linear array

No. of elements excited	Depth of the hole(d) (mm)	6 dB width from B-scan image (2w) (mm)	tan $\theta=w/d$	Half beam spread angle (θ) (deg.)	k_{6dB}
1	35	44.8	0.64	32.6	0.09
2	35	32.8	0.47	25.1	0.18
3	35	27.2	0.39	21.2	0.25
4	35	21.6	0.31	17.2	0.28
6	35	15.2	0.22	12.2	0.31
8	35	12	0.17	9.7	0.33
10	35	9.6	0.14	7.8	0.33

12	2.97	35	8.8	0.13	7.2	0.37
14	3.48	35	8	0.11	6.5	0.39
16	3.98	35	7.2	0.10	5.9	0.41

Table 4.1 (b): k_{6dB} values for 5 MHz, 0.6 mm pitch, 64 elements linear array

No. of elements excited	D/λ	Depth of the hole(d) (mm)	6 dB width from B- scan image ($2w$) (mm)	\tan $\theta=w/d$	Half beam spread angle (θ) (deg.)	k_{6dB}
1	0.40	10	9	0.45	24.2	0.16
2	0.87	10	6.6	0.33	18.3	0.27
3	1.35	35	16.2	0.23	13.0	0.30
4	1.83	35	13.2	0.19	10.7	0.34
6	2.78	35	9	0.13	7.3	0.35
8	3.73	35	7.2	0.10	5.8	0.38
10	4.68	35	6	0.09	4.9	0.40
12	5.63	35	5.4	0.08	4.4	0.43
14	6.59	35	4.8	0.07	3.9	0.45
16	7.54	35	4.2	0.06	3.4	0.45

Table 4.1(c): k_{6dB} values for 10 MHz, 0.3 mm pitch, 128 elements linear array

No. of elements excited	Depth of the hole(d) (mm)	6 dB width from B-scan image ($2w$) (mm)	$\tan \theta = w/d$	Half beam spread angle (θ) (deg.)	k_{6dB}
1	35	34	0.49	25.9	0.17
2	35	21.6	0.31	17.2	0.26
3	35	14.8	0.21	11.9	0.28
4	35	12	0.17	9.7	0.31
6	35	8.7	0.12	7.1	0.34
8	35	6.6	0.09	5.4	0.35
10	35	5.7	0.08	4.7	0.38
12	35	5.1	0.07	4.1	0.41
14	35	4.5	0.06	3.7	0.42
16	35	4.2	0.06	3.4	0.45

4.2.3 Generalized equation for the estimation of sound beam divergence for rectangular piezoelectric elements

From Tables 4.1(a), (b) and (c), the values of k_{6dB} are plotted against D/λ (Figure 4.4). The figure indicates that for very low values of D/λ (< 0.2), the value of k_{6dB} is of the order of 0.1. The value of k_{6dB} increases with D/λ and approaches 0.44 for D/λ value of 10. Based on the above studies, an empirical relationship for estimation of the half beam spread angle, which is applicable for

rectangular miniature elements of an array as well as for the conventional single crystal element, has been obtained. This relationship is given in equation 39:

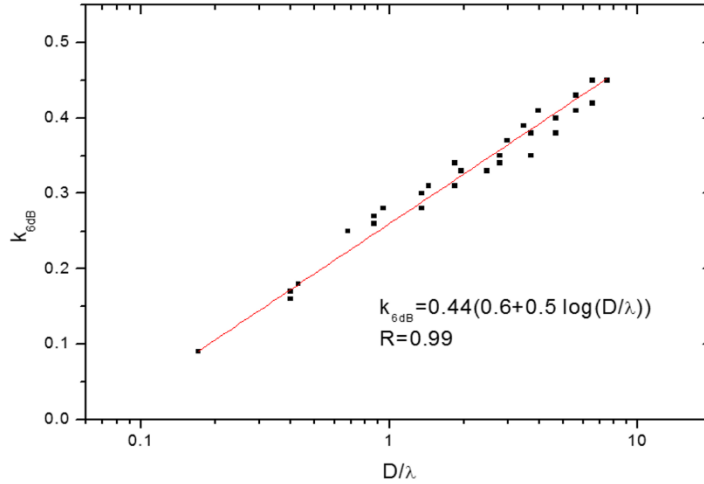


Figure 4.4: Variation of k_{6dB} value with D/λ for miniature piezoelectric elements

$$\sin \theta = 0.44 \left[0.6 + 0.5 \log \left(\frac{D}{\lambda} \right) \right] \cdot \frac{\lambda}{D} \quad [39]$$

The above equation can be used to find out the half beam divergence angle (θ_{6dB}) for rectangular piezoelectric crystal having D/λ values from 0.2 to 10. For rectangular piezoelectric transducers, where D/λ is high, the value of k_{6dB} is 0.44 [1]. From the above equation, one can say that for the rectangular elements in linear array with small D/λ , the value of beam divergence constant k_{6dB} is reduced by the factor given in the parentheses. Additionally, this value is dependent on the ratio D/λ , which is not the case with large piezoelectric elements.

The above empirical relationship is derived and valid only for a single element excitation of an array or when a group of array elements (aperture) are excited simultaneously, essentially acting as a single element having size equal to the width of the aperture. This relationship is not valid when focal laws are employed to achieve steering and/or focusing of the sound beam.

4.2.4 Validation

In order to validate the above equation, the beam spread is determined experimentally for two linear arrays: 10 MHz, 0.5 mm pitch and 8 MHz, 0.5 mm pitch. For different values of D/λ , the beam divergence angle is determined using equation 39 and is compared with the experimentally measured value. The results are given in Tables 4.2(a) and 4.2(b).

Table 4.2(a): Experimental and calculated θ_{6dB} using 10 MHz, 0.5 mm pitch linear array

No. of elements excited	D/λ	Depth of the hole(d) (mm)	6 dB width from B-scan image ($2w$) (mm)	Beam Spread Angle θ_{6dB} (deg.)	
				Experimental $\tan^{-1}(w/d)$	Calculated from equation 39
1	0.6	35	28	21.8	21.2
2	1.4	35	16	12.9	12.2
4	3	35	9	7.3	7
10	7.8	35	4.5	3.7	3.3

Table 4.2(b): Experimental and calculated θ_{6dB} using 8 MHz, 0.5 mm pitch linear array

No. of elements excited	D/λ	Depth of the hole(d) (mm)	6 dB width from B-scan image ($2w$) (mm)	Beam Spread Angle θ_{6dB} (deg.)	
				Experimental (w/d)	Calculated from equation 39
1	0.5	35	31.5	24.2	23
2	1.1	35	20	15.9	15
4	2.4	35	11.5	9.3	8
10	6.2	35	5.5	4.5	4

The Tables indicates that there is a close match between the calculated and the experimentally measured value of the beam divergence. Equation 39 can be used for determining the 6 dB beam divergence for rectangular piezoelectric elements that are used in linear array.

Similar study is carried out to assess the effect of orthogonal dimension of the array on the sound beam divergence. This study is carried out using 5 MHz linear arrays with the orthogonal dimensions of 7 mm and 10 mm. The beam divergence observed experimentally using these arrays matches closely with the value predicted by equation 39. The effect of orthogonal dimension on the observed beam spread angle are shown in Table 4.2(c).

Table 4.2(c): Effect on orthogonal dimensions on beam spread using 5 MHz, linear array

Sr. No.	D/λ	Observed Half Beam Spread Angle (θ_{6dB})	
		Orthogonal 7 mm	Orthogonal 10 mm
1	1.3	12	13
2	2.8	7.3	7.3
3	3.7	5.7	5.8

The above results show that the orthogonal dimension does not play any role in the sound beam divergence, provided it is sufficiently large as compared to D .

During the current research, 10 MHz, 0.3 mm pitch and 5 MHz, 0.6 mm pitch linear arrays have been used for data acquisition. For a single element excitation using these arrays, the value of sound beam divergence calculated using equation 39 is approximately 26 deg. This information has been utilized while carrying out the SAFT processing of raw B-scan images that are acquired on various samples during the experimental work.

4.3 SFLA technique

Sound beam focusing using SFLA technique is based on acquiring the B-scan image element-by-element using the linear array transducer (electronic scanning). At any given instance, a single element is used for sound beam transmission. Unlike, FMC, where all the elements are used as receiver, during SFLA, only the transmitting element is used as a receiver (pulse-echo mode). The raw B-scan image thus acquired is processed by time based SAFT algorithm.

4.3.1 Methodology for data acquisition and processing

Figure 4.5 schematically depicts the methodology followed for imaging of flaws using the SFLA technique. A linear array with L number of elements and element pitch as p' is placed on a sample. The acquisition starts with the 1st element in the array acting as transmitter and receiver. Then comes the second, the third and so on, till the last element of the array is reached (Figure 4.5(a)). Since the individual elements of an array are very small, each element emanates a well divergent sound beam.

Consider that the sample has a point reflector or a flaw F located at a distance d_i from the scanning surface (Figure 4.5(a)) and which lies exactly below the element number i , (i is an integer such that $1 < i < L$). In addition to the element i , the flaw F is also detected by the adjacent elements $[(i-n), \dots (i-2), (i-1), (i+1), (i+2), \dots (i+n)]$, where n is an integer such that $1 \leq (i-n)$ and $(i+n) \leq L$.

The separation between the element i and the element $(i-n)$ is given by $s = n * p'$.

Let d_n be the distance of flaw F from the element $(i-n)$. The distance d_n can then be written as:

$$d_n = [d_i^2 + (s)^2]^{\frac{1}{2}} \text{ or } d_n = [d_i^2 + (np')^2]^{\frac{1}{2}} \quad \text{or} \quad t_n = 2 \times \frac{[d_i^2 + (np')^2]^{\frac{1}{2}}}{c} \quad [40]$$

where, t_n is the time of travel of the signal from the flaw to the element ($i-n$), and c is the velocity of sound in the sample. Since $d_n > d_i$, (or $t_n > t_i$), the signal from the flaw F appears at the larger distance or travel time from the elements which are on either side of element i . This is schematically shown in Figure 4.5(b). Because of the beam divergence effect, the flaw at a location F in the sample gives rise to a hyperbolic signal in the B-scan image generated during electronic scan (Figure 4.5(c)).

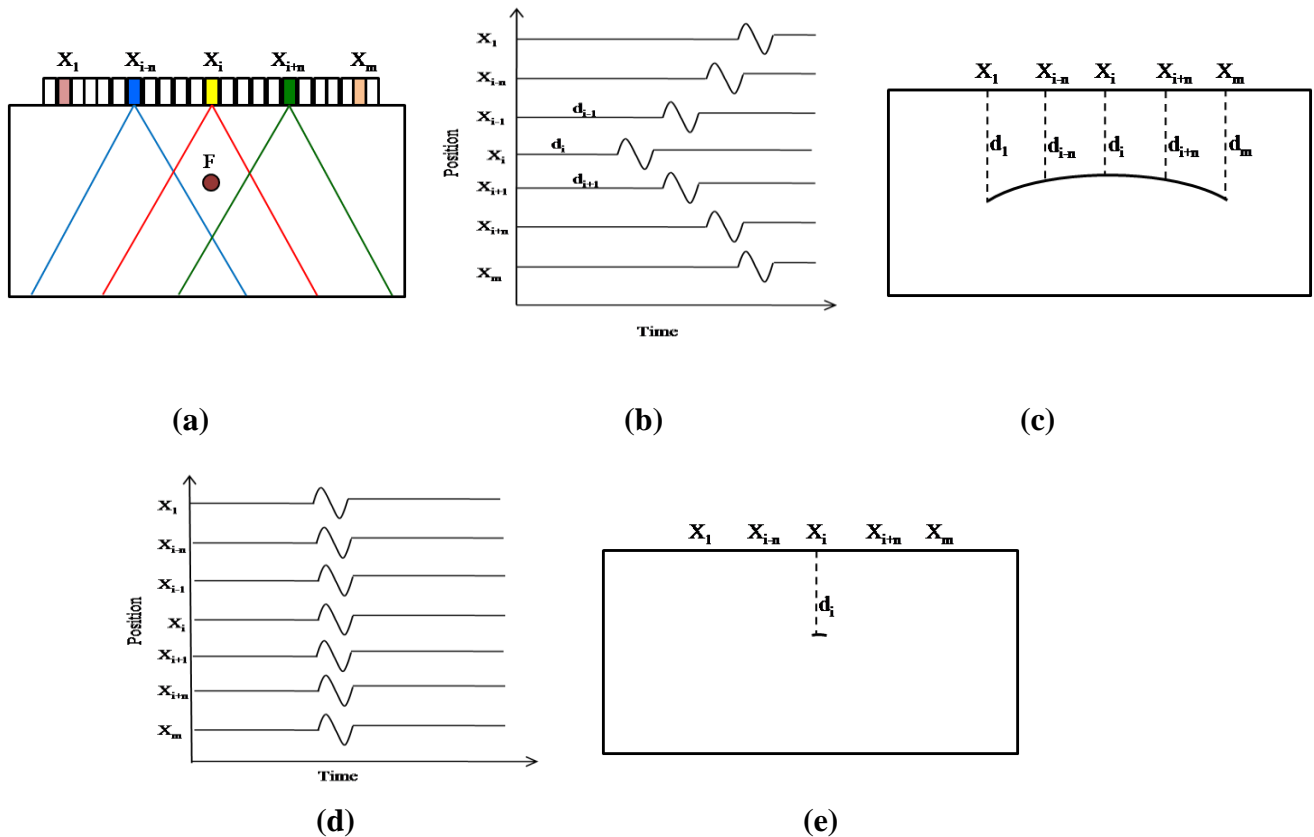


Figure 4.5: SFLA methodology (a) Data acquisition (b) Raw A-scans (c) Raw B-scan image (d) A-scans after time shifting and (e) B-scan image after SAFT processing

During SAFT processing, the signal from the flaw F obtained from all the elements are time shifted by t_s , such that $t_s = t_n - t_i$. The time shift results in the generation of an array of A-scan signals from individual elements as shown in Figure 4.5(d). Finally, all the A-scan signals are summed up and

averaged and the amplitude of the resultant A-scan is plotted on the B-scan image. During the summation process, there is a constructive interference of A-scan signals due to phase matching leading to enhanced amplitude at the location of the flaw F . The same exercise is repeated for all the data points in the B-scan image. When similar time shift, summation and averaging process are carried out for elements other than i , there is a destructive interference of A-scan signals due to phase mismatch, leading to significant drop in the amplitude of resultant A-scan signals. These constructive and destructive interferences lead to the focusing effect. The final result after SAFT processing is shown in Figure 4.5(e).

Figures 4.6 (a) and (b) show the raw B-scan and the SAFT processed B-scan images respectively for an aluminum sample with 0.5 mm dia. side drilled hole located at a depth of 25 mm from the surface using SFLA technique. A 10 MHz, 0.3 mm pitch, 128 elements linear array is used for this purpose. The experimental set-up shown in Figure 4.7 indicates that the linear array is symmetrically placed over the side drilled hole (circled). The raw B-scan image shows a well spread-out signal from the hole. The signal shows some discontinuity at distances of around 7 mm, 15 mm and 26 mm. These discontinuities are because of the dead elements in the linear array used. The SAFT processed image is shown in Figure 4.6(b). The well spread out signal in the raw B-scan gets reduced to a point on SAFT processing. The 6 dB width of the hole, which can be considered as the dimension of focal spot, is found to be 0.46 mm. This indicates that with SFLA technique one can achieve very sharp focusing of the sound beam. Another significant thing is with respect to the amplitude of the hole signal and the extent of the dead zone or the initial ringing. The low amplitude of the hole signal in the raw B-scan data is significantly enhanced after SAFT processing. There is also a significant reduction in the amplitude of the initial ringing and its extent

upon SAFT processing. Both these factors will be helpful in the detection of flaws lying close to the scanning surface.

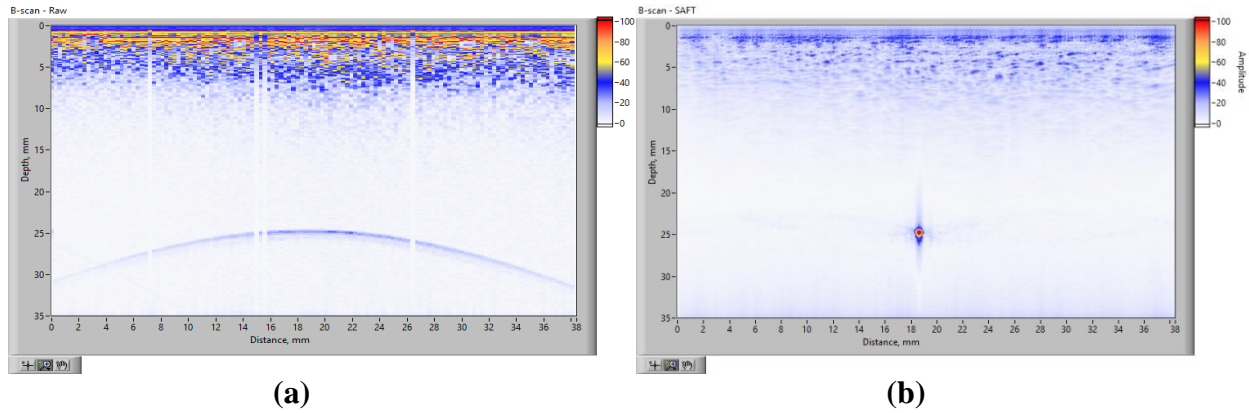


Figure 4.6: (a) Raw and (b) SAFT processed B-scan images for a 0.5 mm dia. side drilled hole at 25 mm depth in an aluminum block using SFLA Technique

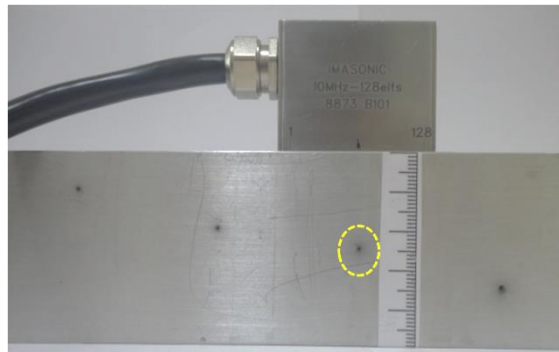


Figure 4.7: Experimental set-up for data acquisition on side drilled holes in an aluminum block using SFLA technique

4.3.2 Factors Affecting Focusing

The sound beam focusing using SFLA depends on several factors related to the data acquisition and processing. During data acquisition, the type of linear array used plays a crucial role in achieving effective focusing. Similarly, during SAFT processing, the parameters which determine the effectiveness with which the constructive interference occur at the flaw location and destructive

interference at the adjacent locations, would determine the dimensions of focal spot size achieved. The effect of various parameters related to the: (i) linear array used during data acquisition and (ii) SAFT processing, has been studied systematically as part of this research work. The study was carried out on an aluminum block containing 0.5 mm dia. side drilled holes located at various distances between 5 mm to 40 mm from the surface. The experimental set-up for the same is shown in Figure 4.7. The results of this study are described below.

4.3.2.1 Linear array based parameters

The following array based parameters affect the sound beam focusing using SFLA technique:

- Aperture Size
- Pitch
- Frequency
- Total effective aperture

The experimental details are given in Chapter 3, Section 3.4.1. The results of the study carried out to assess the effect of each of these parameters on the focal spot size are described below:

4.3.2.1.1 Aperture Size

Aperture size is an important parameter as it affects the beam divergence, which is crucial for SAFT processing. Small aperture size leads to large beam divergence and hence it is expected to give sharp focusing. The effect of aperture size on sound beam focusing is studied using 10 MHz, 0.3 mm pitch, 128 elements linear array. Figure 4.8 shows the variation in the focal spot size with the aperture size (total number of active elements) at various depths from the surface.

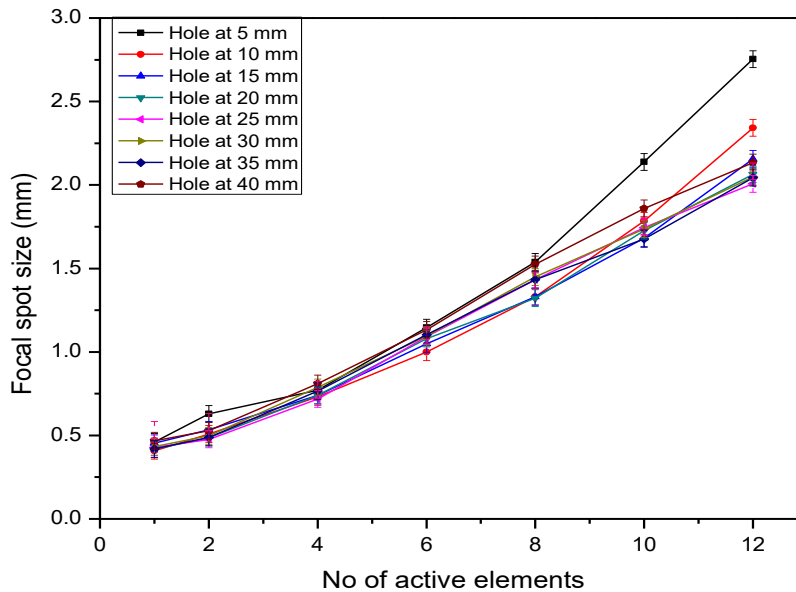


Figure 4.8: Variation in the focal spot size with the aperture size for a 10 MHz, 0.3 mm pitch linear array

The following conclusions can be drawn from these results:

- The best focusing, irrespective of the depth, is achieved while using a single element for sound beam transmission. With single element transmission, the source size is very small. As a result, maximum beam divergence is obtained. This in turn helps to achieve effective SAFT processing and a sharp focal spot.
- The lateral resolution achieved by SAFT, which is a measure of focusing, is directly proportional to the size of the piezoelectric crystal. Since this dimension is smallest for a single element transmission, it gives the best focusing effect as compared to multiple elements.
- As the number of active elements increases, there is also an increase in the focal spot size. With increase in the aperture size, the sound beam achieves directivity. As a result, the beam divergence goes down and so there is an increase in the focal spot size upon SAFT processing.

- An increase in the active aperture size means increase in the effective size of the piezoelectric source and hence the increase in the focal spot size.
- Up to 6 elements active aperture, there is no significant difference in the focal spot size achieved at different depths (5 mm to 40 mm). However, beyond 8 active elements, the focal spot size at various depths shows significant variation. With 12 active elements, the focal spot size at lower depth (5mm and 10 mm) is fairly large as compared to the one at higher depth. With 12 active elements, the near field length is approximately 5 mm. As a result, the side drilled hole at 5 mm is not seen by the divergent sound beam, which is required for effective SAFT processing. Similarly, for the hole at 10 mm, the sound beam divergence is not much. This means lesser number of A-scans with the signal from the hole in the raw B-scan data for SAFT processing. As a result, the focal spot size is fairly large up to a depth of 10 mm. At higher depth, the sound beam attains significant divergence, as a result of which the focal spot size is smaller than the one at lower depth.
- For higher aperture (≥ 4 elements ≈ 1.15 mm), the focal spot size is of the order of $0.6-0.7 D$, where D is the effective size of piezoelectric element. For D of the order of 0.5 mm, the focal spot size is in the range of $0.9D$ to $1D$. For very small values of D (0.25 mm), the focal spot size is in the range of $1.8D$.

From the above results, it can be concluded that for 10 MHz, 0.3 mm pitch linear array, very fine focal spot of less than a millimeter size can be achieved up to an aperture of 4 active elements ($D = 1.15$ mm). Beyond 4 and up to 8 active elements, the focusing is moderate (spot size of 1 mm to 1.5 mm) and beyond 8 active elements, the focusing is rather poor (spot size > 1.5 mm).

4.3.2.1.2 Pitch of linear array

The effect of pitch on the sound beam focusing is studied using 10 MHz, 0.3 mm pitch, 128 elements linear array. The data is acquired at a pitch of 0.3 mm, 0.6 mm, 0.9 mm and 1.2 mm for holes at various depths. For each case, single element is used for sound beam transmission and the data is acquired for 128 elements so that the aperture size, frequency and the total effective aperture remains the same.

Figure 4.9 shows the effect of pitch on the focal spot size achieved at various depths. The following are the observations:

- Up to 5 mm depth, the focusing is not so effective for a pitch of 1.2 mm. At this depth, not only the divergence is less, but the larger pitch means less number of A-scans with useful data for SAFT processing. This leads to increased focal spot size (approximately 1 mm).
- For holes at 10 mm to 40 mm depth, the focusing is satisfactory and does not appear to be affected by pitch. The focal spot size is observed to be in the range of 0.4 mm to 0.6 mm.

It can be concluded that for 10 MHz, 0.3 mm pitch linear array, when a single element is used for sound beam transmission, a very fine focal spot size is obtained for a depth range of 10 mm to 40 mm, even for a pitch of 1.2 mm. The pitch does not greatly affect the focusing, as long as the size of the piezoelectric element remains very small. The above results indicate that the size of the piezoelectric element is a more dominant factor than the pitch to achieve very fine sound beam focusing using SFLA.

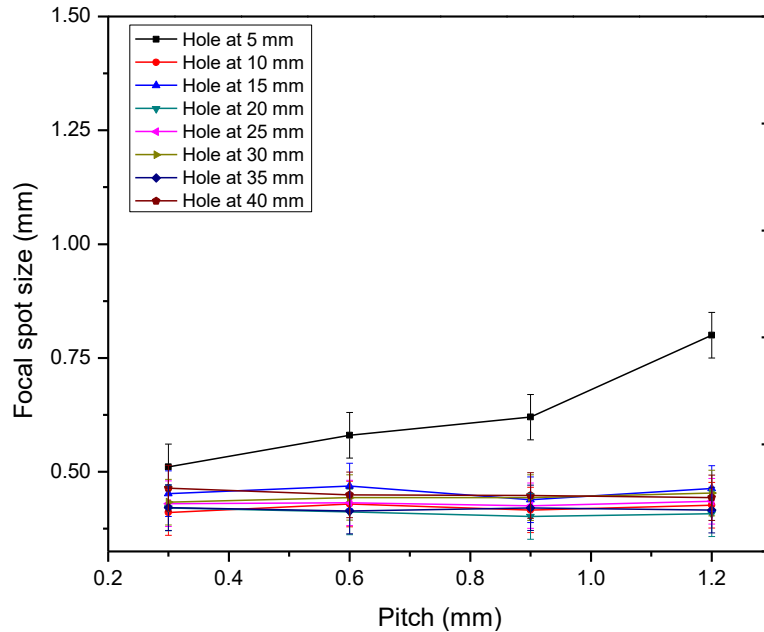


Figure 4.9: Variation in the focal spot size with the pitch used for data acquisition for a 10 MHz, 0.3 mm pitch linear array

4.3.2.1.3 Frequency of sound

The effect of frequency on sound beam focusing is studied using 2 MHz, 5 MHz and 10 MHz linear array. The data is acquired in such a manner that the aperture size, pitch and the total effective aperture remains similar for all the three frequencies.

Figure 4.10 shows the variation in the focal spot size with the frequency at various depths. The following are the observations:

- With 2 MHz, the side drilled hole at 5 mm could not be resolved from the initial pulse and hence no meaningful information on the focal spot size could be obtained for this depth. With further increase in depth, the focal spot size could be evaluated and is found to be rather coarse (>2 mm).

- With 5 MHz too, no meaningful information could be obtained from the hole at 5 mm. Although focusing improves as compared to 2 MHz, but the focal spot size is greater than 1 mm.
- With 10 MHz, focusing is very sharp for all the depths and the focal spot size is found to be in the range of 0.5 to 0.6 mm.

Focusing effect using SAFT is governed by the constructive interference at the flaw location as well as destructive interference at other locations, including the region just adjacent to the flaw. If the destructive interference in this region is not very effective, it leads to the broadening of the flaw signal, and so a larger focal spot. The lateral distance from the defect location for complete destructive interference depends on the pulse width and increases with increasing wavelength. This means that if the wavelength is larger (lower frequency), the lateral distance for complete destructive interference will be higher and the focal spot size will be coarser. The enhancement in focusing with increasing frequency is attributed to the narrow pulse width at higher frequency.

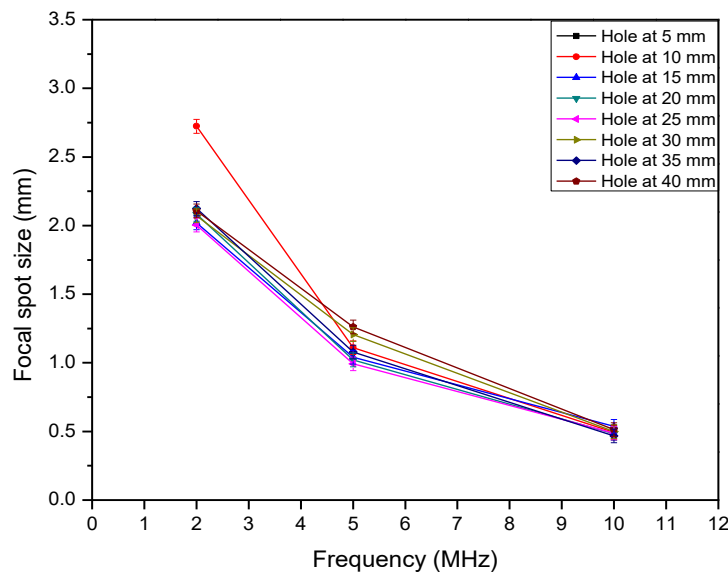


Figure 4.10: Variation in the focal spot size with the frequency for a constant aperture, pitch and total effective aperture

4.3.2.1.4 Total Effective Aperture

The Total Effective Aperture (TEA) represents the length of an array in the scan direction over which the data is acquired. Its effect on the sound beam focusing is studied using 10 MHz, 0.3 mm pitch 128 elements linear array. The data is acquired for all the holes using 64, 80, 100 and 128 elements at 0.3 mm pitch. For each case, a single element is used for sound beam transmission.

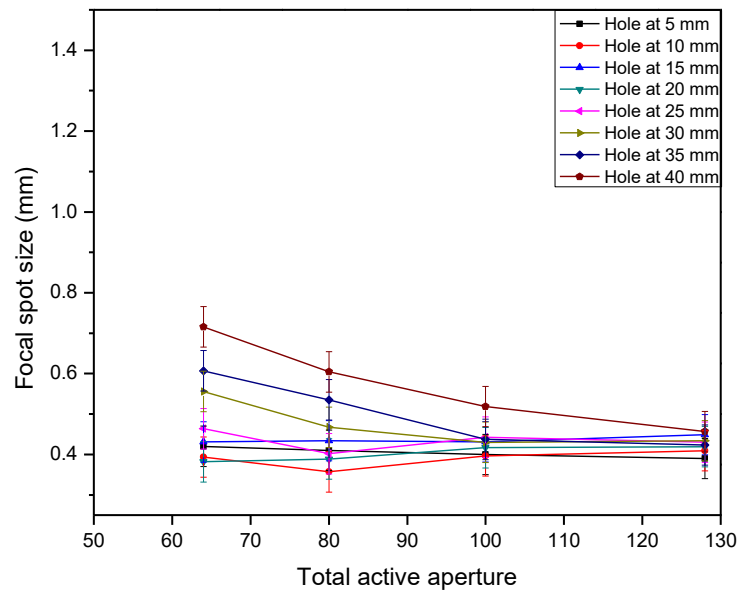


Figure 4.11: Variation in the focal spot size with total effective aperture for 10 MHz, 0.3 mm pitch linear array

Figure 4.11 shows the variation in the focal spot size with the total effective aperture at various depths. The following are the observations:

- For lower depths (up to 25 mm), the focal spot size does not show significant variation with TEA. This is because of the fact that there is significant divergence for lower depth in spite of using less number of elements for data acquisition. The focal spot size is in the range of 0.4 mm to 0.5 mm.

- With TEA of 64 elements, at higher depth (> 25 mm) the focal spot size is slightly large (0.6 to 0.7 mm). One major reason for this is the lower divergence for deeper holes.
- As TEA increases, the focal spot size at higher depth reduces as compared to the size for lower TEA. At TEA of 128 elements, there is enough divergence even at higher depth, and so there is effective focusing during SAFT processing.

It can be concluded that for 10 MHz, 0.3 mm pitch linear array, very fine focal spot size could be obtained for a depth range of 5 mm to 25 mm, even with a TEA of 64 elements. For depth beyond 25 mm, larger TEA is required to achieve similar results.

4.3.2.1.5 Effect of D/λ

The study on the effect of aperture size on the focusing indicated that smaller aperture leads to finer focal spot. The study on the effect of frequency shows that higher frequency or smaller wavelength (λ) leads to better focusing. The results also indicated that the same value of effective aperture (D) using two different frequencies does not give identical focal spot size. Hence one can say that the dimension of focal spot size by SAFT processing does not depend on D alone, but more specifically on the ratio D/λ .

Table 4.3 shows the focal spot size δ_{6dB} , both absolute and in terms of D , at the depth of 25 mm in aluminum using three different frequencies. These values are obtained from the data collected for studying the effect of aperture and the frequency, on focal spot size described in Section 4.3.2.1.1 and 4.3.2.1.2.

Table 4.3: Variation in δ_{6dB} with D/λ

Sr. No.	Frequency (MHz)	Wavelength λ (mm)	Aperture Size D (mm)	D/λ	Focal spot size	
					δ_{6dB} (mm)	δ_{6dB}/D
1	10	0.63	0.25	0.40	0.43	1.7
2	10	0.63	0.55	0.80	0.49	0.9
3	10	0.63	1.15	1.82	0.72	0.6
4	10	0.63	2.35	3.73	1.43	0.6
5	10	0.63	2.95	4.68	1.75	0.6
6	5	1.26	0.50	0.40	0.99	1.9
7	5	1.26	1.1	0.87	1.18	1.1
8	5	1.26	2.3	1.82	1.53	0.7
9	5	1.26	3.5	2.77	2.07	0.6
10	5	1.26	4.7	3.73	2.68	0.6
11	2	3.15	0.55	0.17	2.0	3.6
12	2	3.15	1.35	0.43	2.20	1.6
13	2	3.15	2.95	0.94	2.60	0.9
14	2	3.15	4.55	1.44	3.21	0.7
15	2	3.15	6.15	1.95	3.97	0.6

Table 4.3 indicates the following:

- For the same value of D , δ_{6dB} is smaller when high frequency is used.
- The normalized focal spot size (δ_{6dB}/D) depends on the normalized element size (D/λ).
- Similar values of D/λ give similar values of δ_{6dB}/D .

- For all the three frequencies, the δ_{6dB}/D value remains more or less constant at 0.6 at D/λ value of approximately 2 or more.

The above observations are contrary to what has been reported in the literature that the lateral resolution obtained by SAFT depends on D alone [16,17,98,102,103] and is independent of the frequency (or wavelength λ). This hypothesis holds true while dealing with the conventional piezoelectric transducers (transducers with large value of D/λ). However, the results in Table 4.3, indicate that the focal spot size or the lateral resolution obtained by SAFT on the data acquired by miniature elements of linear array is also dependent on the frequency or λ . The primary reason for this could be the fact that for large piezoelectric crystals, the beam divergence angle is a linear function of λ/D . However, as shown in Section 4.2.3, for the miniature elements of linear array, this is not the case.

Figure 4.12 shows the variation in the normalized focal spot size (δ_{6dB}/D) with normalized element size (D/λ). It can be seen that for very small values of D/λ , the value of δ_{6dB}/D is very large. As D/λ increases, there is a sharp drop in the value of δ_{6dB}/D . At D/λ value of approximately 2 or more, the value of δ_{6dB}/D is independent of D/λ and remains constant at 0.6.

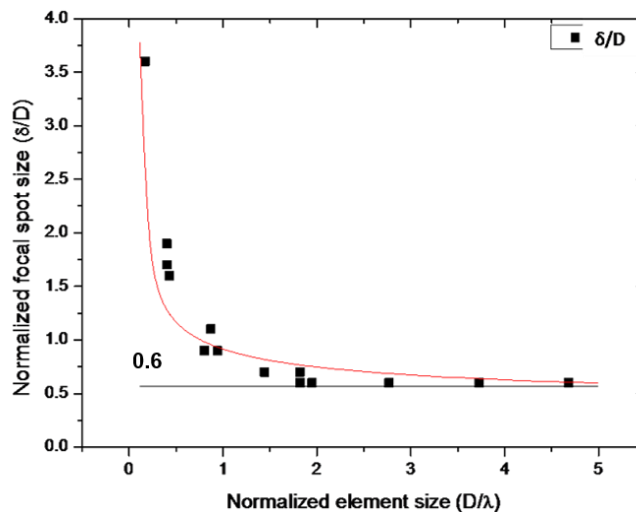


Figure 4.12: Variation in normalized focal spot size with normalized element size

L J Curtona [217] indicated that the focal spot size achieved by SAFT depends on the length of synthetic aperture (L_{eff}). Larger the value of L_{eff} , smaller is the focal spot size. L_{eff} in turn depends on the beam divergence angle, which in turn is governed by the diameter of piezoelectric crystal (D) and the wavelength (λ).

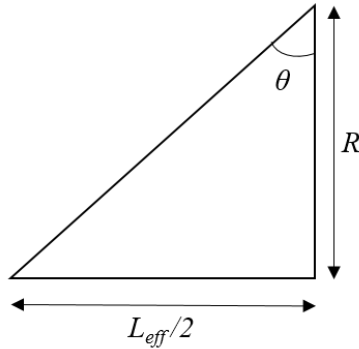


Figure 4.13: Dependence of beam spread on L_{eff}

From Figure 4.13,

$$\tan \theta = \frac{L_{eff}}{2R} \quad [41]$$

where θ is the half beam divergence angle.

The beam divergence angle θ is also given by [1]

$$\sin \theta = \frac{k\lambda}{D} \quad [42]$$

where, k is the beam divergence constant.

The focal spot size δ achieved by SAFT [217] is given by:

$$\delta = \frac{R\lambda}{2L_{eff}} \quad [43]$$

where λ is the wavelength.

From equations [6] and [8],

$$\delta = \frac{\lambda}{4 \tan \theta} \quad [44]$$

For smaller angles, $\sin \theta = \tan \theta$. Hence, equation [44] can be written as,

$$\delta = \frac{\lambda}{4 \sin \theta} \quad [45]$$

From equation [42] and [45],

$$\delta = \frac{D}{4k} \quad [46]$$

The above equation indicates that if k is taken as a constant, then the value of the focal spot size achieved by SAFT depends on D alone and is independent of λ or frequency.

For large circular and rectangular piezoelectric crystals, the value of k for 6 dB beam divergence is 0.5 and 0.44 respectively [1]. However, as shown in Section 4.2.3, equation 39, for miniature rectangular piezoelectric elements in linear arrays, the value of k depends on D/λ , and is given as,

$$k = 0.44[0.6 + 0.5 \log \left(\frac{D}{\lambda} \right)] \quad [47]$$

Based on the above, the 6 dB focal spot size δ_{6dB} achieved by SAFT for large and miniature piezoelectric crystals can be given as:

For large circular crystal:

$$\delta_{6dB-circ} = \frac{D}{4*0.5} = \frac{D}{2} = 0.5D \quad [48]$$

For large rectangular crystal:

$$\delta_{6dB-rect} = \frac{D}{4*0.44} = 0.6D \quad [49]$$

For miniature rectangular crystal:

$$\delta_{6dB-mini} = \frac{D}{4*0.44[0.6+0.5 \log(\frac{D}{\lambda})]} = \frac{0.6D}{[0.6+0.5 \log(\frac{D}{\lambda})]} \quad [50]$$

The above hypothesis matches with the results shown in Figure 4.12.

4.3.2.1.6 Summary of the observations on the effect of array based parameters on sound beam focusing

Based on the studies carried out for the effect of array based parameters on the focusing achieved by SFLA, it can be concluded that, the element size and the frequency play a dominant role in this regard. Small element size and high frequency results in very fine focusing. The finest focal spot size is obtained by using the smallest possible element size and the largest possible frequency. However, these conditions will limit the penetration of sound beam to shallower depth. Also the sensitivity for flaw detection is adversely affected. Hence, there has to be compromise between the smallest focal spot size to be achieved by SFLA technique and largest thickness of the component to be inspected with an acceptable sensitivity for flaw detection. The pitch of the linear array does not affect the focusing to a large extent. Similarly, for shallower depth, the narrower TEA can achieve a very fine focal spot size but at larger depth, wider TEA is required.

4.3.2.2 SAFT processing parameters

In addition to the above mentioned linear array based parameters, sound beam focusing using SFLA technique is also affected by the difference between the actual value and the one given as an input to the SAFT algorithm for some parameters. These include:

- Sound velocity in the material
- Pitch of the linear array
- Beam divergence angle

The experimental details are given in Chapter 3, Section 3.4.2. The results are described below:

4.3.2.2.1 Velocity in the material

During SAFT processing, the sound velocity in the material is given as an input to the algorithm. This value is used to calculate the time-shift applied to the A-scan signals. If the velocity in the material differs significantly from that of the input value taken, then the time-shift applied to the A-scan signals will not be appropriate. As a result, the constructive and destructive interference during the summation and averaging process will not be effective. This will affect the focal spot size achieved adversely.

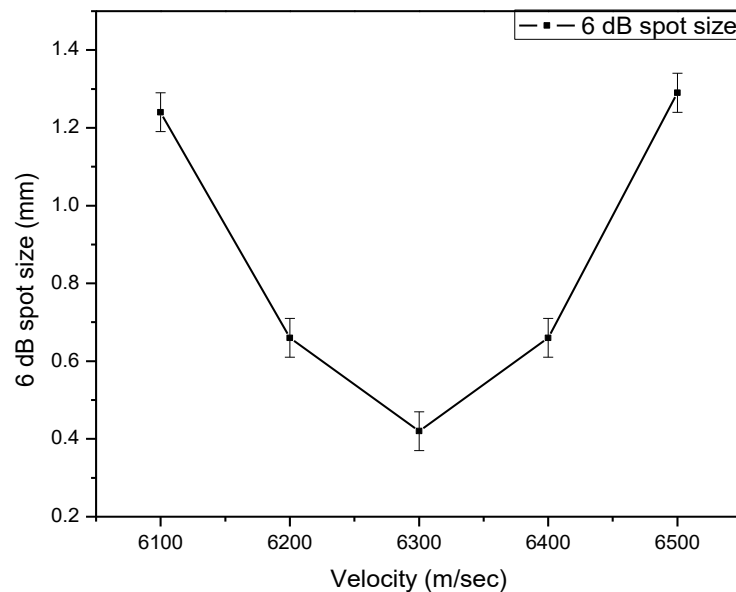


Figure 4.14: Variation in the focal spot size with the input value of sound velocity during SAFT processing for an aluminum sample (Actual Velocity = 6300 m/s)

The effect of the inaccuracy in the assumed sound velocity in the material on the focal spot size achieved is studied by varying the sound velocity during SAFT processing from 6100 to 6500 m/s. The processing was carried out on the data acquired on aluminum having the sound velocity of 6300 m/s. Figure 4.14 shows the results of this variation on the focal spot size. The results indicate that the smallest focal spot size is achieved when the input value of sound velocity matches with the actual value (6300 m/s in the present case). Even with a difference of 1.5%, the increase in the focal spot size is significant (from 0.47 mm to 0.67 mm).

4.3.2.2.2 Pitch of the linear array

The pitch of the linear array used for data acquisition is an input to the SAFT processing algorithm. The pitch value is also used to calculate the time-shift that has to be applied to the A-scans before summation and averaging. Like the sound velocity, if the input value for pitch is different than the actual, it will lead to inappropriate time shift, which in turn affects the constructive and destructive interference. This will lead to the coarsening of focal spot size. Figure 4.15 shows the variation in the focal spot size with the input value of the pitch of the linear array.

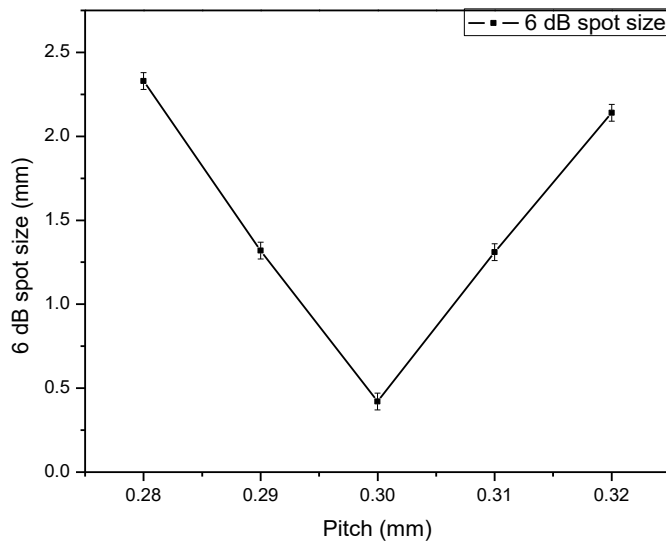


Figure 4.15: Variation in the focal spot size with the input value of the pitch during SAFT processing (Actual Pitch = 0.3 mm)

The results indicate that the best focusing is achieved when the input value of pitch matches with the actual pitch of the linear array (0.3 mm in the present case). Even with the variation of 0.01 mm in pitch (approximately 3.3%), there is significant increase in the focal spot size (from 0.47 to 1.17 mm).

4.3.2.2.3 Beam divergence angle

The beam divergence angle is an important input to the SAFT algorithm. Its value decides the number of A-scans to be considered for time-shifting, summation and averaging. Ideally, this value should be in the same range as the actual beam divergence that is achieved during data acquisition. If the value is less, then there will be less number of A-scans for processing. This will lead to inferior focusing of sound beam. If this value is more, then there may be number of A-scans with no useful information. This may be lead to lower amplitude of the flaw signal in the processed image.

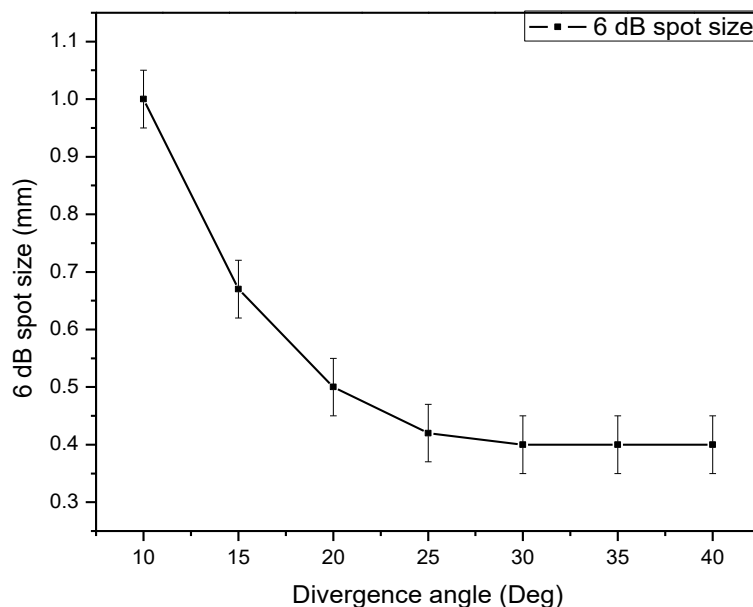


Figure 4.16: Variation in the focal spot size with the input value of the sound beam divergence angle during SAFT processing (Actual divergence = 25 deg.)

In the present study, the 6 dB beam divergence for the 10 MHz, 0.3 mm pitch and 5 MHz, 0.6 mm pitch linear array for a single element excitation (SFLA technique) is experimentally found to be approximately 25 deg. The variation in the focal spot size with the input value of beam divergence angle from 10 deg. to 50 deg. is found out. The results are shown in Figure 4.16.

The results indicate that for the low input value of beam divergence than the actual, the focal spot size is fairly large. As the input value of beam divergence approaches the actual beam divergence, the focal spot size reduces. Beyond this, there is no significant change in the focal spot size with the increase in the input value. The higher value of beam divergence than actual would only add to the processing time without a significant gain on the result.

4.3.2.2.4 Summary of observations on the effect of SAFT processing based parameters on sound beam focusing

Based on the above studies, it can be concluded that when it comes to the SAFT processing, the difference between the actual and the input value of the pitch has a dominant effect on achieving satisfactory focusing. If the sound velocity input is incorrect, there is an increase in the focal spot size, but the effect is not so pronounced. Regarding the input value on sound beam divergence, it should be ensured that to achieve satisfactory results, this value should be at least equal to or more than the actual beam divergence in the material.

4.4 PA-SAFT technique

With SFLA and FMC techniques, a single element is used for sound beam transmission. The sound beam emanating from a single element has a low acoustic power and as a result, these techniques may not be suitable in achieving the required sensitivity during the examination of thick components and/or materials with high sound attenuation. This limitation can be overcome by

using a group of elements for sound beam transmission. When more number of elements are used, the acoustic power improves and hence achieving the required penetration and obtaining a measurable signal from deeper flaws will not be a problem. But one drawback of using multiple elements for sound beam transmission is that, with the increase in the aperture size, the sound beam attains directivity. As a result, the beam spread comes down (when compared to single element excitation), which adversely affects focusing by SAFT. The result of the study on the variation in focal spot size with the increase in the active aperture (Section 4.3.2.2.1) has confirmed this. In order to achieve adequate beam divergence while using multiple elements so as to achieve good focusing by SAFT, the sound beam emanating from a selected aperture is focused right below the aperture selected and very close to scanning surface (at 2 mm depth during this study) using focal laws. By doing this, a highly divergent sound beam beyond a focal point is obtained. The divergent sound beam can then be used to acquire the electronic B-scan, which is then processed by SAFT algorithm. This forms the basis of PA-SAFT technique.

4.4.1 Methodology

Figure 4.17 shows the methodology of data acquisition using PA-SAFT technique. The linear array is placed on the surface of the sample. Active aperture comprising of few elements is then selected, using which the sound beam is focused very close to the surface. The active aperture is then moved electronically to acquire the B-scan. The figure shows active apertures X_1 , X_{i-n} , X_i , X_{i+n} and X_m . The flaw is present below the aperture X_i . The focusing and the electronic scanning creates an array of virtual sources of very small dimensions within the material. A divergent sound beam emanating from these virtual sources interacts with the flaw. The raw B-scan image is processed by time based SAFT algorithm in a similar manner as described for SFLA technique.

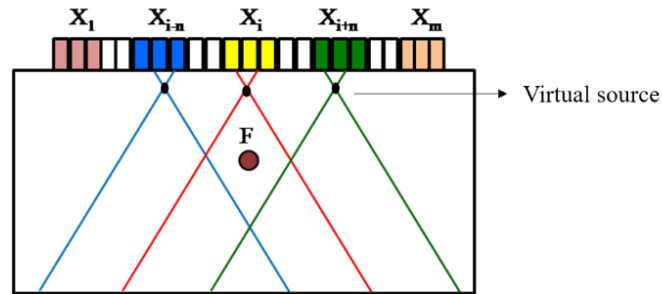


Figure 4.17: Data acquisition using PA-SAFT technique

Figures 4.18(a) and (b) show the raw B-scan and the SAFT processed B-scan images collected on an aluminum block with 0.5 mm dia. side drilled hole located at a depth of 25 mm from the surface using PA-SAFT technique. A 10 MHz, 0.3 mm pitch, 128 elements linear array is used for this purpose, which is kept symmetrically over the hole as shown in Figure 4.7. An active aperture comprising of 8 elements is used for sound beam transmission and reception. A divergent sound beam in the region of interest is obtained by focusing the sound emanating from the active aperture at the depth of 2 mm from the surface.

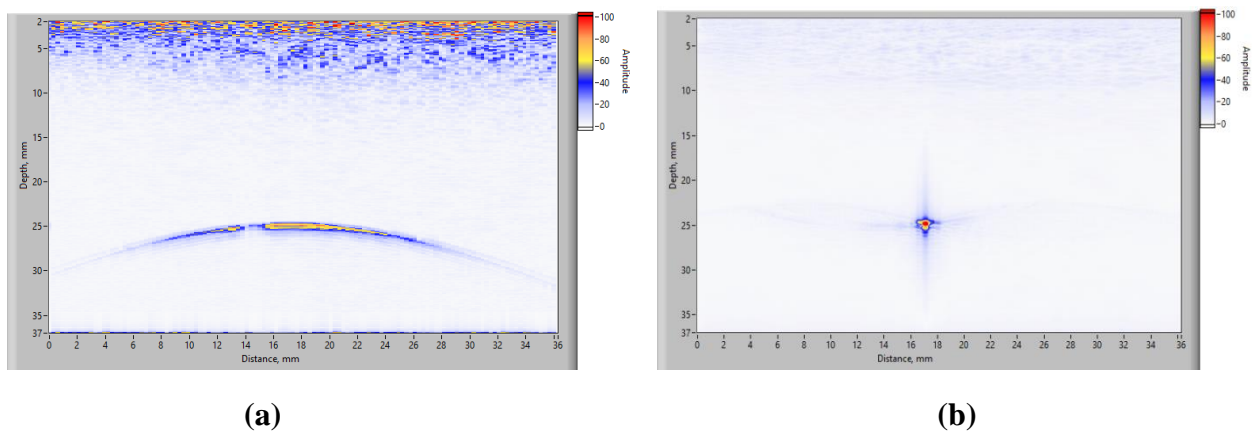


Figure 4.18: (a) Raw and (b) SAFT processed B-scan images collected on a 0.5 mm dia. side drilled hole at 25 mm depth in an aluminum block using PA-SAFT technique

Like SFLA, the raw image shows a well spread-out signal from the side drilled hole. The signal shows high amplitude at the centre, which gradually reduces as one moves on either side of the

central region. The raw B-scan image also shows some discontinuity at a distance of approximately 15 mm. This is because of some dead elements in the linear array used. On SAFT processing, the wide signal of the hole is reduced to a spot. The 6 dB width of the signal from the hole, which can be considered as a dimension of focal spot, is found to be 0.52 mm. This indicates that with PA-SAFT technique, one can achieve very sharp focusing of sound beam. The focal spot size achieved by PA-SAFT is higher than what is achieved using SFLA technique. The primary reason for this is lower sound beam divergence with PA-SAFT technique.

4.4.2 Selection of Active Aperture

Selection of the number of elements to be excited (active aperture) is a crucial step in the application of PA-SAFT technique for sound beam focusing. This number should be such that one gets adequate acoustic power at a higher depth and also significant beam divergence in the region of interest. At the same time, this number should not be too large, wherein one would require high-end phased array instrument.

In the current study, majority of the experimental work is carried out on aluminum and steel samples and the requirement of sound beam focusing is in the depth range of approximately 10 mm to 70 mm from the scanning surface. For carrying out the study on these samples using PA-SAFT technique, the sound beam using a selected aperture is focused at a depth of 2 mm from the scanning surface so that a divergent sound beam is obtained beyond the focal point in the region of interest.

In order to achieve significant divergence beyond the focal point (2 mm), the minimum active aperture should be such that the near field length in the given material is greater than 2 mm. For a

linear array transducer having frequency ν , pitch p' and orthogonal dimension b , when n number of elements are used to create focal law, the near field length N_o , is given by [6,7]:

$$N_o = \frac{jD^2\nu}{4c} \quad [51]$$

where, D is the active aperture ($n * p'$)

j is a constant depending on the aspect ratio (aspect ratio = A/b , $j \approx 1$ for aspect ratio < 0.5)

ν is the frequency and c is the velocity of sound in the material.

While using 10 MHz, 0.3 mm pitch linear array, minimum 8 active elements are required to achieve near field length of greater than 2 mm ($N = 2.5$ mm in steel). With 5 MHz, 0.6 mm pitch linear array, one would need minimum 6 active elements to satisfy the above condition ($N = 2.7$ mm in steel).

4.4.2.1 Sound beam computation using CIVA 11

To visualize the effect of sound beam focusing within the near field on the beam divergence achieved beyond the focal point, sound beam computation is carried out using CIVA 11. Figure 4.19 shows the results of sound beam computation using 10 MHz, 0.3 mm pitch linear array for three cases: (a) single element is excited, (b) 8 elements excited with no delay laws and (c) 8 elements excited with delay laws applied to focus the sound beam at 2 mm from the surface.

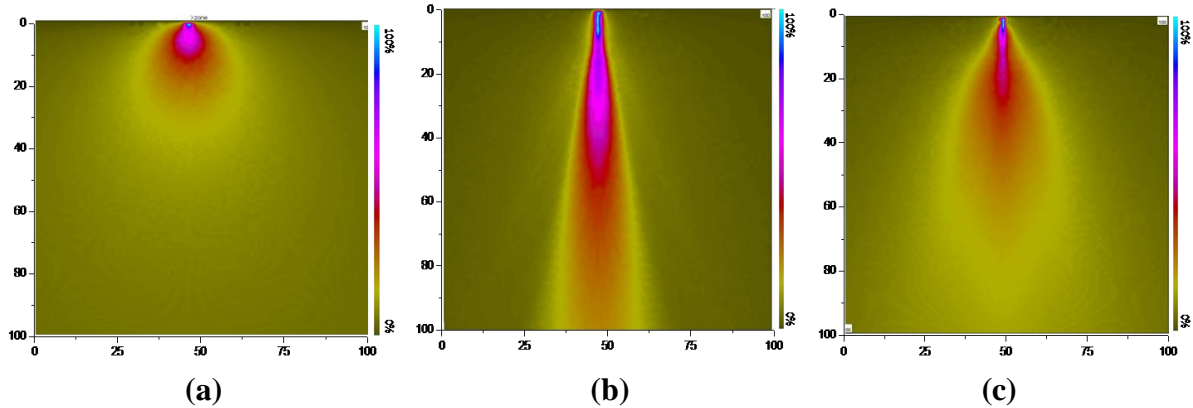


Figure 4.19: Sound beam computation results for 10 MHz, 0.3 mm pitch linear array with excitation of (a) 1 element (b) 8 elements with no delay law and (c) 8 elements with delay law to focus at 2 mm (Simulation)

The simulation results show the sound beam profile within the material, where the amplitude at any given point is colour coded. Blue represents the maximum, pink represents the intermediate and green represents the minimum amplitude. Figure 4.19(a) shows that with single element excitation, the beam spread is very high; approximately ± 26 deg. However, the sound wave amplitude at a depth of more than 20 mm is very low. With 8 element excitation and no delay laws applied as shown in Figure 4.19 (b), the sound wave amplitude is fairly high, even at larger depth, but the beam divergence comes down drastically to a value of ± 9 deg. When these 8 elements are excited with an application of delay law to focus the sound beam within the near field (at a depth of 2 mm from the surface) as shown in figure 4.19(c), significant divergence beyond the focal point is obtained. In this case, the beam divergence is of the order of ± 25 deg. This is a significant improvement when compared to the case when no delay laws are applied. Although the sound wave amplitude at higher depth is low when compared to the case when no delay laws are applied, it still looks adequate up to a depth of 50 mm. Thus, focusing within the near field with optimum number of elements not only helps to achieve reasonable sound wave amplitude at higher depth

for flaw detection, but also improves beam divergence, which helps to achieve effective focusing during SAFT processing. In order to study the effect of aperture size (number of active elements) on the beam divergence achieved beyond the focal point, sound beam computation is carried out using CIVA 11 using apertures varying from 4 to 14 active elements of a 10 MHz, 0.3 mm pitch linear array. The results are given in Figure 4.20. In each case, sound beam is focused at 2 mm depth from the scanning surface using focal laws.

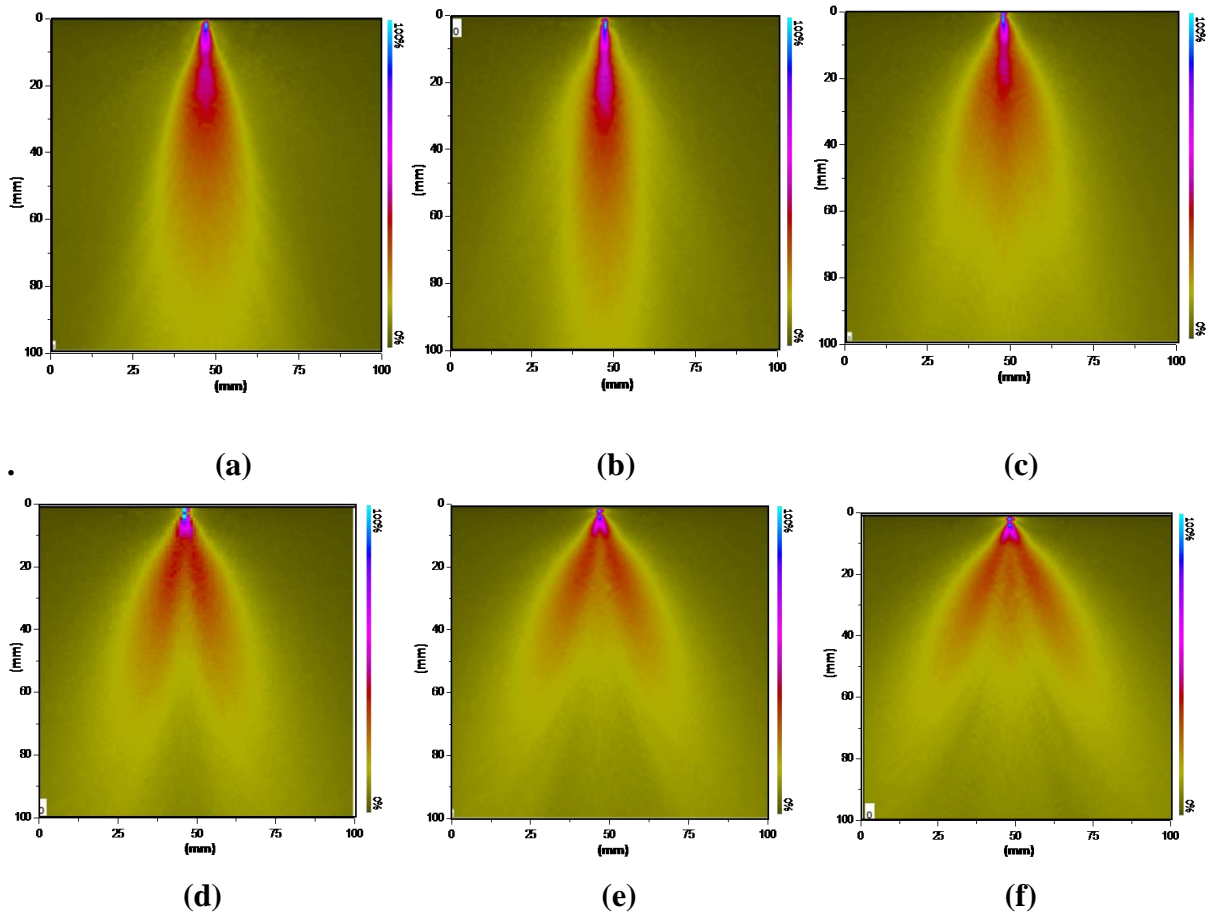


Figure 4.20: Sound beam computation results for 10 MHz, 0.3 mm pitch linear array with delay laws to focus at 2 mm using (a) 4 el (b) 6 el (c) 8 el (d) 10 el (e) 12 el and (f) 14 elements (Simulation)

With 4 and 6 active elements (Figures 4.20 (a) and (b)), the near field length is less than 2 mm. Hence focusing at 2 mm is not possible. As a result, limited divergence is obtained using these two apertures. Also, the beam divergence using 6 active elements is less as compared to 4 active elements, since the beam divergence is inversely proportional to the size of the piezoelectric element (aperture size in this case). With 8 active elements (Figure 4.20 (c)), the near field length becomes more than 2 mm. Because of focusing within the near field, significant divergence beyond the focal point is obtained. With 10, 12 and 14 active elements, there is further increase in the beam divergence as the ratio of near field length (N_o) to the focal distance keeps on increasing. One notable observation from the beam computation results is that beyond 10 active elements, the sound beam splits beyond the focal point (Figures 4.20 (d), (e) and (f)). This splitting creates a zone of low amplitude in the central region of the sound beam. This may result in lower amplitude signals from the flaw from the central apertures in the acquired B-scan image. The following explanation has been added to Section 4.4.2.1. The beam splitting effect is observed when the sound beam is focused very close to the transducer, typically at a distance which is less than half of the near field length. To achieve focusing very close to the scanning surface, the focal law is very steep and there is a significant time delay between the excitation of central elements and the peripheral elements. Under such circumstances, the sound waves emanating from the edge elements of the linear array travelling at a very large angles, may not be interfering constructively with the sound waves emanating from the central elements. This leads to the creation of a zone of very low amplitude in the central region of the array giving rise to the ‘beam splitting’ effect.

4.4.2.2 Effect of active aperture on sound wave amplitude and beam divergence

Two important considerations for choosing the active aperture for PA-SAFT technique are: (i) the beam divergence and (ii) the sound wave amplitude at any given depth. While the beam divergence continues to increase with the aperture size as seen in the above results, one also needs to look at the wave amplitude in the central region of the sound beam because of the beam splitting effect. Simulation studies are carried out using CIVA 11 to compute the sound beam profile using 10 MHz, 0.3 mm pitch and 5 MHz 0.6 mm pitch linear arrays by using different number of active elements for sound beam transmission. For each case, the sound beam is focused at a depth of 2 mm from the surface. From the beam computation results, the variation in the wave amplitude along the depth in the central region of the sound beam is found out.

Figure 4.21 shows the variation in the wave amplitude in the central region of the sound beam over a depth range of 2 mm to 45 mm from the scanning surface for apertures varying from a single element to 14 elements using 10 MHz, 0.3 mm pitch linear array in steel. The sound wave amplitude values using various apertures at different depths are normalized with respect to the maximum, which is obtained for 14 active elements at a depth of 2 mm. For a single element excitation, the sound wave amplitude at 2 mm is rather low, almost 15 dB less than what is observed while using 14 active elements, although the variation in the sound wave amplitude with the depth is not so significant. With 2 active elements, the sound wave amplitude over the selected depth range increases by almost 6 dB and the variation with depth shows a similar trend as seen for single element excitation. With 4 active elements, there is further improvement in the sound wave amplitude (10 dB) over a single active element, although the drop in the sound wave amplitude from 2 mm to 10 mm is significant (6 dB). Beyond 10 mm, the drop in the sound wave

amplitude is gradual. The trend using 6 and 8 active apertures is similar to what is observed for 4 active elements except for the fact that there is a significant improvement in sound wave

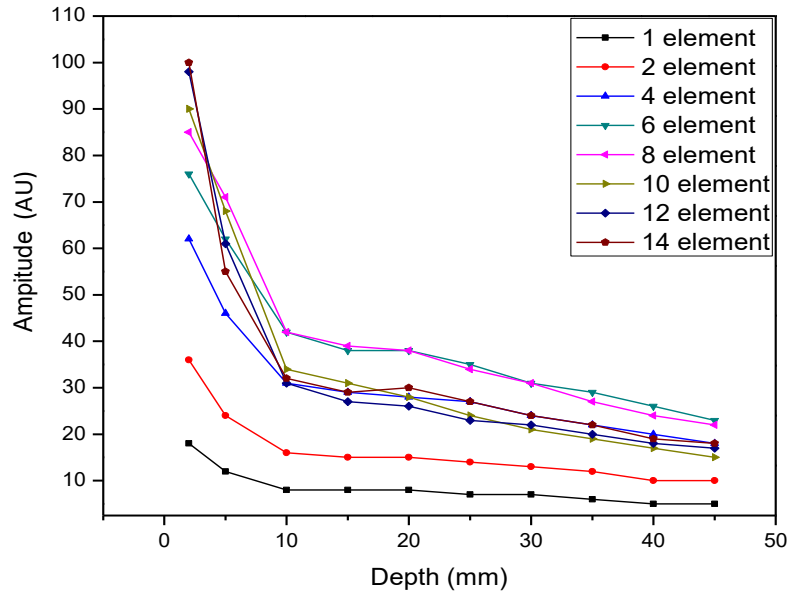


Figure 4.21: Variation in the sound wave amplitude with the depth for different apertures using 10 MHz, 0.3 mm pitch linear array (Simulation)

amplitude (of the order of 14 dB over a single element excitation) over the entire depth range. With 10 and more active elements, the drop in the sound wave amplitude from 2 mm to 10 mm is very sharp. Also, beyond 10 mm, the sound wave amplitude from these active apertures show lower values as compared to the ones observed while using 6 and 8 active elements. The primary reason for this is the splitting of sound beam beyond the focal point while using 10 or more active elements, which creates a region of low wave amplitude in the central region of the sound beam. The above results indicate that while using 10 MHz, 0.3 mm pitch linear array in the thickness range of 10 mm to 40 mm, there is no significant benefit of using more than 8 active elements for data acquisition with PA-SAFT technique.

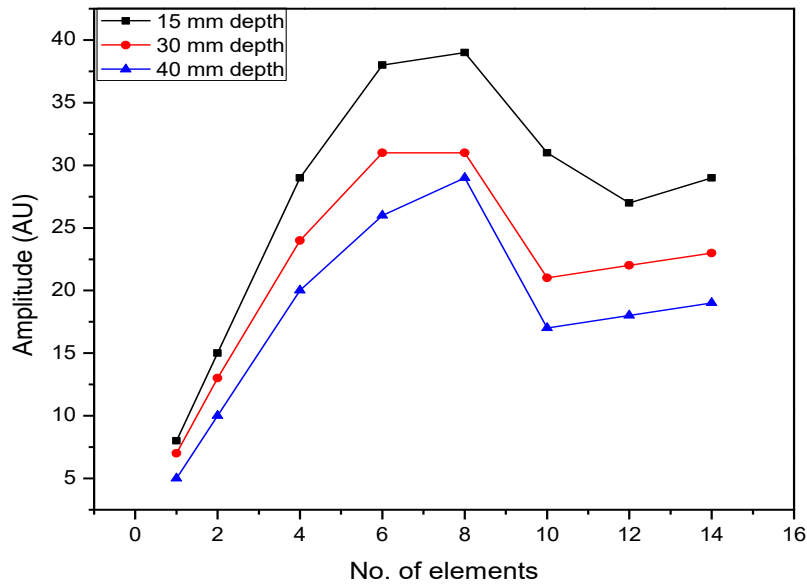


Figure 4.22: Variation in the sound wave amplitude with the active aperture size at different depths for 10 MHz, 0.3 mm pitch linear array (Simulation)

Figure 4.22 shows the variation in the sound wave amplitude in the central region for different active apertures using 10 MHz, 0.3 mm pitch linear array at three different depths. The figure indicates that in the depth range of 15 mm to 40 mm, the maximum sound wave amplitude is obtained using an active aperture of 8 elements. Beyond 8 active elements, the sound wave amplitude drops because of the beam splitting effect.

Figure 4.23 shows the variation in the 6 dB full beam width with the depth using various active elements. With a single active element, which acts like a point source, the beam width is maximum for all the depths. With 2 active elements, the beam width falls drastically. With 4 and 6 active elements, there is a further reduction in the beam width as the sound beam achieves directivity. However, with 8 active elements, the beam width reverses the falling trend and shows higher value as compared to the ones from 4 and 6 active elements. The primary reason for this behavior is the

fact that the sound beam is focused within the near field by delay laws. As a result, the sound beam shows more divergence than what it would exhibit, had it not been focused. With further increase in the aperture size from 10 to 14 active elements, the beam width continues to show an increasing trend. From these results, it can be concluded that from the consideration of beam divergence, more number of active elements give better results. However, more number of active elements would require phased array instrumentation with that many numbers of parallel channels. Also, the simulation results described in the previous section have shown that for a large aperture, the sound beam splits, which is not desirable. Moreover, the use of a large number of elements for sound beam transmission using PA-SAFT may not be very attractive as one can then resort to direct focusing using delay laws.

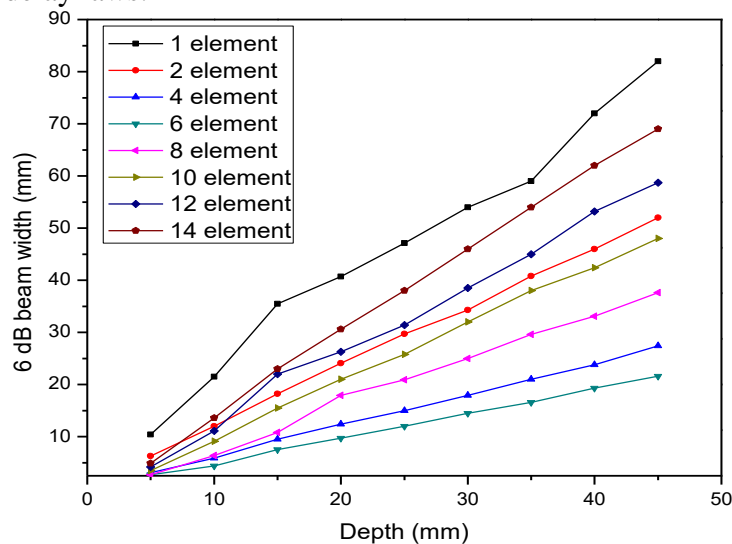


Figure 4.23: Variation in the full beam width with depth for different apertures using 10 MHz, 0.3 mm pitch linear array (Simulation)

Similar study is carried out for a 5 MHz, 0.6 mm pitch linear array. The variation in the sound wave amplitude with the depth is shown in Figure 4.24. The results indicate that beyond 5 mm depth, an active aperture comprising of 6 active elements give higher sound wave amplitude as compared to the lower and higher active apertures.

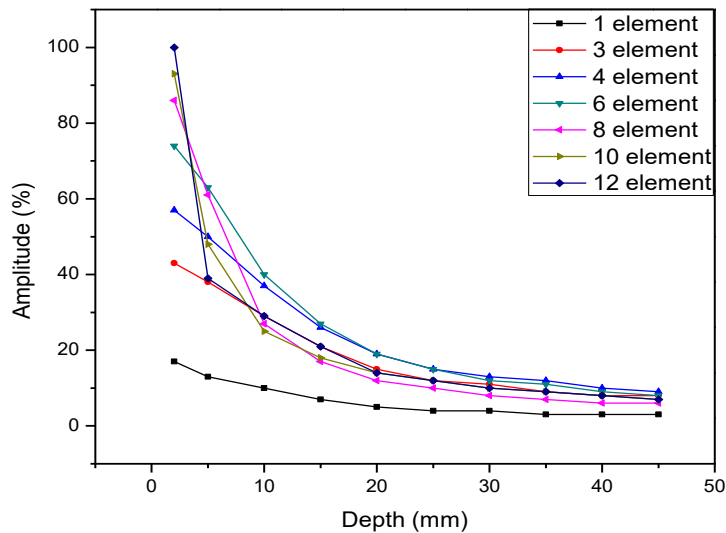


Figure 4.24: Variation in the sound wave amplitude with depth for different apertures using 5 MHz, 0.6 mm pitch linear array (Simulation)

Figure 4.25 shows the variation in the sound wave amplitude in the central region with the active aperture size using 5 MHz, 0.6 mm pitch linear array at three different depths. The figure indicates that in the depth range of 15 mm to 40 mm, the maximum sound wave amplitude is obtained using an active aperture of 6 elements.

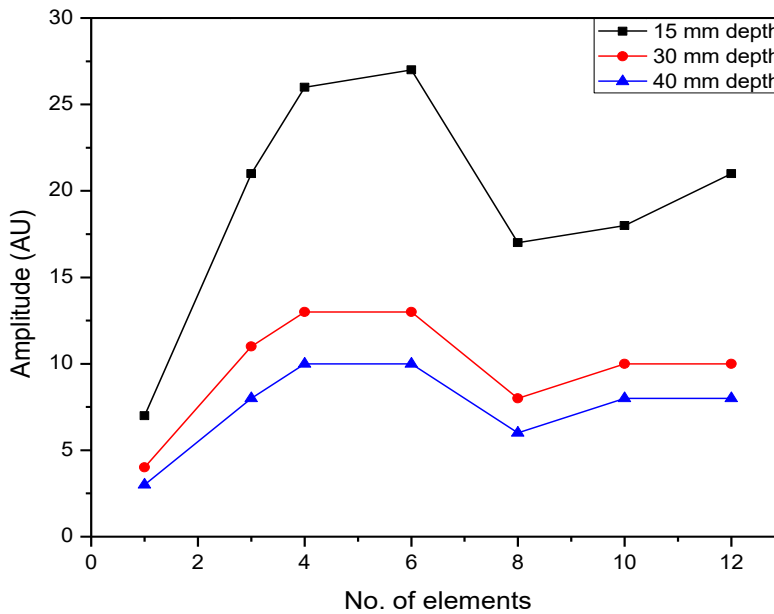


Figure 4.25: Variation in the sound wave amplitude with the active aperture size at different depths for 5 MHz, 0.6 mm pitch linear array (Simulation)

The beam width (Figure 4.26), as expected is highest for a single element excitation. With 3 and 4 active elements, since the near field length is less than 2 mm, the beam width is very less. Aperture size comprising of 6 and 8 active elements show intermediate values, while 12 number of active elements show highest beam width. The above results are similar to the ones observed for 10 MHz, 0.3 mm pitch linear array. In this case too, the sound beam splits beyond an active aperture of 8 elements. The results are shown in Figure 4.27.

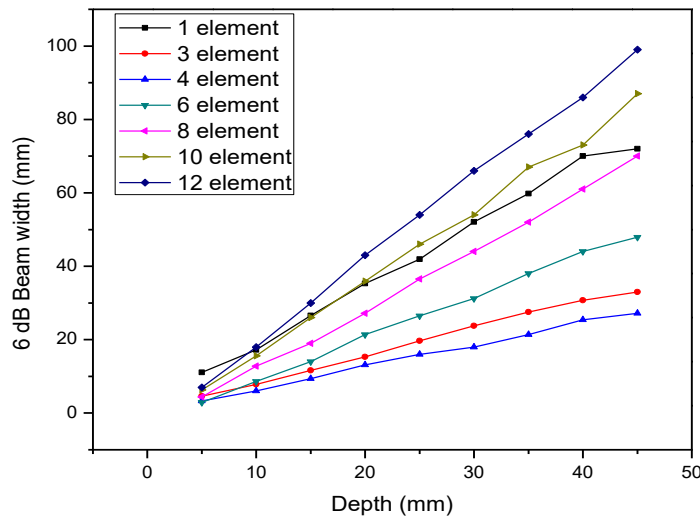


Figure 4.26: Variation in the full beam width with depth for different apertures using 5 MHz, 0.6 mm pitch linear array (Simulation)

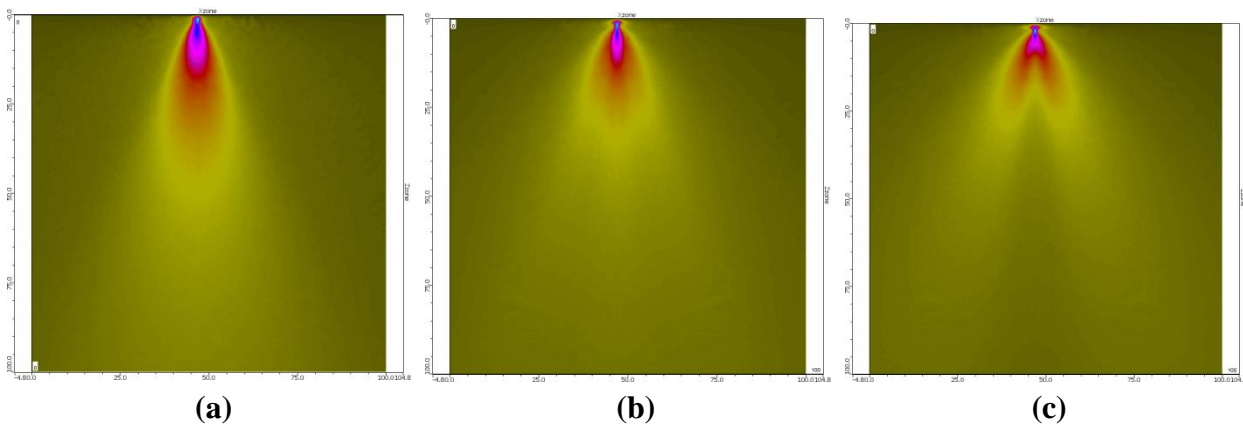


Figure 4.27: Beam computation results for 5 MHz, 0.6 mm pitch linear array with delay law to focus at 2 mm using (a) 3 element (b) 6 element and (c) 8 element (Simulation)

4.4.2.3 Effect of active aperture on the size of the virtual source

Both SFLA and PA-SAFT techniques are based on the use of a divergent sound beam for data acquisition. The fundamental difference between them is that SFLA technique uses a single element excitation, while PA-SAFT uses a group of elements for data acquisition, primarily with an aim to achieve higher acoustic power within the material and hence, better sensitivity at higher depth. The beam divergence during data acquisition by SFLA technique is determined by the size of the individual element (source) in an array. Smaller source size gives rise to larger beam divergence and hence good focusing upon SAFT processing. With PA-SAFT technique, the source size is not the size of the active aperture (the product of number of active elements and pitch), but the size of the focal spot (virtual source) that is created at the focal point (2 mm in the present case).

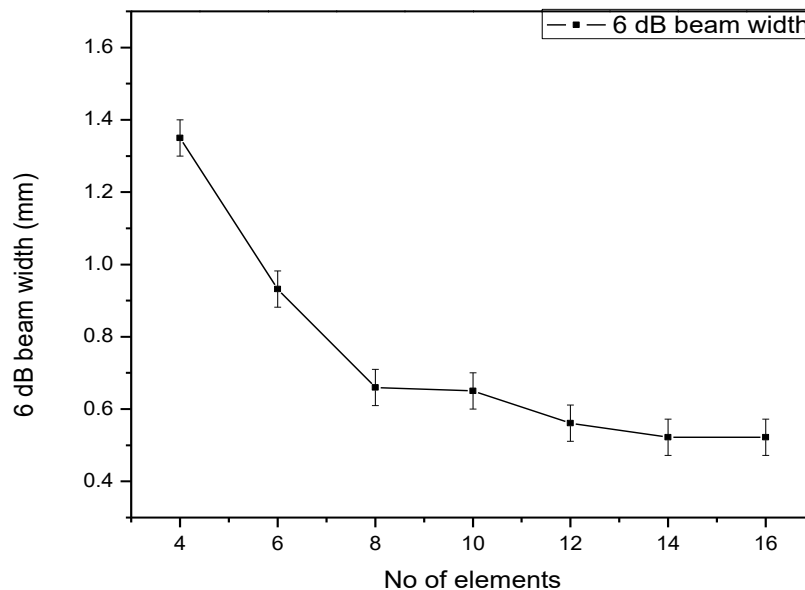


Figure 4.28: Variation in 6 dB width of the virtual source at 2 mm depth from the surface for different number of active elements using 10 MHz, 0.3 mm pitch linear array (Simulation)

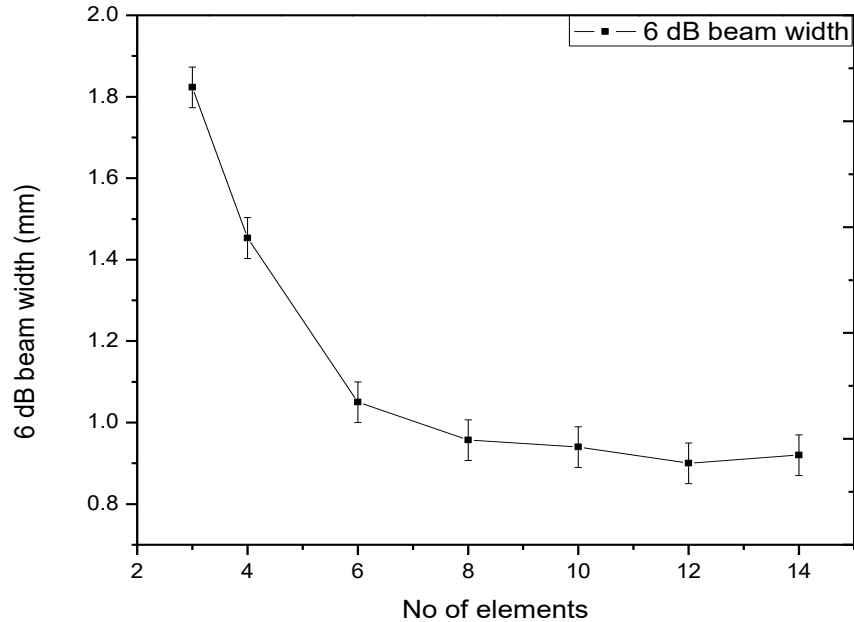


Figure 4.29: Variation in 6 dB width of the virtual source at 2 mm depth from the surface for different number of active elements using 5 MHz, 0.6 mm pitch linear array (Simulation)

If the virtual source is of a smaller dimension, one would expect a well divergent sound beam beyond the focal point and hence good focusing upon SAFT processing. In order to study the effect of aperture size or the number of active elements on the size of the virtual source, sound beam computation is carried out using CIVA 11 for various active apertures. The 6 dB beam width at 2 mm (size of the virtual source), where the sound beam is focused using delay laws, for different number of active elements, while using 10 MHz, 0.3 mm pitch and 5 MHz, 0.6 mm pitch linear array, is found out. The results are plotted in Figure 4.28 and 4.29 for 10 MHz and 5 MHz linear arrays, respectively

For 10 MHz, 0.3 mm pitch linear array, the results indicate that there is a sharp reduction in the size of the virtual source as the number of active elements is increased from 4 to 8. Beyond this,

although the size of the virtual source continues to decrease, the change is not so significant. For 5 MHz, 0.6 mm pitch linear array, the plot indicates that the active aperture of 6 to 8 elements gives a small virtual source size. Beyond this, there is no significant reduction. The 6 dB size of the virtual source using 10 MHz, 8 elements and 5 MHz, 6 elements is found to be 0.7 mm and 1.1 mm respectively.

Based on the above studies and observations, it can be concluded that an active aperture comprising of 8 to 10 elements using 10 MHz, 0.3 mm pitch linear array, and 6 to 8 elements using 5 MHz, 0.6 mm pitch linear array, is optimum for PA-SAFT technique.

The above study is valid for a case, when the sound beam is focused at a depth of 2 mm and the region of interest is from 10 mm to 50 mm from the scanning surface in steel or aluminum. For a depth lower than 10 mm, PA-SAFT technique may not be a good option, as SFLA or FMC+TFM techniques based on a single element excitation are expected to perform better. For depths beyond 50 mm, one may be required to create the virtual source deeper (instead of 2 mm from the surface). In such a case, the optimum number of active elements to be used during PA-SAFT technique will differ from the numbers mentioned above.

4.4.2.4 Validation of the optimization studies

In order to validate the above, experiments are carried out on an aluminum block containing 0.5 mm diameter side drilled holes (simulating a point reflector) located at a depth of 5 mm to 40 mm from the scanning surface. Data is acquired for all the holes using 10 MHz, 0.3 mm pitch and 5 MHz, 0.6 mm pitch linear array for different active apertures. For each case, the sound beam is focused at a depth of 2 mm from the scanning surface. The raw data is then processed by SAFT.

From the processed data, the 6 dB size of the signal from the side drilled hole is found out. This size is considered as the focal spot size, small size indicating sharp focusing.

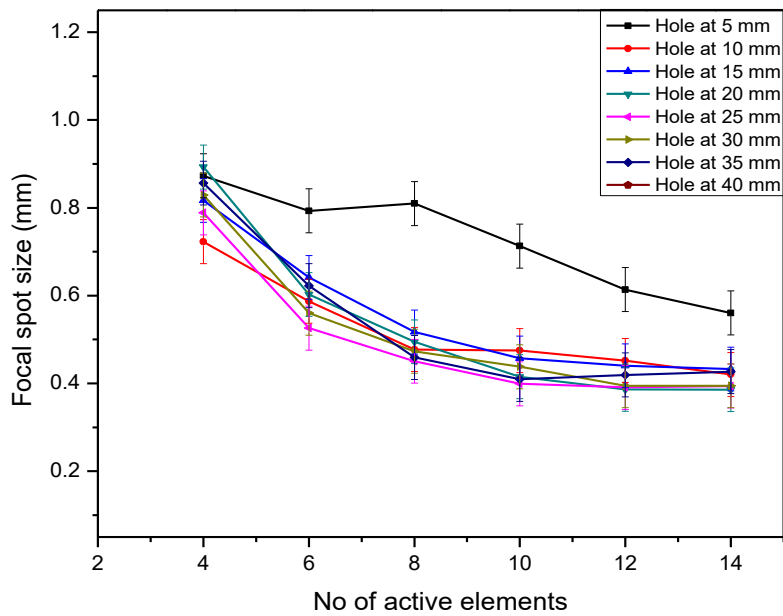


Figure 4.30: Variation in the focal spot size for various active apertures using 10 MHz, 0.3 mm pitch linear array using PA-SAFT technique

The results for 10 MHz, 0.3 mm pitch linear array for various active apertures are plotted in Figure 4.30.

The results indicate the following:

- Focusing is rather poor for the hole at the depth of 5 mm for all the apertures. This is because of the fact that the beam width at this depth is very small and as a result there are lesser number of A-scans with useful data for SAFT processing.
- With 4 active elements, the focal spot size is in the range of 0.7 to 0.9 mm.
- With 6 active elements, there is reduction in the focal spot size as compared to 4 active elements for all the depths

- With 8 and 10 active elements, the focal spot size is in the range of 0.46 mm to 0.6 mm, which can be treated as a very fine focusing.
- With 12 and 14 active apertures, there is slight drop in focal spot size but not very significant
- The reduction in focal spot size with increase in the aperture can be attributed to the increase in the sound beam divergence, which helps in effective SAFT processing

The above results indicate that in the depth range of 10 mm to 40 mm, while using 10 MHz, 0.3 mm pitch linear array, with focusing at 2 mm depth, an aperture comprising of 8 to 10 active elements is optimum.

The results for 5 MHz, 0.6 mm pitch linear array for various active apertures are plotted in Figure 4.31.

The results indicate the following:

- As with 10 MHz, the hole at 5 mm shows large focal spot size for all the apertures indicating that the sound beam focusing at this depth is not effective using PA-SAFT technique.
- For all the other depths, with 3 and 4 active elements, the focal spot size is in the range of 1.5 to 1.8 mm, which is rather coarse.
- With 6 and 8 active elements, there is significant drop in the focal spot size (1.1 mm to 1.6 mm) for all the depths

- With 10 and 12 active elements, the focal spot size remains more or less similar to the one observed for 8 active elements
- In general, the focal spot size for 5 MHz is observed to be higher than the one for 10 MHz, for similar number of active elements (or for similar λ/D , where λ is wavelength and D is the aperture size in mm). This can be attributed to the lower size of the virtual source using 10 MHz as compared to 5 MHz.

The above results also indicate that in the depth range of 10 mm to 40 mm, while using 5 MHz, 0.6 mm pitch linear array with focusing at 2 mm depth, an aperture comprising of 6 to 8 active elements is optimum.

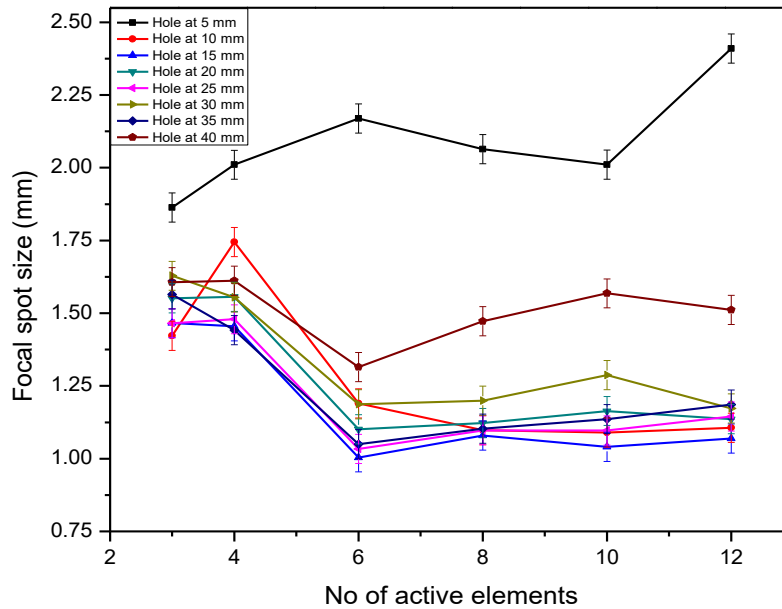


Figure 4.31: Variation in focal spot size with various active apertures using 5 MHz, 0.6 mm pitch linear array using PA-SAFT technique

4.4.3 Effect of Frequency

The simulation studies as well as the experimental validation for the optimization of active aperture for the application of PA-SAFT technique is carried out for two different frequencies: 10 MHz (0.3 mm pitch) and 5 MHz (0.6 mm pitch). One of the significant observations while determining the size of the virtual source using these frequencies (Figures 4.24 and Figure 4.25) is that for the same aperture size (number of elements x pitch), the size of the virtual source using 10 MHz is lower than that of 5 MHz. For example, with 12 active elements using 10 MHz 0.3 mm pitch (active aperture = 3.6 mm), the 6 dB size of the virtual source at 2 mm depth is 0.56 mm. For the same aperture size using 5 MHz, 0.6 mm pitch linear array (6 active elements = 3.6 mm), the 6 dB size of the virtual source at 2 mm depth is 1.12 mm.

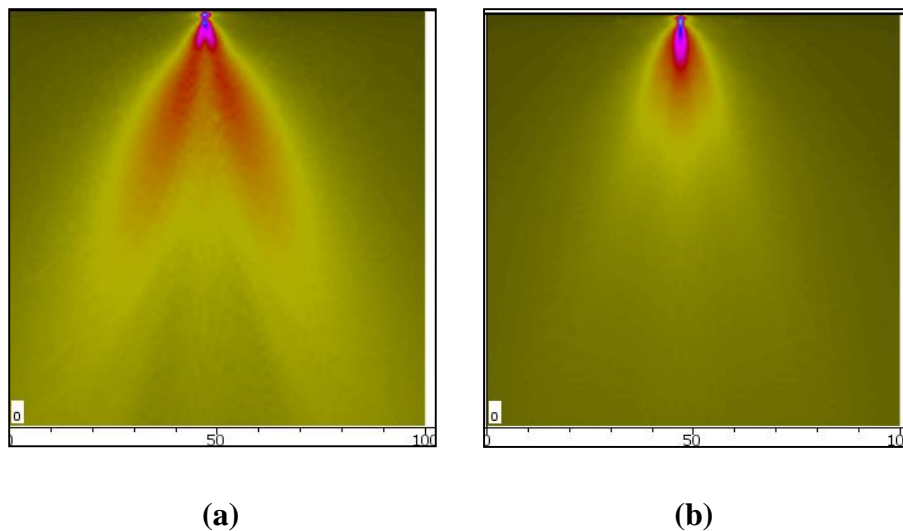


Figure 4.32: Beam computation results for an aperture size of 3.6 mm with focusing at 2 mm using (a) 10 MHz, 0.3 mm pitch linear array with 12 active elements and (b) 5 MHz, 0.6 mm pitch linear array with 6 active elements (Simulation)

Figure 4.32 shows the beam computation results for the above two cases using 10 MHz, 0.3 mm pitch and 5 MHz, 0.6 mm pitch linear array. The beam computation results show that, with 10

MHz linear array the beam divergence beyond the focal point is approximately 33 deg. as compared to 28 deg. for 5 MHz linear array. The higher beam spread using 10 MHz can be attributed to the smaller size of the virtual source.

During the simulation and experimental study to arrive at the active aperture size for PA-SAFT technique, it is concluded that an active aperture comprising of 8 elements using 10 MHz, 0.3 mm pitch and 6 elements using 5 MHz, 0.6 mm pitch linear array, is optimum. Figure 4.33 shows the variation in 6 dB beam width (focal spot size) using 10 MHz and 5 MHz linear array using 8 elements and 6 elements active apertures respectively. These values have been found out experimentally as described in Section 4.4.2.

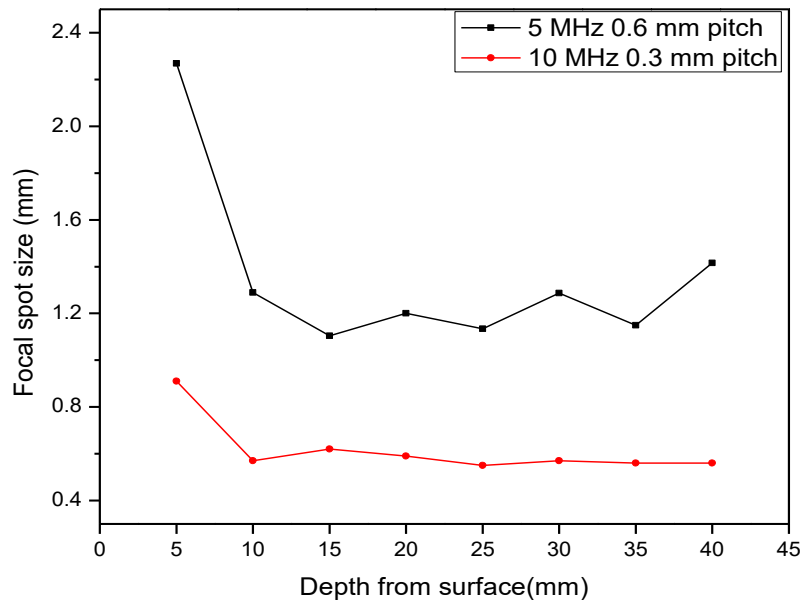


Figure 4.33: Variation in the focal spot size with depth using PA-SAFT technique for 10 MHz, 0.3 mm pitch and 5 MHz, 0.6 mm pitch linear arrays

The results indicate that with both the frequencies, the sound beam focusing up to 5 mm depth is not effective. The 10 MHz linear array shows lower focal spot size as compared to the 5 MHz linear array, which can be attributed to the smaller virtual source using 10 MHz.

There is a similarity between the results obtained by SFLA and PA-SAFT techniques. With SFLA technique, it is observed that the best focusing is obtained when the aperture size (or the source size) is smallest. With PA-SAFT too, it is observed that the size of the virtual source decides the focal spot size. Experimental studies using SFLA technique also indicated that higher frequency results in sharp focusing, which is found to be applicable to PA-SAFT technique also.

4.5 Angle Beam PA-SAFT technique

4.5.1 Methodology

The sound beam focusing by FMC + TFM and normal beam PA-SAFT (NB PA-SAFT) techniques are useful for precisely locating the extremities of planar or crack-like flaws, from which the depth or the through-wall dimension of a flaw can be estimated. This information is useful for taking decision on the acceptance of a flawed component as part of pre-service qualification and also in carrying out fitness-for-service assessment. While using the above techniques, it is important that the linear array is placed symmetrically above the flaw region in such a manner that some elements of the array are on one side of the flaw and the remaining ones are on the other. By doing this, one can ensure that the divergent sound beam emanating from majority of the elements or apertures interact with the flaw and a well divergent signal is obtained from the flaw extremities in the raw B-scan image. This ensures effective processing by SAFT or TFM, which ultimately leads to sharp focusing effect and a high precision in locating the flaw extremities.

While the above condition of placing the linear array above the flaw region can be satisfied in a majority of the cases, there can be few applications in real-life, where this condition is difficult to achieve. A classic example is the weld joint in a plate, pipe or vessel, with an unground weld bead. In such cases, the application of NB PA-SAFT and FMC may pose a problem. Since the linear

array cannot be placed across the weld bead due to very rough surface, the best that one can achieve is to place it in such a way that one end of the array touches the edge of the weld bead. This is schematically shown in Figure 4.34 where a linear array is placed with its edge touching the weld bead for detection of a crack in the weld joint. With this placement, if one uses FMC or NB PA-SAFT technique, then the raw B-scan image will contain useful information from the flaw only from those elements or apertures, which are very near to the edge of the weld bead. The sound beam emanating from majority of the remaining elements (or apertures) will have no interaction with the flaw, since they are placed far away. As a result, the signals from the flaw in the raw B-scan image will have a limited spread and the post processing to achieve sound beam focusing by SAFT or TFM will not be effective. In extreme cases, depending on the thickness of the weld joint, the location of the flaw across the thickness and the width of the weld bead, it may not be possible to get any signal from the flaw, since all the elements of the linear array are significantly away from the flaw for the sound beam to have any interaction. In such cases, the flaw may go undetected.

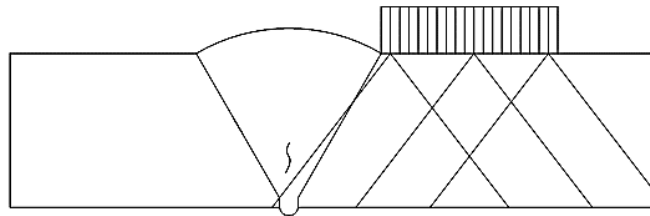


Figure 4.34: Limitation of SFLA, PA-SAFT and FMC techniques for characterization of flaws in the weld joint with an un-ground weld bead

One way of overcoming the above limitation is to place the linear array on the wedge so that there is an increase in the angle of the transmitted sound beam in the material. This is schematically shown in Figure 4.35. With this approach, one can ensure that the sound beam emanating from some elements or apertures interacts with the flaw extremities. A major drawback of this approach

is that there is an additional travel of the sound beam in the wedge. With FMC technique, where a single element is used for sound beam transmission, the attenuation in the wedge limits the useful penetration of sound in the material and adversely affects the sensitivity.

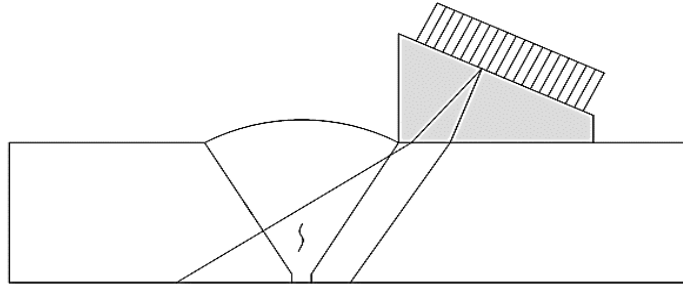


Figure 4.35: Placement of linear array on the wedge to generate angle beam

Another way of generating a divergent angle beam without mounting the linear array on to the wedge is by use of a focal law. A group of elements (active aperture) are excited in a sequential manner with the calculated time delay to steer the sound beam by the required angle. The steering angle would depend on how far the flaw is located from the array. Depending on the aperture size or the number of elements in an aperture, it is possible to obtain a divergent sound beam in the region of interest. The selected aperture is then moved electronically to acquire the B-scan image. If the transmitted sound beam has adequate divergence the raw B-scan data thus acquired will have well spread-out signals from the flaw extremities. This helps to achieve fine focusing during SAFT processing, thereby precisely locating the flaw tips for accurate depth assessment. This forms the basis of Angle Beam PA-SAFT (AB PA-SAFT) technique. The process of data acquisition is schematically shown in Figure 4.36.

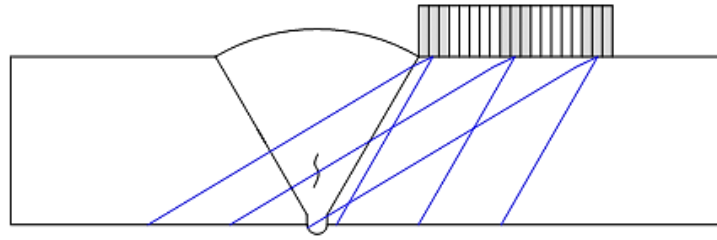


Figure 4.36: Methodology for data acquisition by angle beam PA-SAFT

While dealing with the weld joint having an unground weld bead, if the flaw to be detected is at the back surface or in the lower region of the weld joint, then the raw B-scan image is acquired in the first leg ($1/2 V$ path) by keeping the linear array close to the weld joint. This is schematically shown in Figure 4.37 (a). If the flaw to be detected is on the scanning surface or in the upper region of the weld joint, then the B-scan is acquired up to the second leg ($1 V$ path) by placing the linear array slightly away from the weld joint. This is schematically shown in Figure 4.37 (b).

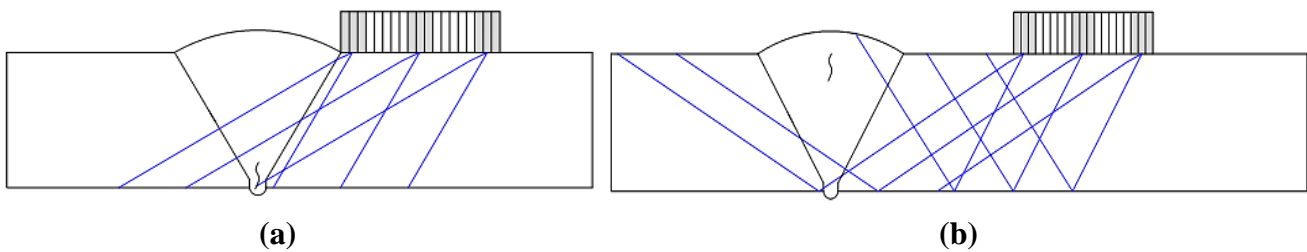


Figure 4.37: Data acquisition by AB PA-SAFT technique (a) flaw near the back surface and (b) flaw near the scanning surface

4.5.2 Optimization of active aperture size for data acquisition

One of the crucial steps in the application of AB PA-SAFT technique is the selection of number of elements in an active aperture. This in turn decides the divergence of the sound beam and the wave amplitude in the region of interest. Wooh et. al [127-129] analyzed in details the effect of array parameters viz. the number of elements in an active aperture and the element pitch, on the

beam directivity as a function of beam steering angle. It was shown that when the sound beam is steered using focal laws, then in addition to the main lobe and low amplitude side lobes, there exists an additional lobe called as grating lobe. Grating lobes are undesirable since they produce unwanted signals and also take away significant amount of the available acoustic energy emanating from the elements of the linear array. With the conventional phased array technique based on focal law, it is desirable to have a good directivity of the sound beam being transmitted in the given direction. One way of quantifying the directivity of the sound beam is the width of the main lobe. The sound beam is said to have a good directivity if the width of the main lobe is very small. The directivity of the transmitted sound beam deteriorates with an increase in the steering angle. For a given linear array and the required steering angle, the directivity of the sound beam can be improved (with the consequent reduction in the amplitude of the grating lobe) by increasing the number of elements in an active aperture.

During the application of AB PA-SAFT technique, it is required that the acoustic power in the region of interest should be as high as possible and the grating lobe amplitude should be as low as possible. This would ensure that the maximum amount of acoustic energy is directed towards the flaw extremities. At the same time, it is also required that the sound beam divergence in the region of interest should be as high as possible. This would ensure that the raw B-scan image will contain a well spread out signal from the flaw extremities so that effective sound beam focusing can be achieved during SAFT processing. This requirement implies that the main lobe width should be as high as possible. The requirement of high acoustic power in the intended region and the low grating lobe amplitude can be achieved by using a large number of elements in an active aperture as the available hardware permits. However, with this approach the beam divergence angle will be very small since the width of main lobe reduces with an increase in the number of elements. If one uses

lesser number of elements in an active aperture, the beam divergence will be very high as a result of poor sound beam directivity. But at the same time, the acoustic power in the region of interest will be very low, primarily because of lesser number of elements for sound beam transmission and also because of an increase in the amplitude of the grating lobe. Hence there is an optimum number of elements that should be used in an active aperture during data acquisition by AB PA-SAFT technique.

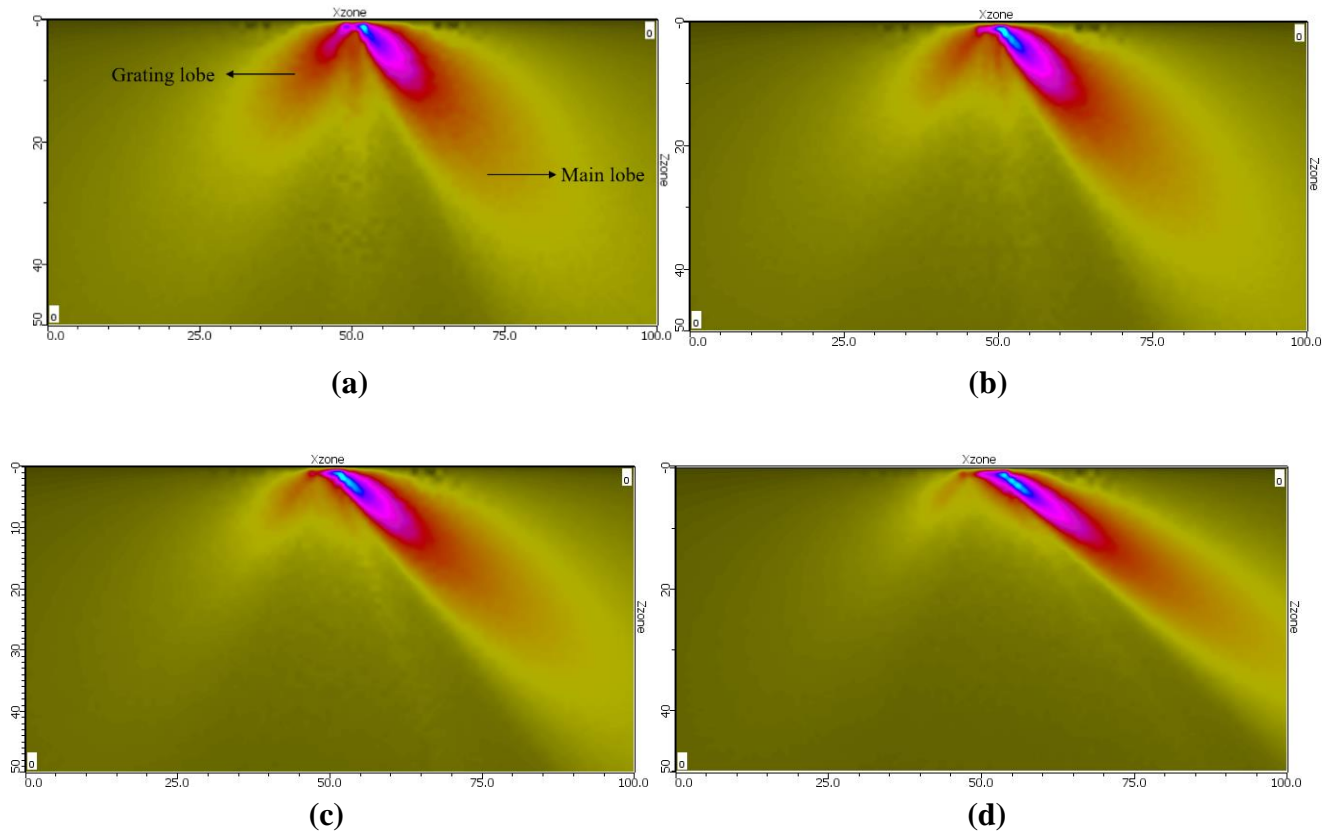


Figure 4.38: Sound beam computation results using 5 MHz, 0.6 mm pitch linear array with sound beam steered at 60 deg. for an active aperture comprising of (a) 3 elements (b) 4 elements (c) 6 elements and (d) 10 elements (Simulation)

In order to visualize the effect of aperture size on the sound beam directivity and the amplitude of grating lobe, sound beam computation studies are carried out using CIVA 11 for 5 MHz 0.6 mm

pitch linear array. Figure 4.38 shows the results of sound beam computation for five different apertures: (i) 3 elements, (ii) 4 elements, (iii) 6 elements, and (iv) 10 elements. In each case, the sound beam is steered by 60 deg. using focal laws.

The results indicate that with 3 active elements, the width of the main lobe is very high but there is also a very strong grating lobe. As the number of active elements increases, there is reduction in the amplitude of the grating lobe as well as the width of the main lobe. From the beam computation results, two parameters have been found out: (i) the half beam spread angle and (ii) how much dB lower is the amplitude of the grating lobe with respect to the maximum sound wave amplitude in the main lobe. It is desirable to have a high value for both these parameters.

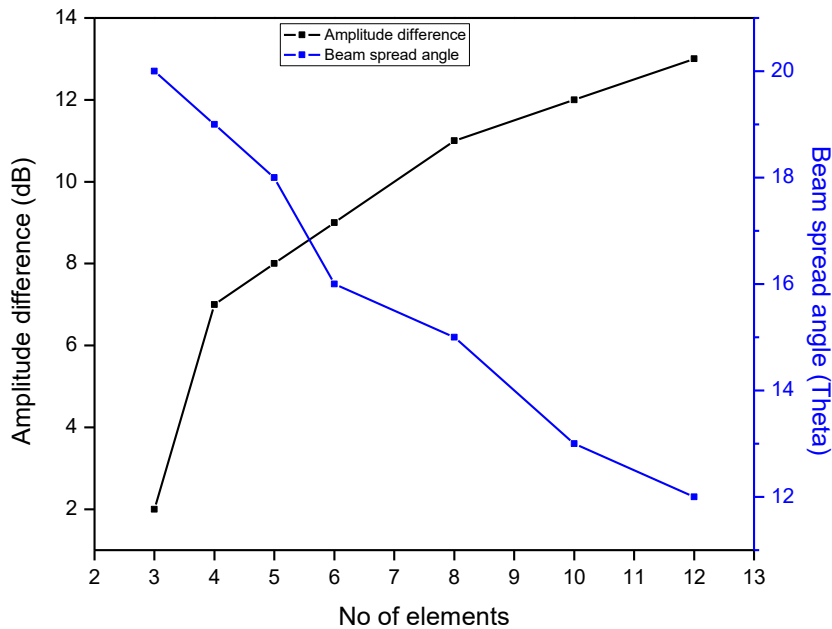


Figure 4.39: Variation in the beam spread angle and the grating lobe amplitude with number of elements in an active aperture using 5 MHz, 0.6 mm pitch linear array (Simulation)

Figure 4.39 shows the variation in the half beam spread angle and the amplitude of the grating lobe in terms of dB with respect to the maximum sound wave amplitude. The results indicate that with an active aperture of 3 elements, the sound beam divergence angle is fairly high at approximately 20 deg., but the grating lobe amplitude is just 2 dB lower than the maximum. With 12 active elements, the grating lobe amplitude is almost 13 dB lower than the maximum, but the sound beam divergence angle has reduced to approximately 12 deg. With 6 active elements, one gets a reasonable beam divergence angle of approximately 16 deg. and at the same time the grating lobe amplitude is also significantly lower (approximately 8 dB than the maximum). Based on these results an active aperture comprising of 6 elements is chosen as an optimum value for data acquisition by AB PA-SAFT technique while using 5 MHz, 0.6 mm pitch linear array.

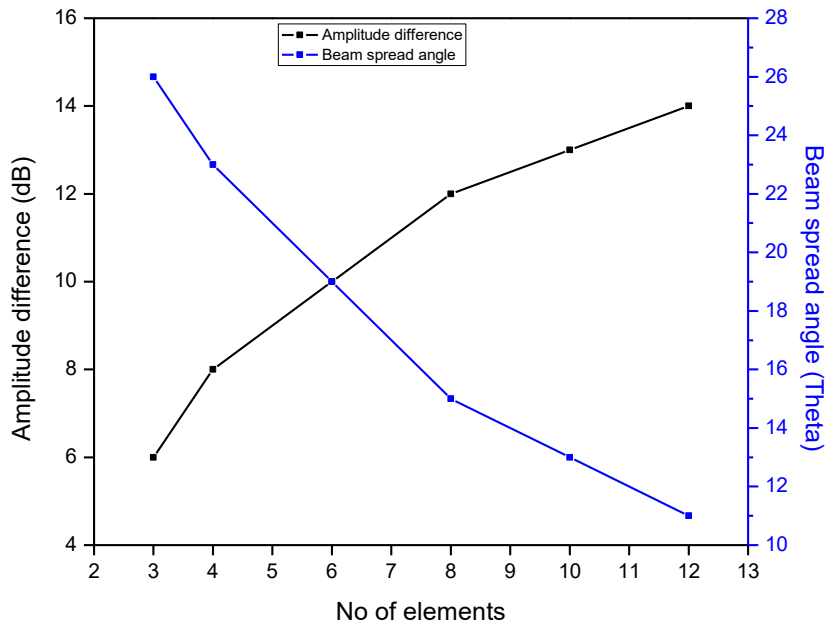


Figure 4.40: Variation in the beam spread angle and the grating lobe amplitude with number of elements in an active aperture using 10 MHz 0.3 mm pitch linear array (Simulation)

A similar exercise is carried out for 10 MHz, 0.3 mm pitch linear array. The plot of variation in the half beam spread angle and the amplitude of grating lobe with the number of active elements in an aperture is shown in Figure 4.40. In this case too, the sound beam is steered by an angle of 60 deg. using focal laws. The results indicate that an active aperture comprising of 6 elements is optimum for data acquisition by AB PA-SAFT technique.

In order to assess the effectiveness of AB PA-SAFT technique for sound beam focusing, data is acquired on a 0.5 mm dia. side drilled hole, located distance of 25 mm from the scanning surface, in an aluminum block. A 10 MHz, 0.3 mm pitch linear array is used. Figure 4.41 shows the experimental set-up. The linear array is not placed over the hole, but laterally shifted so that the hole is detected by a divergent angle beam.

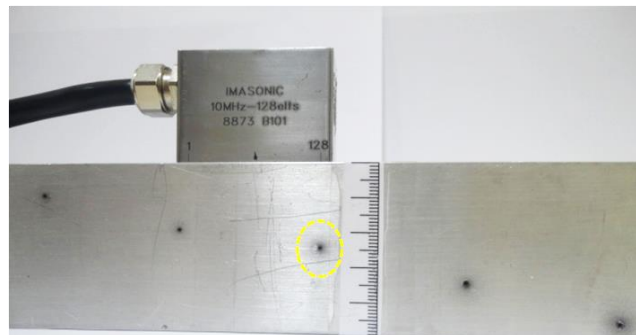


Figure 4.41: Experimental set-up for data acquisition on a 0.5 mm dia. side drilled hole in an aluminum block using Angle Beam PA-SAFT

The raw B-scan and the SAFT processed B-scan images are shown in Figures 4.42 (a) and (b) respectively. The raw B-scan image shows the divergent signal from the side drilled hole at the expected depth. During SAFT processing, the divergent signal from the hole is reduced to a point. The 6 dB size of the hole in the lateral direction in the processed image is found to be approximately 0.5 mm, which indicates that Angle Beam PA-SAFT can achieve sharp focusing

like SFLA and normal beam PA-SAFT techniques. Unlike SFLA and normal beam PA-SAFT, where the hole signal has a uniform spread in lateral and depth directions, with angle beam PA-SAFT, the signal spread in the lateral direction is considerably lesser as compared to the spread in the depth direction. Also, the hole is imaged in the direction, which is perpendicular to the direction of primary incident sound beam. Because of this characteristics, the angle beam PA-SAFT is expected to give very good lateral resolution.

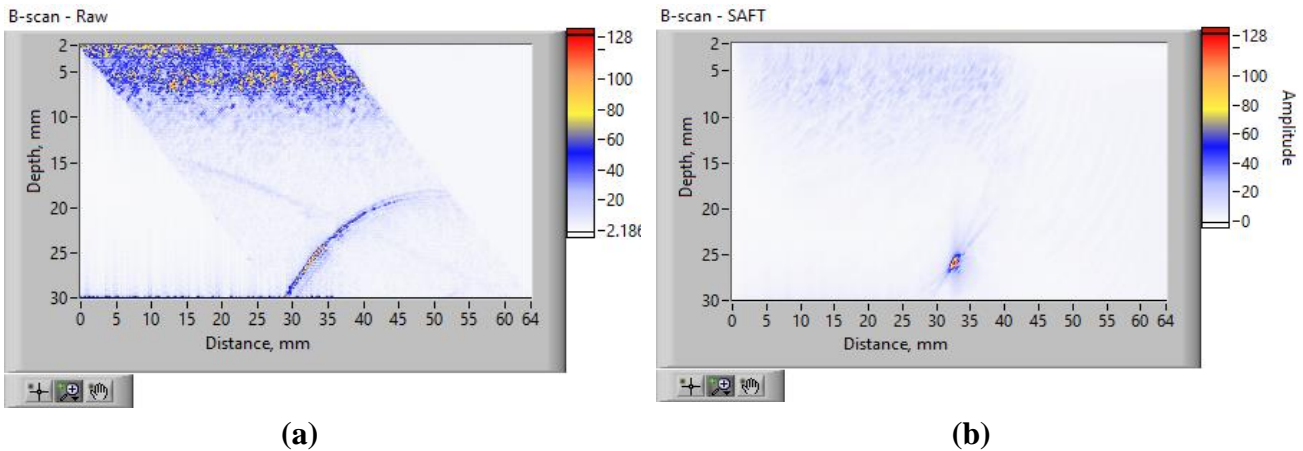


Figure 4.42: (a) Raw and (b) SAFT processed B-scan images of a 0.5 mm dia. side drilled hole in an aluminum block using angle beam PA-SAFT technique

SFLA and PA-SAFT techniques are used to characterize the flaws that are present within the thickness of the material, including the ones which are opening to the back surface. If the flaw is open to the scanning surface or very close to it, then its characterization in terms of depth using these techniques would be difficult. This is because of the fact that there would be a dead zone (depending on the linear array), which would mask the signal from the flaw-tip. Moreover, since the beam divergence near the scanning surface would be less, the spread of signal from the flaw in the raw B-scan image would be limited, because of which the focusing during SAFT would not be effective. With Angle Beam PA-SAFT, this limitation does not exist, as the linear array is kept

away from the flaw and not directly over it. When the flaw is not present very close to the scanning surface and both the extremities can be seen by the ‘direct’ divergent angle beam, then the data is acquired up to $\frac{1}{2}$ V-path. When the flaw is present on the scanning surface or just below it, the data is acquired by the sound beam after bouncing up to full V-path. By doing this, not only the problem of dead zone is overcome, but because of the higher beam path, large beam divergence is achieved at the flaw location.

Since the angle beam PA-SAFT technique is based on the use of a group of elements for sound beam transmission, the acoustic power within the material is going to be considerably higher than SFLA and FMC techniques. As a result, it is expected to perform better than these techniques while dealing with thick and attenuating materials.

4.6 Comparison of sound beam focusing using SFLA, PA-SAFT and FMC techniques

The focal spot size achieved by SFLA and PA-SAFT techniques is compared with the one obtained by FMC + TFM technique for a depth range of 5 mm to 40 mm in aluminum. The comparison is made using 10 MHz, 0.3 mm pitch, 128 elements and 5 MHz, 0.6 mm pitch, 64 elements linear arrays. Figure 4.43 shows the results for 10 MHz.

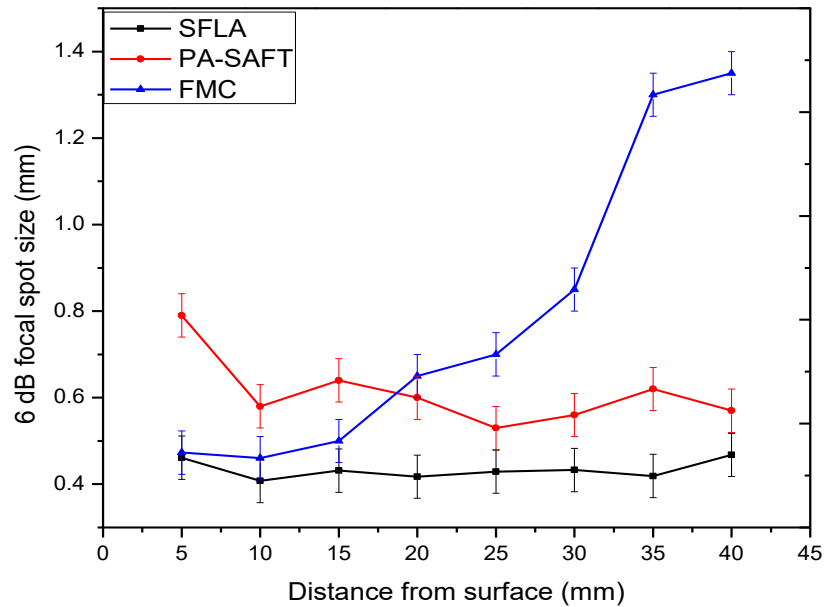


Figure 4.43: Variation in focal spot size with depth by SFLA, PA-SAFT and FMC+TFM techniques using 10 MHz, 0.3 mm pitch linear array

The results indicate the following:

- With SFLA technique, the focal spot size is very fine and is smaller than the one achieved using PA-SAFT technique for all the depths
- With FMC technique, the focal spot size is smaller for shallower depth and increases as one goes deeper than 25 mm.
- The better focusing at larger depth using SFLA when compared to FMC + TFM technique could be attributed to the fact that with SFLA all the 128 elements, hence the larger total effective aperture of an array could be used for data acquisition. Due to the limitation on the total number of parallel receiver channels with the available phased array instrument, only 64 of the total 128 elements could be used with FMC+TFM technique. As a result of lower TEA, the focusing at higher depth is expected to be inferior.

Similar exercise is carried out using 5 MHz, 0.6 mm pitch, 64 elements linear array. In this case, the experimental conditions are identical for all the three techniques, including the TEA for data acquisition. Figure 4.44 shows the variation in focal spot size with depth for SFLA, PA-SAFT and FMC+TFM techniques.

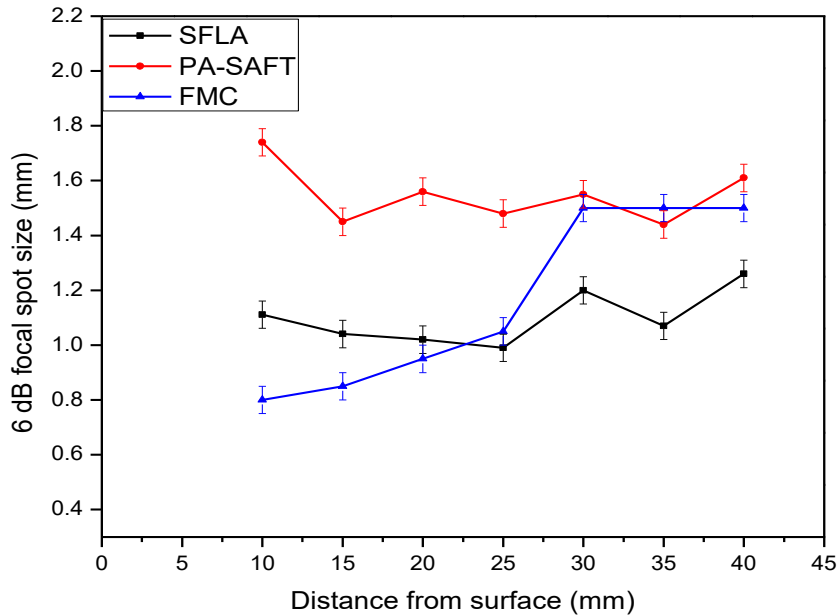


Figure 4.44: Variation in focal spot size with depth by SFLA, PA-SAFT and FMC+TFM techniques using 5 MHz, 0.6 mm pitch linear array

The results indicate the following:

- For shallower depth (< 20 mm), the focal spot size achieved by FMC is better than the one achieved by SFLA technique.
- At a depth of 30 mm or more, SFLA technique gives smaller focal spot size than FMC.
- The focal spot size by PA-SAFT technique is found to be more than SFLA for all the depths.

From the above results it can be concluded that although SFLA technique does not acquire the full matrix data, the focal spot size up to a depth of 25 mm in aluminum or steel is comparable

to the one obtained by FMC + TFM. In fact, the need of parallel receiver channels with FMC for the purpose of faster data acquisition, necessitates using an array with lesser number of elements. This has an adverse effect on achieving satisfactory focusing at higher depth and so limits the usefulness of FMC + TFM technique to shallower depths. Since no such limitation exists with SFLA technique, a very fine focal spot could be achieved using this technique for a depth range, which is beyond the useful range of FMC + TFM technique. The PA-SAFT technique gives a coarser focal spot size than SFLA technique under identical test conditions. Hence, it should be employed only under the circumstances, where the sensitivity or the penetration requirements cannot be met by SFLA technique.

4.7 Summary of the chapter

- ✓ The sound beam divergence for a miniature piezoelectric element in a linear array is much smaller than the one predicted by the beam spread equation in the literature
- ✓ Based on the experimental work, the following empirical relationship to evaluate the half beam divergence angle has been derived for piezoelectric elements with small values of D/λ :

$$\sin \theta = 0.44 \left[0.6 + 0.5 \log \left(\frac{D}{\lambda} \right) \right] \cdot \frac{\lambda}{D}$$

- ✓ The empirical relationship can be used to find out the beam spread of the rectangular piezoelectric elements that are used in linear arrays.
- ✓ Two sound beam focusing techniques viz. SFLA and PA-SAFT have been investigated. The techniques are based on using a divergent sound beam emanating from a linear array to acquire the raw B-scan image, which is subsequently processed by SAFT algorithm to

achieve focusing. The SFLA technique uses a single element for sound beam transmission and reception, unlike FMC where the data is acquired for all the transmitter-receiver combinations. The PA-SAFT technique uses a group of elements for sound beam transmission and reception and is based on the concept of virtual array of sources.

- ✓ The effect of array based variables on sound beam focusing using SFLA technique is studied. It is observed that the focusing is affected by the aperture size, pitch, frequency of sound and total effect aperture. Smaller element size, lower pitch, higher frequency and higher TEA give improved focusing.
- ✓ The effect of SAFT based variables viz. the difference in the actual and the input value of sound velocity, element pitch and the beam divergence angle to the processing algorithm on the focusing achieved is studied. It is observed that a small variation in sound velocity and pitch with respect to the actual value greatly affects the focusing achieved. With the divergence angle, if the input value is smaller than the actual, then the focusing is inferior. Beyond the actual divergence angle, there is no significant improvement in the focusing with the higher input value.
- ✓ While using linear array for data acquisition, the size of the focal spot achieved by SAFT depends on the element size as well as the frequency
- ✓ The following empirical relationship has been derived to calculate the focal spot size while using SFLA technique for sound beam focusing.

$$\delta_{6dB} = \frac{0.6D}{[0.6 + 0.5 \log \left(\frac{D}{\lambda} \right)]}$$

- ✓ The active aperture for PA-SAFT technique using 10 MHz, 0.3 mm pitch and 5 MHz, 0.6 mm pitch linear array is optimized. It is observed that, for a depth range of 5 mm to 40 mm in aluminum and steel, the active aperture comprising of 6 elements using 5 MHz, 0.6 mm pitch and 8 elements using 10 MHz, 0.3 mm pitch linear array are optimum.
- ✓ As observed with SFLA technique, the focusing using PA-SAFT technique is better for higher frequency. This can be attributed to the smaller size of the virtual source while using higher frequency.
- ✓ Angle beam PA-SAFT technique has been standardized for specific cases, where SFLA, normal beam PA-SAFT and FMC techniques cannot be used. The sound beam focusing using angle beam PA-SAFT is found to be comparable to SFLA and normal beam PA-SAFT techniques.
- ✓ Under identical experimental conditions, the sound beam focusing using SFLA is found to be comparable to the one achieved by FMC + TFM technique for a depth up to 25 mm in aluminum. For higher depths, focusing by SFLA is found to be better. The focusing using PA-SAFT is found to be inferior to both, for shallow as well as higher depth. However, it does have an advantage over SFLA and FMC techniques, in terms of the sensitivity for the detection and characterization of flaws located deeper in the material or while dealing with attenuating materials.

5.1 Introduction

One of the major objectives of this research work is to explore the possibility of SFLA and PA-SAFT techniques for detection and characterization of flaws. This aspect is studied by extensive experimental work on two broad categories of flaws viz. volumetric and planar. The volumetric flaws are simulated by side drilled holes in carbon steel and aluminum samples while the planar flaws are simulated by EDM slots in stainless steel plates. The results obtained by SFLA and PA-SAFT techniques are compared with the ones obtained by conventional phased array using focal laws and FMC + TFM technique. The results of the experimental work carried on these samples, their analysis and the quantitative evaluation of the capabilities of SFLA and PA-SAFT techniques for detection and characterization of volumetric and planar flaws are discussed in this Chapter.

5.2 Volumetric Flaws

The study for the evaluation of the capability of SFLA and PA-SAFT techniques for the detection and characterization of volumetric flaws is carried out to address two specific issues: (i) determine the sensitivity of SFLA and PA-SAFT techniques for detection of volumetric flaws and (ii) determine the focusing ability of SFLA and PA-SAFT techniques laterally and across the depth in a given material so that the two closely spaced volumetric flaws are resolved from each other.

The sensitivity for detection of a volumetric flaw in a given material and with a given test set-up (transducer, instrument, cable etc.) by ultrasonic testing depends on two factors viz. the size of the flaw and the depth at which it is located from the scanning surface. The inspection set-up is

considered to be sensitive if a smaller flaw is detected at a larger depth. Both these factors are combined in to a parameter called Size to Distance Ratio (SDR). For example, a 1 mm dia. flaw at a distance of 100 mm from the scanning surface has a SDR of 0.01. In the present study, the sensitivity is assessed in terms of the smallest SDR flaw that is detected reliably by SFLA and PA-SAFT techniques. Smaller SDR corresponds to better sensitivity. Another factor that is considered while assessing the sensitivity is the Gain Reserve (GR) of the phased array instrumentation. This is found out by subtracting the value of amplifier gain required during the acquisition of raw B-scan data from the total amplifier gain available in the instrument. For example, if an amplifier gain of 70 dB is required for data acquisition and the total gain available in the instrument is 86 dB, then the GR is 16 dB. Higher value of GR corresponds to better sensitivity and better signal to noise ratio in the processed data.

The focusing ability is determined from the 6 dB spread of the signals in the processed B-scan images. A lower value of this parameter is an indication of good focusing, which is essential to resolve two closely spaced volumetric flaws.

The experimental data is acquired on four samples: (i) carbon steel sample with 1 mm dia. side drilled holes located one below the other at different depths, (ii) aluminum sample with 0.5 mm side drilled holes located at a much larger depth (up to 200 mm), (iii) aluminum sample with side drilled holes at the same depth but separated laterally and (iv) carbon steel sample with side drilled hole at the same depth and located very close-by. From the results obtained from the first sample, the sensitivity for flaw detection as well as the focusing ability across the depth is assessed for SFLA and PA-SAFT techniques. From the results of the second sample, the limit of sensitivity that can be achieved using these techniques is found out in terms of SDR and GR. The results from the third sample are used to evaluate the lateral coverage that can be obtained by SFLA and PA-

SAFT techniques. While the results from the fourth sample are used to arrive at the limit of resolution for volumetric flaws that can be achieved by SFLA and PA-SAFT techniques. The data from these four samples are acquired using 10 MHz, 0.3 mm pitch, 128 elements linear array. The attenuation in these samples is found to be negligible at this frequency.

5.2.1 Assess the sensitivity and focusing ability for detection of volumetric flaws

The sensitivity for detection of volumetric flaws and the ability of the inspection technique to produce the focused image of the flaw is assessed on carbon steel sample of 50 mm thickness. The sample has 1 mm dia. side drilled holes located at various distances from 10 mm to 45 mm from the scanning surface. This corresponds to the SDR values of 0.1 to 0.022. Figure 5.1(a) shows the experimental set-up for data acquisition using SFLA, PA-SAFT and FMC techniques. Figure 5.1(b) shows the experimental set-up for data acquisition using conventional phased array where the transducer is placed not directly over the holes, but laterally shifted to facilitate the detection of all the holes by a focused angle beam. Experimental details are given in Chapter 3 Section 3.6.1.



Figure 5.1: Experimental set-up for detection and characterization of vertically stacked holes in carbon steel sample (a) SFLA, PA-SAFT and FMC techniques (b) Conventional angle beam phased array using focal laws (Scale in mm)

5.2.1.1 Conventional angle beam phased array using focal laws

The sector scan (S-scan) images obtained by using focal laws corresponding to multi-point focusing for 16, 32, 48 and 64 active elements are shown in Figures 5.2(a) to (d) respectively.

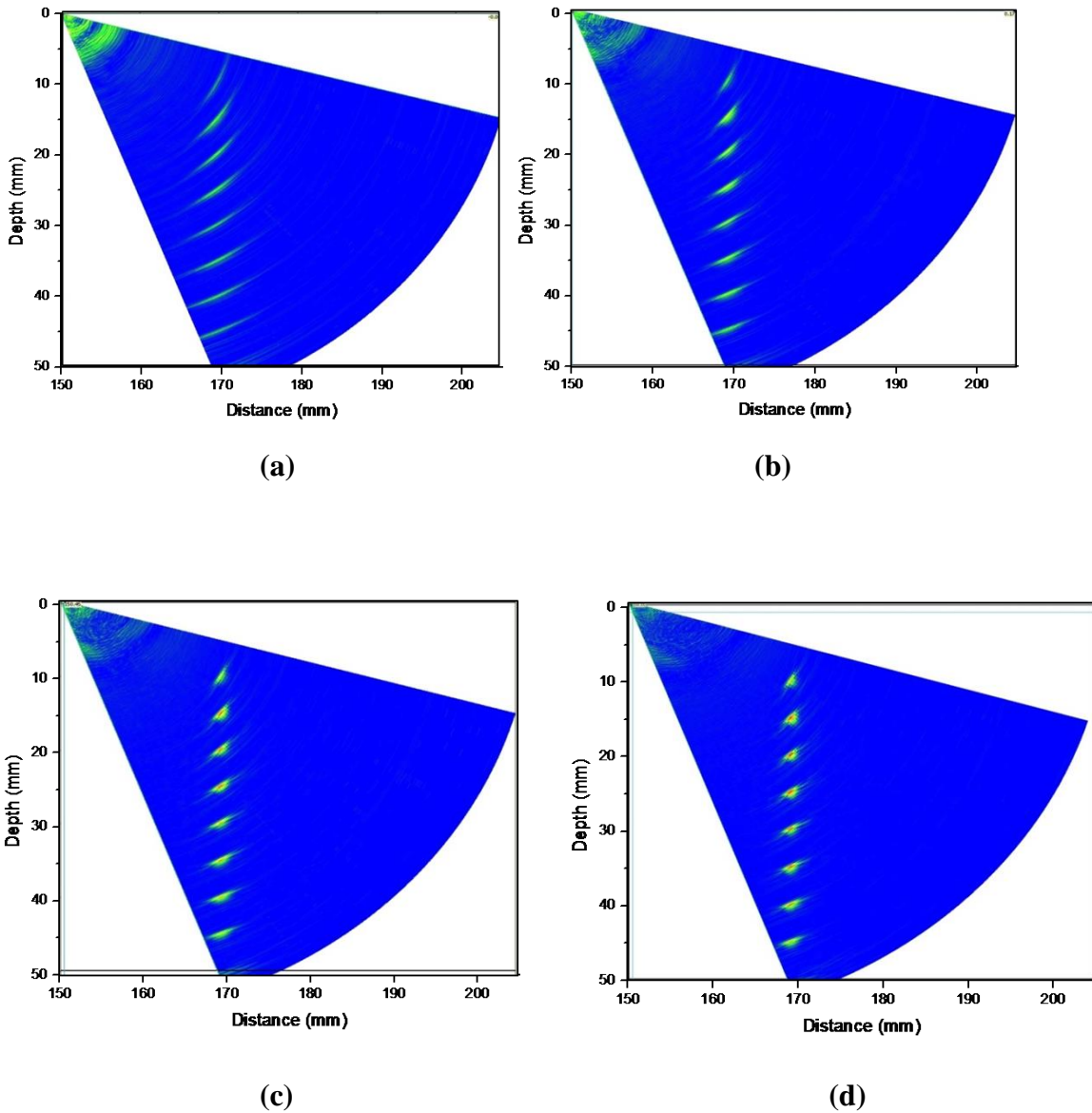


Figure 5.2: Sector scan images using (a) 16 (b) 32 (c) 48 and (d) 64 active elements for a carbon steel block with vertically stacked side drilled holes

The following observations can be made from the above images:

- All the eight holes in the sample are detected by apertures comprising of 16 to 64 active elements with an acceptable signal to noise ratio
- The spread in the signals from the holes, which is a measure of focal spot size, reduces as the active aperture size increases from 16 elements to 64 elements
- The amplitudes of the signals from the holes are not significantly different from each other for all the apertures

Table 5.1 gives the results in terms of sensitivity, amplitude variation and lateral spread.

Table 5.1: Results on carbon steel sample with vertically stacked holes using conventional angle beam phased array technique

Sr. No.	Active aperture	Sensitivity		Amplitude variation (dB)	6 dB spread (mm)	
		SDR	GR (dB)		Min.	Max.
1	16 el	0.022	17	6.2	5.3	7.2
2	32 el	0.022	17	4.8	2.9	4.0
3	48 el	0.022	17	3.6	1.6	2.5
4	64 el	0.022	23	3.8	1.6	1.8

The following conclusions can be drawn from the Table 5.1:

- The SDR of 0.022 at GR of 17 in carbon steel could be obtained by using focal law based phased array examination using active aperture comprising of 16 to 48 active elements. With 64 active elements the same SDR is achieved with higher GR value, indicating better sensitivity
- The amplitude variation between the signals from the side drilled holes reduces as one

moves from an aperture of 16 to 48 active elements. With further increase (64 elements) there is no significant change in the amplitude variation.

- The 6 dB spread of the signals using active apertures comprising of 16 elements is not satisfactory. With this aperture, the near field length is 10 mm, which means that none of the holes are seen by the focused sound beam as they lie beyond the near field. As one goes deeper, the sound beam divergence increases and hence there is an increase in the 6 dB spread of signals.
- With 32 active elements, the near field length is approximately 40 mm. This means that the holes closer to the scanning surface are seen by the focused sound beam and hence there is a reduction in the 6 dB spread of the signals.
- With 48 and 64 active elements, there is further increase in the near field and all the holes are seen by the focused sound beam. This is reflected in the lower 6 dB spread of the signals.
- The lower bound value of 6 dB spread is similar using 48 and 64 active elements, but there is a significant reduction in the upper bound value using 64 active elements. The lower bound value corresponds to the focal spot size up to the mid-thickness of the sample, while the upper bound value is for the region, which lies towards the back surface. With increased aperture, the near field length is large and hence one can achieve smaller focal spot size at higher depths.
- Based on the above results, it can be concluded that to achieve the focal spot size of less than 2 mm across the depth range of 10 mm to 45 mm in carbon steel, one will have to use 64 active elements of 10 MHz, 0.3 mm pitch linear array using focal law based phased array examination

5.2.1.2 SFLA Technique

Figures 5.3 (a) and (b) show the raw B-scan images acquired using the SFLA technique. The data is acquired at two gain levels: lower gain, corresponding to the one used for data acquisition using PA-SAFT technique and higher gain, to facilitate the detection of the bottommost hole.

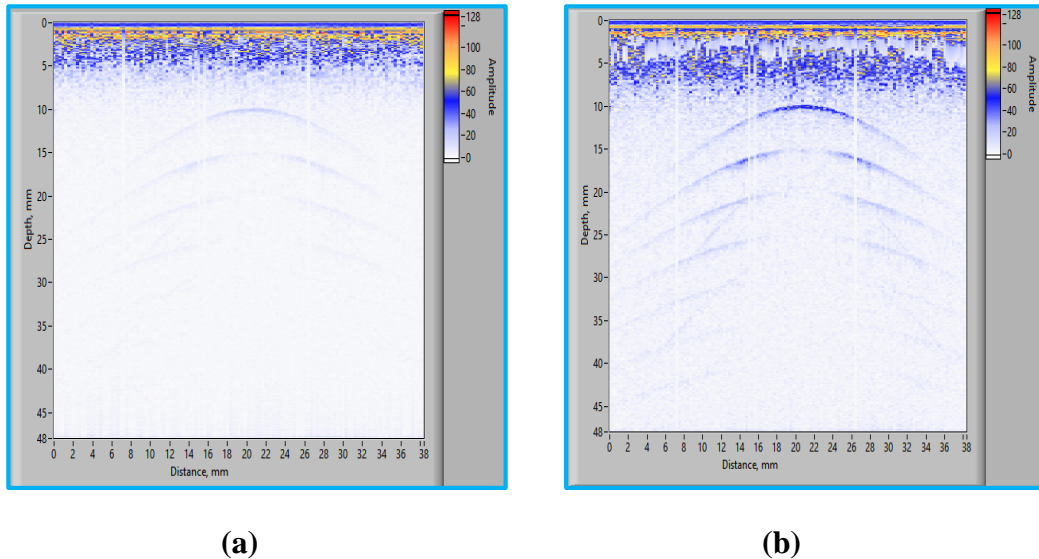
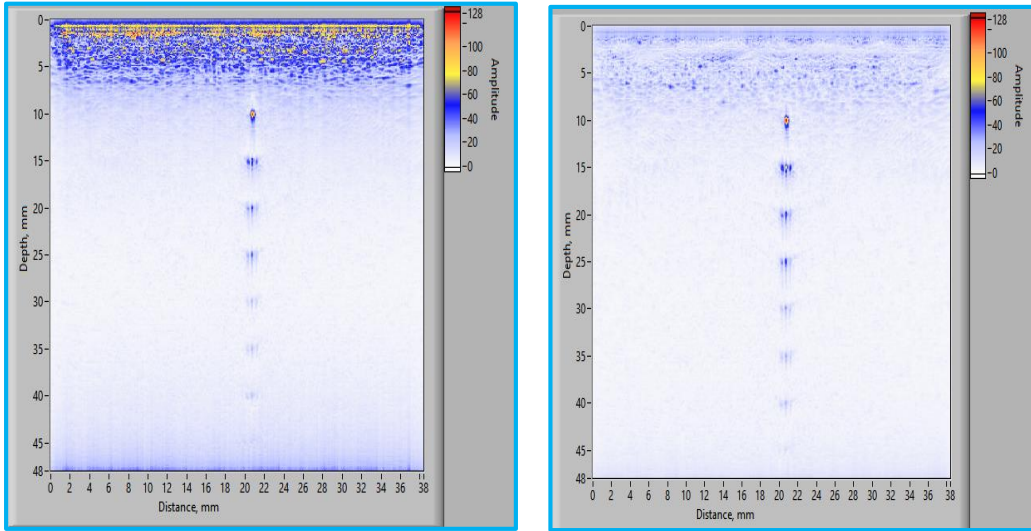


Figure 5.3: (a) Raw B-scan images for carbon steel block with vertically stacked side drilled holes acquired using SFLA technique (a) lower gain and (b) higher gain

The raw B-scan images show number of signals with the shape of a hyperbola at various depths corresponding to the side drilled holes in the sample. The image at lower gain does not show signals at higher depth, while the one acquired at higher gain shows signals in the depth range of 10 mm to 45 mm. For the topmost hole, there is no obstruction to the sound beam during the transmission and reception. As a result, an uninterrupted signal is seen in the raw B-scan image. For the first elements of the array, the direct sound path to the hole is the longest, which gets shorter as one moves towards the centre of the array. The sound path for the hole reaches a minimum for the elements, which are placed right above the hole, and then starts increasing as one moves towards the other end of an array. As a result, a typical ‘hyperbolic’ signal, which is

obtained when a divergent sound beam scans across a point reflector, is seen from the topmost hole in the raw B-scan image. As one moves towards the holes located at greater depths in the block, a distinct shadow region is seen in the central part of the raw image. The shadow region gets wider and wider for the holes at larger depths. The shadow region is an indication of the fact that the holes at larger depths are not imaged by the central elements of an array. This is because of the fact that the topmost hole prevents the sound beam from the central elements in reaching to the bottom holes and in a way that top holes masks these bottom holes. The bottom holes are however detected by the elements, which are away from the central part of an array, by the divergent sound beam. The signals from the bottom holes, although absent from the central region, are seen on the left and right hand side of the image. It is this divergence that is crucial during the post-processing of the raw data using SAFT algorithm. In addition to the signals from the individual holes, the raw B-scan image also shows some additional signals in the shape of hyperbolae crossing the primary signals from the holes. These signals are because of the mode converted shear wave, which is generated when the primary longitudinal beam emanating from the linear array strikes the hole.

The SAFT processed B-scan images for lower and high gain are shown in Figure 5.4 (a) and (b) respectively. The images indicate that at lower gain, the side drilled holes at the depth of 10 mm to 40 mm are detected, while the signal from the one at 45 mm depth is merging with the noise. At higher gain, all the holes, including the one at 45 mm, are clearly seen. There is also an increase in the signal amplitude from all the holes. The topmost hole shows the least lateral spread and highest signal amplitude as compared to the bottom holes, which shows the minimum amplitude and the largest spread. The signals from the mode converted shear wave do not participate constructively in the SAFT processing. Hence these are not seen in the processed image.



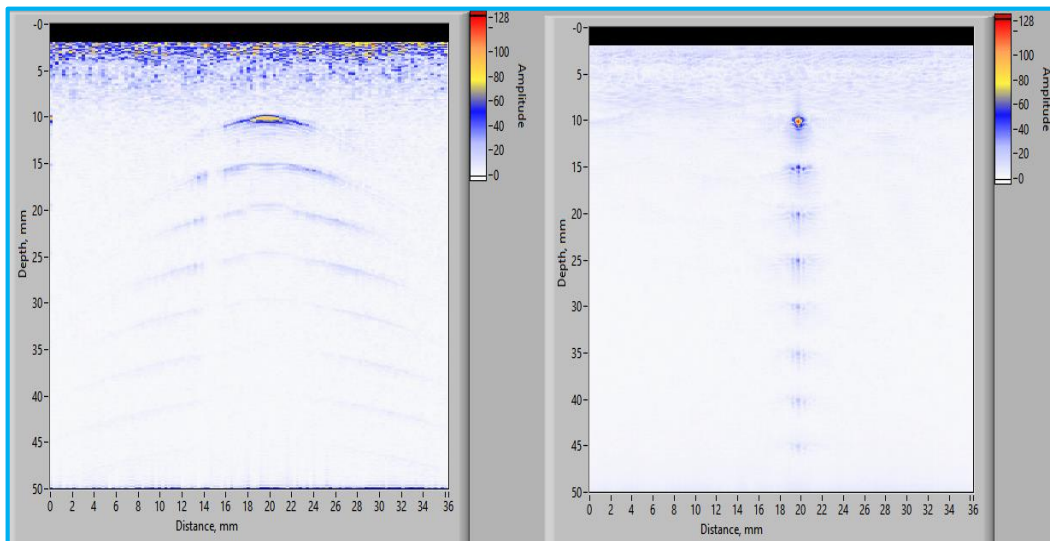
(a)

(b)

Figure 5.4: SAFT processed B-scan images for carbon steel block with vertically stacked side drilled holes acquired using SFLA technique (a) lower gain and (b) higher gain

5.2.1.3 PA-SAFT technique

Figures 5.5 (a) and 5.5 (b) shows the raw and the SAFT processed B-scan images respectively.



(a)

(b)

Figure 5.5: (a) Raw B-scan and (b) SAFT processed B-scan images for carbon steel block with vertically stacked side drilled holes acquired using PA-SAFT technique

The raw image shows wide hyperbolic signals from the holes. The processed image shows all eight holes present in the block. The

5.2.1.4 FMC + TFM technique

Figures 5.6 (a) and (b) show the TFM processed B-scan images at lower gain (corresponding to gain setting for PA-SAFT) and higher gain (corresponding to high gain setting of SFLA). At lower gain setting, only the top seven of the total eight holes are detected. The image at higher gain shows all the eight holes.

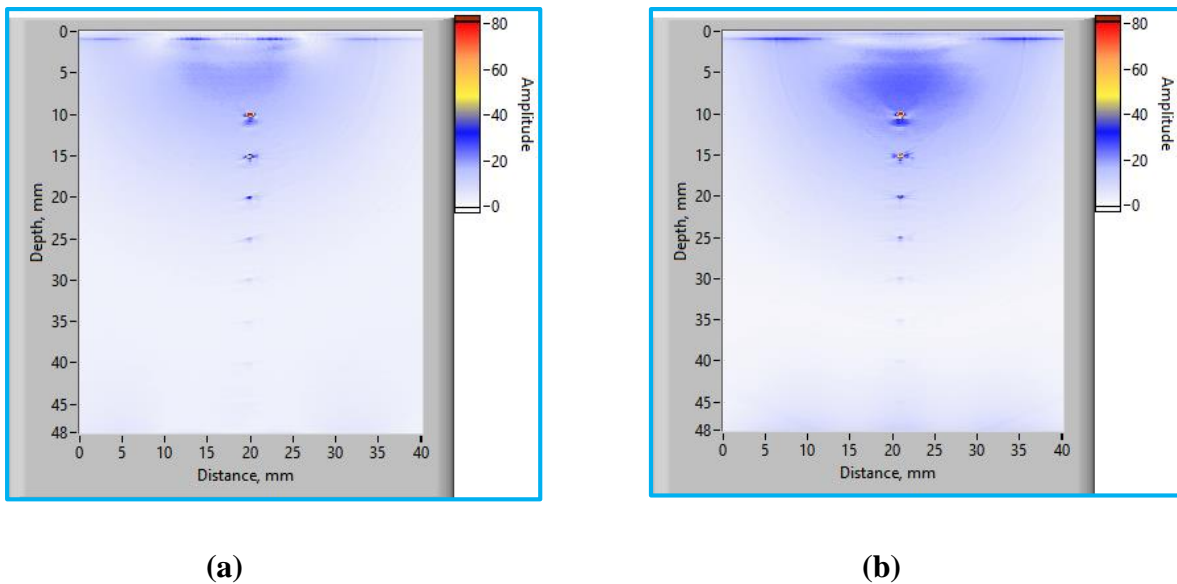


Figure 5.6: B-scan images for carbon steel block with vertically stacked side drilled holes using FMC + TFM technique (a) lower gain and (b) higher gain

5.2.1.5 Comparison and analysis of results by different techniques

The results obtained by conventional phased array, SFLA, PA-SAFT and FMC techniques are compared in terms of: (i) sensitivity for detection of volumetric flaws expressed in terms of SDR and GR (ii) maximum amplitude variation between the signals from various holes and (iii) the lateral spread in the signals from the holes in the processed B-scan image. Small value of SDR and

high GR value are indicators of good sensitivity. The lower value of 6 dB spread is an indication of good focusing and hence the ability to resolve closely spaced flaws. In addition to 128 elements, the data using SFLA and PA-SAFT techniques are acquired using 64 elements to compare the results with FMC + TFM under identical test conditions.

Table 5.2 shows the variation in the SDR, GR, 6 dB spread and the amplitude variation for SFLA, PA-SAFT and FMC + TFM techniques.

Table 5.2: Comparison of SDR, GR, 6 dB spread and the amplitude variation for carbon steel sample with volumetric flaws by various techniques

Sr. No.	Technique	Sensitivity achieved		6 dB spread variation (mm)	Amplitude variation (dB)
		SDR	GR (dB)		
1	PA-SAFT (128 el)	0.022	17	0.7 to 1.4	18
2	PA-SAFT (64 el)	0.022	17	0.8 to 3.0	20
3	SFLA- lower gain (128 el)	0.025	17	0.4 to 1.4	21*
4	SFLA- higher gain (128 el)	0.022	5	0.4 to 1.4	23
5	SFLA- higher gain (64 el)	0.022	5	0.4 to 3.0	25
4	FMC + TFM - lower gain	0.025	17	0.5 to 3.0	27*
5	FMC + TFM- higher gain	0.022	5	0.6 to 3.1	29

* For seven holes only

The following conclusions can be drawn from the Table 5.2:

- Under identical test conditions, the best sensitivity is achieved by PA-SAFT technique, which is reflected in lower value of SDR at the same GR value
- SFLA and FMC + TFM techniques show the same SDR at lower gain setting

- One can improve the sensitivity with SFLA and FMC techniques, but at the cost of lower GR value
- The 6 dB lateral spread for all the techniques is similar, although the lower bound value is smaller for SFLA and FMC + TFM than PA-SAFT technique. This indicates that at shallower depths, focusing and hence the resolution for volumetric flaws is better using SFLA and FMC as compared to PA-SAFT technique.
- The amplitude variation is found to be lowest for PA-SAFT technique indicating better sensitivity over a large depth range
- With SFLA and FMC techniques, the bottom most holes show very less signal amplitude because of which the amplitude variation for these techniques is more in comparison to that of PA-SAFT technique
- SFLA and PA-SAFT techniques using 128 elements appears to perform better than FMC + TFM, both in terms of amplitude variation and the upper bound value of 6 dB spread. The primary reason for this is the fact that with FMC technique, the data is acquired using only 64 elements. The lower value of total effective aperture (TEA) not only leads to inferior focusing at larger depths but also lower signal amplitude from the holes located deeper. With SFLA and PA-SAFT techniques when the TEA is reduced from 128 to 64 elements to match that of FMC, there is a significant increase in the upper bound value of lateral spread. This result is similar to the one observed while studying the effect of TEA on focal spot size by SFLA technique (Chapter 4, Section 4.3.2.1.4)
- Under identical test conditions i.e. 64 elements for data acquisition, all the techniques show lateral spread in a similar range
- When compared with conventional phased array, it is observed that the techniques based

on linear array and SAFT or TFM could achieve similar SDR. However, the focusing these techniques is much superior that what can be achieved by the conventional phased array using large number of active elements. The upper bound value of 6 dB spread by SFLA and PA-SAFT techniques is found to be lower than the lower bound value of this parameter obtained by using 48 and 64 active elements.

- The results indicate that, a good sensitivity for detection of volumetric flaws can be achieved by focal laws based phased array inspection as well as SFLA and PA-SAFT techniques. However, in order to achieve good resolution (of an order of a millimeter) in the depth range of 10 mm to 50 mm in steel, SFLA and PA-SAFT techniques are more effective.

5.2.2 Sensitivity for the detection of volumetric flaws at higher depth

The sensitivity of SFLA and PA-SAFT techniques for detection of volumetric flaws is assessed using an aluminium sample with 0.5 mm dia. holes at various depths in the range of 40 mm to 200 mm from the scanning surface. This corresponds to the SDR range of 0.0125 to 0.0025. Figure 5.7 shows the experimental set-up for data acquisition using SFLA, PA-SAFT and FMC techniques. The experimental details are given in Chapter 3 Section 3.6.2.

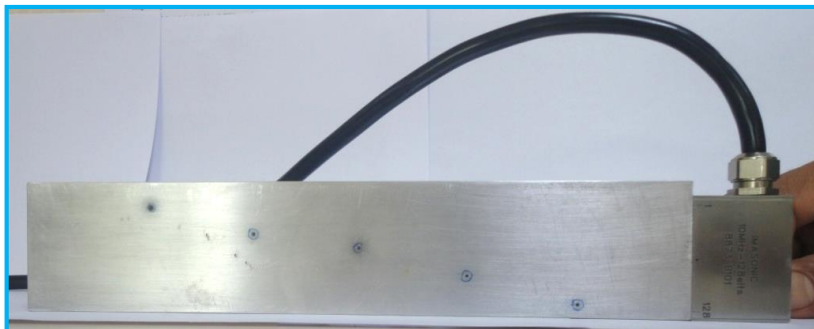


Figure 5.7: Experimental set-up to determine the sensitivity for SFLA and PA-SAFT techniques for detection of volumetric flaws

5.2.2.1 SFLA technique

Figures 5.8 (a) and (b) show the results obtained by SFLA at lower and higher gain values. The lower and higher gain values correspond to the GR of 15 and 0 dB respectively.

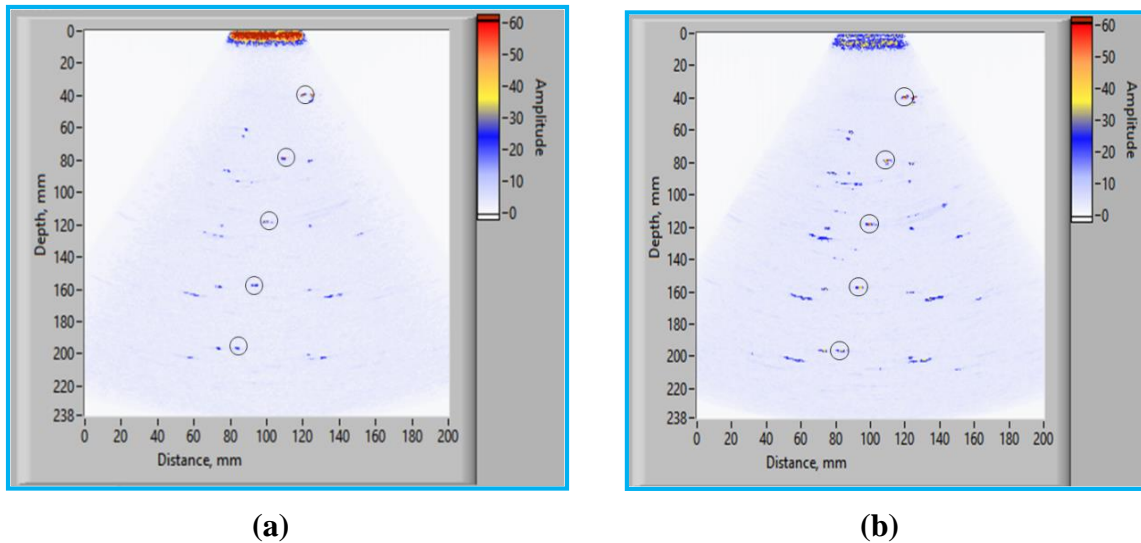


Figure 5.8: SAFT processed B-scan images for aluminum block with 0.5 mm dia. side drilled holes using SFLA technique (a) lower gain and (b) higher gain

The results indicate the following:

- Even at lower gain, all the side drilled holes are detected by SFLA technique. This means that with SFLA technique one can achieve the sensitivity corresponding to SDR of 0.0025 with sufficient gain reserve
- At higher gain, there is an overall increase in the amplitude of signals from all the holes, without a significant increase in the spread of the signals
- Complete coverage of the thickness is achieved by SFLA technique
- Apart from the signals from the holes, the processed image shows additional signals of similar nature adjacent to the signals from the holes. These signals are from the sidewall

of the sample. The lateral distance between the direct signal from the side drilled hole (circled) and the additional signal is same as the distance between the side drilled hole and the sidewall of the sample. For example, the hole at 40 mm depth is at a distance of 5 mm from the sidewall. As a result, an additional signal (on the right) is seen next to the direct signal from the hole. The bottommost side drilled hole at the depth of 200 mm is located at 10 mm away from the sidewall. In this case too, an additional signal (on the left) is seen next to the direct signal from the hole.

5.2.2.2 PA-SAFT technique

Figure 5.9 shows the results obtained by PA-SAFT technique at the gain value corresponding to the GR of 15 dB.

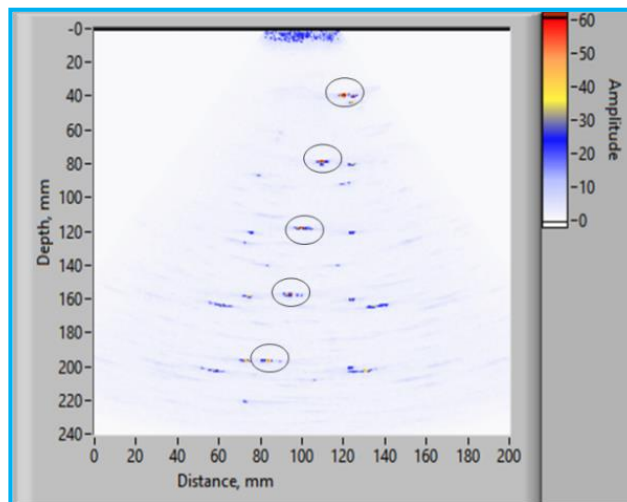


Figure 5.9: SAFT processed B-scan image for aluminum block with 0.5 mm dia. side drilled holes using PA-SAFT technique

The following observations are made from the above results:

- As with SFLA, the bottommost hole corresponding to SDR of 0.0025 is detected with sufficient gain reserve.

- There is complete lateral coverage of the sample and all the side drilled holes have been detected. Like SFLA, signals from the sidewall are also seen.

5.2.2.3 FMC + TFM technique

With FMC, the data could not be acquired for a depth of 200 mm in a single file as the large data size limits the acquisition to a thickness of approximately 100 mm using 64 elements linear array. The FMC + TFM processed B-scan images for two depth ranges viz. 25 mm to 140 mm and 140 mm to 250 mm are shown in Figure 5.10 (a) and (b), respectively.

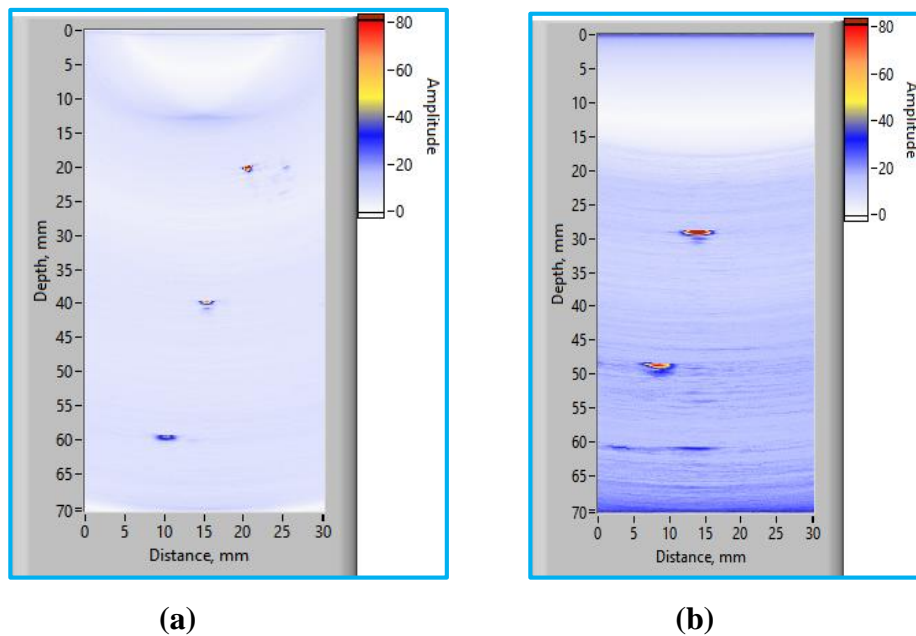


Figure 5.10: FMC + TFM images for aluminum block with 0.5 mm dia. side drilled hole (a) 25 mm to 140 mm and (b) 140 mm to 250 mm

The results indicate that all the holes including the one at 200 mm is detected by FMC + TFM technique.

5.2.2.4 Comparison of results by various techniques

All the techniques viz. SFLA, PA-SAFT and FMC + TFM could detect the 0.5 mm dia. side drilled hole at 200 mm depth from the surface in aluminum with sufficient gain reserve. Under identical conditions, the signal amplitude from all the holes using PA-SAFT technique is found to be higher as compared to the ones observed using SFLA technique. The spread of the signals from the side drilled holes, even at the depth of 200 mm, using SFLA and PA-SAFT techniques is found to be less than 2 mm. The results by SFLA and PA-SAFT techniques in terms of lateral spread are comparable to the ones obtained by FMC + TFM technique.

5.2.3. Extent of lateral coverage for detection of volumetric flaws

To determine the extent of lateral coverage for the detection of volumetric flaws by SFLA and PA-SAFT techniques, experiments are carried out on an aluminium sample with 2 mm dia. side drilled holes at 25 mm depth from the surface. This sample has fifteen side drilled holes at the same depth and aligned laterally. The distance between the extreme holes is approximately 90 mm. Figure 5.11 shows the experimental set-up for data acquisition.

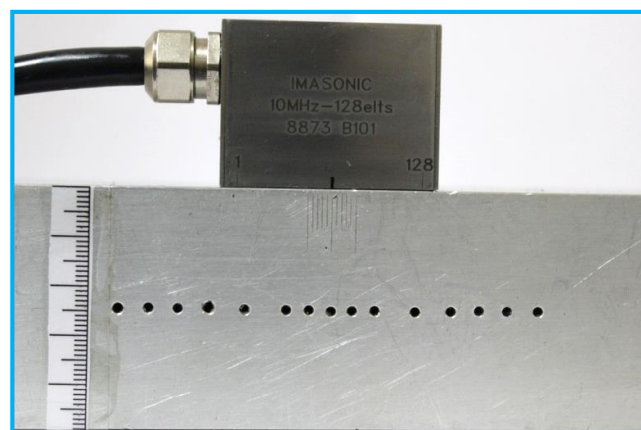


Figure 5.11: Experimental set-up for data acquisition on aluminum block with laterally separated side drilled holes

The linear array of 10 MHz, 0.3 mm pitch, 128 elements is placed on the sample so that the central elements are positioned over the middle hole. The four extreme holes on both sides-do not lie below the array. The experimental details are given in Chapter 3 Section 3.6.3.

5.2.3.1 Conventional Phased Array

Figure 5.12 shows the results of conventional phased array by beam steering and focusing with active apertures from 16 to 48 elements. With this approach, the sound beam is focused at multiple focal points which are aligned at a given depth using the selected aperture.

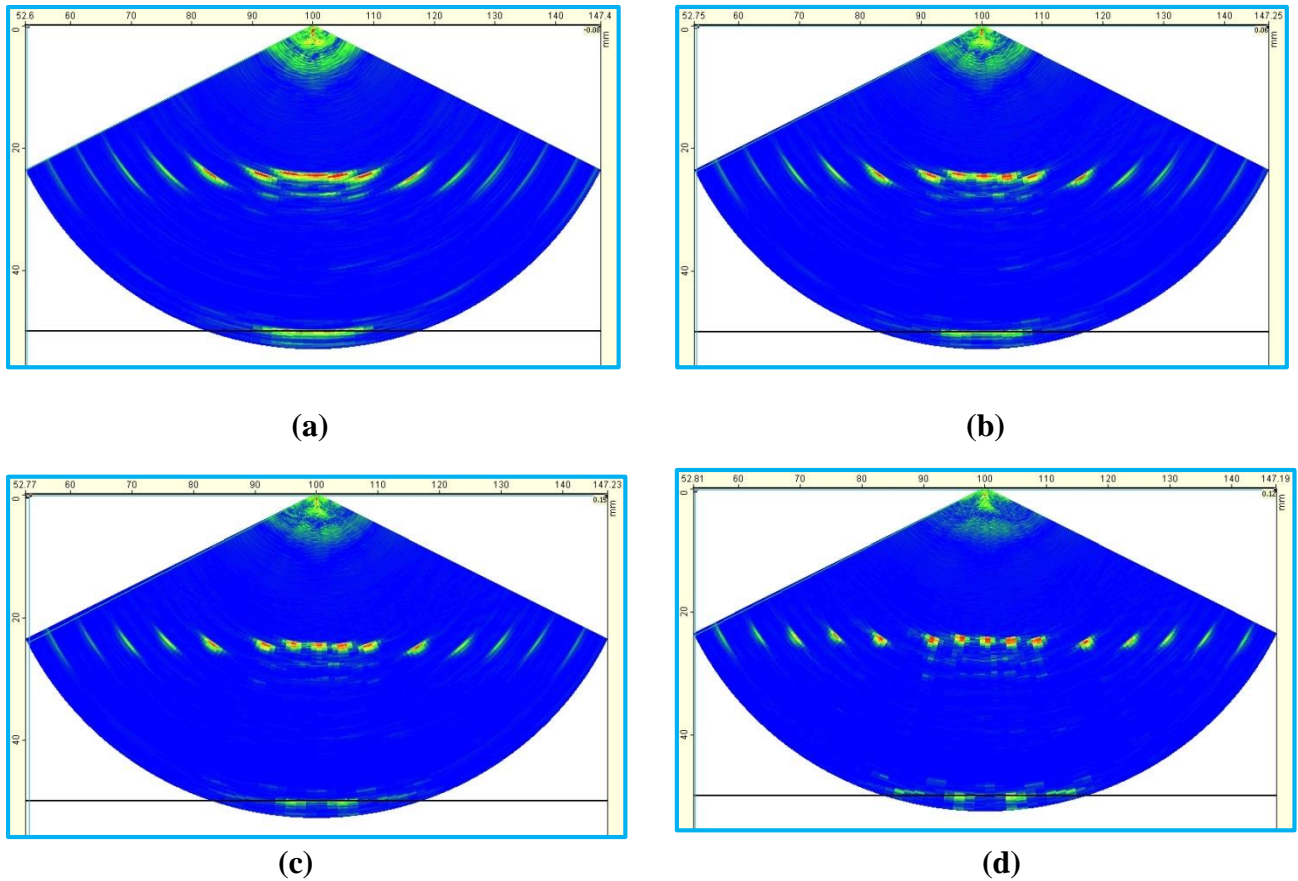


Figure 5.12: B-scan images using conventional phased array multi-point focusing on aluminum block with laterally separated side drilled holes (a) 16 el, (b) 24 el, (c) 32 el and (d) 48 el

The results indicate that all the fifteen holes are detected using this approach. With regard to the

spread of the signals, as the active aperture increases, the spread of signals decreases. Table 5.3 summarizes the results obtained by conventional phased array.

Table 5.3: Comparison of results on aluminum block with laterally separated side drilled holes using conventional phased array

Sr. No.	Parameter	Active aperture			
		16 el	24 el	32 el	48 el
1	Lateral coverage (mm)	87	87	87	87
2	Minimum 6 dB spread (mm)	3.0	2.4	2.1	1.5
3	Amplitude variation (dB)	22	22	21	20

Table 5.3 indicates the following:

- With beam steering, complete lateral coverage is obtained, which means that the volumetric flaws that do not lie below the active aperture are also detected
- The 6 dB lateral spread for the holes that do not lie below the active aperture is higher in comparison to those lie below the aperture. This is because of the larger sound path and also the deterioration in the sound beam directivity at higher steering angles.
- The variation in the amplitude of the signals from the holes for all the apertures is significantly higher.
- It can be concluded that by beam steering and focusing using conventional phased array, one can detect volumetric flaws that do not lie beneath the linear array. However, the focusing at higher steering angles is not satisfactory. Even in the region below the active aperture, the focal spot size with large number of elements (48 el) is of the order of 1.5 mm. This indicates that if the lateral spacing between the volumetric flaws is less than this,

then they would not be resolved by conventional phased array technique.

5.2.3.2. SFLA Technique

Figures 5.13(a) and (b) show the raw and the SFLA processed B-scan images respectively, for this sample using 10 MHz, 0.3 mm pitch, 128 elements linear array. The raw image shows overlapping signals from the holes in the sample. The overlapping occurs, since the holes are closely spaced and each hole gives a wide hyperbolic signal. From the raw image, one cannot get any information on the number of holes and lateral separation between them. The raw data is processed by SAFT algorithm. The processing range not only includes the material beneath the linear array, but also the material on either side of the array up to a distance of approximately 30 mm. This is to ensure that the holes which do not lie directly beneath the linear array, but are detected because of the divergent sound beam are imaged in the processed data.

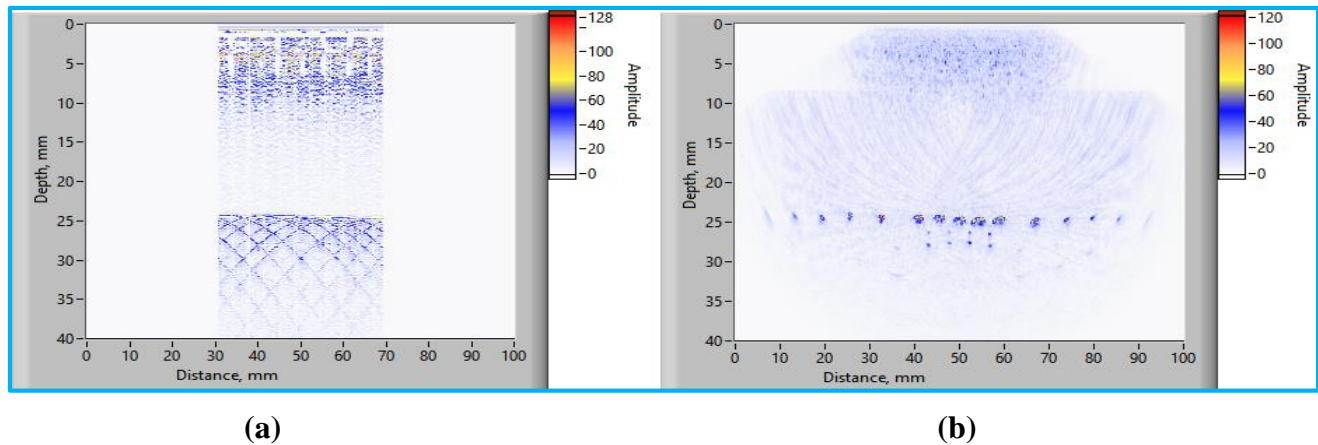


Figure 5.13: (a) Raw B-scan and (b) SAFT processed B-scan image of an aluminum sample with laterally separated side drilled holes using SFLA technique

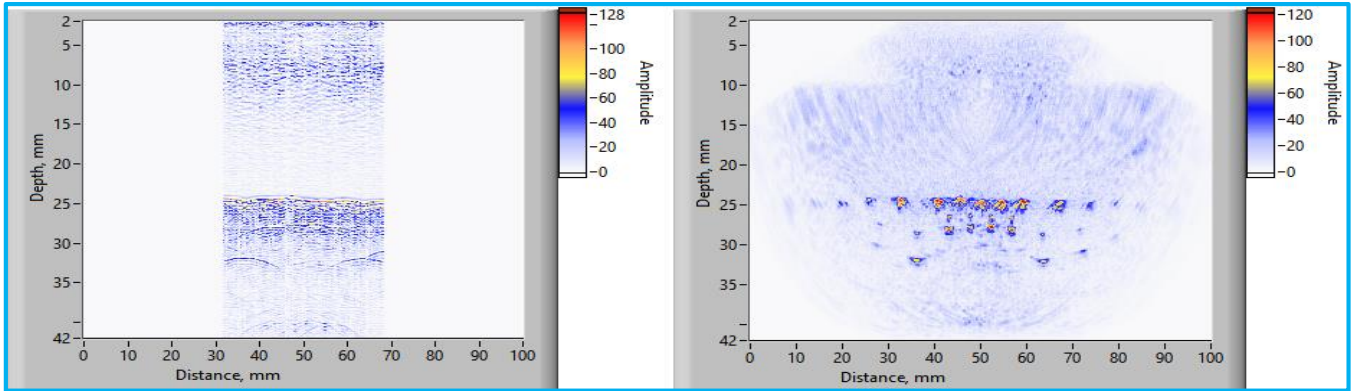
The processed B-scan image shows all the fifteen holes that are present in this block, including the ones that do not lie below the array. The extreme four holes at both ends, which are not located beneath the linear array show lower amplitude and higher spread as compared to the central holes. The primary reason for this is the fact that unlike the central holes, which are detected by all the

elements of the linear array, the peripheral holes are detected by the sound beam emanating from fewer elements (first few elements detect the holes on the left side and the last few elements detect the holes on right side). Moreover, the signal amplitude in the raw A-scan data from these holes is much lower, as these are detected by the peripheral sound beam and not the central beam. As a result, for these holes, there are fewer A-scans and lower signal amplitude during SAFT processing. Hence, their amplitude is lower and the spread is higher in the processed B-scan image as compared to the central holes. The results indicate that SFLA technique is able to detect and resolve the volumetric flaws that are located close to each other in the region below the array as well as away from it.

In addition to the signals from the holes at the expected depth, the processed B-scan image shows some additional indications beneath the indications from the hole. These low amplitude indications are seen prominently at the locations where the central five holes are present and appear at slightly longer path than the indications from the holes. When the sound beam is incident on any one of these closely spaced holes, there is a direct reflection that goes back to the receiving aperture. Since the reflecting beam is also divergent, a part of this reflected sound beam from the hole goes towards the adjacent hole from where it gets reflected and finally reaches the receiving aperture producing an indication. The sound path of this signal is marginally higher than the direct sound path and so after processing it appears as a separate signal in the image at slightly higher depth.

5.2.3.3. PA-SAFT technique

Figures 5.14 (a) and (b) show the raw and the processed B-scan images using PA-SAFT technique respectively. The processed image shows all the fifteen holes that are present in the block. The extreme holes on either side show very low amplitude. The holes in the central region, where they are closely spaced, are well resolved from each other.



(a)

(b)

Figure 5.14: (a) Raw B-scan and (b) SAFT processed B-scan image of an aluminum sample with laterally separated side drilled holes using PA-SAFT technique

5.2.3.4. FMC + TFM technique

Figure 5.15 shows the FMC + TFM B-scan image. The images show all the holes that are present in the block. Unlike SFLA and PA-SAFT technique, the amplitude of the signals from the holes is uniform. All the holes are detected and clearly resolved.

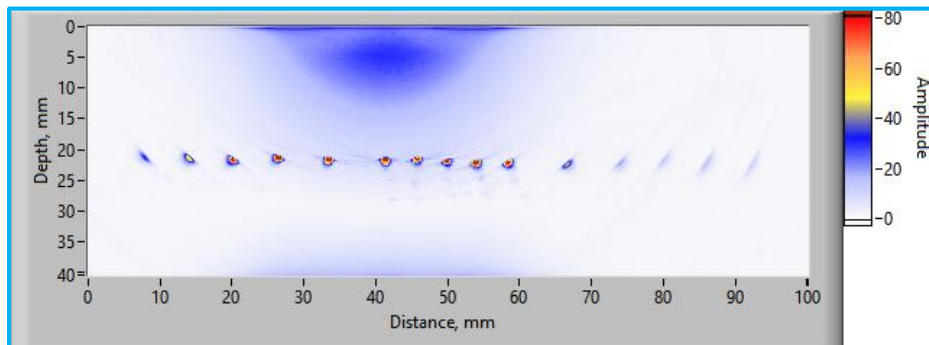


Figure 5.15: FMC + TFM image of an aluminum sample with laterally separated side drilled holes

5.2.3.5. Comparison and analysis of results by different techniques

Table 5.4 gives the comparison of results obtained by SFLA, PA-SAFT and FMC + TFM techniques. The results obtained by 48 active elements using beam steering and focusing by

conventional phased array are also given for the sake of comparison.

Table 5.4: Comparison of 6 dB spread, lateral coverage and amplitude variation for the laterally separated holes using conventional phased array, SFLA, PA-SAFT and FMC techniques in an aluminum block

Parameter	SFLA	PA-SAFT	FMC+TFM	Conventional Phased array
				with sector scan using 48 elements
Minimum 6 dB lateral spread (mm)	1.0	1.2	1.0	1.5
Lateral Coverage (mm)	86	86	86	86
Amplitude variation (dB)	16	27	21	20

Complete lateral coverage of approximately 86 mm is obtained by all the techniques. With PA-SAFT technique, the extreme two holes show very low amplitude. This is reflected in the higher value of amplitude variation as compared to SFLA and FMC techniques. In order to analyze the reasons for better sensitivity for the detection of holes located far away from the linear array with SFLA technique as compared to PA-SAFT, simulation studies are carried out using CIVA 11. From the sound beam computation results, the variation in the sound wave amplitude in the lateral direction at a depth of 25 using a single element excitation (SFLA) and multi-element excitation (PA-SAFT) is found out. The results are shown in Figure 5.16.

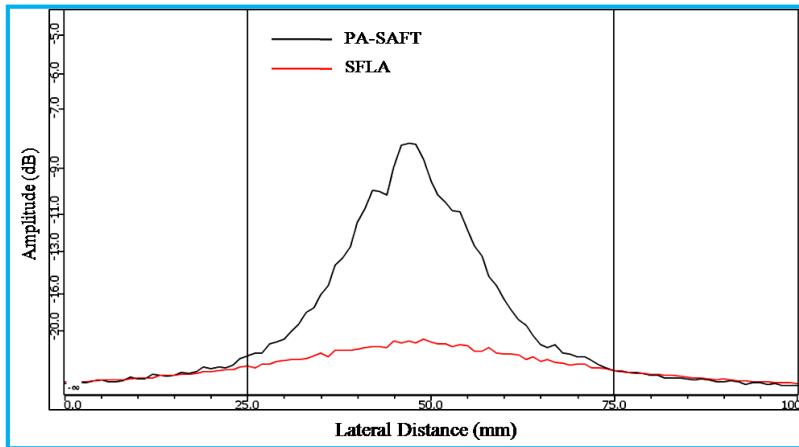


Figure 5.16: Variation in the sound wave amplitude at 25 mm depth in the lateral direction by SFLA and PA-SAFT technique using 10 MHz, 0.3 mm pitch linear array (Simulation)

The results indicate that with PA-SAFT technique, the wave amplitude in the central region of the sound beam is almost 12 dB higher than SFLA technique. This means that if the flaw is located in the central region of the sound beam, PA-SAFT technique would show higher signal amplitude. However, as one moves away from the central region, there is a sharp drop in the sound wave amplitude with PA-SAFT technique. With SFLA technique, the drop in the sound wave amplitude is gradual. With PA-SAFT technique, the sound wave amplitude at the lateral distance of 25 mm (where the extreme side drilled hole is located from edge of the array) is approximately 16 dB lower than the sound wave amplitude in the central region. This value is approximately 5.6 dB for SFLA technique. Figure 5.16 also indicates that at the lateral distance of 25 mm, the sound wave amplitude by PA-SAFT and SFLA techniques is almost similar. This means that during the data acquisition, the sound wave amplitude of the sound beam incident on the extreme hole by both the techniques is almost similar and so the amplitude of the reflected signal in the raw B-scan data is expected to be similar in both the cases. However, the processed B-scan images shown in Figures 5.13 (b) and 5.14 (b) for SFLA and PA-SAFT techniques respectively, are normalized in terms of

amplitude. Because of the large difference in the sound wave amplitude (16 dB) at the lateral distance of 25 mm with respect to the central region using PA-SAFT technique, and the process of normalization results in much lower signal amplitude of the extreme holes in the processed B-scan data. With SFLA, the smaller amplitude difference between the signals from the holes in the central and peripheral holes in the raw data results in the smaller variation in the processed B-scan image.

The lateral spread, corresponding to the holes beneath the linear array, is smaller for SFLA and FMC techniques as compared to PA-SAFT. This is line with the observations made during the study on an aluminum block containing 0.5 mm dia. side drilled holes (Chapter 4, Section 4.6) that under identical test conditions, the focal spot size achieved by SFLA is smaller than PA-SAFT technique. Thanks to the full matrix data available for processing from multiple directions, FMC + TFM image does not show artifacts, which are observed in SFLA and PA-SAFT images.

Based on the above observations, it can be concluded that for moderate depths, SFLA and FMC techniques are more sensitive than PA-SAFT technique for the detection of volumetric flaws in the region, which is significantly away from the linear array. The results obtained by SFLA techniques in terms of sensitivity and resolution are comparable to the ones obtained by FMC + TFM technique.

5.2.4 Resolving power of SFLA and PA-SAFT techniques

In order to determine the resolving power of SFLA and PA-SAFT techniques, experiments are conducted using a carbon steel sample having side drilled holes of 0.5 mm diameter located at a depth of 20 mm from the surface and separated centre-to-centre in lateral direction by 0.6 mm to 1.5 mm. The spatial resolution is considered to be satisfactory if the signal from the hole appears after 6 dB drop of the signal from the adjacent holes. The data from this sample is acquired using

conventional phased array, SFLA, PA-SAFT and FMC techniques. A 10 MHz, 0.3 mm pitch, 128 elements linear array is used for this purpose. Figure 5.17 shows the experimental set-up. The details are given in Chapter 3, Section 3.6.4.

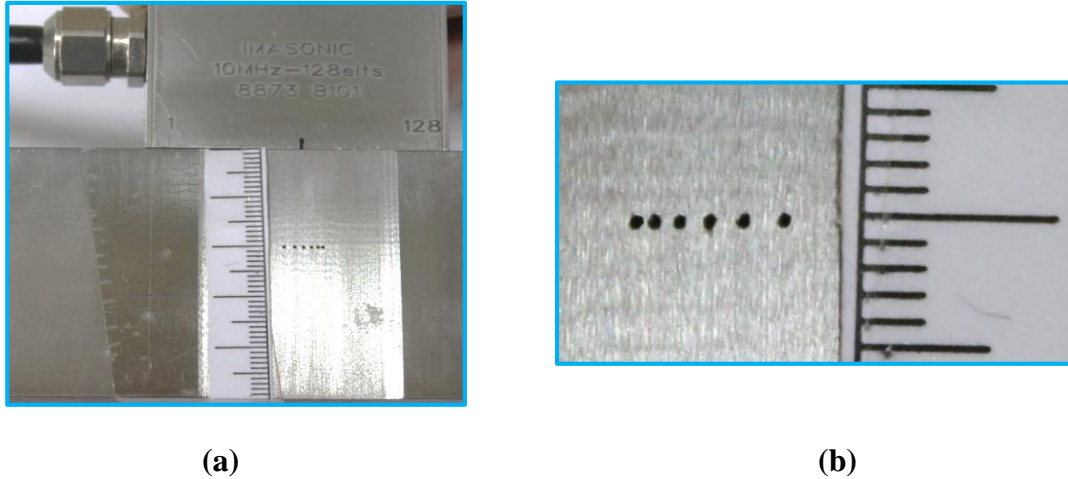


Figure 5.17: Carbon steel sample with closely spaced side drilled holes for determining the resolving power of SFLA and PA-SAFT techniques (a) Placement of linear array and (b) Magnified view of holes (Scale in mm)

5.2.4.1 Conventional phased array technique

Figures 5.18(a) and (b) show the B-scan images acquired by conventional phased array using single point focusing with two apertures comprising of 16 and 64 active elements respectively. Using these apertures, the sound beam is focused at a depth of 20 mm and the B-scan image is acquired during electronic scan. With an aperture of 16 elements, none of the holes is resolved. This indicates that the focal spot size achieved by 16 elements is larger than the maximum separation distance between the holes (> 1.5 mm). With 64 active elements, although the signals from the last three holes are seen distinctly, the first three holes, which are separated by much lesser distance, are not resolved. This indicates that in spite of using 64 active elements, the lateral resolution is not better than 1 mm.

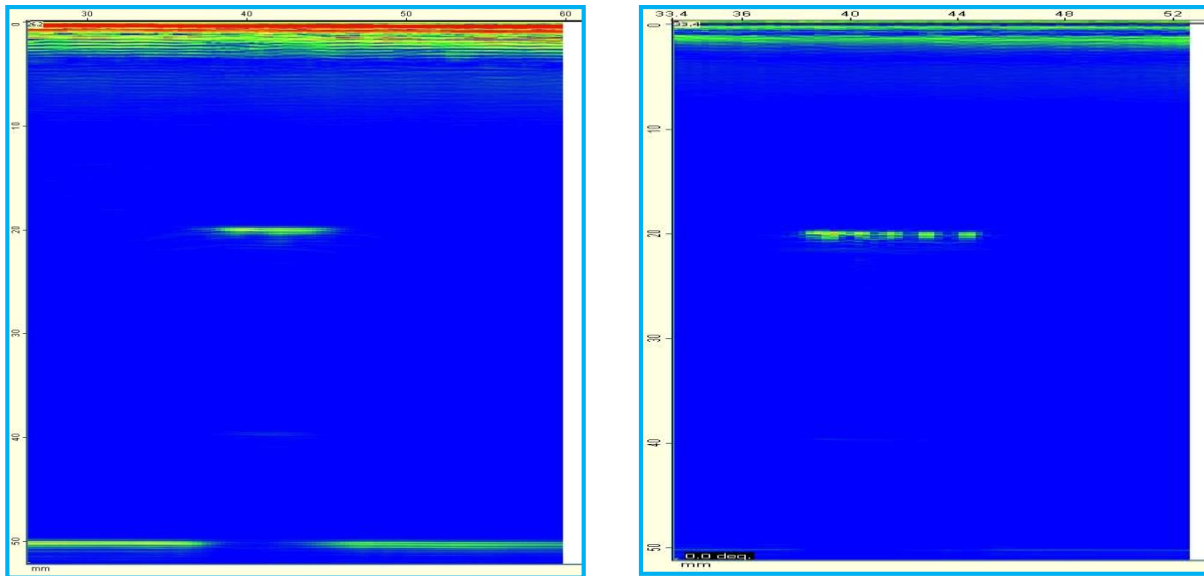


Figure 5.18: B-scan image of a carbon steel block with closely spaced side drilled holes using conventional phased array (a) 16 el aperture and (b) 64 el aperture (Scale in mm)

5.2.4.2 SFLA technique

Figure 5.19 shows the processed B-scan image for this sample using SFLA technique. The echodynamic curve is also shown alongside.

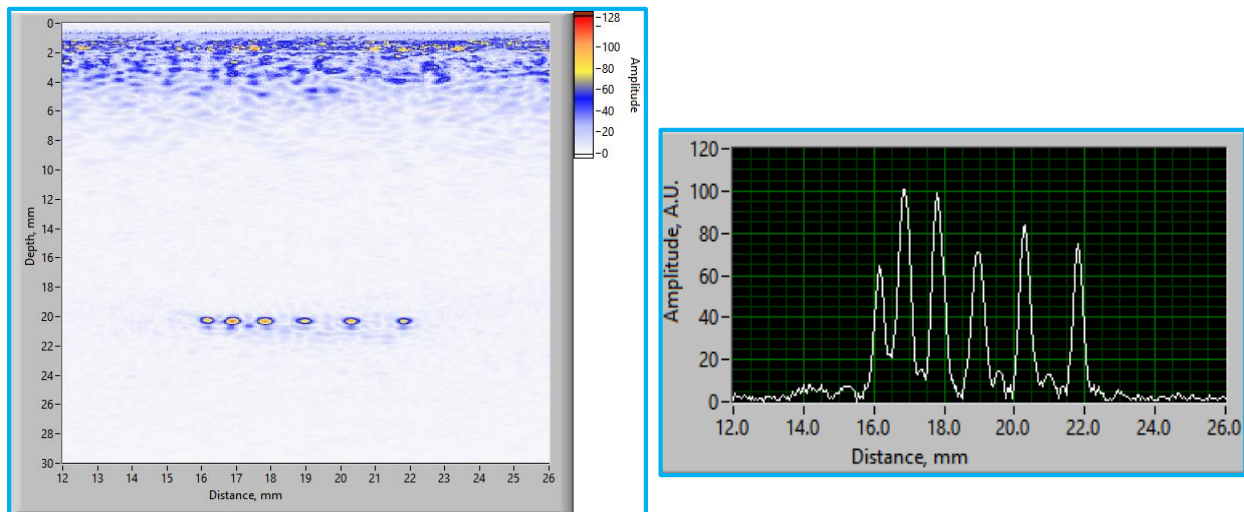


Figure 5.19: B-scan image and echodynamic plot of a carbon steel block with closely spaced side drilled holes using SFLA technique

The image shows that all the holes that are present in this sample are well resolved, including the ones that are separated by 0.6 mm. The above result indicates that the sound beam focusing achieved by SFLA is very effective and the technique is able to resolve very closely spaced volumetric flaws.

5.2.4.3 PA-SAFT technique

Figure 5.20 shows the processed B-scan image of this sample along with the echodynamic plot using PA-SAFT technique. The echodynamic plot shows six distinct peaks, each corresponding to the side drilled holes in the sample. However, the resolution between the first two peaks is not satisfactory. The result indicates that the resolution is not as good as SFLA, but much superior to what is obtained by conventional phased array using 64 active elements. From the observations, one can conclude that for this block a resolution of the order of 0.9 mm could be achieved using PA-SAFT technique.

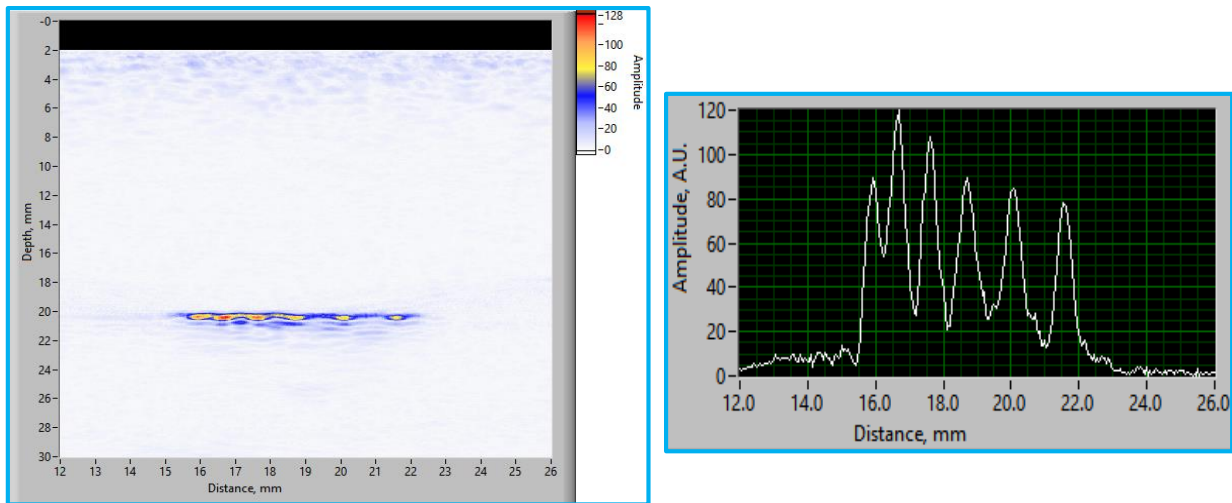


Figure 5.20: B-scan image and echodynamic plot of a carbon steel block with closely spaced side drilled holes using PA-SAFT technique

5.2.4.4 FMC+ TFM technique

Figure 5.21 shows the B-scan image using FMC + TFM technique. The image indicates that the holes separated by 0.6 mm are not resolved clearly. The resolution for the other holes is satisfactory.

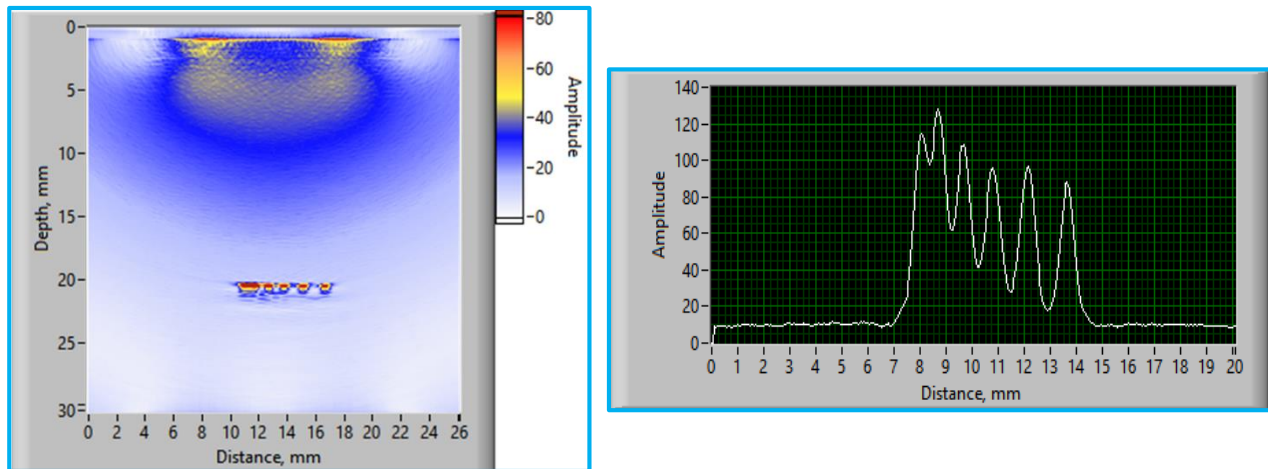


Figure 5.21: FMC + TFM image and echodynamic plot of a carbon steel block with closely spaced side drilled holes

Based on the above results, it can be concluded that the SFLA technique performed better than the PA-SAFT technique in terms of the resolution for separate detection of two very closely spaced volumetric flaws. This can be attributed to the smaller size of the piezoelectric source using SFLA as compared to PA-SAFT technique. SFLA results are also slightly better than ones obtained by FMC technique. This can be attributed to larger TEA (128 elements) used for SFLA as compared to FMC (64 elements). All the techniques performed much better than the conventional phased array using 64 active elements.

5.3 Planar Flaws

Planar flaws are two-dimensional and pose a threat to the integrity of pressurized components. From ultrasonic examination point of view, there are two requirements for planar flaws: (i) detection and (ii) characterization in terms of through-wall dimensions (depth or height) and orientation. The effectiveness of SFLA and PA-SAFT techniques for these two requirements is studied by carrying out experiments on steel plate samples with simulated planar flaws in the form of inclined slots made by EDM process. The assessment on the satisfactory detection of a planar flaw is done based on whether the given technique is able to detect the upper and lower tip of the flaw and produce measurable signals (above the background noise) in the B-scan image. The assessment on the characterization is done by comparing the through-wall dimension and the orientation of the flaw with the true values.

The study is carried out using two samples viz. 24 mm thick and 60 mm thick stainless steel plate. The objective of the study on the thicker sample is to assess the effectiveness of SFLA and PA-SAFT techniques on the detection and characterization of planar flaws that are located deeper in the material. The data on these blocks is acquired using 5 MHz, 0.6 mm pitch, 64 elements linear array. A lower frequency is chosen since the blocks are made of stainless steel. The raw B-scan images acquired by SFLA and PA-SAFT techniques are processed by SAFT algorithm and the one acquired using FMC by TFM.

5.3.1 Stainless steel plate of 25 mm thickness with simulated planar flaws

Six slots, 8.5 mm length, 2 mm width and 25 mm depth, oriented at from 0° to 51° , are machined from one of the faces. The upper tip of all the slots is at approximately 8 mm from the scanning surface. Figure 5.22 shows the experimental set-up. Details are given in Chapter 3 Section 3.7.1.

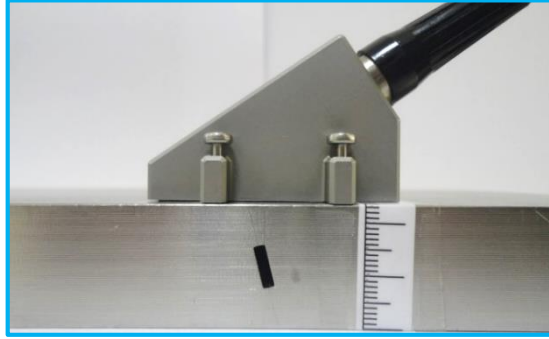


Figure 5.22: Experimental set-up for data acquisition on inclined slots in 24 mm thick stainless steel plate using SFLA, PA-SAFT and FMC techniques

5.3.1.1 SFLA technique

Figure 5.23(a) shows the raw B-scan image for a 16° inclined slot in the stainless steel plate using SFLA technique. The raw B-scan image shows that the signal from the upper tip of the flaw is quite a strong and is present over a wide range as it is detected by the sound beam emanating from all the elements. Contrary to this, the bottom tip signal is seen over a relatively narrow range. As the flaw is tilted in one direction, the bottom tip signal is detected only by the elements which lie on one side of the flaw. The image also shows a signal at approximately 1.5 times the time-of-flight of the signal corresponding to the upper flaw tip. This signal is from the mode converted shear wave. The longitudinal wave emanating from the transducer falls on the upper tip of the flaw, where, in addition to the diffracted longitudinal wave, a mode converted shear wave is also generated. Both these wave modes travel back to the receiving elements and produce indications on the B-scan image. For the mode converted signal in the B-scan image, the sound beam travels in the longitudinal mode (L) during the onward path and as a shear wave (S) during the return path. Hence, the time-of-flight of this signal (LS) is approximately 1.5 times the time-of-flight of the signal (LL) that travels as longitudinal wave, both during onward and return paths. The SAFT processed image is shown in Figure 5.23(b).

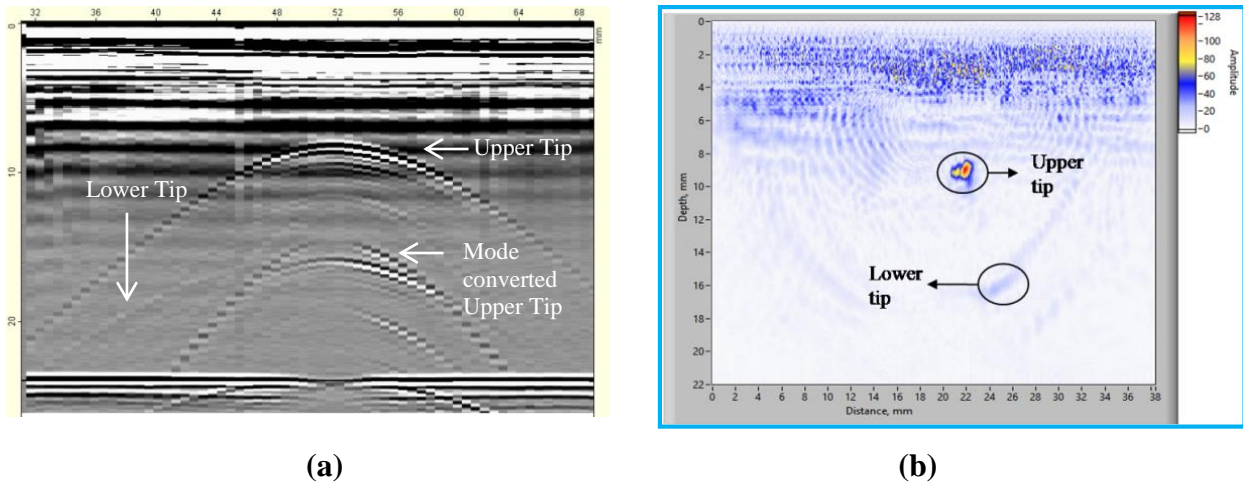


Figure 5.23: (a) Raw B-scan and (b) SAFT processed B-scan image of a 16° inclined slot in stainless steel plate by SFLA technique

During the SAFT processing, the mode converted shear wave signal (LS) gets eliminated due to the averaging, leaving behind only the LL signals from the upper and the lower tips of the flaws. This happens due to the fact that the velocity used for the SAFT processing is of the longitudinal wave and hence the signals from the flaw travelling during both onward and return path with the longitudinal wave velocity will only interfere constructively upon SAFT processing. From the SAFT processed image, one can accurately locate the flaw extremities and evaluate the height of the flaw and its orientation. Both these parameters are vital for the acceptance of a flawed component during manufacturing and for fitness-for-service assessment.

Figures 5.24(a) and (b) show the raw and the SAFT processed B-scan image for the flaw oriented at 51° respectively. As compared to the 16° oriented flaw, the processed image for the 51° oriented flaw shows the flaw surface in addition to the tip signals. When the divergent sound beam is incident on the flaw surface, a part of the reflected sound beam goes back to the receiving element since it is at near normal incidence to its surface. These signals are not seen clearly in the raw data, but appear prominently in the processed image. For flaw of lower orientations (16°), the reflected

signal from the flaw surface does not reach the receiving element due to unfavorable angle of incidence of the transmitted sound beam. As a result of the flaw surface is not imaged and only the extremities are seen.

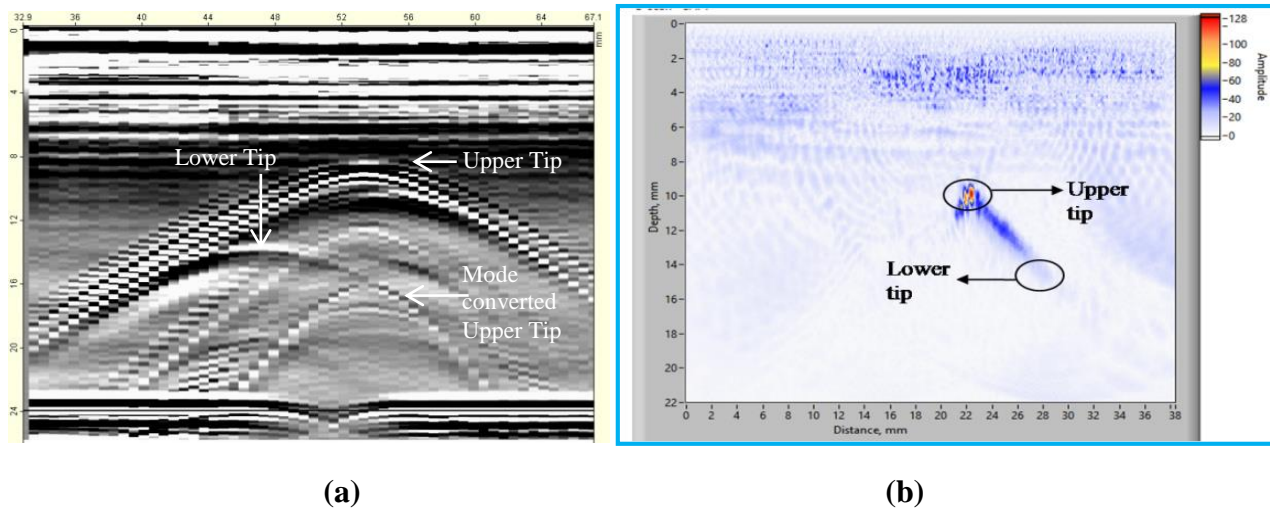
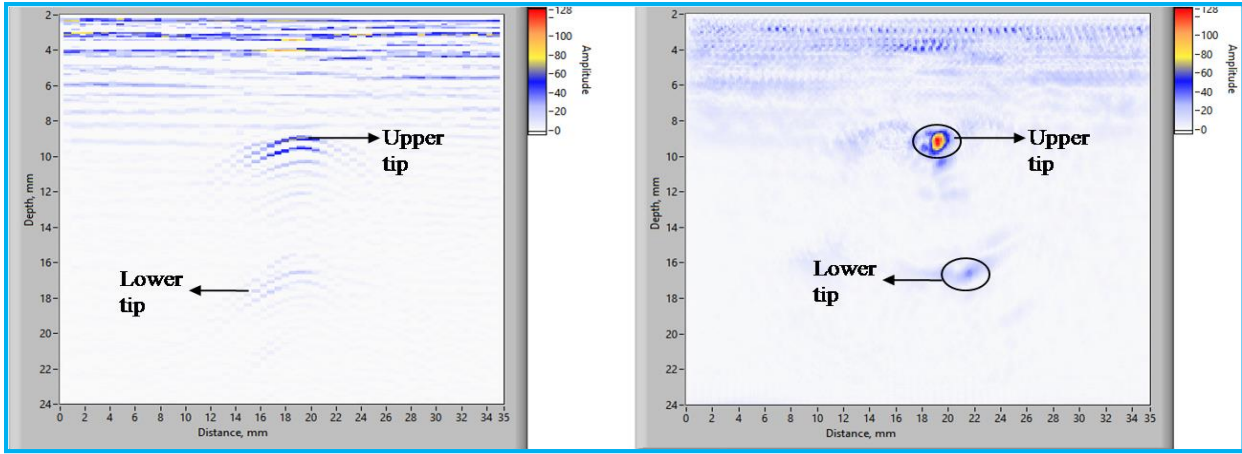


Figure 5.24: (a) Raw B-scan and (b) SAFT processed B-scan image of a 51° inclined slot in stainless steel plate by SFLA technique

5.3.1.2 PA-SAFT technique

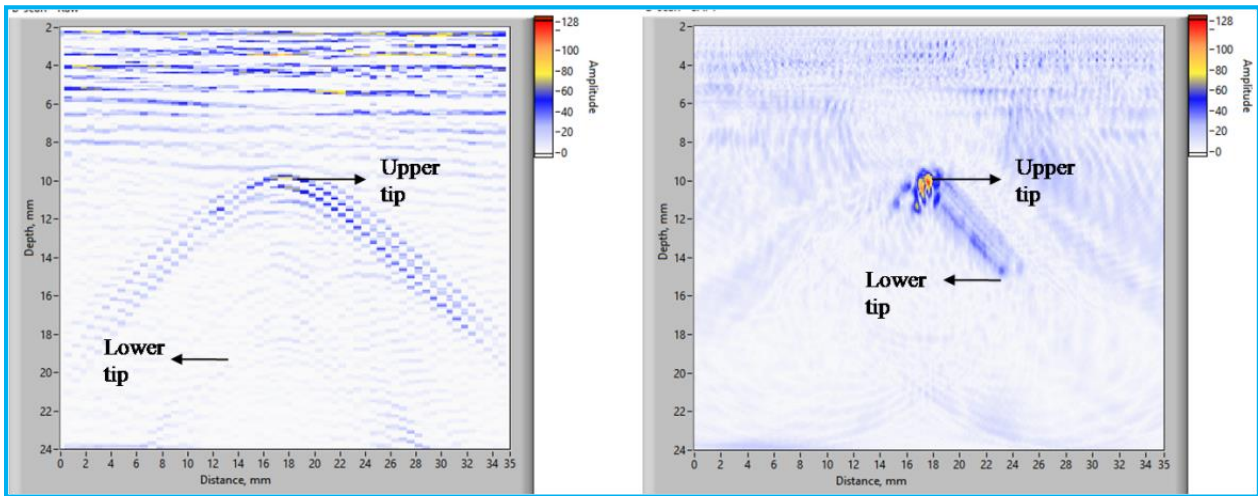
Figures 5.25(a) and (b) show the raw and SAFT processed B-scan images respectively for a 16° inclined slot in the stainless steel plate using PA-SAFT technique. The results are similar to that obtained by SFLA technique. The processed image clearly shows the upper and lower tip of the flaw. The lower tip signal shows larger spread as compared to upper tip, which indicates that the focusing is not as effective as that for the upper tip. One major reason for this is the lesser spread of the lower tip signal in the raw image as compared to the upper tip signal. Figures 5.26(a) and (b) show the raw and the SAFT processed B-scan images respectively for the slot inclined at 51°.



(a)

(b)

Figure 5.25: (a) Raw B-scan and (b) SAFT processed B-scan image of a 16° inclined slot in stainless steel plate by PA-SAFT technique



(a)

(b)

Figure 5.26: (a) Raw B-scan and (b) SAFT processed B-scan image of a 51° inclined slot in stainless steel plate by PA-SAFT technique

5.3.1.3 FMC + TFM technique

Figures 5.27(a) and (b) show the FMC+TFM processed B-scan images for the slots oriented at 16° and 51° respectively in the stainless steel plate. In this case too, the flaw of higher orientation (51°) shows the flaw surface. The results are similar to the ones obtained by SFLA and PA-SAFT techniques.

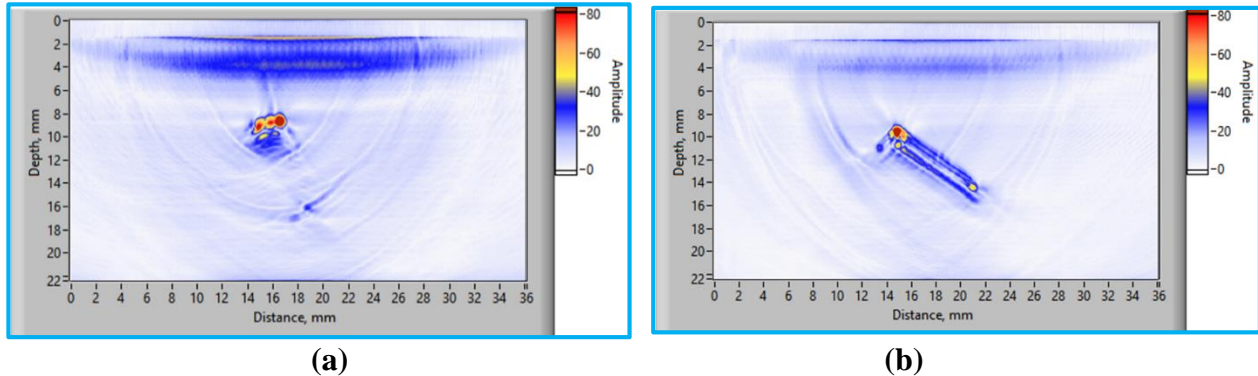
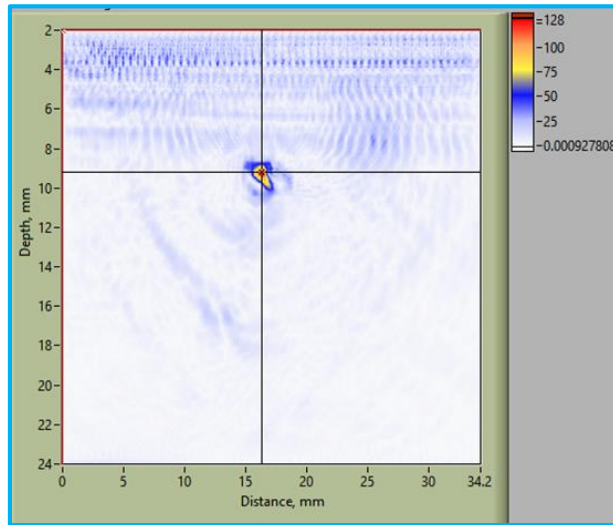


Figure 5.27: FMC + TFM B-scan images for inclined slots in stainless steel plate (a) 16° oriented slot and (b) 51° oriented slot

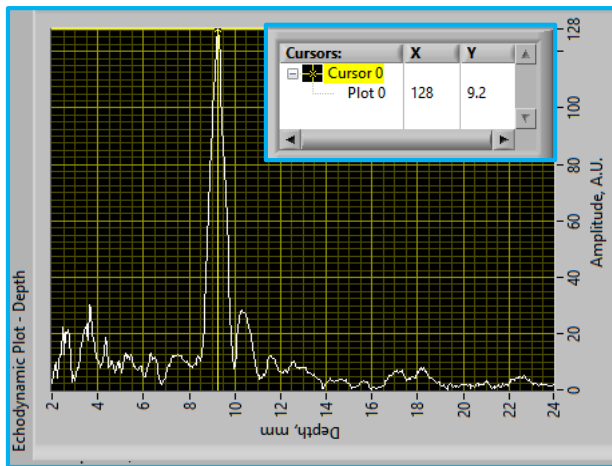
5.3.1.4 Evaluation of depth and orientation of inclined slots

The depth and the orientation of inclined slots are evaluated from the coordinates of the upper and the lower tips of the flaw. These coordinates are found out from the processed B-scan image using echodynamic plots in depth and lateral directions. Figure 5.28 (a) shows the processed B-scan image using PA-SAFT technique for the 28 deg. slot. The image shows a strong signal from the upper tip and a relatively weak signal from the lower tip with the two cursors intersecting at the upper tip signal. Figure 5.28 (b) and (c) shows the echodynamic plot in the depth and the lateral (distance) directions respectively for the upper tip signal. The echodynamic plots show distinct peaks, which corresponds to the positions (depth and distance) of the upper tip signal. Similar echodynamic plots in the depth and lateral directions are shown for the lower tip signal in Figure 5.28 (d) and (e), from where it's coordinates are found out. From the

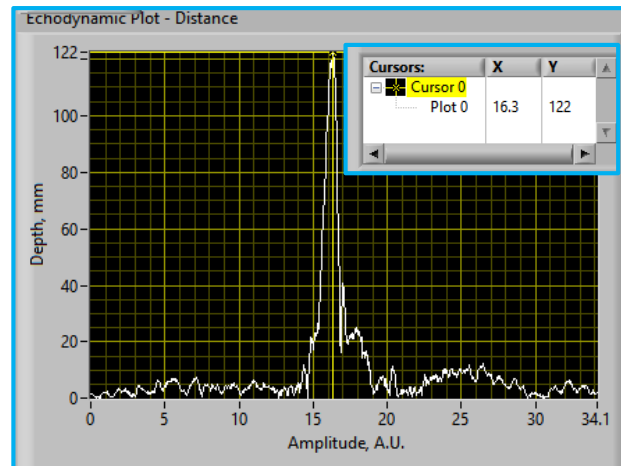
coordinates of upper and lower tips, the depth and the orientation of this flaw is evaluated as 7.5 mm and 32 deg. respectively. Similar methodology is adopted for all the inclined slots.



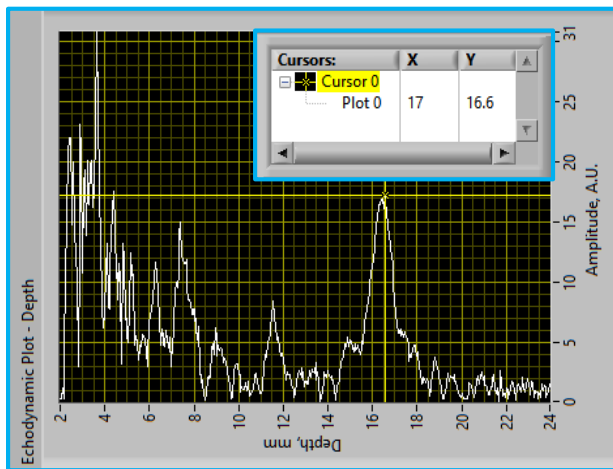
(a)



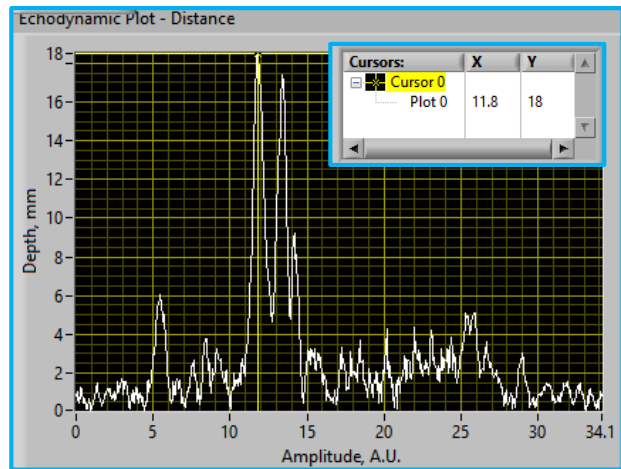
(b)



(c)



(d)



(e)

Figure 5.28: Methodology for assessment of depth and orientation of inclined slots from echodynamic plots (a) Processed B-scan image (b) Echodynamic in the depth direction for the upper tip (c) Echodynamic in the lateral direction for the upper tip (d) Echodynamic in the depth direction for the lower tip and (e) Echodynamic in the lateral direction for the lower tip

5.3.1.5 Comparison of results

From the processed B-scan images, the depth (height or through-wall dimension) and orientation of the flaws are found out. Table 5.5 gives the results obtained by SFLA, PA-SAFT and FMC techniques.

Table 5.5: Results of depth and orientation assessment of inclined slots in the stainless steel plate by SFLA, PA-SAFT and FMC+TFM approaches

True angle (deg.)	True depth (mm)	SFLA		PA-SAFT		FMC	
		Angle(deg.)	Depth(mm)	Angle(deg.)	Depth(mm)	Angle(deg.)	Depth(mm)
0	8.5	0	8.2	0	8.5	0	8.2
16	8.2	16	8.6	19	8.2	16	8.6
28	7.5	29	7.9	32	7.5	30	7.9
36	6.9	37	6.7	33	7.2	35	6.8
42	6.3	41	6.5	40	6.4	42	6.6
51	5.3	52	5.2	51	5.3	52	5.2

The following conclusions can be drawn from the above results:

- With SFLA and PA-SAFT techniques, it is possible to detect and locate the extremities of planar flaws that are located up to a distance of approximately 15 mm and less.
- The results obtained by SFLA and PA-SAFT techniques on the assessment of depth and orientation of planar flaws are accurate.
- The results obtained by these two techniques are comparable to the ones obtained by FMC+TFM technique.
- For the planar flaws that are oriented at larger angles, it is possible to carry out full face mapping of the flaws using SFLA and PA-SAFT techniques.

5.3.2 Stainless steel plate of 60 mm thickness with simulated planar flaws

In order to assess the effectiveness of SFLA and PA-SAFT techniques for the detection and characterization of planar flaws that are located at higher depths, experiments are conducted on a 60 mm thick stainless steel sample. This sample has two planar flaws: one oriented at 0 deg. and the other at 20 deg. with respect to the surface normal. Both the flaws are 10 mm long and have a width of 0.5 mm. The upper tip of these flaws is located at 30 mm from the scanning surface unlike the previous case, where it is located very close. Figure 5.29(a) shows the experimental set-up for data acquisition using SFLA, normal beam PA-SAFT and FMC techniques during which the linear array is symmetrically placed over the planar flaw. Figure 5.29(b) shows the experimental set-up for Angle beam PA-SAFT during which the linear array is placed laterally shifted with respect to the flaw. Experimental details are given in Chapter 3 Section 3.7.2.

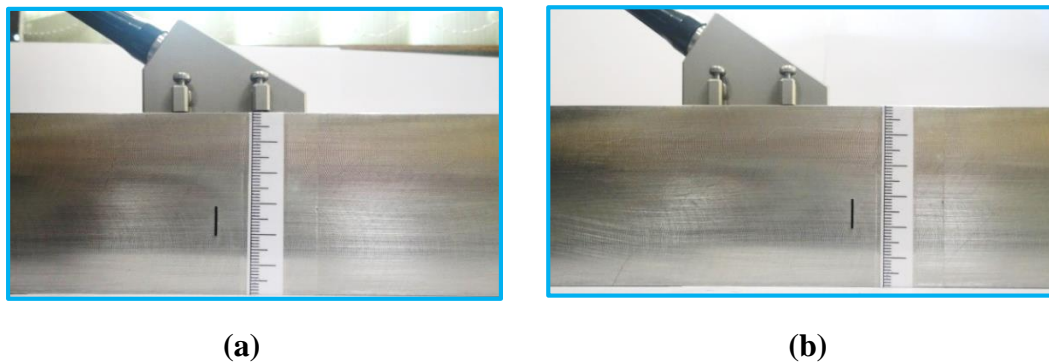


Figure 5.29: Experimental set-up for detection and characterization of planar flaw in 60 mm thick stainless steel plate (a) SFLA, PA-SAFT and FMC, (b) Angle Beam PA-SAFT

The results obtained by SFLA, PA-SAFT, Angle Beam PA-SAFT and FMC + TFM techniques for a 0 deg. oriented slot are shown in Figures 5.30 (a) to (d).

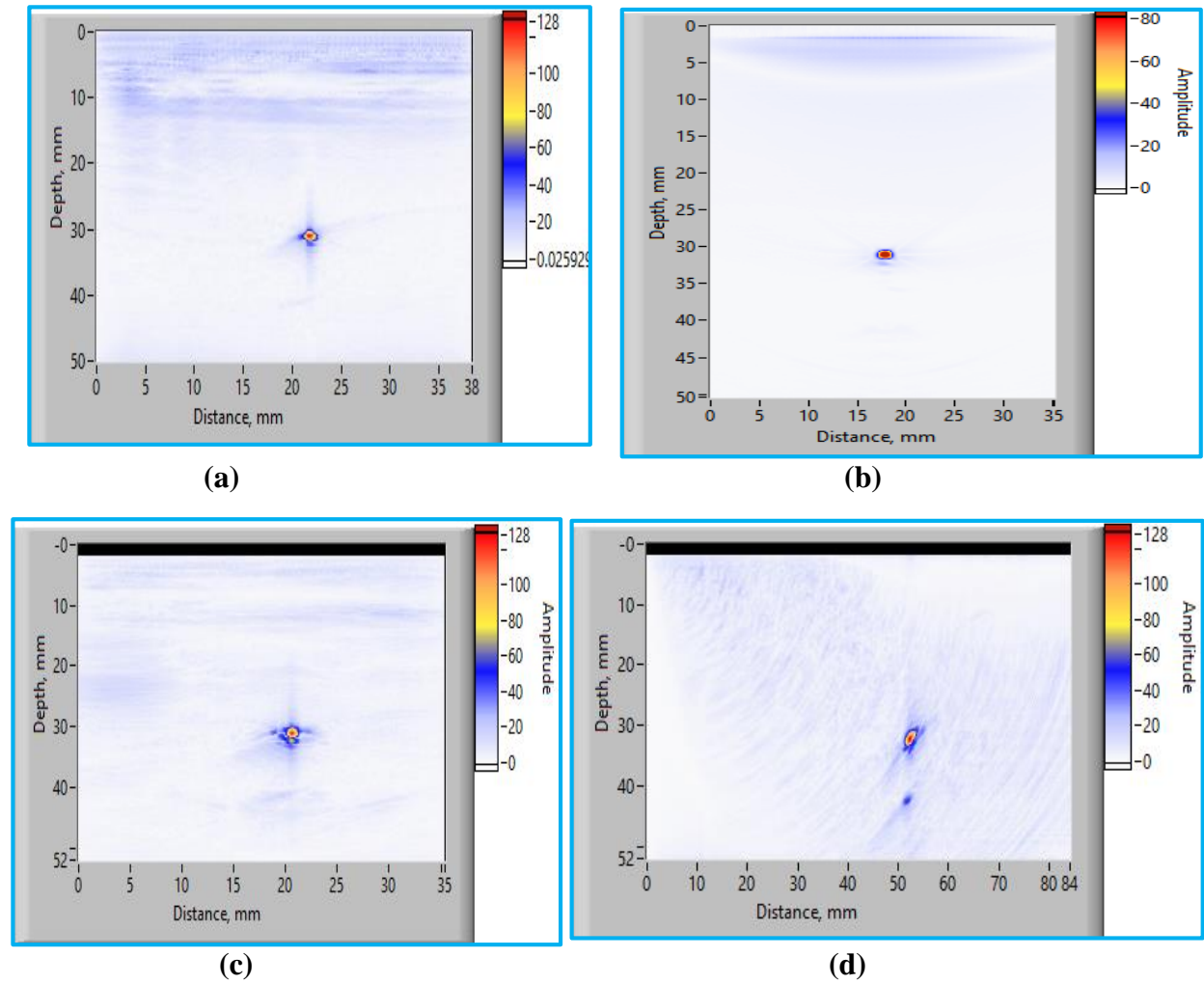


Figure 5.30: Processed B-scan images for a 0 deg. oriented planar flaw in 60 mm thick stainless steel plate (a) SFLA, (b) FMC+TFM, (c) Normal Beam PA-SAFT and (d) Angle Beam PA-SAFT

Figures 5.31(a) to (d) shows the results for a 20 deg. oriented slot by various techniques. The results are similar to the observations of a 0 deg. oriented slot.

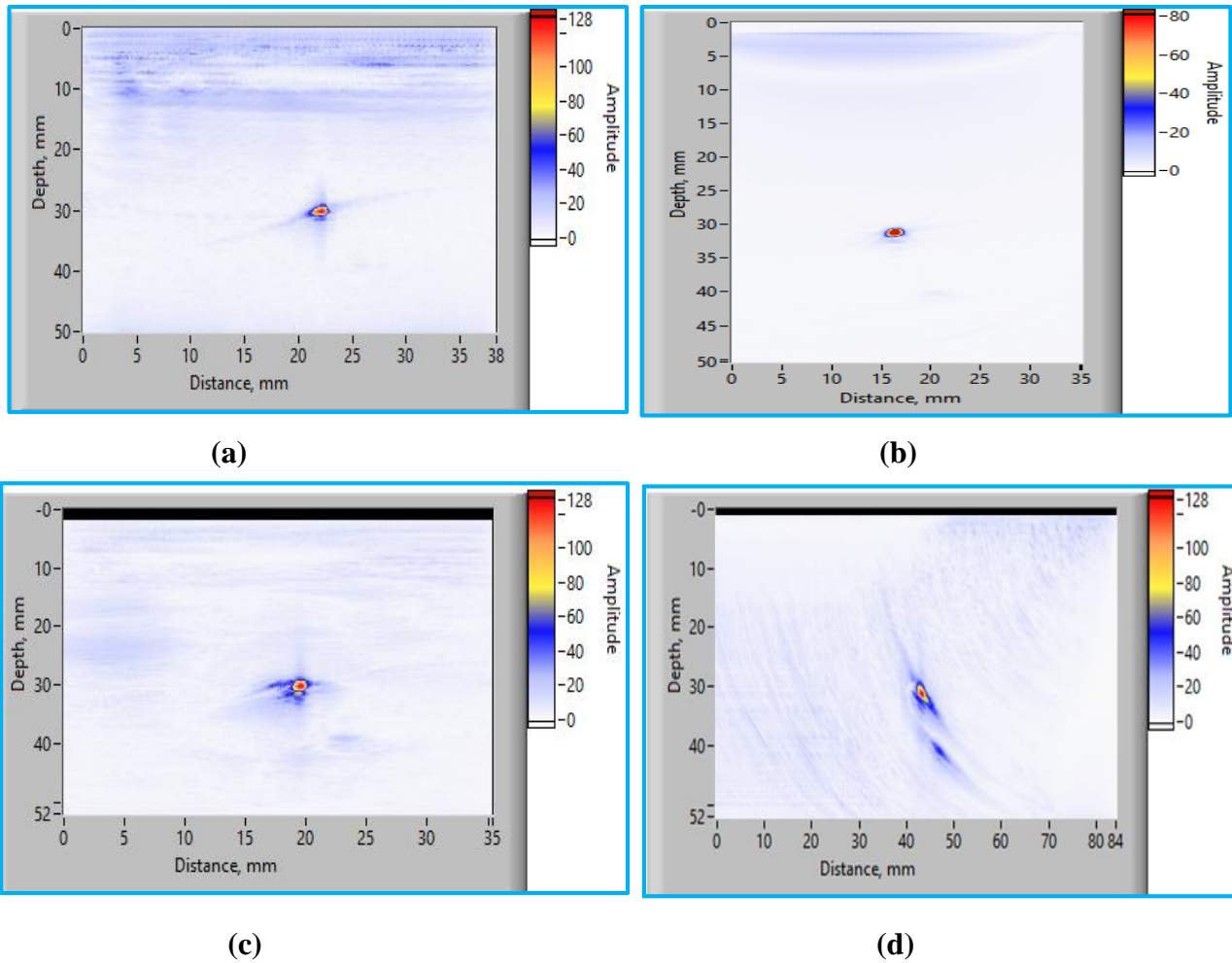


Figure 5.31: Processed B-scan images for a 20 deg. oriented planar flaw in 60 mm thick stainless steel plate (a) SFLA, (b) FMC+TFM, (c) Normal Beam PA-SAFT and (d) Angle Beam PA-SAFT

Table 5.6 gives the comparison of the results obtained by various techniques for a 0 deg. and 20 deg. inclined slots in this sample. The coordinates of the upper and lower tip are evaluated from the echodynamic plots as described in Section 5.3.1.4. The results are compared in terms of: (i) the accuracy of the assessment of depth (through-wall dimensions) and orientation of the flaw, and (ii) the relative amplitude difference between the upper and lower tip signals. For a 0 deg. oriented flaw, the true depth is 10 mm, while for a 20 deg. oriented flaw, the true depth is 9.6 mm.

Table 5.6: Comparison of results obtained on assessment of depth and orientation on thick SS block with simulated planar flaws by various techniques

Technique	Measured Depth (mm)	Measured Orientation (deg.)	Amplitude difference between upper and lower tip signals (dB)
SFLA 0 deg. slot	10.2	6	26
SFLA 20 deg. slot	9.3	23	25
PA-SAFT (NB) 0 deg. slot	10.1	5	18
PA-SAFT (NB) 20 deg. slot	9.1	21	16
PA-SAFT (AB) 0 deg. slot	10.2	3	9
PA-SAFT (AB) 20 deg. slot	9.1	21	8
FMC 0 deg. slot	10.5	3	36
FMC 20 deg. slot	9.5	22	28

The results indicate the following:

- The sensitivity for the detection of the lower tip by SFLA and FMC techniques is very poor. The amplitude difference between the upper and the lower tip is very high. It means that these two techniques are un-reliable for the detection and characterization of planar flaws located at a larger depth.
- The primary reason for the poor performance of SFLA and FMC techniques is the use of a single element for sound beam transmission, because of which the acoustic power incident on the flaw tip is very low.
- With PA-SAFT technique, there is a significant improvement in the amplitude of the lower

tip signal. This technique performed better than SFLA and FMC techniques.

- All the techniques are accurate in assessing the depth of the flaw and its orientation
- The best results in terms of the detection of flaw extremities are obtained by Angle beam PA-SAFT technique. This can be attributed to the better diffraction of the incident sound beam while using angle beam [218, 219]. This technique appears to be the most suitable for the detection and characterization of planar flaws in thick sections.

5.4 Angle Beam PA-SAFT technique

Angle beam PA-SAFT technique is used for the characterization of a 2.2 mm deep surface notch in a 25 mm thick aluminum plate, which simulates a surface breaking planar flaw like a crack. The linear array transducer is kept away from the notch (to simulate the field restrictions encountered during inspection of unground welds) and the data is acquired using 45 deg. longitudinal wave. The experimental set-up is shown in Figure 5.32. Details are given in Chapter 3, Section 3.8.



(a)



(b)

Figure 5.32: Experimental set-up for detection of surface planar flaw by Angle Beam PA-SAFT technique (a) Flaw on the back surface and (b) Flaw on the scanning surface

Figures 5.33(a) and (b) show the raw and the processed B-scan images respectively for the notch on the back surface.

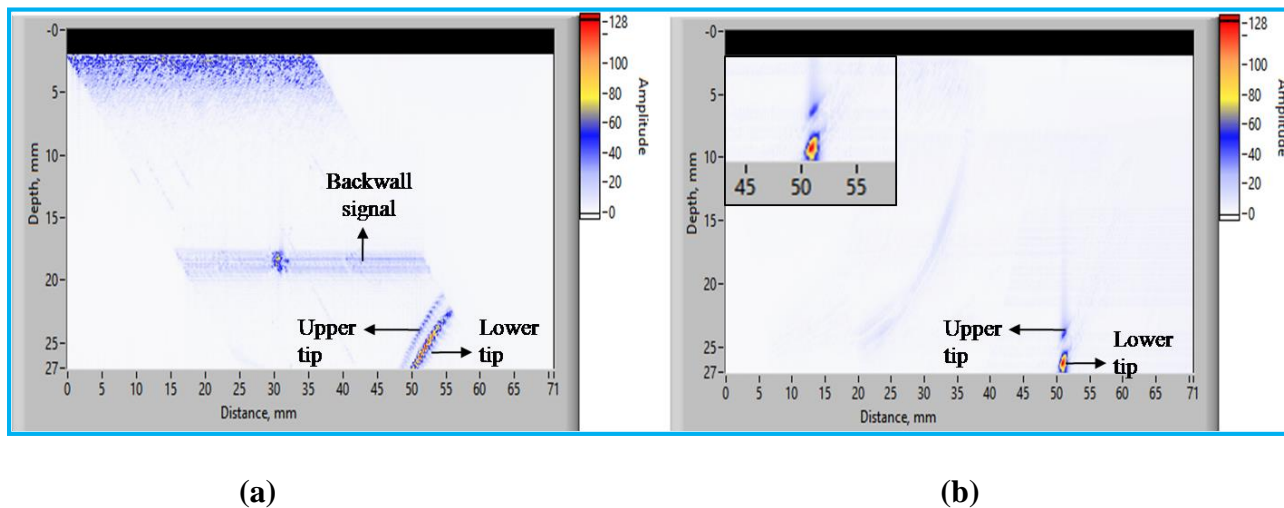


Figure 5.33: (a) Raw B-scan and (b) SAFT processed B-scan image for the notch on the back surface by Angle Beam PA-SAFT

The raw B-scan image shows signals of two types, one with constant time-of-flight, at a depth of around 18 mm, and others having a shape of hyperbola at the depth of around 25 mm. The signal with the constant time-of-flight is from the backwall and appears because of the normal beam component in the transmitted sound beam. This component gets generated as a result of excessive steering. Since the raw B-scan image in Figure 5.33(a) is depth-corrected, the sound path is multiplied by the cosine of the beam angle (which is 45 deg. in the present case). As a result, the signal from the backwall appears at the distance of 18 mm ($25 \text{ mm} \times \cosine \text{ of } 45 \text{ deg.}$). The raw B-scan image also shows signals with varying time-of-flight or depth. These signals are from the surface notch. The signals show varying time-of-flight because the notch extremities are seen by the divergent sound beam emanating from active apertures during electronic scan. Since the notch is on the backwall, the depth corrected path for the corner trap signal is approximately 25 mm. In

addition, there is another hyperbolic signal that appears before the corner trap signal. This signal is from the upper tip of the surface notch. The SAFT processed B-scan image is shown in Figure 5.33(b), which shows two spot indications, one for the corner trap and the other for the upper tip. From their locations with respect to the scanning surface, the depth of the notch is evaluated to be 2.2 mm, which is the true value.

The data for the same notch is also acquired at 1 skip, to simulate the flaw on the scanning surface. Figure 5.34(a) shows the raw B-scan image. The image shows the backwall signal at 18 mm and its multiple at 36 mm. The image also shows the hyperbolic signals from the notch at the depth of around 50 mm, one from the corner trap and the other from the notch tip. In addition, the raw B-scan image also shows similar hyperbolic signals at higher depth. In order to assess the origin of these signals, simulation studies are carried out by CIVA 11.

Figure 5.34(b) shows the simulation results under identical experimental conditions. The experimental raw B-scan image matches closely with the simulation results. From the simulation, the wave modes responsible for various signals in the raw B-scan image are assessed. The simulation studies indicated that the signals with constant time of flight are because of the normal beam component, the first set of hyperbolic signals are because of the interaction of longitudinal wave component with the notch and the second set of hyperbolic signals appearing at higher depths are because of the interaction of mode converted shear wave with the notch. The backwall and the signals from the shear wave component disappear completely on SAFT processing. Only the signal from the corner trap and the tip signal from the notch due to the longitudinal component are left behind. These two signals are clearly visible in the processed B-scan image as shown in Figure 5.34(c). The magnified view of the signal from the notch tip is shown in the top-left corner. The depth of the notch assessed by angle beam PA-SAFT from the processed B-scan image is found

to be 2.2 mm, which is the actual value.

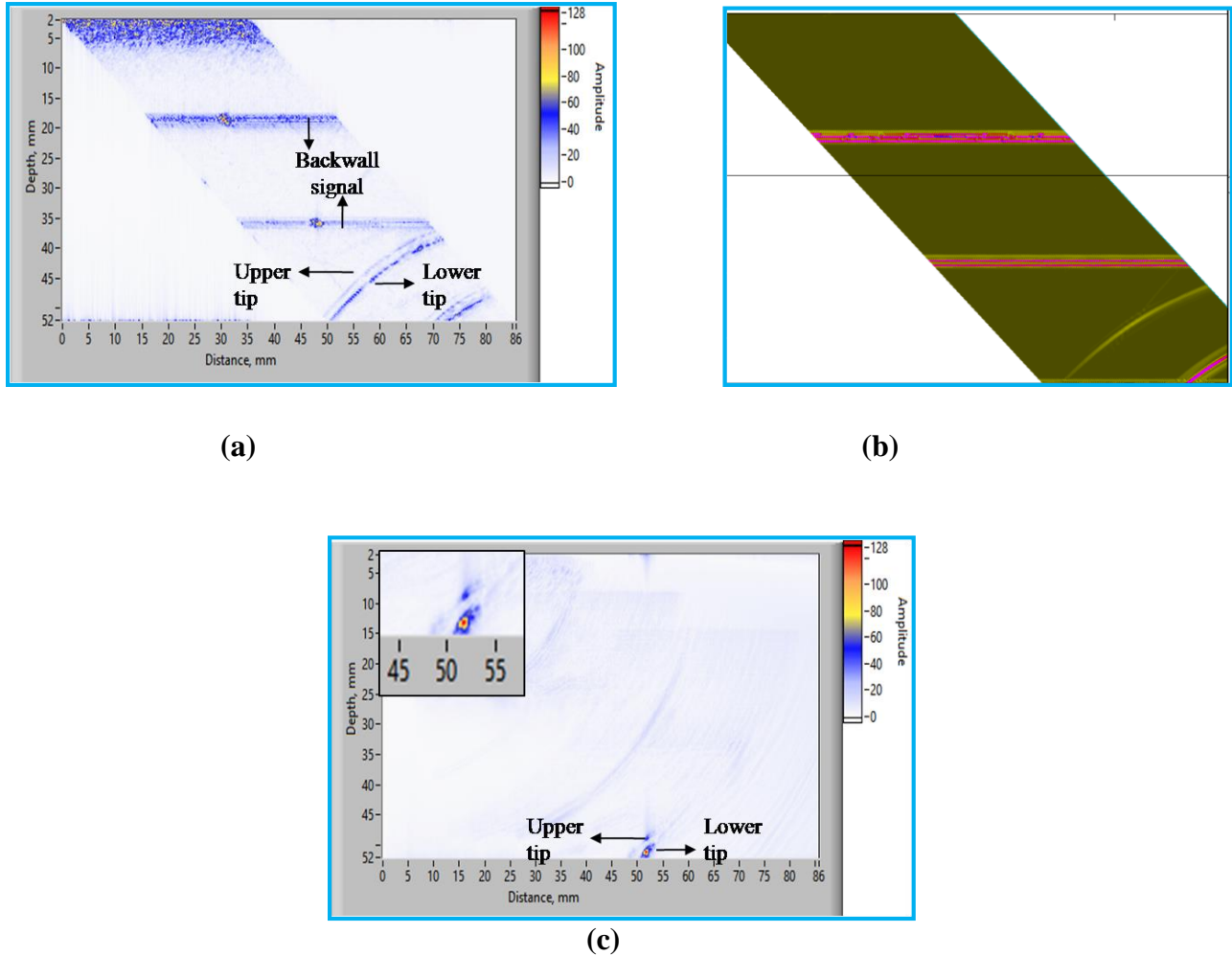


Figure 5.34: (a) Raw B-scan and (b) Simulation result and (c) SAFT processed B-scan image for the notch on the scanning surface by Angle Beam PA-SAFT

5.5 Uncertainty in depth sizing of planar flaws using SFLA and PA-SAFT Techniques

Depth sizing (height or through-wall dimension) of planar flaws using SFLA and PA-SAFT techniques is based on the location of the flaw extremities from the scanning surface. The uncertainty in the depth sizing is governed by the uncertainty associated in locating upper and

lower tips of the flaw. The following factors contribute to uncertainty in depth sizing while using SFLA and PA-SAFT techniques:

- **Time of Flight measurement (E1)**

The raw data for SFLA and PA-SAFT techniques is acquired at 100 MHz sampling rate. This corresponds to a time of flight error of 10 ns. In terms of distance in the material (Velocity in steel = 6 $\mu\text{m}/\text{ns}$), this will lead to an error of 0.03 mm ($(10/2) \text{ ns} \times (6 \mu\text{m}/\text{ns})$) in locating the upper or lower tip of the flaw. Hence, the maximum error in depth sizing due to time-of-flight measurement will be 0.06 mm.

- **Assumed sound velocity in the material (E2)**

The sound velocity in the test sample may be different than the sound velocity which is given as an input to the software for SAFT processing of acquired data. This will introduce errors in position of upper and lower tips of the flaw from the scanning surface. Unlike in the case of the error due to time of flight measurement, the direction of error in this case will be the same for upper and lower tips of the flaw. In the case of steel, 2% error in the assumed velocity with respect to the actual velocity will lead to an error $\pm 0.2 - 0.3$ mm in the position of the flaw tips located at a distance of 10 to 15 mm from the scanning surface. The magnitude of this error will increase as one goes deeper into the material. However, the through-wall dimension is calculated from the difference in the location of the upper and the lower tips of the flaw from the scanning surface. Hence the error in depth sizing due to sound velocity will be affected by the actual depth of the flaw instead of the relative position of the upper and the lower tips from the scanning surface. For instance, for a 10 mm height flaw, an error of 2% in sound velocity will lead to an error of 0.2 mm in estimation of the through-wall dimension.

The error in sound velocity will also affect the quality of SAFT processed image, as discussed in Chapter 4 Section 4.3.2.2.1. Figures 5.35(a) and (b) show the SAFT processed B-scan images processed with the correct sound velocity (6300 m/s) and the incorrect sound velocity (6200 m/s) respectively. The magnified view is also shown in the top-left corner. The raw data is collected on an aluminum block containing 2.2 mm deep notch on the back surface by SFLA technique.

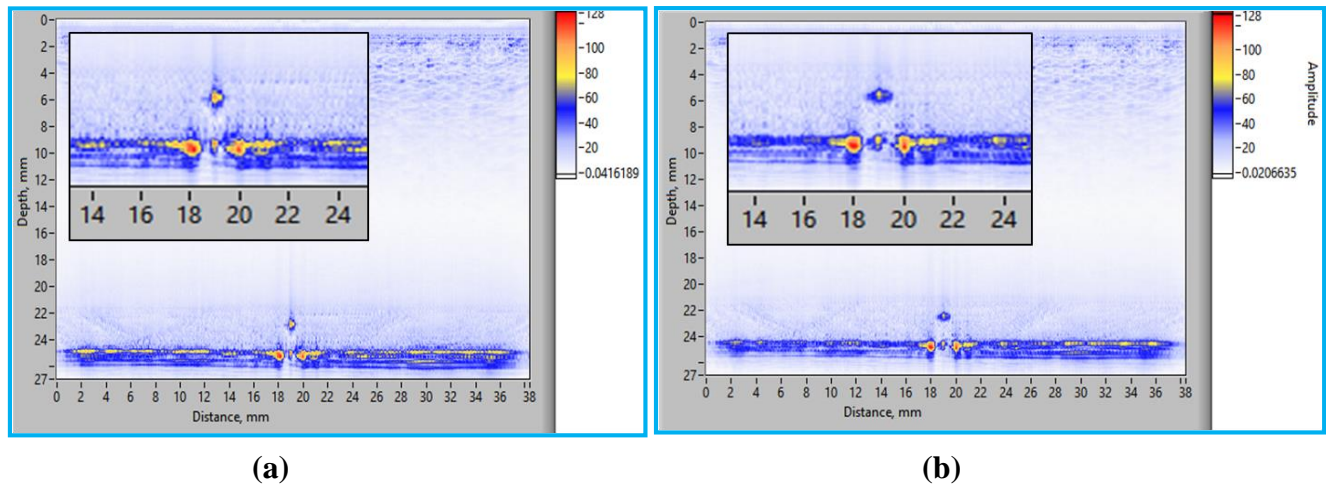


Figure 5.35: SAFT processed B-scan images of a notch on the back surface in aluminum plate (actual sound velocity = 6300 m/s) by SFLA technique processed with (a) Sound velocity 6300 m/s and (b) Sound velocity 6200 m/s

When the input sound velocity during SAFT processing matches with the velocity in the sample (6300 m/s), the signal from the flaw tip is very sharp in the processed B-scan data due to satisfactory constructive interference. The location of the flaw tip from the scanning surface is found to be 22.8 mm. With the plate thickness as 25 mm, the depth of the notch evaluated by SFLA is 2.2 mm, which is the real depth. When the input velocity during SAFT processing does not match with the velocity in the material, there is a broadening of the signal from flaw tip. This is also observed while studying the effect of SAFT processing parameters on the sound beam focusing using SFLA (Chapter 4, Section 4.3.2.2.1). The location of the flaw tip from the surface

is found to be 22.5 mm (lower than the previous case because of lower value of the input sound velocity). This gives the value of 2.5 mm for the depth of the notch, which is 0.3 mm higher than the true value. The broadening of the flaw tip signal, when the input sound velocity differs from the actual, is because of the fact that the constructive interference at the tip location and the destructive interference adjacent to it are not effective. During the characterization of planar flaws, if the upper and lower tips show wide signals, then it can serve as a feedback that the assumed sound velocity in the material could be different than the actual velocity. In such a case, the sound velocity in the material should be checked and used during SAFT processing. Incorrect sound velocity not just affect the positioning of the tip signal but also its amplitude. Hence in addition to the depth sizing error, this parameter also affects signal to noise ratio.

- **Half cycle error (E3)**

For a 5 MHz linear array, the half cycle of the pulse corresponds to 100 ns. In terms of distance, this will correspond to 0.6 mm in steel. With pulse-echo mode of data acquisition, this will lead to an error of 0.3 mm in locating the upper tip and the lower tip of the flaw. Since this error can be in opposite direction for both the tips, for depth assessment of the flaw the total error due to half cycle will be 0.6 mm.

Considering the above factors, uncertainty in terms of the root mean square error in the depth sizing (E) of planar flaws by SFLA and PA-SAFT techniques comes to 0.4 mm ($E = \sqrt{E_1^2 + E_2^2 + E_3^2}$) [220, 221].

5.6 Summary of the chapter

- ✓ SFLA and PA-SAFT techniques showed excellent ability to the detection of volumetric flaws located one below the other up to a depth of 60 mm in steel. The sensitivity of the order of 0.022 SDR could be achieved by these techniques.
- ✓ Under identical test conditions, PA-SAFT technique could detect volumetric flaws that are located deeper when compared to the results obtained by SFLA and FMC techniques. This can be attributed to a higher acoustic power of the sound beam in the material while using PA-SAFT technique.
- ✓ The lateral resolution obtained by SFLA and PA-SAFT techniques is smaller than the ones observed by conventional phased array using large number of elements as active aperture and comparable to FMC + TFM technique.
- ✓ SFLA and PA-SAFT techniques could detect very fine volumetric flaw (0.5 mm dia.) located at the distance of 200 mm from the surface in aluminum.
- ✓ With respect to the detection of volumetric flaws at the same depth, both SFLA and PA-SAFT techniques showed good resolving ability. Both the techniques could detect the flaw located in the region beyond the linear array. The lateral coverage achieved by both the techniques is approximately 90 mm, which includes the region of approximately 25 mm out of the array. However, with both the techniques the focusing beneath the array is better than in the region away from it.
- ✓ With SFLA technique, it is possible to achieve the resolution of 0.6 mm at the depth of 20 mm in steel using 10 MHz, 0.3 mm pitch linear array. With PA-SAFT technique, the resolution achieved under similar conditions is 0.9 mm. The lower value for the resolution for SFLA

technique could be attributed to the smaller size of the piezoelectric element for sound beam transmission as compared to the size of the virtual source in PA-SAFT.

- ✓ For planar flaws in thin sections (25 mm), both SFLA and PA-SAFT techniques are able to detect and accurately characterize the flaws in terms of the depth and orientation. The results are comparable to the ones obtained by FMC + TFM technique.
- ✓ For thick section (60 mm), SFLA and FMC + TFM are unable to detect the lower tip of planar flaws satisfactorily. With PA-SAFT technique, the detection improves, but there is also a slight increase in the spread of the signals. The best results for the detection of upper and lower tips of a planar flaw in thick section are obtained by Angle beam PA-SAFT technique.
- ✓ Angle beam PA-SAFT technique is able to accurately assess the depth of a surface notch (scanning surface and back surface) in 25 mm thick aluminum plate.
- ✓ The factors contributing to the errors in the depth estimation of planar flaws by SFLA and PA-SAFT techniques are identified. The cumulative root mean square error in the depth sizing of planar flaws by SFLA and PA-SAFT techniques in steel using 5 MHz linear array and 100 MHz sampling rate is found to be 0.4 mm. The error observed during the experimental work in the depth sizing of simulated planar flaws in thin and thick stainless steel plate is found to be within this value.

DEMONSTRATING THE EFFECTIVENESS OF SFLA AND PA-SAFT TECHNIQUES FOR DETECTION AND CHARACTERIZATION OF FLAWS IN WELD JOINTS

6

6.1 Introduction

The effectiveness of SFLA and PA-SAFT techniques for the detection and characterization of volumetric and planar flaws is assessed using samples containing simulated flaws in the form of side drilled holes and EDM slots of different orientations. The results are described in Chapter 5. Unlike simulated flaws, the real flaws do not have smooth reflecting surfaces. They may be unfavorably oriented to the incident ultrasound, can exhibit branching and are much tighter (very fine opening) as compared to the simulated flaws. These conditions may pose additional challenges in their detection and characterization. In order to study these aspects and demonstrate the effectiveness of SFLA and PA-SAFT techniques for the detection and characterization of real flaws, experiments are carried out using different weld samples in the plate geometry made of carbon steel and austenitic stainless steel. These samples contain volumetric flaws in the form of clustered porosity and slag, and the planar flaws in the form of cracks and lack of sidewall fusion. The results of flaw characterization studies on these weld samples are described in this Section.

Further, a study is also undertaken towards the application of SFLA and PA-SAFT techniques for in-service inspection of a weld joint in thick pressure vessel. In this regard, experiments are carried out on the mock-up block of a circumferential weld joint (C1) in the reactor pressure vessel of a nuclear boiling water reactor (BWR). First, the conventional phased array technique based on focal laws for in-service inspection of this weld joint is employed. Subsequently, a

study is undertaken to assess whether similar or better results can be obtained by SFLA and PA-SAFT techniques using much lesser resources (in terms of total number of active elements and the configuration of phased array instrumentation) as compared to the conventional phased array. The study involved both, simulation using CIVA 11 and the experimental work on the mock-up. The simulation studies are aimed at the optimization of the active aperture for PA-SAFT technique and evaluate the sound beam coverage in the weld location by various techniques. Based on the results of simulation studies, experimental work is undertaken using the mock-up. The challenges involved with the in-service inspection of this weld joint, the results of the conventional phased array examination, the analysis of the results obtained by simulation studies, the results of experimental work using SFLA and PA-SAFT techniques and the comparison of various techniques in terms of the detection and characterization of reference flaws on the mock-up of C1 weld joint are described in this chapter.

6.2 Velocity Profiling across the weld

In the previous chapter (Section 5.5), it is shown that the difference in the actual sound velocity in the material and the one assumed during SAFT processing has a significant impact on the image quality and the accuracy in flaw characterization. During the application of SFLA and PA-SAFT techniques for characterization of real flaws in carbon steel weld joints, the linear array is placed across the flushed weld bead as shown in Figure 6.1. With this arrangement, the sound beam passes through different regions comprising of: (i) completely base metal, (ii) partially base metal and partially weld and (iii) completely weld metal. During SAFT processing, the sound velocity is assumed to be constant for the above three regions. To confirm this, a B-scan image containing the first and the second backwall signals is acquired by electronic scanning using a 10 MHz, 0.3 mm pitch linear array by placing the array as shown in Figure 6.1. A single

element is used for transmission and reception. From the B-scan image, A-scan signals for each element are extracted. From the time of flight difference between the two backwall signals and the thickness (measured by micrometer), the sound velocity corresponding to each A-scan is determined with an accuracy of ± 3 m/s.

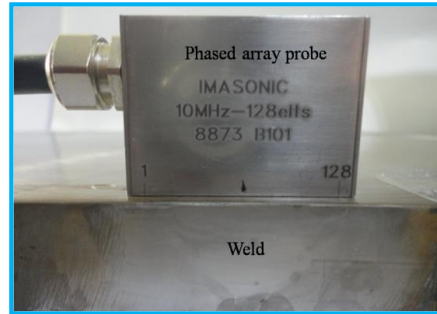


Figure 6.1: Experimental set-up for data acquisition on weld samples by SFLA, PA-SAFT and FMC techniques

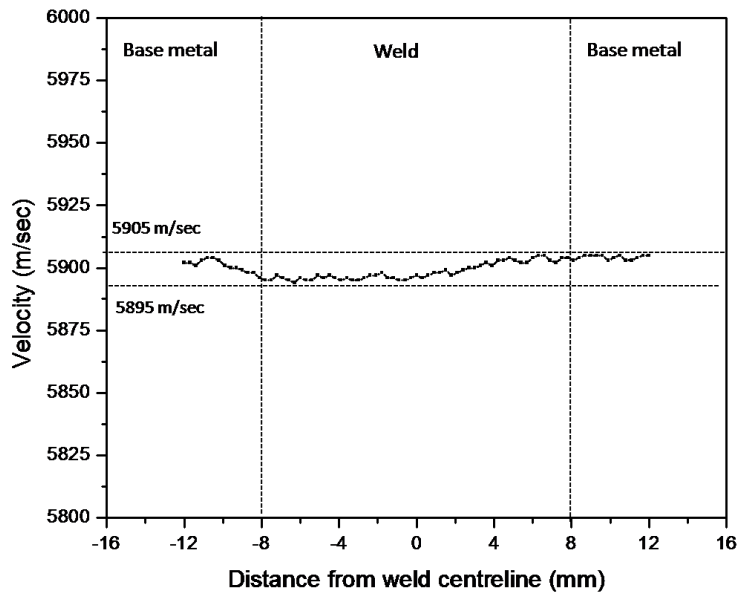


Figure 6.2: Sound velocity profile across the weld and base metal region

Figure 6.2 shows the results of sound velocity measurement across the carbon steel weld sample. The velocity is found to vary from 5895 m/s to 5905 m/s, which is negligible. Based on this

result, a single value of sound velocity is used for processing of the entire data in all the weld samples made of carbon steel, including the weld region.

While dealing with an acoustically an-isotropic material such as austenitic stainless steel weld, a significant difference in sound velocity is expected between the weld metal and the parent metal. Moreover, the sound beam also experiences skewing. If a single value of sound velocity is used during SAFT processing and the beam skewing effect is not considered, the sound beam focusing will not be effective, leading to poor quality of the processed image and uncertainty in depth assessment of weld flaws. In the present investigation, the austenitic stainless steel weld samples are used to study the effectiveness of Angle Beam PA-SAFT technique for characterization of flaws in the weld with an un-ground weld beam. During data acquisition on these samples, the sound beam passes through the parent metal only. Hence, a single value of sound velocity corresponding to the austenitic stainless steel plate material (base metal) is used for processing of raw B-scan images. Since the travel path of the sound beam is limited to the base metal, the acoustic anisotropy in the weld material is not expected to affect the image reconstruction and thereby the accuracy in depth assessment of weld flaws.

6.3 Characterization of volumetric weld flaws

The carbon steel plate samples with weld flaws in the form of clustered porosity and slag are examined by SFLA, PA-SAFT and FMC techniques. The data from these samples is acquired using 10 MHz, 0.3 mm pitch, 64 elements linear array. For data acquisition, the linear array is placed on the sample as shown in Figure 6.1. The experimental details are given in Chapter 3, Section 3.9.

6.3.1 Clustered Porosity

The photograph of the clustered porosity is shown in Figure 6.3. The photograph shows that the clustered porosity is present in the weld of approximately 15 mm thickness. Some porosities are circular while the others are elongated. They have different dimensions and are closely spaced. The porosities are located very close to the back surface of the weld.



Figure 6.3: Clustered porosity in the weld sample (Scale in mm)

The raw and the processed SFLA images of the clustered porosity are shown in Figures 6.4(a) and (b) respectively. The raw B-scan image shows multiple signals from the cluster of porosities. The signals are well spread out, which is typically obtained when a divergent sound beam scans across a point reflector. Since porosities are very closely spaced, the signals from them cannot be resolved in the raw image. The SAFT processed image shows numerous spot indications, very closely spaced, like a cluster.

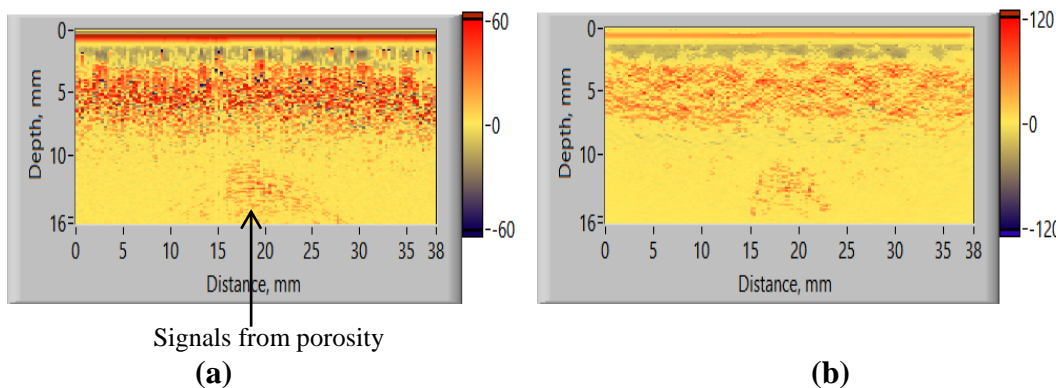


Figure 6.4: (a) Raw B-Scan (b) SAFT processed B-scan image showing multiple spot indications from clustered porosity in the weld sample by SFLA technique

Figures 6.5(a) and (b) shows the raw and the processed B-scan images of the clustered porosity by PA-SAFT technique respectively. The results are similar to SFLA technique, except that the spread of signals in the processed B-scan image is higher.

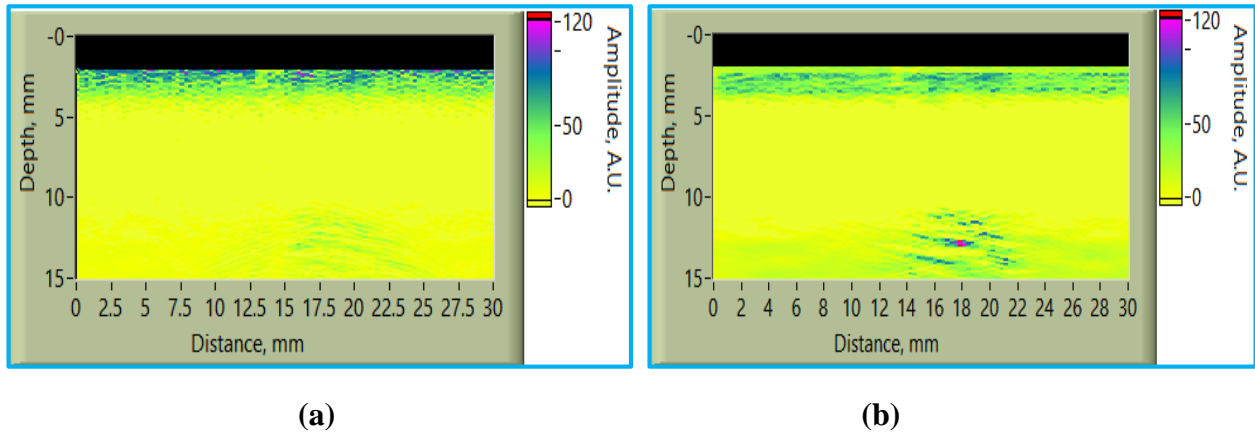


Figure 6.5: (a) Raw B-Scan (b) SAFT processed B-scan image showing multiple spot indications from clustered porosity in the weld sample by PA-SAFT technique

Figure 6.6 shows the FMC + TFM image of the clustered porosity. The results are similar to the ones obtained by SFLA technique.

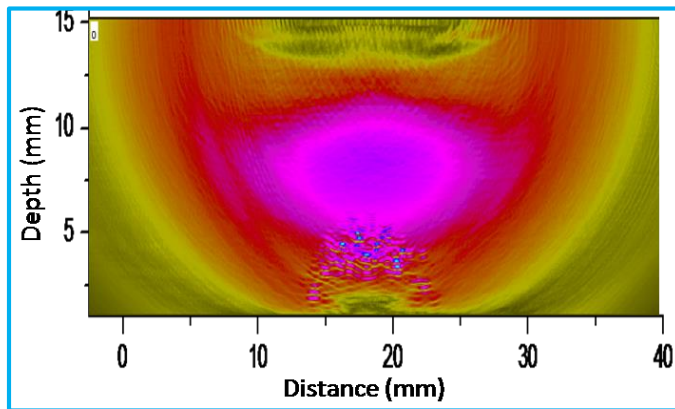


Figure 6.6: B-scan image showing multiple spot indications from clustered porosity in the weld sample by FMC + TFM technique

The processed B-scan images by SFLA, PA-SAFT and FMC techniques show more number of porosities than what are seen in the photograph. This is because of the fact that while the

photograph shows porosities only for a one section (where the sample has been cut), the raw B-scan data acquired by these techniques has signals from porosities in the adjacent sections also that fall within the beam spread. Each of these sections has porosities of different size and distribution, which get imaged in the raw as well as the processed B-scan. Another reason for more number of indications in the processed B-scan images is the multiple scattering of sound beam by closely spaced pores. During the study on closely spaced volumetric flaws (Section 5.2.3), it is observed that multiple scattering from side drilled holes is responsible for additional signals in the processed B-scan images. The results obtained from the clustered porosity is in line with these observations. Although the B-scan images clearly bring out that the flaw under consideration is a cluster of porosities, an accurate assessment regarding the number of pores cannot be made by these techniques.

6.3.2. Slag Inclusion

Figure 6.7 shows the photograph of the slag inclusion. The photograph shows that the slag inclusion is present in the weld of approximately 15 mm thickness. It is fairly wide and has an elongated shape. The inclusion is located close to the back surface and is slightly tilted towards one side.

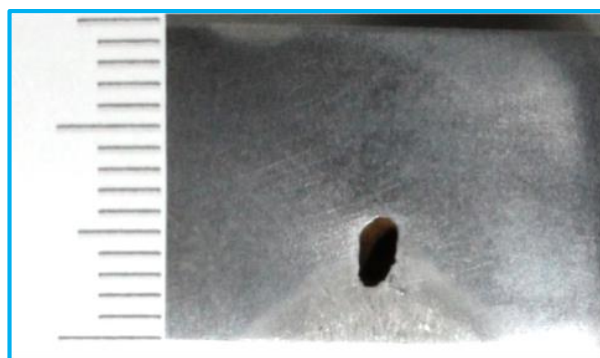


Figure 6.7: Slag inclusion in the weld sample (Scale in mm)

The raw and the SAFT processed B-scan images for the slag inclusion by SFLA technique is shown in Figures 6.8(a) and (b) respectively. The raw image shows typical hyperbolic signals from the upper and the lower tips of the slag. The upper tip signal in the raw B-scan image is fairly stronger and shows a larger spread as compared to the lower tip signal.

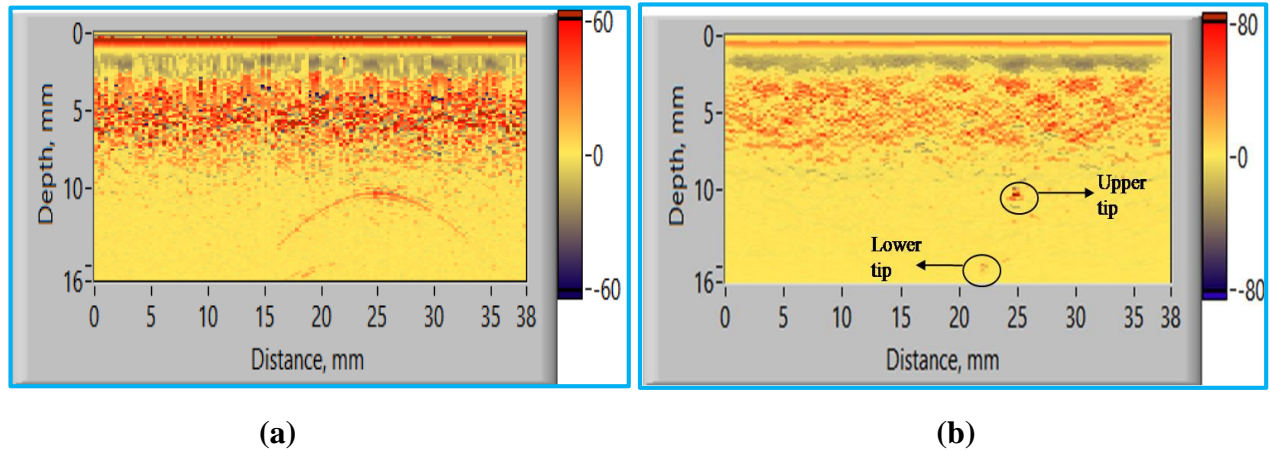
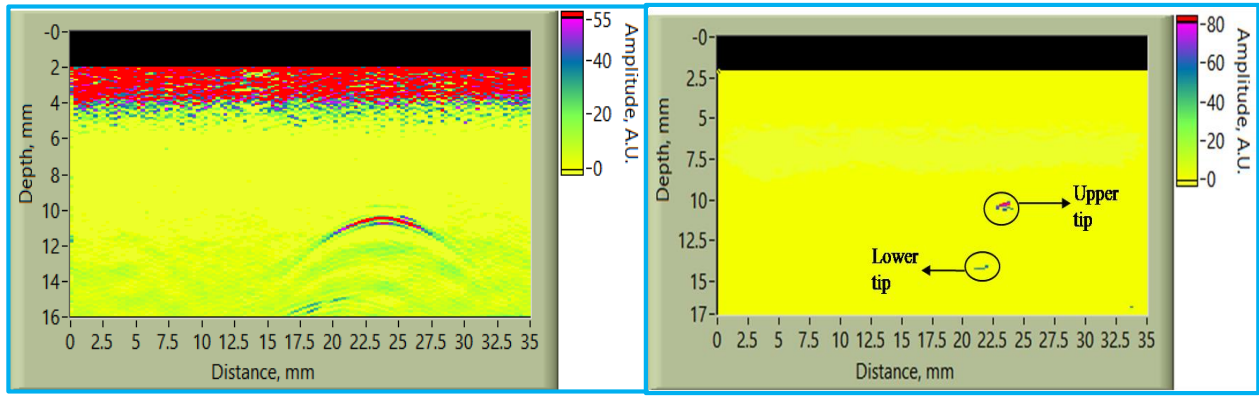


Figure 6.8: (a) Raw B-Scan (b) SAFT processed B-scan image showing the upper and the lower tip signals from the slag inclusion in the weld sample by SFLA technique

On SAFT processing, the two signals are reduced to spot indications. The spots are laterally shifted indicating that the flaw is tilted to the right side, which is indeed the case.

The raw and the processed B-scan images of the slag inclusion by PA-SAFT technique are shown in Figures 6.9(a) and (b) respectively. The image clearly shows the upper and the lower tips of the slag.



(a)

(b)

Figure 6.9: (a) Raw B-Scan (b) SAFT processed B-scan images showing the upper and the lower tip signals from the slag inclusion in the weld sample by PA-SAFT technique

The FMC + TFM result is shown in Figure 6.10. In spite of using only 64 of the total 128 elements, the FMC results are comparable to the results obtained by SFLA and PA-SAFT techniques.

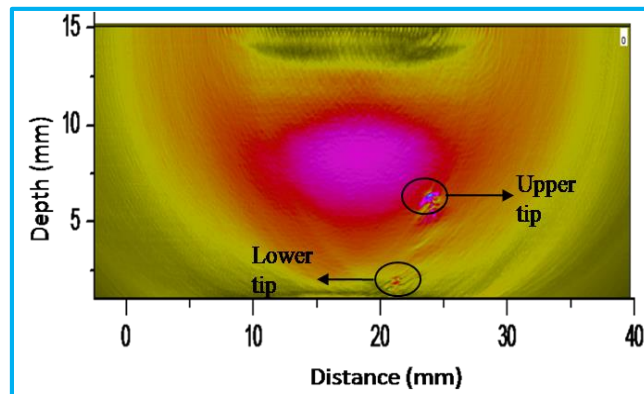


Figure 6.10: B-scan image showing the upper and the lower tip signals from the slag inclusion in the weld sample by FMC + TFM technique

6.3.3 Summary of observations on volumetric flaws

The following is the summary of observations from the results obtained by various techniques for the detection and characterization of volumetric weld flaws:

Table 6.1 shows the results of the depth sizing of clustered porosity and slag inclusion by various techniques. The depth sizing is done by finding out the location of the flaw extremities with

respect to the scanning surface from the processed A-scan data and the echodynamic plot as described in Section 5.3.1.4. The true depth is found out by metallography after sectioning the sample at the flaw location.

Table 6.1: Results of depth sizing of volumetric flaws by various techniques

Flaw Type	True depth (mm)	Depth measured by SFLA (mm)	Depth measured by PA-SAFT (mm)	Depth measured by FMC (mm)
Clustered porosity	3.7	4.0	3.6	3.5
Slag	3.9	4.1	3.8	3.8

- For the cluster porosity, all the techniques show numerous closely spaced spot indications that are typically obtained from a cluster of flaws.
- The number of signals in the SAFT processed B-scan images are more than what are observed in the photograph. This can be attributed to the beam spread effect, which is responsible for the detection of more number of porosities from the adjacent sections as well as multiple scattering from closely spaced pores.
- For the slag inclusion, all the techniques could detect and locate its upper and lower tips. The amplitude of the lower tip signal is found to be lesser than the upper tip, but still sufficiently above the background noise.

- The depth sizing of the cluster porosity and the slag inclusion by SFLA and PA-SAFT techniques is found to be accurate and comparable to FMC+TFM technique.

6.4. Characterization of planar weld flaws

The planar flaws in the form of lack of side wall fusion and root crack in the weld are characterized by SFLA and PA-SAFT techniques. The data on these samples is acquired using 10 MHz, 0.3 mm pitch, 128 elements linear array. The SFLA, PA-SAFT and FMC data is collected by placing the transducer over the weld as shown in Figure 6.1. The raw data is then processed by SAFT for SFLA and PA-SAFT techniques and by TFM algorithm for FMC. The experimental details are given in Chapter 3, Section 3.9.

6.4.1 Lack of sidewall fusion

The photograph of the lack of sidewall fusion is shown in Figure 6.11.

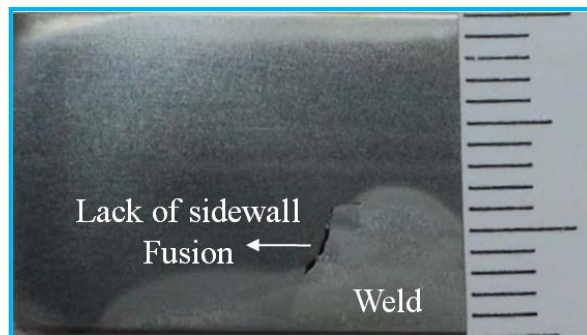


Figure 6.11: Lack of sidewall fusion in the weld sample (Scale in mm)

The photograph shows that the lack of sidewall fusion is present in the weld having a thickness of approximately 15 mm. It has a very narrow width, unlike the volumetric flaws described above, and is oriented in the thickness direction. It is present at the interface of the weld pool and the parent metal, and is located close to the backwall.

The raw and SAFT processed B-scan images using SFLA technique for the lack of sidewall

fusion are shown in Figures 6.12(a) and (b) respectively. The raw image indicates two hyperbolic signals corresponding to the upper and lower tip of the lack of sidewall fusion. These signals are laterally shifted, which indicates that the flaw is tilted towards one side. Due to the presence of the flaw, there is also a slight reduction in the amplitude of the backwall signal just below the flaw. On SAFT processing, the hyperbolic signals are reduced to two spot indications. From the processed B-scan image, the coordinates of the upper and the lower tips are found out, from where the through-wall dimension of the lack of sidewall fusion and its orientation are found out.

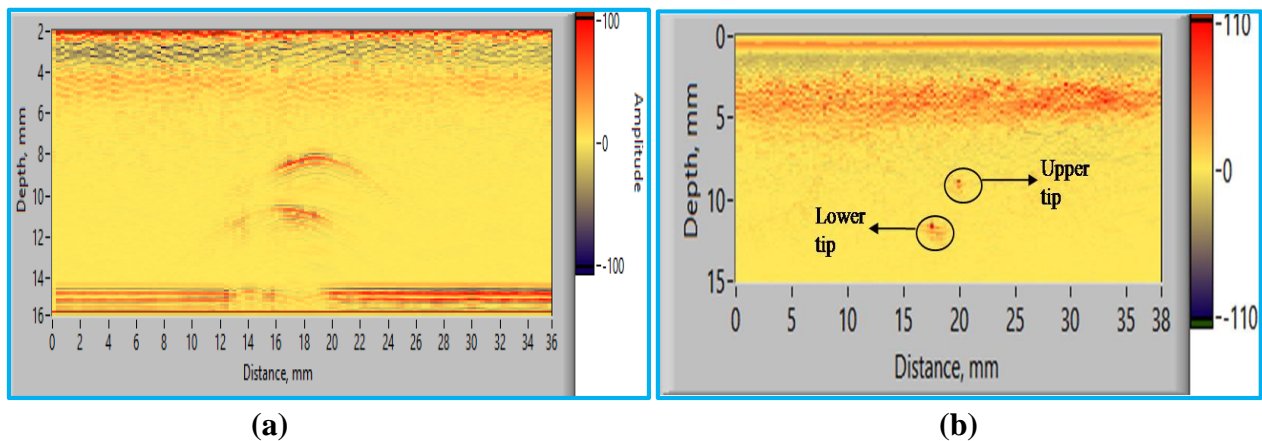


Figure 6.12: (a) Raw B-Scan (b) SAFT processed B-scan image showing the upper and the lower tip signals from the lack of fusion in the weld sample by SFLA technique

Figures 6.13 (a) and (b) shows the raw and the SAFT processed B-scan images respectively using PA-SAFT technique. The results are similar to the ones observed by SFLA technique. Since the PA-SAFT technique uses a group of elements for sound beam transmission, the sound wave amplitude incident at the flaw tips is expected to be higher. This is reflected in better signal to noise ratio in the raw as well as in the processed B-scan images using PA-SAFT technique as compared to SFLA.

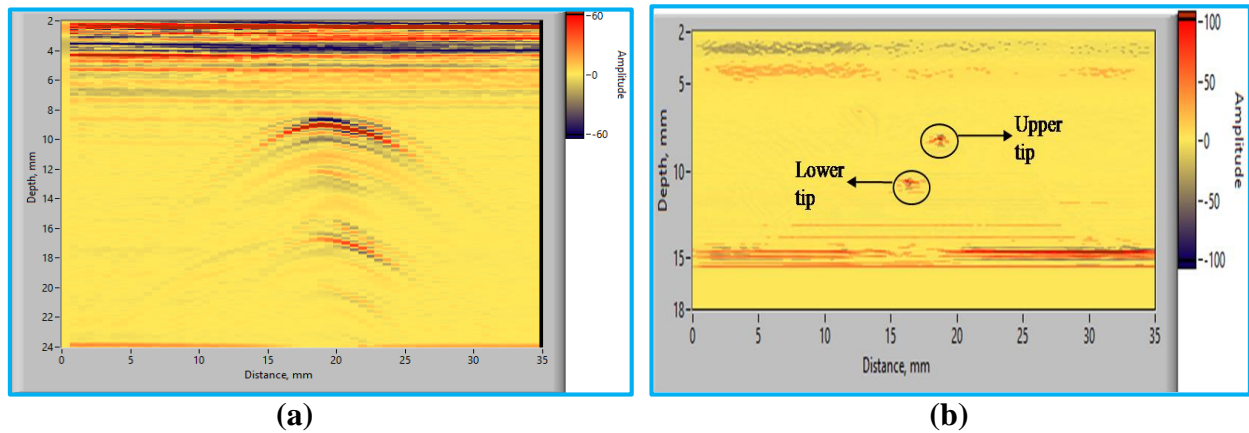


Figure 6.13: (a) Raw B-Scan (b) SAFT processed B-scan image showing the upper and the lower tip signals from the lack of fusion in the weld sample by PA-SAFT technique

Figure 6.14 shows the FMC + TFM image for the lack of sidewall fusion. In this case too, fairly strong signals corresponding to the upper and the lower tips of the flaw are seen. Although the total effective aperture (TEA) at the scanning surface comprise of only 64 elements as compared to 128 elements using SFLA and PA-SAFT techniques, the flaw tips are imaged satisfactorily.

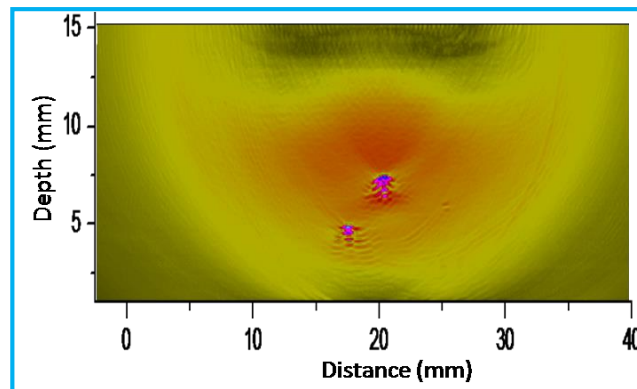


Figure 6.14: B-scan image showing the upper and the lower tip signals from the lack of fusion in the weld sample by FMC + TFM technique

One reason for this is that the flaw tips are located within the depth of 15 mm from the scanning surface. It is observed during the study on the effect of TEA on sound beam focusing (Chapter 4, Section 4.3.2.1.4) that up to 25 mm depth, even with lesser TEA (64 elements instead of 128 elements with 10 MHz, 0.3 mm pitch linear array) one can achieve satisfactory focusing.

6.4.2 Root crack

The photograph of the root crack is shown in Figure 6.15. The crack is present in the weld having a thickness of approximately 10 mm. Like the lack of sidewall fusion, the root crack also has a very narrow width, and is oriented in the thickness direction. The crack is connected to the backwall and does not show much tilt.

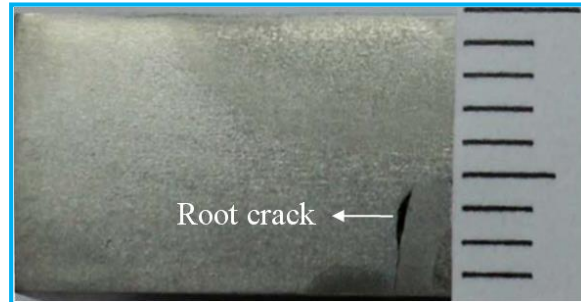


Figure 6.15: Root crack in the weld sample (Scale in mm)

The raw and the SAFT processed B-scan images using SFLA technique for the root crack are shown in Figures 6.16(a) and (b) respectively.

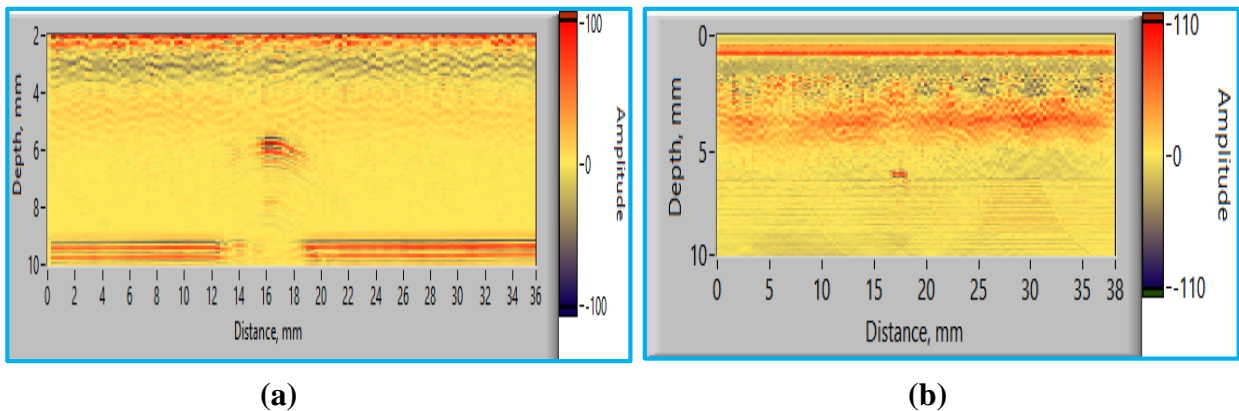


Figure 6.16: (a) Raw B-Scan (b) SAFT processed B-scan image showing the crack tip signal of the root crack in the weld sample by SFLA technique

The raw image indicates a single hyperbolic signal, corresponding to the upper tip of the crack. There is no bottom tip signal as the crack is open to the surface. Due to the presence of the crack, there is a significant drop in the amplitude of the backwall signal. On SAFT processing, the

hyperbolic signal is reduced to a spot indication. From the processed image, the depth of the crack is found out.

Figures 6.17(a) and (b) shows the raw and the processed B-scan images respectively using PA-SAFT technique. As seen with the lack of fusion, the signal to noise ratio is better than SFLA technique.

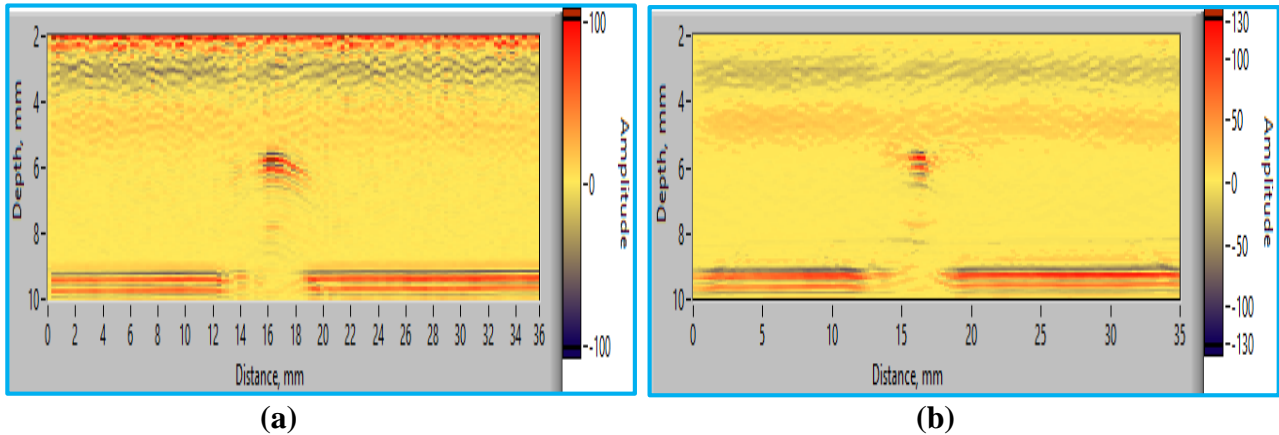


Figure 6.17: (a) Raw B-Scan (b) SAFT processed B-scan image showing the crack tip signal of the root crack in the weld sample by PA-SAFT technique

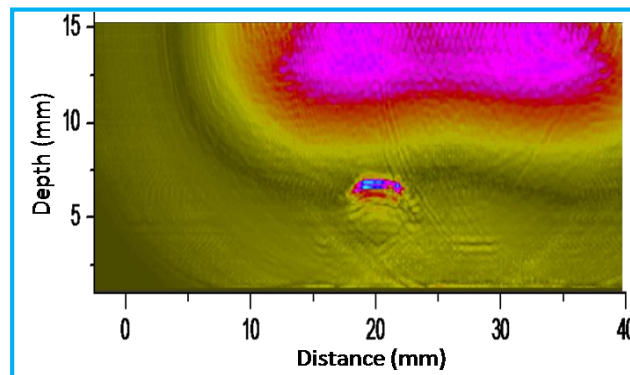


Figure 6.18: B-scan image showing the crack tip signal of the root crack in the weld sample by FMC + TFM technique

Figure 6.18 shows the FMC+TFM image for the root crack. In this case too, a distinct high amplitude signal from the upper tip of the crack is seen in the B-scan image.

6.4.3 Summary of observations on planar flaws

The following is the summary of observations on the results obtained by various techniques for the detection and characterization of planar weld flaws:

Table 6.2 shows the results of depth sizing and orientation of lack of fusion and root crack by various techniques. The coordinates of the flaw tip(s) are found out from echodynamic plot as described in Section 5.3.1.4.

Table 6.2: Assessment of flaw height and orientation of planar flaws in the weld samples by SFLA, PA-SAFT and FMC techniques

Flaw Type			SFLA		PA-SAFT		FMC	
	True orientation (deg.)	True depth (mm)	Angle (deg.)	Depth (mm)	Angle (deg.)	Depth (mm)	Angle (deg.)	Depth (mm)
Lack of sidewall fusion	40	3.0	39	2.9	39	2.8	42	2.8
Root crack	-	3.3	-	3.5	-	3.5	-	3.6

- For the lack of sidewall fusion, all the techniques show two spot signals corresponding to the upper and lower tips of the flaw. These signals show good amplitude, well above the background noise level.

- For the root crack, all the techniques could detect and locate the crack tip. There is a significant drop in the amplitude of the backwall signal, which indicates that the crack is opening to the back surface.
- The depth sizing of lack of fusion and the root crack and the assessment of orientation of the lack of fusion are found to be very accurate using SFLA and PA-SAFT techniques.
- The results on the detection and characterization of planar flaws in the weld joint in relatively thin sections (up to 15 mm) by SFLA and PA-SAFT techniques are comparable to the results obtained by FMC + TFM technique

6.5. Characterization of planar weld flaws by Angle beam PA-SAFT technique

During the study on the characterization of weld flaws using SFLA and PA-SAFT techniques, the linear array is placed over the weld bead so that the majority of elements take part in the image formation. This may not be possible in cases, when the weld bead is not flushed. In such cases, Angle Beam PA-SAFT provides a good alternate. The effectiveness of Angle Beam PA-SAFT for the detection and the depth sizing of planar flaws is assessed on the machined notch in aluminum plate. The results are described in Chapter 5, Section 5.4. In order to assess, whether this technique shows promising results on the real weld flaws, experiments are carried out on a 26 mm thick butt weld of austenitic stainless steel with an unground weld bead. One of the welds has a crack at the root while the other has a toe-crack on the scanning surface. To detect the root crack, the linear array is kept very close to the weld bead, while for the detection of the toe-crack; the array is placed approximately 35 mm away from the weld bead. The experimental arrangement is shown in Figures 6.19(a) and (b). Since the sample is made of austenitic stainless steel and is 25 mm thick, the raw B-scan data in this case is acquired using a lower frequency

array of 5 MHz, 0.6 mm pitch, 64 elements. The experimental details are given in Chapter 3, Section 3.9.

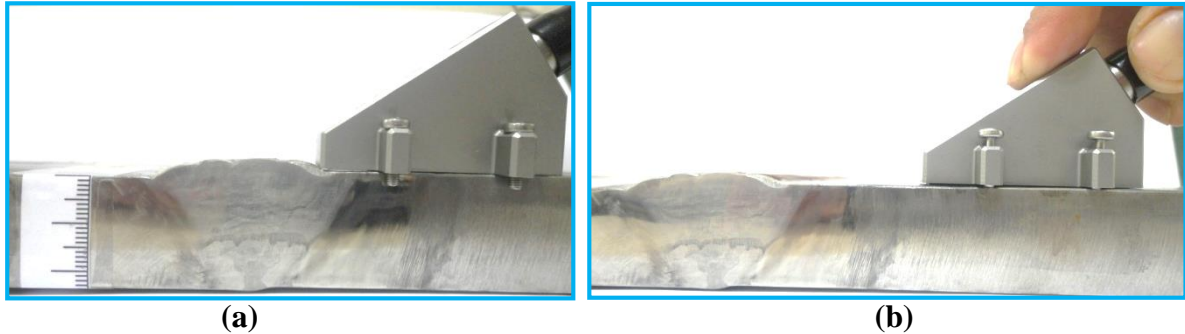


Figure 6.19: Experimental arrangement for data acquisition by Angle beam PA-SAFT technique (a) Root crack and (b) Toe crack (Scale in mm)

6.5.1 Root Crack

Figure 6.20 shows the photograph of the root crack in a 25 mm thick V-groove weld with an unground weld beam.

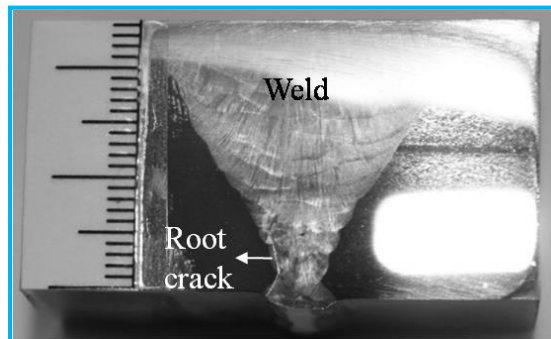


Figure 6.20: Photograph of the root crack in the austenitic stainless steel weld joint (Scale in mm)

The photograph shows that the crack is at the interface between the weld bead and the parent metal. The crack has a very fine opening (a sharp upper tip) and is almost perpendicular to the backwall.

Figure 6.21 (a) shows the raw B-scan image acquired using a divergent sound beam with the principle angle of 55 deg. The image shows signals of two types: (i) signals with constant time of flight (almost straight throughout the scan length) and (ii) signals with varying time-of-flight (in the shape of hyperbola). The signals with constant time of flight are from the backwall. This signal appears due to the normal beam component in the sound beam created as a result of excessive steering.

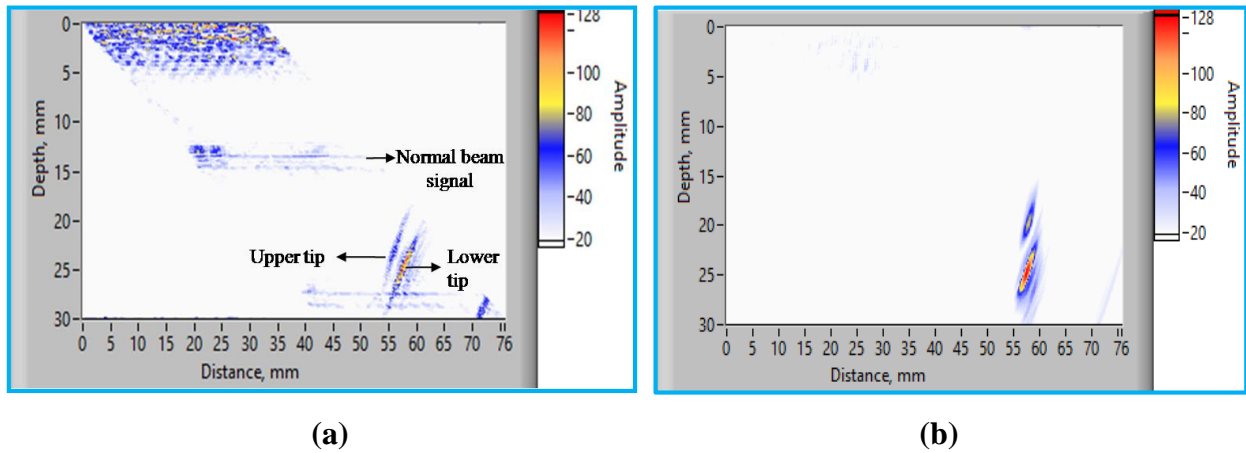


Figure 6.21: (a) Raw B-Scan (b) SAFT processed B-scan image showing the crack tip signal and the corner trap signal from the root crack in the weld sample by Angle beam PA-SAFT technique

The raw B-scan is depth corrected during which the sound path is multiplied by the cosine of the beam angle. Hence the backwall signal due to the normal beam component appears at a distance of 14 mm ($25 \times \cos(55)$). The signals with varying time-of-flight are from the crack. Since the crack is at the backwall, a strong hyperbolic signal from the corner trap is seen around the depth of 25 mm in the raw B-scan image. Additionally, a weak hyperbolic signal with a lesser time-of-flight than the corner trap signal is also seen. This signal is from the upper tip of the crack. The SAFT processed B-scan image is shown in Figure 6.20(b). The processed image

shows a strong signal from a corner trap at the expected depth and a relatively weaker signal from the upper tip. From the difference in the depth of the corner trap signal and the upper tip signal in the B-scan image, the through-wall dimension or the depth of the root crack is evaluated.

6.5.2. Toe crack

Figures 6.22 show the photograph of the toe crack in a 26 mm thick butt weld with an unground weld bead. The photograph shows that the crack is at the scanning surface and is located at the interface between the weld bead and the parent metal. Figures 6.23(a) and (b) show the raw and the SAFT processed B-scan images respectively. The raw B-scan image is acquired using a 55 deg. divergent longitudinal sound beam. The data is acquired for a path of more than full V path. In this case too, signals from the backwall, its multiples and the hyperbolic signals from the crack are seen. The raw B-scan image shows the corner trap signal from the crack at the depth of approximately 54 mm (corresponding to twice the thickness as the crack is detected by full V-path) and the signal from the crack tip at slightly lower depth. The SAFT processed B-scan image shows a strong signal from the corner trap and the signal from the crack tip. From the difference in the locations of these two signals relative to the scanning surface, the depth of the toe-crack is evaluated.

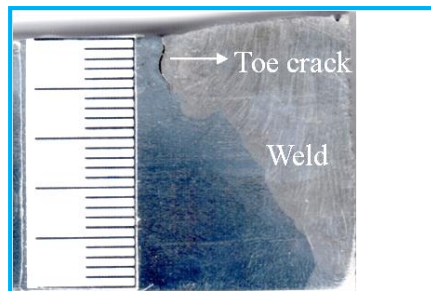


Figure 6.22: Photograph of the toe crack in austenitic stainless steel weld joint

(Scale in mm)

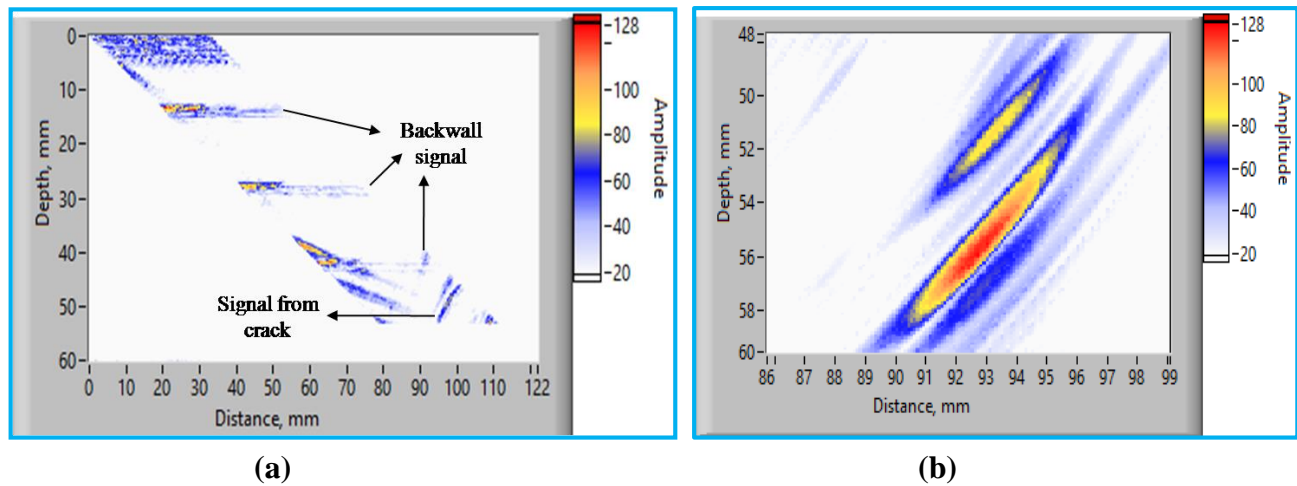


Figure 6.23:(a) Raw B-Scan (b) SAFT processed B-scan image showing the crack tip signal and the corner trap signal from the toe-crack in the weld sample by Angle beam PA-SAFT technique

6.5.3 Summary of observations on the detection and the characterization of planar flaws by Angle Beam PA-SAFT

Table 6.3 shows the results of the depth sizing of the root crack and the toe-crack by Angle Beam PA-SAFT technique.

Table 6.3: Assessment of the depth of the cracks in the weld samples by Angle Beam PA-SAFT technique

Flaw Type	True depth (mm)	Depth by Angle Beam PA-SAFT(mm)
Root crack	5.0	5.2
Toe crack	5.8	5.4

- In addition to the signals of interest, the raw B-scan data shows additional signals in the form of backwall because of the normal beam component, and from the crack because of the shear wave component in the sound beam. These signals are effectively eliminated during SAFT processing
- Based on the above results, it can be concluded that the Angle Beam PA-SAFT technique is very effective in the detection and the characterization of planar flaws in an unground weld bead, where the application of SFLA, PA-SAFT and FMC techniques may not be possible

6.6 Comparison of different techniques for depth sizing of planar flaws

Three techniques viz. SFLA, normal beam PA-SAFT and Angle Beam PA-SAFT are studied during this research work. The results on the application of these techniques to detect and characterize the planar flaws in welds are described above. In order to compare their performance under identical experimental conditions, experiments are conducted on a carbon steel weld sample with a planar flaw in the form of lack of sidewall fusion and an austenitic stainless steel weld sample with a root crack, which is described in Section 6.4.1. Experimental details are given in Chapter 3 Section 3.9.

6.6.1 Lack of sidewall fusion

Figure 6.24 shows the photograph of the carbon steel weld sample with the lack of sidewall fusion. The photograph shows the 22 mm thick butt weld joint, with the lack of sidewall fusion at the interface between the weld and the parent metal. The flaw is located at the mid-wall, with its upper tip at approximately 6 mm from the scanning surface. Prior to the removal of the weld bead to facilitate the examination by SFLA and normal beam PA-SAFT techniques, the data on

this sample is collected using Angle Beam PA-SAFT by keeping the linear array away from the weld bead. Subsequent to the weld bead removal, the data is acquired using SFLA and PA-SAFT and FMC techniques by keeping the linear array above the weld region.

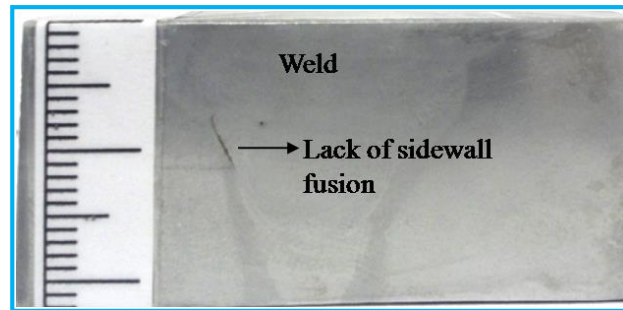


Figure 6.24: Photograph of carbon steel weld sample with lack of sidewall fusion (Scale in mm)

Figures 6.25(a), (b), (c) and (d) show the processed B-scan images by SFLA, PA-SAFT, Angle Beam PA-SAFT and FMC + TFM techniques respectively.

The results indicate the following:

- All the techniques detected the lack of sidewall fusion in the weld joint
- The depth of the lack of fusion estimated by SFLA, PA-SAFT, Angle Beam PA-SAFT and FMC+TFM techniques is found to be 4.4 mm, 4.6 mm, 4.5 mm and 4.3 mm, as against the true value of 4.6 mm found out by metallography. These results indicate that all the techniques could accurately assess the depth of the lack of sidewall fusion
- The signal amplitude by SFLA technique, especially for the bottom tip, is rather low. This can be attributed to lower acoustic power of the transmitted sound beam
- The signal amplitude of the bottom tip signal improves considerably with normal beam PA-SAFT, since a group of elements are used for sound beam transmission

- The best results are obtained by Angle Beam PA-SAFT, which shows strong signals from both, the lower and the upper tips. This indicates that for reliable detection and characterization of weld flaws, there is no need for the removal of weld crown, by employing Angle Beam PA-SAFT technique
- The above results show a similar trend, which is observed for the depth sizing of artificial planar flaws in 60 mm thick stainless steel plate (Chapter 5, Section 5.3.2).

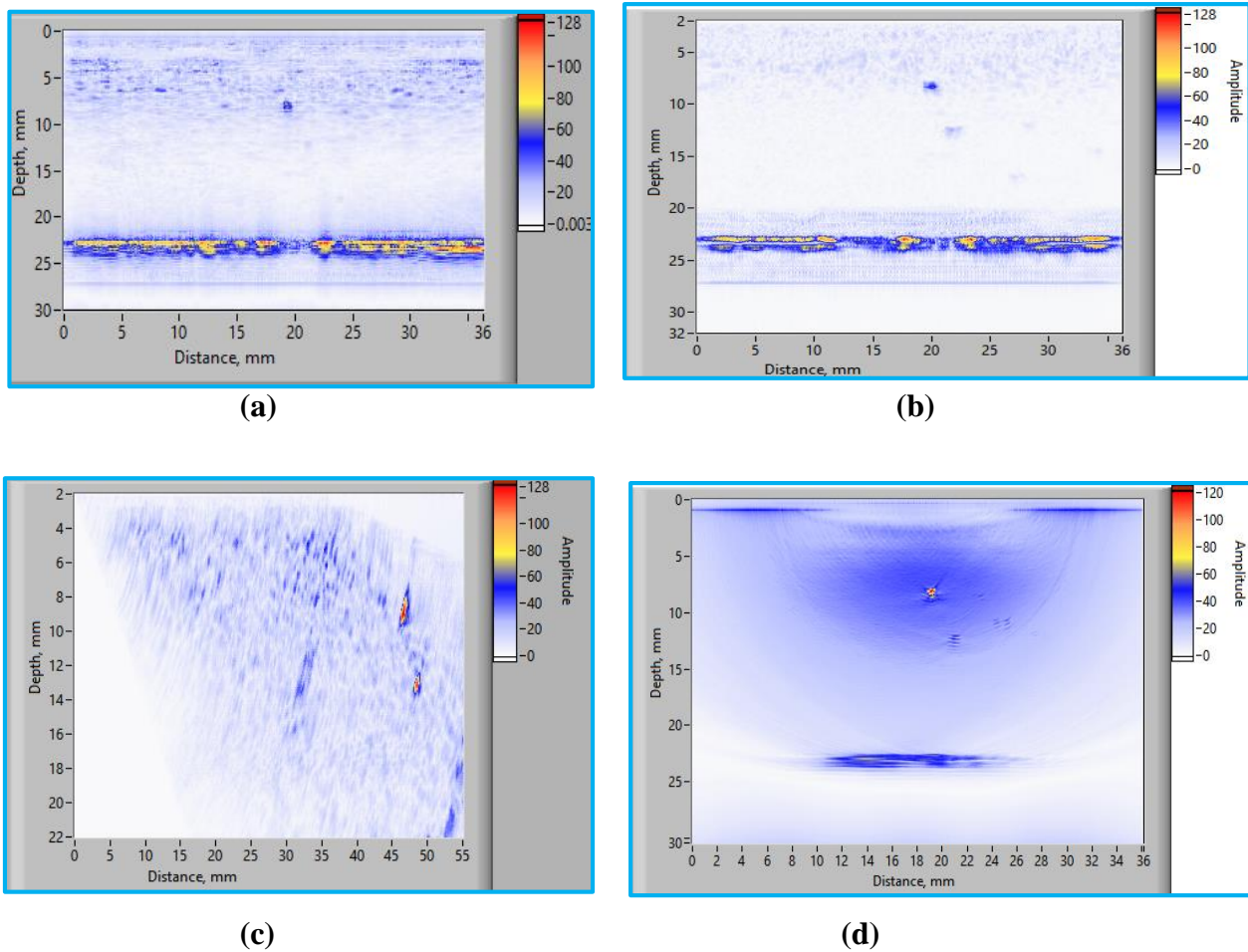
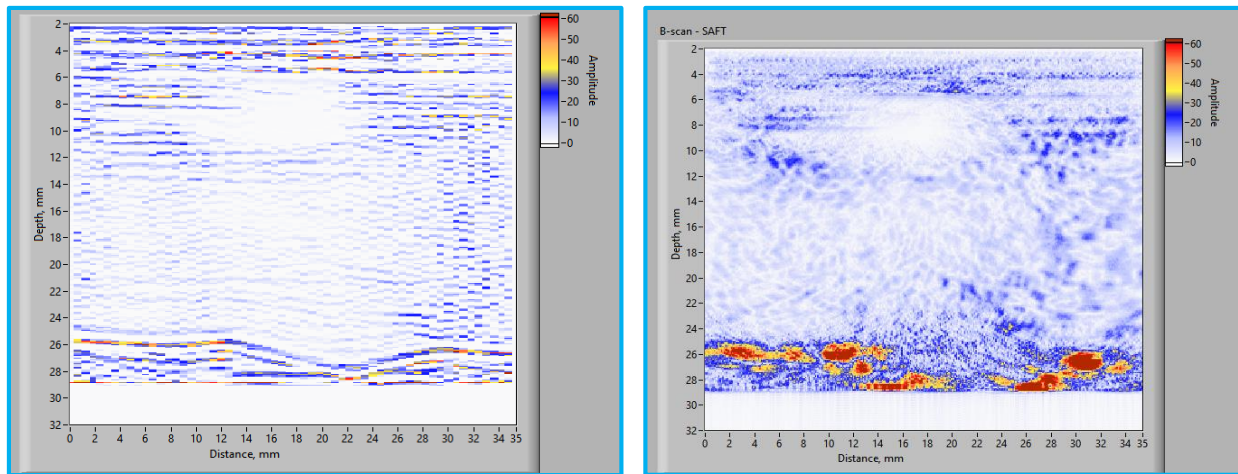


Figure 6.25: SAFT processed B-scan images by (a) SFLA (b) PA-SAFT and (c) Angle Beam PA-SAFT (d) FMC + TFM techniques showing the upper and lower tip signals from the lack of sidewall fusion in the carbon steel weld joint

6.6.2 Root crack

The photograph of the root crack in a 25 mm thick austenitic stainless steel weld sample is shown in Figure 6.20. In this case too, prior to the removal of the weld bead, the raw B-scan data is first acquired by Angle beam PA-SAFT technique. Subsequently, the weld bead is removed and the data is acquired by SFLA, normal beam PA-SAFT and FMC + TFM techniques.

Figures 6.26 (a) to (e) show the raw B-scan and the processed B-scan images obtained by various techniques. The raw B-scan image (Figure 6.26 (a)) using normal beam PA-SAFT is acquired at a gain level corresponding to the gain reserve of only 4 dB. In spite of using such a high gain, the image does not show any hyperbolic signal from the upper tip of the crack. The image shows a weak signal from the backwall and multiple low amplitude signals because of sound beam scattering. The backwall signal shows an increase in the time-of-flight in the central region. This is because of the presence of excess penetration at the root of the weld joint.



(a)

(b)

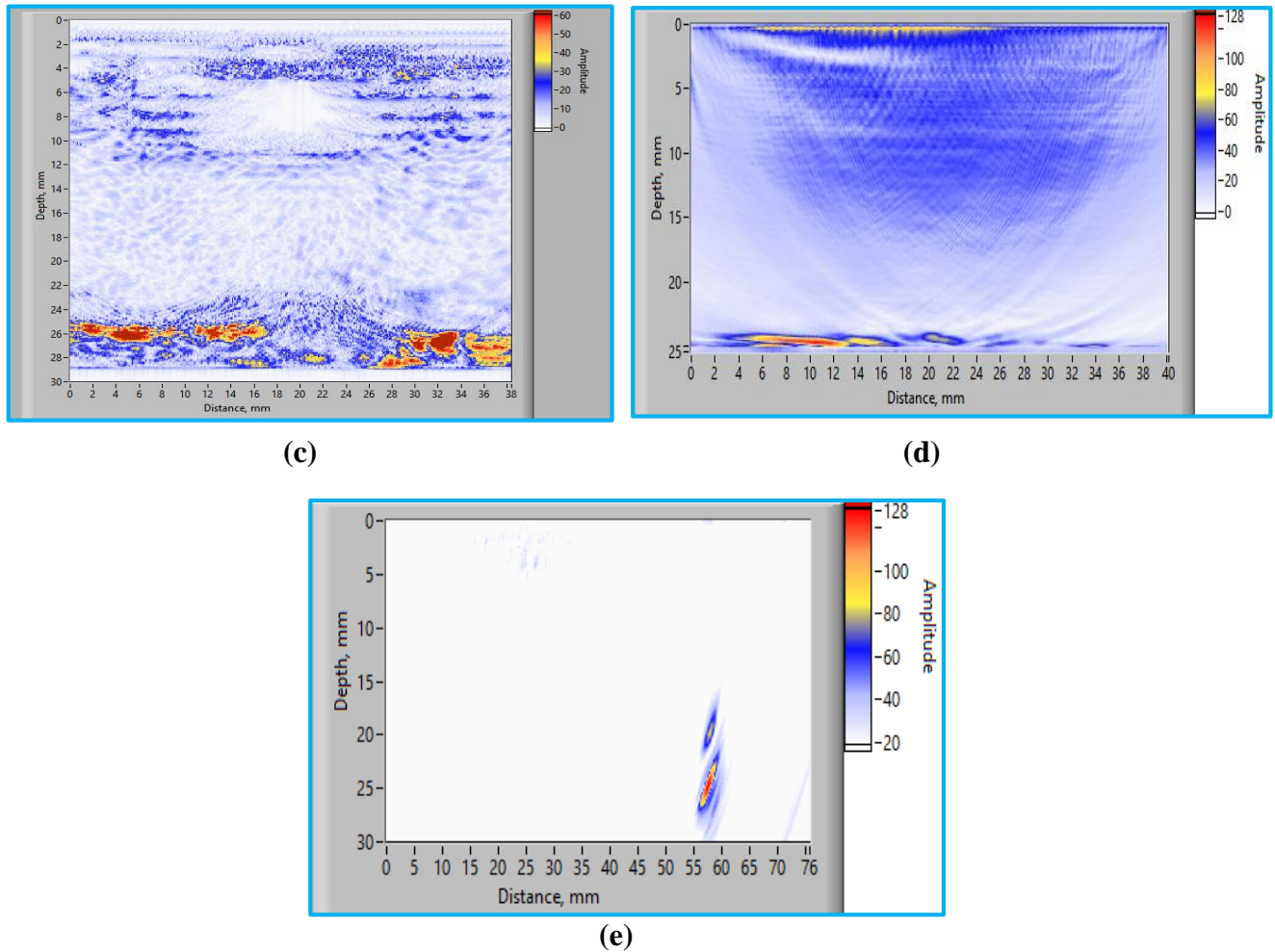


Figure 6.26: B-scan images for the root crack in austenitic stainless steel weld joints (a) Raw B-scan image by normal beam PA-SAFT, (b) SAFT processed image by normal beam PA-SAFT, (c) SAFT processed SFLA image (d) FMC+TFM and (e) SAFT processed image by Angle beam PA-SAFT showing the crack-tip and corner trap signal

The crack is located at the edge of the excess penetration. For the normal beam PA-SAFT technique, the data is acquired by placing the linear array over the weld bead. Under such condition, the sound beam emanating from majority of the apertures travel through-out the thickness of the coarse dendritic grain structure of austenitic weld. As a result, the sound beam experiences excessive scattering and attenuation. Hence, even the backwall, which is a large size

reflector, produces a low amplitude signal in the B-scan image. The dimension of the crack-tip is infinitesimally smaller as compared to backwall. Therefore, the crack does not produce a discernable signal in the raw B-scan image. The processed image (Figure 6.26 (b)) also does not show any signal corresponding to the crack-tip. With SFLA and FMC + TFM techniques, the situation is further worsened because of a very low acoustic power of the transmitted sound beam, since only a single element is used for sound beam transmission. As a result, no crack-tip signal is seen in the processed B-scan images (Figure 6.26 (c) and (d)). Contrary to these results, Angle beam PA-SAFT shows distinct high amplitude signals from the crack extremities (Figure 6.26(e)). From the location of these signals with respect to the scanning surface, the depth of the crack can be found out. With Angle beam PA-SAFT technique, the linear array is placed over the parent metal and not on the weld bead. With this arrangement, the sound beam emanating from the linear array travels for majority of its path in the parent metal, unlike with other techniques, where the sound beam travels in the weld material. As a result, the scattering, and so the attenuation of the sound beam during Angle beam PA-SAFT is much less. Hence, signals with high amplitude, well over the background noise, could be obtained from the corner trap and the upper tip of the crack. From these results, one can conclude that SFLA and PA-SAFT techniques failed to detect the root crack in the austenitic stainless steel weld joint. Angle beam PA-SAFT techniques is not only advantageous in cases where the weld bead is unground, but also exhibits better sensitivity and enhanced characterization of flaws in austenitic stainless steel weld joints, with or without the weld bead.

6.7 Application of SFLA and PA-SAFT techniques for in-service inspection of circumferential weld joint in a pressure vessel of a nuclear boiling water reactor

The twin Boiling Water Reactors (BWRs) at Tarapur, India are in operation since late 1960s [222]. The in-service inspection programme for these reactors is based on the guidelines of ASME Boiler & Pressure Vessel Code Section XI [52, 223]. The Code demands periodic inspection of the weld joints in the reactor pressure vessel (RPV) to ensure its structural integrity during its service life. The inspection is required to be carried out by ultrasonic testing. The BWR pressure vessel at Tarapur Atomic Power Station (TAPS) is made from 124 mm thick low alloy steel. The vessel is clad from the inside surface with approximately 6-8 mm thick 308L austenitic stainless steel. The RPV at TAPS has four circumferential (C1 to C4) and six longitudinal (L) welds (Figure 6.27). The uppermost circumferential weld C1 is the weld joint between the top flange and the RPV shell. During manufacturing, this weld is examined from the outside surface and inside surface (prior to cladding) by ultrasonic angle beam and normal beam techniques. During in-service inspection, there are two ways to carry out ultrasonic testing of this weld joint: from the inside surface of the RPV or from the top surface of the flange. The outside surface of the RPV is not accessible due to the presence of shielding. There are several inspection methodologies developed world over for in-service inspection of various weld joints in RPV of BWRs and PWRs [224-227]. Majority of these inspection methodologies, use several single crystal ultrasonic transducers, mounted in a transducer assembly, to detect the flaws of concern in the weld joints and the heat affected zones.

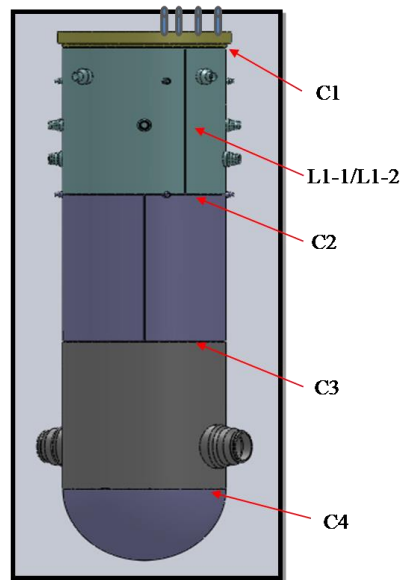


Figure 6.27: Longitudinal and circumferential welds in RPV

Phased array ultrasonic testing offers a very effective alternative to the conventional, single crystal based ultrasonic techniques for the examination of C1 weld joint [137-141]. The examination is carried out from the top surface of the flange. The technique uses a linear array transducer having 64 elements. The sound beam is focused at the weld location and steered from ID to OD using appropriate focal laws to cover the entire thickness of the weld. Although phased array technique is very effective in detection of significant flaws through-out the thickness of the RPV weld joint, it requires high-end phased array instrumentation, which should be capable of sequentially exciting a large number of array elements. To overcome this drawback, a detailed study is carried out on the application of SFLA and PA-SAFT techniques for in-service inspection of the C1 weld joint. The objective is to achieve sound beam focusing using much lesser resources as compared to the conventional phased array. The methodology followed for the data acquisition and processing using these techniques, the results of the experiments carried out on a mock-up block and the comparison of the results obtained by SFLA and PA-SAFT techniques with the conventional phased array are described below.

6.7.1 Configuration of C1 weld joint and the examination requirements

The circumferential weld joint is located at a distance of 425 mm from the flange top surface, where the transducer is placed during in-service inspection. The schematic of this weld joint is shown in Figure 6.28. The flange is thick at the top (260 mm thick) and is matched in thickness with that of RPV shell (124 mm) at the weld location by providing a taper on its outside surface. The weld joint is Single-V groove full penetration butt weld with the edge preparation angle of approximately 7° from the radial normal. Since the weld joint is circumferential, the manufacturing flaws are expected to be oriented in radial-circumferential plane. To detect these flaws as well as those which may get initiated during service and oriented in this plane, ultrasonic normal beam examination from the top surface of the flange is an easier option, as compared to inspection from the ID surface.

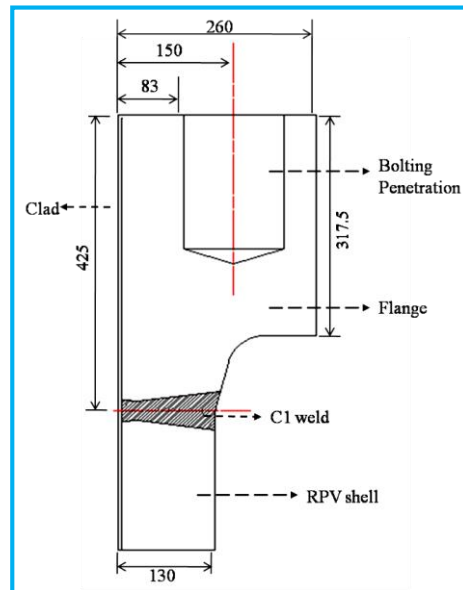


Figure 6.28: Schematic of C1 weld joint and its distance from the top flange

The top surface of the flange has 54 penetrations, equally spaced over the entire circumference, for bolting the top cover over the RPV shell. The schematic with the locations of these penetrations on the flange surface is shown in Figure 6.29.

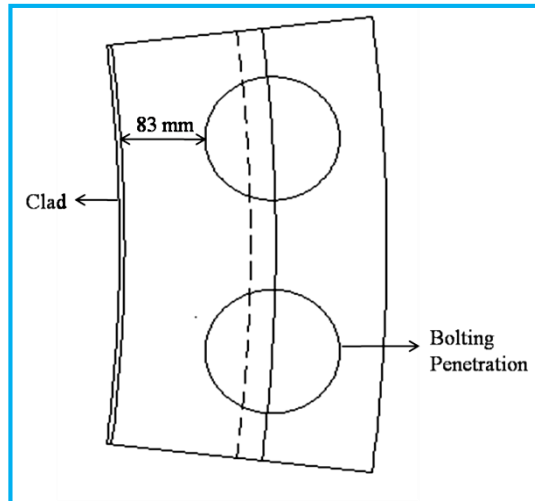


Figure 6.29: Location of the bolt penetrations on the flange surface with respect to the clad on RPV ID surface

Figure 6.29 shows that there is a limited space available, approximately 83 mm, at the location of penetrations, over which the ultrasonic transducer can be placed or moved for normal beam examination of C1 weld. The examination technique should ensure that: (i) the full thickness of the weld joint is inspected, (ii) the reference flaws should be detected with adequate signal-to-noise ratio, (iii) the reference flaws should get resolved, to ensure that multiple flaws at any given cross-section are detected, and (iv) the depth sizing of crack-like flaws starting from ID and OD surface is accurate for fitness-for-service assessment.

6.7.2 Ultrasonic simulation results

In order to study the effectiveness of various technique viz. normal beam using single crystal transducer, beam steering and focusing using a linear array, and SFLA and PA-SAFT using a linear array, with respect to the coverage of C1 weld while inspecting from the top flange surface, simulation studies are carried out using CIVA 11.

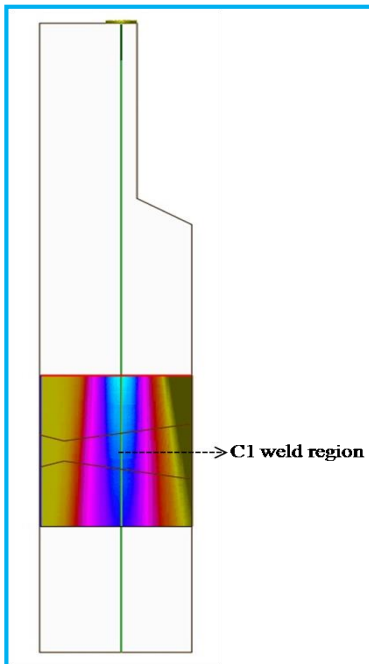


Figure 6.30: Beam Computation result at the C1 weld location using 2 MHz, 25 mm dia. single crystal normal beam transducer (Simulation)

Figure 6.30 shows the results of the beam computation for a 25 mm diameter, 2 MHz normal beam transducer at the C1 weld location. The magnitude of the sound wave amplitude in the computation zone (examination region) is colour coded, blue indicates the maximum, pink indicates the intermediate and dark green indicates the background. Using the above single crystal transducer, although the sound beam covers significant region of the weld, the wave amplitude near OD is very less. This may lead to poor sensitivity for the detection of flaws near the OD surface. Moreover, the sound beam at the weld location is very wide (6 dB width = 27 mm). As a result, two or more flaws separated by less than this distance, may not get resolved. Another major limitation of this approach is that the transducer needs to be moved in two directions over the top flange surface, radially (from ID towards OD) and circumferentially, to cover the entire volume of the C1 weld.

The above drawbacks can be overcome by using a linear array transducer, wherein one can steer the sound beam from ID to OD surface using appropriate focal laws, without the requirement of radial movement.

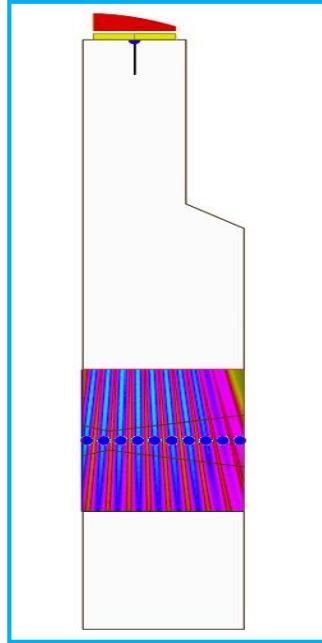


Figure 6.31: Beam Computation result at the C1 weld location with beam focusing and steering using 5 MHz, 1 mm pitch, 64 active elements linear array (Simulation)

Figure 6.31 shows the result of beam computation using a 5 MHz, 1mm pitch, 64 element, when the sound beam is steered and focused at C1 weld location by placing the transducer on the top flange surface. The results show that the entire thickness of the weld joint is covered by the focused sound beam when all the 64 elements are used as active aperture.

There are two major advantages of this approach. The first one is that the entire thickness of the weld gets inspected by beam steering from a single transducer location with almost uniform sensitivity. Secondly, it is not required to move the transducer radially, as is the case with conventional single crystal transducer. To examine the entire circumference of the C1 weld, the linear array is required to be moved only circumferentially over the top flange. As a result, not

only there is a significant reduction in the inspection time, but the manipulator design for field inspection also becomes simpler. Moreover, using phased array, the sound beam can also be focused, which leads to higher sensitivity and resolution as compared to conventional single crystal transducer. However, with phased array, one needs high-end instrumentation to excite all the 64 elements in the array simultaneously so as to achieve focusing at a depth of 425 mm.

SFLA and PA-SAFT techniques provide an effective alternate to achieve sound beam focusing at higher depth, without the use of high-end instrumentation. Figure 6.32 shows the sound beam computation using SFLA technique for C1 weld configuration.

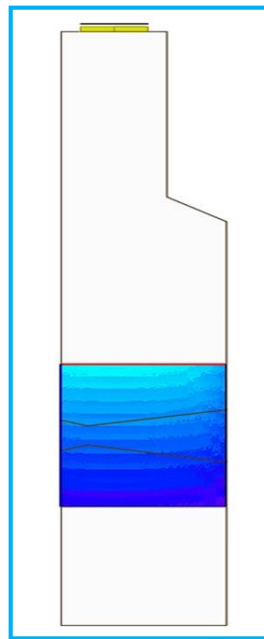


Figure 6.32: Beam Computation result at C1 weld location with single element excitation (SFLA) using 2 MHz, 0.8 mm pitch, 64 elements linear array (Simulation)

A linear array of 2 MHz, 0.8 mm pitch, 64 elements is used. The image indicates that full thickness coverage is obtained using SFLA technique. Since a single element is used for sound beam transmission, the wave amplitude at the weld location using SFLA technique is expected to

be much lower than the conventional phased array using large number of elements as active aperture.

The limitation of lower wave amplitude at higher depth can be overcome by PA-SAFT technique, which uses a group of elements for the sound beam transmission. One of the crucial parameters with PA-SAFT technique is the number of elements to be used for an active aperture and the depth at which the sound beam should be focused from the scanning surface (location of virtual sources). For the C1 weld, this optimization is carried out by finding out the sound beam profile for various active apertures.

The depth up to which the sound beam can be focused using a given linear array is determined by the near field, which in turn is determined by the active aperture used [6,7]. During PA-SAFT technique, the location of the virtual sources from the scanning surface is before the near field, so that a well divergent beam is obtained beyond the focal point.

During the present study, sound beam computation for the optimization of active aperture size for PA-SAFT technique using 2 MHz, 0.8 mm pitch linear array is carried out for 6 different apertures viz. 8, 16, 24, 32, 40 and 48 elements. For each case, the sound beam is focused at the depth of 0.7 times the corresponding near field. Table 6.4 gives the near field length and the depth at which the sound beam is focused (location of virtual array of sources) using various apertures. The methodology is schematically shown in Figure 3.21, Chapter 3. During PA-SAFT, a virtual array of sources is created at certain distance from the scanning surface. The divergent sound beam emanating from these virtual sources is used to acquire the B-scan image.

The variation in the sound wave amplitude from ID to OD at a distance of 425 mm from the scanning surface for various active apertures is shown in Figure 6.32. For 48 active elements, the sound wave amplitude at the ID surface is highest, but beyond 60 mm from ID surface, the

sound wave amplitude falls gradually and at the OD surface it is almost 10 dB lower than the sound wave amplitude at the ID surface. Similar results are observed for 40 and 32 active elements. For 8, 16 and 24 active elements, the sound wave amplitude is uniform across the full thickness of the vessel. However, for 8 active elements, the sound wave amplitude at the weld location is very low and it may have the same adverse effect of poor sensitivity and signal to noise ratio as that of SFLA technique.

Table 6.4: Near field length and the focusing depth using various apertures

Sr. No	No of elements	Pitch (mm)	Aperture size (mm)	Frequency (MHz)	Near field (mm)	Focal depth (mm)
1	8	0.8	6.4	2	3	2
2	16	0.8	12.8	2	14	10
3	24	0.8	19.2	2	31	22
4.	32	0.8	25.6	2	56	39
5	40	0.8	32	2	87	61
6	48	0.8	38.4	2	125	87

For 16 and 24 active elements, the sound wave amplitude is reasonably high. Since there is not much of difference between the two in terms of the sound wave amplitude and the coverage, and 16 active elements would require lower-end phased array hardware as compared to 24 active elements, an aperture of 16 active elements is chosen for acquiring the data using PA-SAFT technique in the current study.

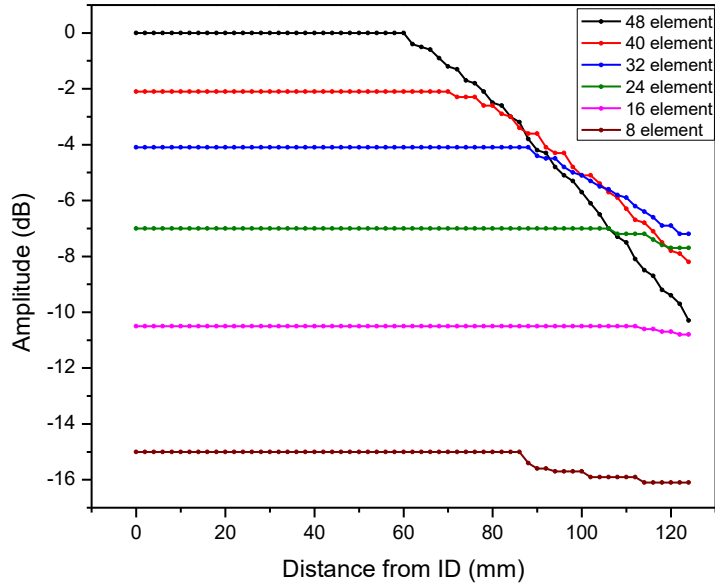


Figure 6.33: Variation in sound wave amplitude at C1 weld location for various active apertures of 2 MHz, 0.8 mm pitch linear array using PA-SAFT technique (Simulation)

Figure 6.33 shows the beam computation results for PA-SAFT using 16 active elements. The image indicates that full thickness coverage is obtained using PA-SAFT technique.

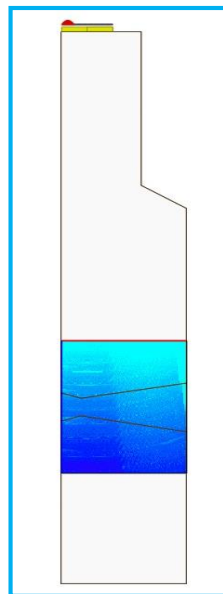


Figure 6.34: Beam computation results at C1 weld location with 16 active elements of 2 MHz, 0.8 mm pitch, 64 elements linear array using PA-SAFT technique (Simulation)

6.7.3 Comparison of various techniques for C1 weld examination

Figure 6.35 shows the variation in the sound wave amplitude from ID to OD surfaces at C1 weld location using various techniques. For the normal beam single crystal transducer of 2 MHz, 25 mm diameter, the profile indicates that the amplitude is uniform up to a thickness of 70 mm from ID surface. As the transducer moves away from the ID surface, the vertical face of the bolting penetration obstructs the sound beam. As a result, the sound wave amplitude drops gradually and beyond 100 mm from the ID surface, the sound wave amplitude is almost 24 dB less than the amplitude at the centre of the weld. The profile using 2 MHz, 0.8 mm pitch, 64 elements linear array for three different cases viz. beam steering using focal laws, SFLA technique using single active element and PA-SAFT technique using 16 active elements are also shown in Figure 6.35.

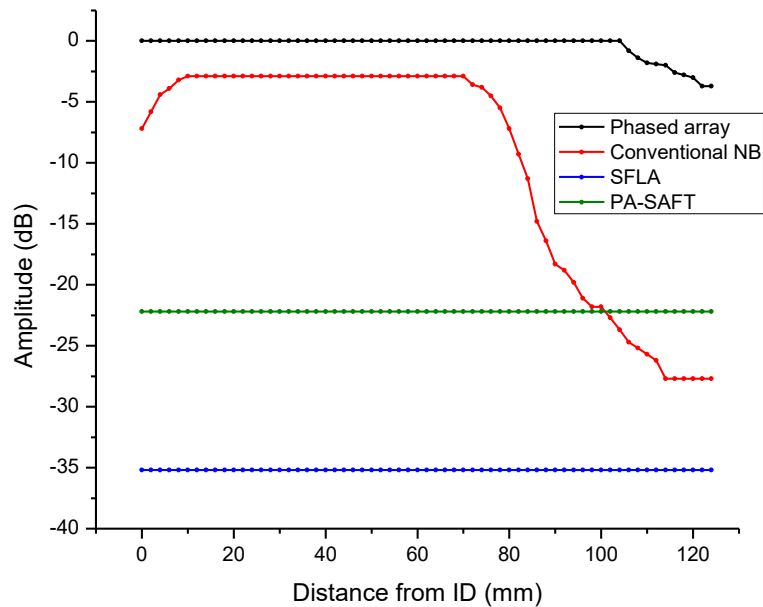


Figure 6.35: Variation in sound beam amplitude profile from ID to OD at C1 weld location using single crystal normal beam transducer (2 MHz, 25 mm dia.), Conventional phased array with steering and focusing, SFLA and PA-SAFT technique using 2 MHz, 0.8 mm pitch, 64 elements linear array (Simulation)

By beam steering using 64 active elements, there is a complete coverage of the weld, and as expected the sound wave amplitude is very high and uniform across the thickness, with a marginal reduction (around 4 dB) near the OD surface. With SFLA technique, although there is complete coverage of the weld, the sound wave amplitude is very less, almost 35 dB lower than the conventional phased array. As a result, the sensitivity as well as the signal-to-noise ratio are expected to be inferior with the SFLA technique. With PA-SAFT technique, there is a significant improvement in sound wave amplitude over the SFLA technique (13 dB). In this case also, the entire thickness of the weld is covered with uniform sound wave amplitude.

Based on the above, it is observed that in order to obtain complete coverage of C1 weld joint with uniform sensitivity, an array based inspection is required. Although focal law based approach using large number of active elements provides high sound wave amplitude at the weld location, one needs a high-end phased array instrumentation to excite 64 elements of an array simultaneously. With SFLA technique, although a single channel instrument with multiplexing is adequate to acquire the data, the sound wave amplitude is too low at the weld location and this may have an adverse effect on the sensitivity and signal-to-noise ratio. PA-SAFT technique provides a good alternative to conventional phased array and SFLA techniques, wherein one doesn't need the high-end instrumentation and at the same time, one may achieve the required sensitivity and signal-to noise ratio.

6.7.4 Experimental Results

6.7.4.1 Conventional Phased Array

Figure 6.36 shows the B-scan image using 2 MHz, 0.8 mm pitch, 64 elements linear array using 16, 32, 48 and 64 active elements.

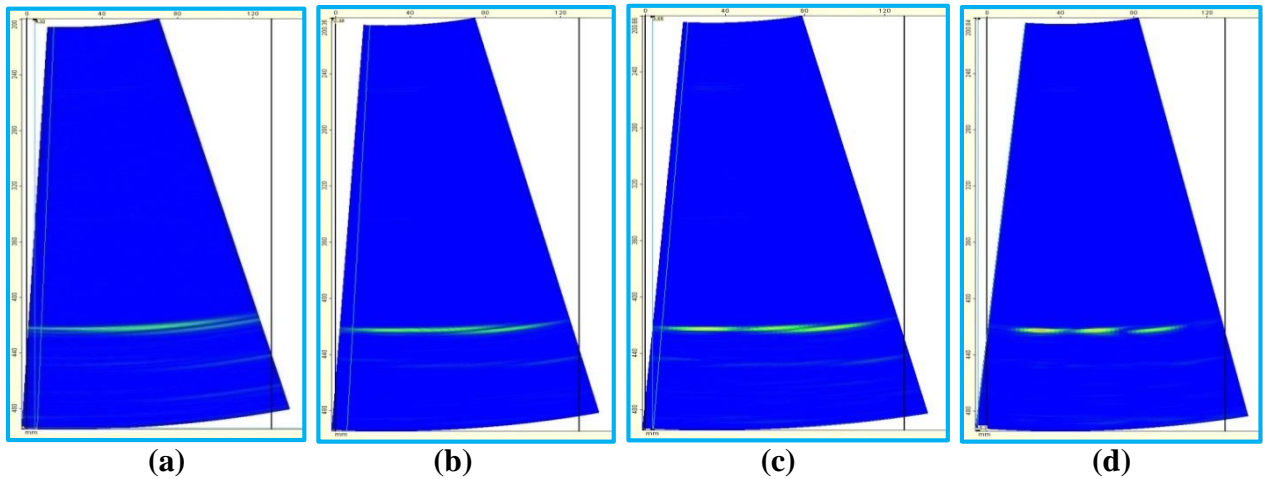


Figure 6.36: B-scan image using 2 MHz, 0.8 mm pitch, 64 elements linear array with steering and focusing at C1 weld location using an active aperture of (a) 16, (b) 32, (c) 48 and (d) 64 active elements

The image using 16 active elements shows considerable spread in the signals from side drilled holes indicating that the sound beam focusing is not achieved. As the aperture is increased to 64 active elements, the spread of signals from side drilled hole is reduced considerably. In order to achieve effective sound beam focusing using linear array, the near field should be greater than the depth at which the focusing is desired. Longer the near field, in comparison to the focusing depth, smaller is the dimension of the focal spot [1-4]. For a given frequency and the material, the near field is determined by the active aperture used. For C1 weld configuration, the focusing depth is 425 mm from the scanning surface. Table 6.5 shows the near field for various active apertures using 2 MHz, 0.8 mm pitch and 5 MHz, 1 mm pitch linear array.

Table 6.5: Near field for various active apertures

Sr. No	No of elements	Pitch (mm)	Aperture size (mm)	Frequency (MHz)	Near field (mm)
1	16	0.8	12.8	2	14
2	32	0.8	25.6	2	56
3	48	0.8	38.4	2	125
4	64	0.8	51.2	2	222
5	16	1	16	5	54
6	32	1	32	5	217
7	48	1	48	5	488
8	64	1	64	5	868

From the above table, it is clear that with 2 MHz, 0.8 mm pitch linear array, sound beam focusing at C1 weld location will not be achieved even when one uses 64 active elements. As a result, the side drilled holes show significant spread in the B-scan image. With 5 MHz, 1 mm pitch linear array, Table 6.5 indicates that with 48 and 64 active elements, the near field exceeds the desired focusing depth. However, sharp focal spot at a depth of 425 mm will be obtained by using 64 active elements.

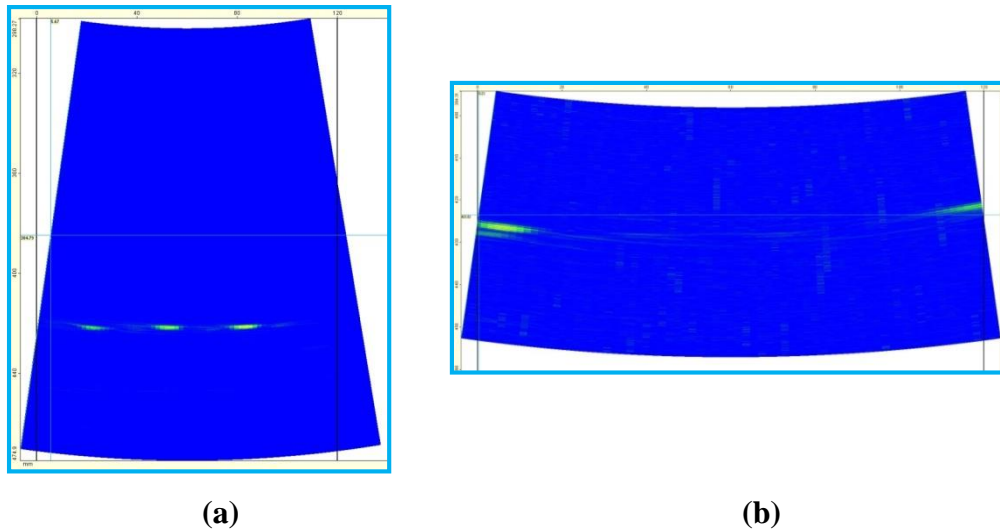


Figure 6.37: B-scan image using 5 MHz, 1 mm pitch, 64 elements linear array with steering and focusing at C1 weld location (a) side drilled holes and (b) ID and OD notches

Figures 6.37(a) and (b) show the B-scan images using 5 MHz, 1 mm pitch linear array using 64 active elements for side drilled holes and notches respectively. The image in Figure 6.37(a) shows that all the side drilled holes are detected and resolved. The notches on ID and OD surface are also well detected (Figure 6.4(b)) indicating that there is a complete coverage of the weld joint with the focused sound beam.

6.7.4.2 SFLA technique

Figures 6.38(a) and (b) show the raw B-scan images acquired using SFLA for the detection of side drilled holes and notches. The raw data is acquired at the gain reserve of 0 dB, which means that the amplifier gain of the phased array instrumentation is set to the maximum value. Although raw data shows weak signals at a depth of 425 mm and beyond, no assessment in terms of the number of flaws, their size and location with respect to the ID surface can be made from this image. This is primarily because of the fact that when the sound beam reaches C1 weld

location, it has large beam width and at the same time, the sound wave amplitude is also very low.

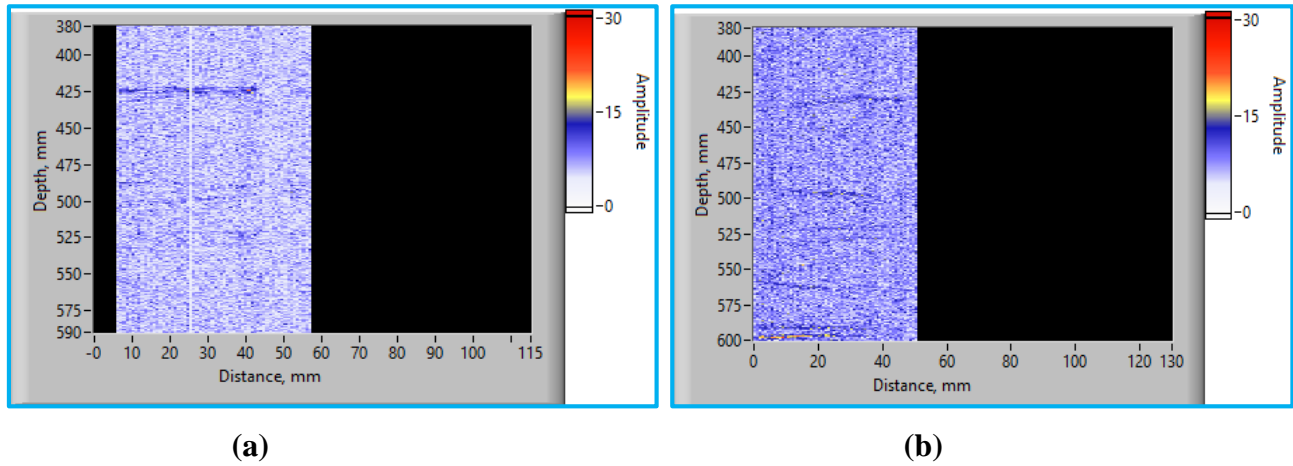


Figure 6.38: Raw B-scan image using 2 MHz, 0.8 mm pitch, 64 elements linear array with SFLA technique for the detection of (a) side drilled holes and (b) notches

Figures 6.39 (a) and (b) show the SAFT processed B-scan images for side drilled holes and notches respectively.

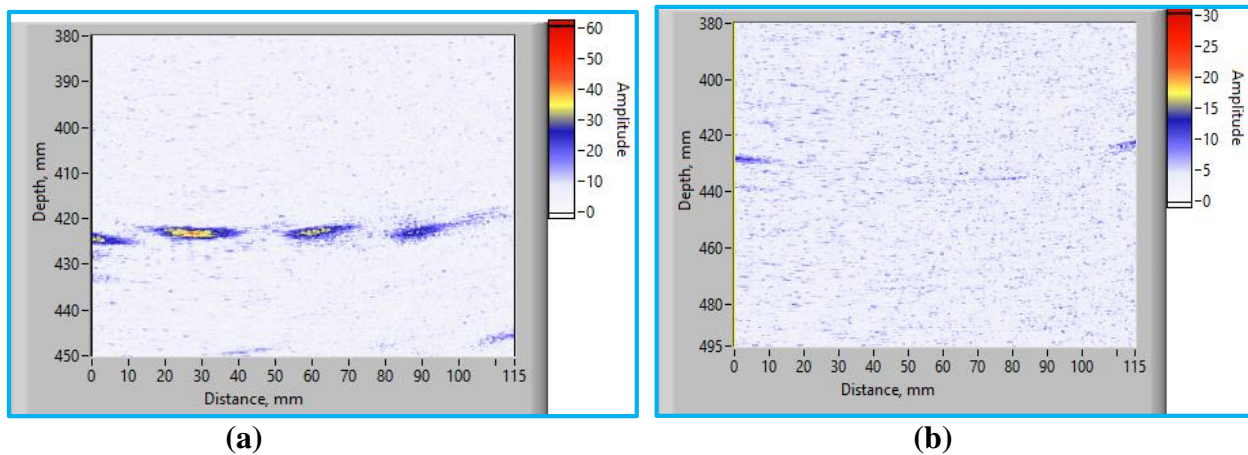


Figure 6.39: SAFT processed B-scan images with 2 MHz, 0.8 mm pitch, 64 elements linear array using SFLA technique showing signals from (a) side drilled holes and (b) notches

The image for side drilled holes shows three indications at the depth of 425 mm from the

scanning surface. The image for the notches shows two signals at the extreme ends at the depth of 425 mm from the scanning surface. Both the B-scan images show low amplitude background signals because of noise. The signal-to-noise ratio for notch is poor as compared to side drilled holes. From these results, one can conclude that using SFLA technique; one can obtain complete coverage of the C1 weld joint. The reference holes are detected and resolved. The notches too are detected. However, the signal-to-noise ratio is inferior.

6.7.4.3 PA-SAFT technique

Figures 6.40 (a) and (b) show the raw B-scan images acquired using PA-SAFT technique for the detection of side drilled holes and notches respectively. The images are acquired at the gain reserve of 15 dB, which means that as compared to SFLA, the gain required for PA-SAFT technique is much less. The lower gain is also reflected in a good signal to noise ratio in the raw B-scan data as compared to the data acquired by SFLA technique. The images show strong signals at a depth of 425 mm and beyond.

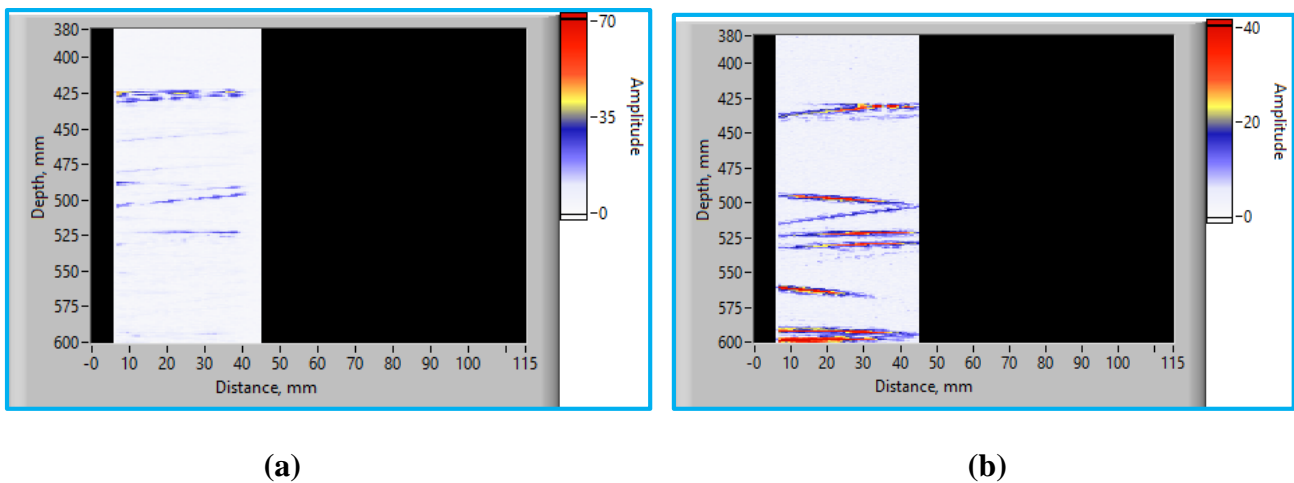


Figure 6.40: Raw B-scan image with 2 MHz, 0.8 mm pitch, 64 elements linear array using PA-SAFT for the detection of (a) side drilled holes and (b) notches

The SAFT processed B-scan images for side drilled holes and notches are shown in Figures 6.41(a) and (b) respectively. In this case too, the side drilled holes are clearly resolved and the ID and OD notches are detected. As compared to SFLA, the signal-to-noise ratio is significantly better using PA-SAFT technique.

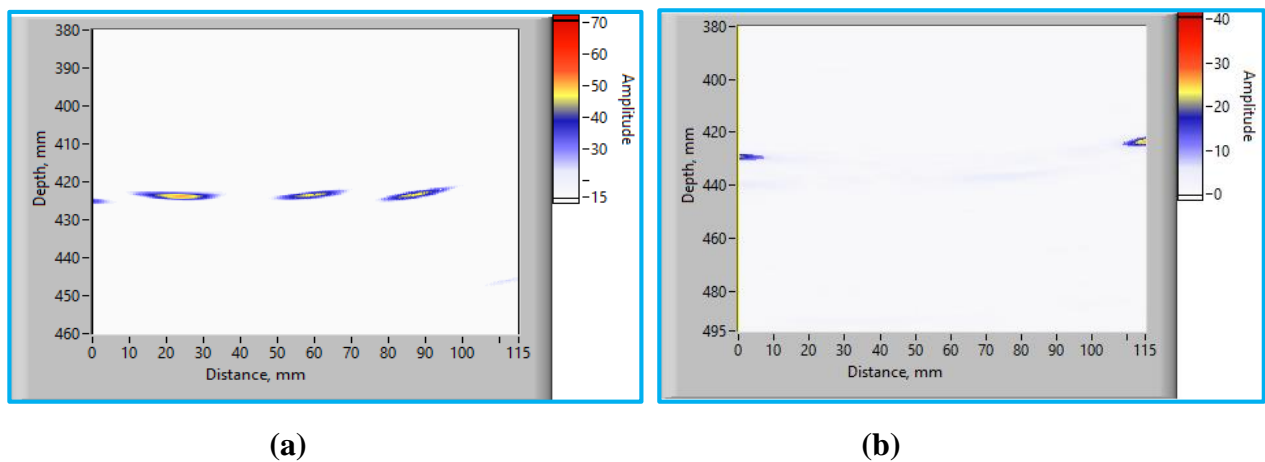


Figure 6.41: SAFT processed B-scan images with 2 MHz, 0.8 mm pitch, 64 elements linear array using PA-SAFT technique showing signals from (a) side drilled holes and (b) notches

6.7.4.4. Comparison of various approaches

The focusing effect obtained using conventional phased array, SFLA and PA-SAFT techniques is compared by measuring the 6 dB width (Full Width at Half Maximum: FWHM) of the reference holes and the notches from the corresponding B-scan images. The results are given in Table 6.6.

Table 6.6: 6 dB spread of side drilled holes and notches obtained by various techniques

Reference defect No.*	Conventional Phased Array (mm)					SFLA (mm)	PA-SAFT (mm)
	2 MHz, 0.8 mm pitch		5MHz, 1 mm pitch, 64 element aperture				
	16 el	32 el	48 el	64 el			
Hole 1	-	-	27	18	8	18	20
Hole 2	-	-	29	18	8	12	15
Hole 3	-	-	33	23	8	11	11
Notch 1	35	20	17	12	8	7	7
Notch 2	35	14	12	10	8	7	7

* *The holes and notches are numbered based on their position from ID surface*

Using 16 active elements of 2 MHz, 0.8 mm pitch linear array, the signals from the holes and the notches are very wide. As a result, no meaningful measurement of 6 dB width could be done. For 32 active elements, the signals from the holes overlap and as a result, 6 dB spread assessment could not be done. However, the notch depths are estimated as 20 mm and 14 mm, which are much higher than the actual depth of 6 mm. For 48 active elements, the 6 dB spread for the holes varies from 27 to 33 mm, while the notches are sized as 17 and 12 mm. This indicates that, even with 48 active elements, the desired sound beam focusing has not been achieved using the conventional phased array. As the active aperture is increased to 64, it is observed that the 6 dB spread decreases significantly for both the holes and the notches, but the values are still more than the actual size. These results indicate that although one can achieve complete coverage of the C1 weld by phased array using 2 MHz, 0.8 mm pitch, 64 elements linear array, the focusing required for the accurate sizing of the flaws could not be achieved.

With 5 MHz, 1 mm pitch linear array using 64 active elements, the 6 dB spread for side drilled holes and notches is found to be 8 mm, which is less than 2 MHz linear array. With 5 MHz linear array, the near field length is more as compared to 2 MHz linear array. As a result, the focal spot size at the same depth (425 mm from the scanning surface) is much smaller using 5 MHz as compared to 2 MHz. This is reflected in the lower value of 6 dB spread for the signals from the side drilled holes and the notches. With 5 MHz linear array, if an aperture of 48 or less elements is used instead of 64 elements, the spread of the signals from side drilled holes and notches is going to be much larger than 8 mm.

With SFLA and PA-SAFT techniques, the 6 dB width for the holes is less than the ones obtained using conventional phased array for the same transducer (2 MHz, 0.8 mm pitch). When compared with 5 MHz, 1 mm pitch linear array, these dimensions are larger. However, the depth of ID and OD notches are estimated accurately by using SFLA and PA-SAFT techniques.

The effectiveness of focusing using SFLA and PA-SAFT techniques depends primarily on the beam divergence. When the beam divergence is large, there are more number of A-scans available for SAFT processing, which helps to achieve sharp focusing. With the present geometry, the focusing of sound beam is required at a depth of 425 mm from the scanning surface. This distance is much larger as compared to the lateral distance between the centre of the array and the side drilled holes. As a result, the A-scan data are available for SAFT processing at a lesser divergence angle as compared to the instance when the data is acquired for relatively thinner geometries. For the three side drilled holes, the useful beam divergence for SAFT processing is approximately 4 deg., 8 deg. and 12 deg. Hence the first hole (with reference to ID) shows maximum spread, while the third hole shows the minimum. For the notches, the beam divergence is approximately 15 deg. and hence they are sized accurately.

The effectiveness of various techniques for the examination of C1 weld is also compared in terms of the amplitude difference between the reference holes located at different positions from the ID surface. The small difference among them is an indication that the sensitivity for the flaw detection is uniform across the thickness. It is observed that using conventional phased array technique, the amplitude difference is 5 to 6 dB as against 2 to 3 dB observed using SFLA and PA-SAFT techniques.

The above study indicates that the complete coverage of C1 weld joint is obtained using SFLA and PA-SAFT techniques. It is also possible to detect the reference holes in the mock-up with uniform sensitivity and adequate resolution. The depth sizing of the reference notches on ID and OD surface simulating cracks is found to be very accurate by SFLA and PA-SAFT techniques. PA-SAFT technique performed much better than SFLA technique in terms of signal to noise ratio.

6.8. Summary of the chapter

The effectiveness of SFLA and PA-SAFT techniques on the characterization of real flaws is demonstrated on carbon steel and austenitic stainless steel weld samples with volumetric and planar flaws. These techniques are also found to be effective in the detection of reference flaws in the mock-up of a circumferential weld joint in the pressure vessel of a nuclear boiling water reactor. The following are the salient observations on the results of experimental work carried out to assess the effectiveness of SFLA and PA-SAFT techniques for the detection and characterization of weld flaws:

- ✓ The volumetric flaws in the form of clustered porosity and slag inclusion and the planar flaws in the form of lack of sidewall fusion and crack are reliably detected and accurately characterized by SFLA and PA-SAFT techniques
- ✓ The performance of these two techniques is found to be comparable to FMC+TFM technique
- ✓ Angle Beam PA-SAFT could reliably detect and accurately size the depth of near surface and far surface cracks in the unground weld bead where SFLA, PA-SAFT and FMC could not be used
- ✓ Under identical conditions, Angle Beam PA-SAFT performed better than SFLA and normal beam PA-SAFT techniques in terms of the detection of flaw extremities in a thick carbon steel weld joint. The depth sizing of flaw is accurate by all the techniques
- ✓ SFLA and PA-SAFT techniques failed to detect the root crack in the austenitic stainless steel weld joint. Angle beam PA-SAFT not only detected this crack with good signal to noise ratio but also sized it accurately for its depth, without the removal of weld bead.
- ✓ For circumferential weld joint in a pressure vessel, SFLA could detect and resolve the reference flaws, although the signal to noise ratio is inferior. PA-SAFT technique performed better than SFLA in this regard.
- ✓ When compared with conventional phased array, the study on the mock-up block of a circumferential weld joint in a pressure vessel shows that SFLA and PA-SAFT techniques are able to meet the inspection requirements using much lesser resources as compared to the focal law based conventional phased array technique.

CONCLUSIONS, CONTRIBUTIONS AND SUGGESTIONS FOR FUTURE WORK

7.1 Conclusions

The following are the conclusions of the research work carried out as part of this PhD:

- The current study deals with the investigation of an integrated approach to sound beam focusing using linear array and SAFT. Two techniques viz. Synthetic Focusing using Linear Arrays (SFLA) and Phased Array – SAFT (PA-SAFT) have been studied to achieve the sound beam focusing within the material. Since the focusing is achieved by SAFT processing, both the techniques rely on the divergence of the sound beam emanating from a linear array while acquiring the raw B-scan data. The key to better focusing is the large beam divergence during data acquisition, which is achieved by using a very small source size.
- In the case of SFLA technique, a single miniature piezoelectric element of a linear array is used for sound beam transmission. As a result, significant sound beam divergence is obtained during data acquisition as compared to the relatively large size piezoelectric element used in the conventional ultrasonic testing.
- In the case of PA-SAFT technique, the sound beam is focused very close to the scanning surface by focal laws using a group of elements (active aperture) to create a virtual source much smaller than the size of the active aperture. In this case too, a significant beam divergence is obtained in the region of interest, which lies beyond the focal point.

- A dedicated algorithm using LabView is developed to carry out the time based SAFT processing of the raw B-scan data acquired by both the techniques.
- With both SFLA and PA-SAFT techniques, the crucial factor to achieve the sound beam focusing is the sound beam divergence during the acquisition of raw the B-scan image. It is observed that owing to small values of D/λ , the divergence of a sound beam emanating from a miniature piezoelectric element in a linear array is much smaller than the one predicted by the mathematical equation given in the literature, which is valid for piezoelectric crystals with large D/λ values. As part of this study, an empirical relationship is derived to evaluate the sound beam divergence for a sub-millimeter size piezoelectric element. The relationship is validated by carrying out experimental studies using arrays of different frequencies, element size and orthogonal dimensions.
- The effect of array based parameters and the SAFT processing parameters on the sound beam focusing using SFLA technique are studied in details. It is observed that the best focusing is achieved by using the smallest possible piezoelectric element and the largest possible frequency. However, because of low amplitude of the sound wave emanating from a miniature piezoelectric element and increased attenuation at higher frequency, these requirements adversely affect the signal to noise ratio and the sensitivity for flaw detection, especially at higher depth. Hence, one has to strike a balance between the smallest focal spot size to be achieved at the largest depth of interest. The pitch of the linear array does not greatly affect the focusing unlike the above two parameters. It is observed that larger the total effective aperture on the scanning surface better is the focusing, especially at larger depths. This is primarily because of the fact with large TEA, the raw data is available for larger divergence angles, leading to better focusing during

SAFT processing. The difference between the actual value and the input value of SAFT processing parameters viz. sound velocity in the material, pitch of the linear array used and the sound beam divergence angle, also affect sound beam focusing using SFLA. This difference adversely affects the constructive interference at the flaw location and destructive interference adjacent to it, leading to inferior focusing.

- It is also observed that the focal spot size achieved by SAFT, when applied on a data acquired using a miniature size piezoelectric element, does not depend of the size of the piezoelectric element (D) alone, but more specifically on the ratio of D/λ , where λ is the wavelength. This is because of the fact that for miniature rectangular piezoelectric elements, the sound beam divergence constant $k_{\delta dB}$ does not have a fixed value of 0.44 (as applicable to large piezoelectric rectangular elements) but is dependent on D/λ ratio. An empirical relationship to evaluate the focal spot size by SFLA technique has been derived.
- For PA-SAFT technique, the active aperture size (number of elements to be used for sound beam transmission and reception) is optimized for the linear arrays that are used during this study. This size does not depend on the array parameters alone (element size, pitch and frequency) but also on the depth range over which the focusing is desired. It is observed that the active aperture size along with the frequency decides the size of the virtual source created at the focal point. Since focusing during SAFT depends on the source size (real or virtual), the size of virtual source determines the focal spot size achieved in the region of interest during SAFT.
- For a given linear array, the focal spot size using SFLA technique is smaller than the one achieved by PA-SAFT technique, primarily because of the fact that the source size during

data acquisition by SFLA technique (element size) is smaller than PA-SAFT technique (virtual source). For both the techniques, the focusing improves with the use of high frequency linear array. This can be attributed to the narrow pulse width at higher frequency. With PA-SAFT technique, there is also a reduction in the size of the virtual source as the frequency increases leading to better focusing. Under identical test conditions, the focal spot size achieved by SFLA technique is comparable to the one achieved by FMC + TFM technique, since both the techniques use a single element for sound beam excitation. However, the image quality is better with FMC + TFM since full matrix data is available for processing leading to better signal averaging and image reconstruction.

- The effectiveness of SFLA and PA-SAFT techniques for the detection and characterization of volumetric flaws is studied by experimental work on samples containing simulated flaws in the form of side drilled holes. The sensitivity for detection of these flaws is defined in terms of size to distance ratio (SDR) and the gain reserve (GR) of the phased array instrument. It is observed that, under similar experimental conditions (linear array, instrument controls and test sample), PA-SAFT technique shows better sensitivity than SFLA. PA-SAFT technique is able to detect volumetric flaws in carbon steel located one below the other with the SDR of the order of 0.022 with a good signal to noise ratio and high GR as compared to SFLA and FMC + TFM techniques. Similar SDR could be achieved by SFLA and FMC techniques, but at the lower GR value. The better sensitivity of PA-SAFT can be attributed to the use of higher dimension of the active aperture for data acquisition, which results in higher sound wave amplitude at any given depth in the material. Both SFLA and PA-SAFT techniques could detect 0.5

mm dia. side drilled hole located at a depth of 200 mm from the surface in aluminum using 10 MHz, 0.3 mm pitch linear array, which corresponds to the SDR of 0.0025. These results indicate that the sensitivity for detection of volumetric flaws by SFLA and PA-SAFT techniques is excellent.

- The ability of SFLA and PA-SAFT techniques for the detection of volumetric flaws in the region that does not lie below the linear array is also studied. It is observed that SFLA technique could detect volumetric flaws up to a distance of approximately 25 mm away from the edge of the array. With PA-SAFT technique too, this coverage could be achieved, but the sensitivity was slightly inferior as compared to SFLA technique. The flaws that do not lie beneath the array show lower amplitude and larger spread as compared to the flaws located below the array. The primary reason for this is the fact that the flaws, which lie below the array, are detected by all the elements. While those, which are away from the array are detected by fewer elements (edge elements). Moreover, the signal amplitude in the raw A-scan data from the flaws away from the array is much lower, as these are detected by the peripheral sound beam and not the central beam. As a result, for these flaws, there are fewer A-scans and lower signal amplitude during SAFT processing. Hence, their amplitude is lower and the spread is higher in the processed B-scan image as compared to the flaws below the array. These results indicate that the sound beam focusing using SFLA and PA-SAFT techniques is more effective in the region beneath the array than away from it.
- The ability to resolve two closely spaced volumetric flaws by SFLA and PA-SAFT techniques is studied to determine the limit of resolution. It is observed that for moderate depth (≈ 20 mm in steel), SFLA technique could resolve flaws separated centre-to-centre

by 0.6 mm (edge to edge by 0.1 mm). With PA-SAFT technique, the resolution is found to be slightly inferior i.e. 0.9 mm (edge to edge by 0.4 mm). This can be attributed to a larger focal spot size achieved using PA-SAFT technique (because of the larger virtual source size) as compared to SFLA technique. However, both these techniques showed far better resolution as compared to the focal law based phased array examination using large number of active elements for sound beam focusing.

- The effectiveness of SFLA and PA-SAFT techniques for the detection and characterization of planar flaws is studied on stainless steel samples, both lower and higher thickness, containing simulated flaws in the form of machined slots of various orientations made by EDM. The characterization of these flaws in terms of their through-wall dimension (height or depth) and orientation is carried out by locating the extremities of these flaws with respect to the scanning surface. For reliable detection and accurate characterization, it is important that the signals from the flaw extremities have lower lateral spread and sufficient amplitude above the background noise. It is observed that SFLA and PA-SAFT techniques are able to reliably detect the planar flaws and characterize them accurately for thin sections (≈ 25 mm thick stainless steel). The results obtained by these techniques are comparable to the results obtained by FMC + TFM technique. When the planar flaw is located deeper (> 30 mm from the scanning surface in stainless steel), SFLA and FMC + TFM techniques could not detect the lower tip of the flaw reliably. With PA-SAFT, the detection as well as the characterization of such flaws is satisfactory. The better detection by PA-SAFT technique can be attributed to a higher amplitude of the incident sound wave (at the flaw tip) due to multiple element excitation as compared to a single element excitation while using SFLA and FMC techniques.

- One of the major limitations of SFLA and PA-SAFT techniques is that the linear array is required to be placed symmetrically over the flaw so that the sound emanating from majority of elements or aperture interacts with the flaw for better detection and characterization. In some cases, for example during the inspection of weld joint in an unground weld bead, this condition cannot be satisfied. A variant of PA-SAFT named Angle Beam PA-SAFT technique is standardized for this purpose. The technique is found to be very effective in the detection and accurate depth sizing of planar flaws open to the back surface and the scanning surface. The technique also gave better results as compared to SFLA, PA-SAFT (normal beam) and FMC + TFM techniques for the detection and characterization of embedded planar flaws in 60 mm thick stainless steel plate. This is because of the better diffraction of the incident sound beam by flaw tips while using angle beam as compared to normal beam employed during SFLA, PA-SAFT and FMC + TFM techniques.
- One of the major objectives of this research work is to assess the usefulness of SFLA and PA-SAFT techniques for field application, wherein it is required to inspect engineering components for the detection and characterization of ‘real’ volumetric and planar flaws. This aspect is studied on carbon steel weld samples containing volumetric flaws in the form of clustered porosity and slag inclusion, and the planar flaws in the form of lack of sidewall fusion and crack. The results indicated that SFLA and PA-SAFT techniques could reliably detect and accurately characterize volumetric and planar flaws in terms of their through-wall dimension. The through-wall dimension of the flaws evaluated by these techniques matched closely with the actual dimensions found out by metallography after sectioning the sample.

- The effectiveness of Angle Beam PA-SAFT technique for ‘real’ flaws is studied on austenitic stainless steel weld sample with an unground weld bead having a root crack and a toe-crack. The technique is able to detect and accurately characterize the cracks for their depth. The depth of the cracks evaluated by Angle Beam PA-SAFT matched closely with the actual depth found out by metallography after sectioning the sample.
- The performance of SFLA, normal beam PA-SAFT and Angle beam PA-SAFT techniques is compared under identical test conditions by carrying out experiments on a 22 mm thick carbon steel weld sample with lack of sidewall fusion and a 25 mm thick austenitic stainless steel weld sample with a root crack. It is observed that, while all the techniques could detect the lack of sidewall fusion, the signal to noise ratio for the flaw extremities is much higher using Angle beam PA-SAFT technique as compared to SFLA and normal beam PA-SAFT techniques. Since the detection of the flaw tips is based on the diffraction of the incident ultrasonic waves, higher signal amplitude of the diffracted signals during Angle beam PA-SAFT is responsible for better signal to noise ratio using this technique as compared to other techniques. SFLA and normal beam PA-SAFT techniques failed to detect the root crack in the austenitic stainless steel weld. While using these techniques, the linear array is placed over the weld bead during data acquisition. With this arrangement, the sound beam has to pass through the coarse grain dendritic structure of the weld metal. Because of excessive scattering, attenuation and beam skewing, the crack tip is not detected by these techniques. Angle Beam PA-SAFT is able to reliably detect this crack with a good signal to noise ratio and also size it accurately for its depth. In this case, the linear array is placed away from the weld bead, because of which the sound beam travels for majority of its path in the base metal and

hence suffers from negligible scattering and attenuation. As a result, a high amplitude signal from the crack-tip is obtained in the acquired data leading to better detection and characterization of the root crack by Angle Beam PA-SAFT technique. The results indicate that the Angle beam PA-SAFT technique gives better sensitivity and accurate depth sizing of planar flaws in austenitic stainless steel weld joints, with or without the removal of weld bead.

- The feasibility of using SFLA and PA-SAFT techniques for in-service inspection of a circumferential weld joint in the pressure vessel of a nuclear boiling water reactor is studied on the mock-up block of the weld joint. Both SFLA and PA-SAFT techniques could detect the simulated volumetric and planar flaws in the mock-up, with much lesser resources in terms of the requirements of parallel channels in the phased array instrumentation, as compared to the conventional phased array technique. The signal to noise ratio using PA-SAFT technique is found to be much better than SFLA technique. This can be attributed to a higher amplitude of the sound wave at the flaw location while using PA-SAFT technique as compared to SFLA technique.
- In conclusion, the two techniques viz. SFLA and PA-SAFT, which are based on SAFT processing of the raw B-scan data acquired by the divergent sound beam from a linear array, can achieve sound beam focusing using much lesser resources, such as lesser number of elements in a given aperture and the phased array instrumentation with less number of parallel transmitter/receiver channels, as compared to the conventional phased array technique using focal laws. In spite of using a single or very few elements for sound beam transmission, the focal spot size achieved by SFLA and PA-SAFT techniques is found to be much finer than what could be achieved by conventional phased array using

similar or large number of elements as active aperture. The sound beam focusing by these techniques is comparable to the one obtained by FMC + TFM technique. The advantage of SFLA technique over FMC + TFM is that the data size for post-processing is very small. As a result, a single channel instrument with multiplexing can be used to built-up a real-time system for industrial use. The advantage of PA-SAFT technique over FMC + TFM is the enhanced sensitivity for the detection of flaws, especially planar, at larger depth. The focusing of the sound beam by SFLA and PA-SAFT techniques can be utilized to detect, locate and characterize volumetric and planar flaws in engineering components. Based on the experimental results on weld samples with real volumetric and planar flaws, it can be concluded that both SFLA and PA-SAFT techniques hold a very good potential for field applications.

7.2 Specific Innovative and Novel Contributions

The following are the specific innovative and novel contributions from the research work carried out as part of this PhD:

- **Empirical relationship to evaluate the sound beam divergence for miniature piezoelectric element**

During the course of the study, it is observed that the sound beam divergence from a sub-millimeter size piezoelectric element used in a linear array is much smaller than the one predicted by the equation given in the literature. An empirical relationship to evaluate the half beam divergence angle for a miniature size piezoelectric element has been derived for the first time. The equation has been validated and is useful to evaluate the half beam

divergence angle for the rectangular piezoelectric element having D/λ ratio of 0.2 to 10, where D is the size of the piezoelectric element and λ is the wavelength of sound.

- **Dependence of focal spot size on the D/λ**

It has been widely reported in the literature that the lateral resolution or the focal spot size achieved by SAFT is independent of the wavelength and is of the order of $D/2$. While this may hold true for the SAFT processing on the data acquired by large size piezoelectric elements, it has been observed during this study that while dealing with miniature size piezoelectric element, the focal spot size achieved by SAFT does not depend on D alone, but more specifically on the ratio D/λ . The non-linearity in the dependence of the beam divergence angle on λ/D ratio (while dealing with the miniature elements) could be the reason for this. An empirical relationship has been developed for the first time to evaluate the 6 dB focal spot size of the sound beam focused using an integrated approach (linear array + SAFT).

- **An integrated approach to sound beam focusing using phased array and SAFT**

Two sound beam focusing techniques viz. Synthetic Focusing using Linear Arrays (SFLA) and Phased Array-SAFT (PA-SAFT) have been investigated as part of this study. These techniques are useful for the detection and characterization of volumetric and planar flaws in engineering components. A variant of PA-SAFT technique using angle beam has been standardized for detection and characterization of flaws in the weld joint with an unground weld bead, where SFLA, normal beam PA-SAFT and FMC + TFM techniques are ineffective

- **Alternate to Full Matrix Capture – Total Focusing Method**

During the experimental work on various samples, the performance of SFLA and PA-SAFT techniques in terms of sound beam focusing, ability to detect flaws and characterize them in terms of dimensions, is found to be comparable with the established advanced array based technique called Full Matrix Capture – Total Focusing Method (FMC + TFM). One major drawback with FMC technique is the large data size for processing, especially while using an array with large number of elements. Also to realize a ‘real time’ FMC + TFM system, one needs to have large number of parallel receiver channels in the phased array instrumentation, which adds to the cost. SFLA technique, without such drawbacks, offers a good alternative to FMC + TFM, without compromising on the ability to focus the sound beam and produce high resolution images. Another problem with FMC+TFM technique is its inability to detect planar flaws at larger depth due to low wave amplitude during sound beam transmission. PA-SAFT technique using normal beam and angle beam are very useful to overcome this limitation.

- **Low cost compact phased array instrumentation**

The two techniques investigated during this research work viz. SFLA and PA-SAFT, require excitation of a single or a very few elements for sound beam transmission to achieve sound beam focusing over a considerable depth. On the other hand, the conventional phased array using focal laws requires excitation of large number of elements in a linear array to achieve similar sound beam focusing. Even FMC + TFM technique needs large number of parallel receiver channels for applications demanding a real time system. This research has paved the way towards the development of a compact, low cost phased array instrumentation for

industrial applications, which can replace the bulky and the expensive current generation phased array instruments.

7.3 Suggestions for future work

- **Flaw characterization in anisotropic materials**

It has been observed during the current study that the input value of sound velocity during SAFT processing plays a significant role in achieving a very fine focal spot size in the processed B-scan image. During the processing of raw B-scan data, it is assumed that the velocity of the sound in the material remains constant through-out the path length of the acquired A-scan data and for all the individual A-scans. While dealing with anisotropic materials such as austenitic stainless steel weld and forgings of certain materials, this assumption may not remain valid. Moreover, the ultrasonic beam may not travel in the straight path (as assumed during SAFT processing) and can undergo beam skewing due to material anisotropy. As a result, the constructive and destructive interference during SAFT processing may not be effective leading to poor focusing and inaccurate location of the flaw extremities. One can address this issue by modeling the beam skewing effect for a given grain structure and include the results of the model in the SAFT processing algorithm. A study can be undertaken on the application of SFLA and PA-SAFT techniques for characterization of flaws in anisotropic materials.

- **Inter-element variability on imaging performance**

During the application of SFLA (or PA-SAFT) technique, the raw B-scan data is acquired by individual elements (or a small group of elements) using a linear array. Subsequently, the B-scan data is processed by SAFT, which involves time-delay, summation and averaging of the individual A-scans in the acquired data. The variability in the array elements in terms of

amplitude, phase and time delay may affect the sound beam focusing and so the final image quality achieved on SAFT processing. A separate study involving simulation and experimental work can be undertaken to study this aspect for SFLA and PA-SAFT techniques.

- **Depth profiling of a planar flaw along its length**

During the current research, the experimental work is carried out using linear arrays, with which the B-scan data is acquired by electronic scanning. When this approach is used for the detection and characterization of a flaw, one can get the information for that section of a flaw, over which the linear array is placed. In order to carry out depth profiling of the flaw over its length, one needs to acquire multiple B-scans followed by SAFT processing of each one. This process is time consuming. One way to address this issue is to use a 2-D matrix array, acquire C-scan data and then carry out SAFT processing. The use of SFLA and PA-SAFT techniques for the depth profiling of planar flaws as suggested needs realization through systematic studies.

- **Estimating probability of detection (POD)**

During the current research work, it has been demonstrated that SFLA and PA-SAFT techniques are capable of the detection and characterization of volumetric and planar flaws. It is also concluded that these two techniques hold a very good potential for field applications. In order to benchmark the performance of these two techniques for engineering applications, a systematic study on the probability of detection using SFLA and PA-SAFT can be undertaken.

REFERENCES

1. Josef Krautkramer and Herbert Krautkramer, Ultrasonic testing of materials, 4th fully revised edition, Springer international student's edition, 1993
2. G Maes, M. Delaide, Ph. Dombert, On the use of the ultrasonic beam focusing techniques, Proc. of the 11th International Conference on NDE in the Nuclear and Pressure Vessel Industries, New Mexico, USA, 1992
3. H Djelouah, JC Baboux, M Perdrix, Theoretical and experimental study of the field radiated by ultrasonic focussed transducers, Ultrasonics, 29, 1991, 188-200
4. A Karpelson, Piezo-transducers with acoustic lenses forming narrow weakly diverging ultrasonic beams, Proceedings of 9th European Conference on NDT, Berlin, Germany, September, 2006
5. Jack Blitz and Geoff Simpson, Ultrasonic methods of non-destructive testing, Chapman and Hall, London, 1996, ISBN 0412604701
6. Introduction to phased array ultrasonic technology applications, Advanced practical NDT series, Olympus NDT, 2007, ISBN 0-9735933-4-2
7. Phased array testing, Basic theory to industrial applications, NDT field guide, Olympus NDT, 2014
8. J. Rooney and A. Reid, Ultrasonic Inspection of Small Diameter Thin-Wall Tubing, Ultrasonics, 4, April 1966, 57-63
9. M. Ezzaidi, D. Decultot, G. Maze, A. Moudden, Measurement of Thickness of a Cylindrical Shell with a Focused Beam, NDT & E International, 35, 2002, 433-436
10. K. Shiloh, L.J. Bondt, A.K. Som, Detection limits for single small flaws and groups of flaws when using focussed ultrasonic transducers, Ultrasonics, 31, 1993, 395-404
11. O Martinez, M Parrilla, MAG Izquierdo, LG Ullate, Application of digital signal processing techniques to synthetic aperture focusing technique images, Sensors and Actuators A: Physical, 76, 1999, 448-456
12. Aldo O. De La Haza, Andrey A. Samokrutov, Pavel A. Samokrutov, Assessment of Concrete Structures using the Mira and Eyecon Ultrasonic Shear Wave Devices and the SAFT-C Image Reconstruction Technique, Construction and Building Materials, 38, 2013, 1276-1291
13. W. Muller, V. Schmitz, G. Schafer, Reconstruction by the Synthetic Aperture Focussing Technique (SAFT), Nuclear Engineering and Design, 94, 1986, 393-404
14. A. Chahbaz, R. Sicard, Comparative Evaluation between Ultrasonic Phased Array and Synthetic Aperture Focusing Techniques, Review of Quantitative Non-destructive Evaluation, 22, 2002, 769-776

15. V. Schmitz, S. Chakhlov, W. Muller, Experiences with Synthetic Aperture Focusing Technique in the field, *Ultrasonics*, 38, 2000, 731–738
16. RN Thomson, Transverse and longitudinal resolution of the synthetic aperture focusing technique, *Ultrasonics*, January 1984, 9-15
17. J. Pitkanen, P. Oy, Olkiluoto, SAFT – Is it a Tool for Improved Sizing in Ultrasonic Testing, ECNDT, 2006, 1-13
18. Michael Berke and Johannes Buechler, Practical, Experiences in Manual Phased Array Inspections, 17th World conference on Non Destructive Testing, Shanghai, China, 2008
19. K Uchida, S Nagai, H Kashiwaya, M Arii, Availability Study of a Phased Array Ultrasonic Technique, *Nuclear Engineering and Design*, 81, 1984, 309-314
20. J. Dias, Construction and performance of an Experimental Phased Array Acoustic Imaging Transducer, *Ultrasonic Imaging*, 3, 1981, 352-368
21. Paul A. Meyer, J.W. Anderson, Ultrasonic Testing Using Phased Arrays, Proc. of 15th WCNDT, Rome, 2012
22. H. Wüstenberg, A. Erhard, G. Schenk, Scanning Modes at the Application of Ultrasonic Phased Array Inspection Systems, Proc. of 15th WCNDT, Rome, 2012
23. Shi-Chang Wooh and Yijun Shi, Optimization of ultrasonic phased array, Review of Progress in Quantitative Non-destructive Evaluation, Edited by D.O. Thompson and D.E. Chimenti, Plenum Press, New York, 17, 1998, 883-890
24. Guy Lafontaine, Potential of Ultrasonic Phased Arrays for Faster, Better and Cheaper Inspections, <http://www.ndt.net/article/v05n10/lafont2/lafont2.htm>
25. Non-destructive Inspection by Phased Array Ultrasonic Method for Steel Structures, JFE technical report, No. 17, Apr. 2012
26. Jorge F Cruza, Jorge Camacho, Jose M Moreno and Carlos Fritsch, Ultrafast hardware based focal law calculator for automatic focusing, *NDT & E International*, 74, Sept. 2015, 1-7
27. P. Pugalendhi and D. Veeraraju, Use of Phased Array Ultrasonic Testing (PAUT) & Time of Flight Diffraction (TOFD) in Lieu of Radiography Testing on ASME U Stamp Pressure Vessel fabrication Projects, Singapore International NDT Conference & Exhibition, 2013, 19-20
28. O. Tumsys and E. Jasiuniene, The focusing of the ultrasonic phased array in the case of non-contact NDE methods, *Electronika IR Elektrotechnika*, 20, 2014, 44-47
29. R. J. Ditchburn and M. E. Ibrahim, Ultrasonic Phased Arrays for the Inspection of Thick-Section Welds, DSTO-TN-0911, Defence Science and Technology Organization, Australia, 2009, 1-8
30. Wissam M. Alobaid, Entidhar A. Alkuam, Hussain M. Al-Rizzo, Eric Sandgren, Applications of Ultrasonic Techniques in Oil and Gas Pipeline Industries: A Review, *American Journal of Operations Research*, 5, 2015, 274-287

31. D.S. Caravaca, C. Bird and D. Kleiner, Ultrasonic Phased Array Inspection of Electrofusion Joints in Polyethylene Pipes, *Insight: Non-Destructive Testing and Condition Monitoring*, 49, 83-86
32. François X. de Fromont, How Ultrasonic Phased Array is Shaping the Industry, *Quality Magazine*, July 2008, <http://www.qualitymag.com/articles/89597-how-ultrasonic-phased-array-is-shaping-the-industry>
33. Seunghan Yang, Byungsik Yoon, Yongsik Kim, Using phased array ultrasonic technique for the inspection of straddle mount-type low-pressure turbine disc, *NDT & E International*, 42, March 2009, 128-132
34. M. Tabatabaeipour, J. Hettler, S. Delrue, K. Van Den Abeele, Non-destructive ultrasonic examination of root defects in friction stir welded butt-joints, *NDT & E International*, 80, June 2016, 23-34
35. M Krause, F Mielentz, B Milman, W Müller, V Schmitz, H Wiggenghauser, Ultrasonic imaging of concrete members using an array system, *NDT & E International*, 34, September 2001, 403-408
36. Chuan Li, Damien Pain, Paul D. Wilcox, Bruce W. Drinkwater, Imaging composite material using ultrasonic arrays, *NDT & E International*, 53, January 2013, 8-17
37. C. Holmes, B.W. Drinkwater, P.D. Wilcox, Post-Processing of the Full Matrix of Ultrasonic Transmit–Receive Array Data for Non-Destructive Evaluation, *NDT & E International*, 38, 2005, 701–711
38. R. Long, J Russell, P Cawley, Through-Weld Ultrasonic Phased Array Inspection Using Full Matrix Capture, *Review of Progress in Quantitative Nondestructive Evaluation*, 29, 2009, 918-925
39. C. Holmes, B.W. Drinkwater, P.D. Wilcox, The post-processing of ultrasonic array data using the total focusing method, *Insight*, 46, 2004, 677-680
40. Bruce W. Drinkwater, Paul D. Wilcox, Ultrasonic arrays for non-destructive evaluation: A review, *NDT & E International*, 39, 2006, 525-541
41. S. Alavudeen, C. V. Krishnamurthy, and Krishnan Balasubramaniam, Technique for imaging using virtual array of sources (TIVAS), *Review of Progress in Quantitative Non-destructive Evaluation*, 30, 2011, 1687-1694
42. Jacob Kortbek, Jorgen Arendt Jensen and Kim Lokke Gammelmark, Sequential beamforming for synthetic aperture imaging, *Ultrasonics*, 53, 2013, 1-16
43. S. Bannouf, S. Robert, O. Casula and C. Prada, Data set reduction for ultrasonic TFM imaging using the effective aperture approach and virtual sources, *Journal of Physics, Conference Series*, 457, 2013, 1-13
44. B. Chassignole, R.E. Guerjouma, M.A. Ploix, T. Fouquet, Ultrasonic and Structural Characterization of Anisotropic Austenitic Stainless Steel Welds: Towards a Higher Reliability in Ultrasonic Non-Destructive Testing, *NDT & E International*, 43, 2010, 273–282

45. I.D. Culverwell, J.A. Ogilvy, Scattering of Ultrasound from Clusters of Inclusions, *Ultrasonics*, 30, 1992, 8-14
46. K.B. Kim, D.K. Hsu, D.J. Barnard, Estimation of Porosity Content of Composite Materials by Applying Discrete Wavelet Transform to Ultrasonic Backscattered Signal, *NDT & E International*, 56, 2013, 10-16
47. ASME Boiler and Pressure Vessel Code Section III: Rules for construction of nuclear facility components, Division 1, NB 5112, Non-destructive Examination Procedures, 2014
48. ASME Boiler and Pressure Vessel Code Section V: Non-Destructive Examination, Article 23, Ultrasonic Standards, 2014
49. ASME Boiler and Pressure Vessel Code Section VIII: Rules for construction of pressure vessel, Division 1, UCS: Requirements for pressure vessels constructed of carbon and low alloy steel, 2014
50. Nuclear Safety Standard Commission – KTA, Components of the Reactor Coolant Pressure Boundary of Light Water Reactors, Part 3: Manufacture, Annex C: Performance of manual ultrasonic examinations, 2007, 134-149
51. RCC-MRx, Design and Construction Rules for mechanical components of nuclear installations: High-temperature, research and fusion reactors, 2015
52. ASME Boiler and Pressure Vessel Code Section XI: Rules for in-service inspection of nuclear power plant components, Division 1, Rules for Inspection and Testing of Components of Light-Water Cooled Plants, 2014
53. CAN CAS N285.4, Periodic inspections of CANDU nuclear power plant components, Inspection methods and procedures, 2014, 19-22
54. Welding Handbook, American Welding Society, 9th edition Vol. 1, Welding Science and Technology, Ed.: Cynthia L. Jenney and Annette O'Brien, Welding Inspection and Non-Destructive Examination, 579-636
55. DE Rawl, SL West, DA Wheeler, MR Louthan, Defect Characterization in Pipe-to-Pipe Welds in Large-Diameter Stainless-Steel Piping, *Material Characterization*, 33, 1994, 155-162
56. R Bullough, FM Burdekin, OVJ Chapman, VR Green, DPG Lidbury, H Pisarski, RG Warwick, JB Wintle, The probability of large defects in thick-section butt welds in nuclear components, *International Journal of Pressure Vessel and Piping*, 78, 2001, 553-565
57. S. Crutzen, F. Frank, L. Fabbri, P. Lemaitre, Q. Schneider, W. Visser, Compilation of NDE Effectiveness Data, SINTAP Task 3.4, European Commission, March 1999
58. B.K. Shah, Significance of flaws in performance of engineering components, IAEA-RCA training course on in-service inspection of research reactors, 2002, 257-270
59. CF. Boulton, Acceptance Levels of Weld Defects for Fatigue Service, *Welding Research Supplement*, 1977, 13-22

60. Ultrasonic testing of materials at Level II, IAEA TECDOC-462, Training Course Series No. 10, International Atomic Energy Agency, 1999
61. Ultrasonic flaw detection tutorials, <http://www.olympus-ims.com/en/ndt-tutorials/flaw-detection/dac-tvg>
62. Ultrasonic Testing Level II, Krautkramer Training Material
63. S.F. Burch, An amplitude correlation and differencing method for the monitoring of flaws in repeat ultrasonic inspections, *Ultrasonics*, 1985, 246-252
64. SR Ahmed, M. Saka, A new ultrasonic angle-beam technique for sensitive evaluation of closed cracks, *NDT & E International*, 33, 2000, 261-271
65. AN Sinclair, J Fortin, B Shakibi, F Honarvar, M Jastrzebski, MDC Moles, Enhancement of ultrasonic images for sizing of defects by time-of-flight diffraction, *NDT & E International*, 43, 2010, 258-264
66. FA Ravenscroft, K Newton, CB Scruby, Diffraction of ultrasound by cracks: comparison of experiment with theory, *Ultrasonics*, 29, 1991, 29-37
67. Fundamentals of Ultrasonic Imaging and Flaw Detection, <http://www.ni.com/white-paper/3368/en/>
68. Reinhold Ludwig and Dino Roberti, A non-destructive ultrasonic imaging system for detection of flaws in metal blocks, *IEEE transactions on instrumentation and measurement*, 38, Feb. 1989, 113-118
69. G. Por, M. Agocs, E. Kocso, B. Palotas, P. Trampus, 3D Ultrasound Imaging of Flaws, Electronics and Spot Welds, *Proceedings of ECNDT 2014*
70. Roman Ruzek, Radek Lohonka, Josef Jironc, Ultrasonic C-Scan and shearography NDI techniques evaluation of impact defects identification, *NDT & E International*, 39, 2006, 132-142
71. T. Tarnoczy, Sound Focussing Lenses and Waveguides, *Ultrasonics*, 3, 1965, 115-127
72. Virginia Griffing and Francis E. Fox, Theory of Ultrasonic Intensity Gain Due to Concave Reflectors, *The Journal of the Acoustical Society of America* 21, 1949, 348
73. F. L. Hopwood, Experiments with high frequency sound waves, *Journal of Scientific Instruments*, 6, 1929, 34-40
74. F. L. Hopwood, Some properties of inaudible sound, *Nature*, 128, 1931, 748-751
75. F. L. Hopwood, Ultrasonic Lenses and Prisms, *Journal of Scientific Instruments*, 23, March 1946, 63
76. P. J. Ernst, Ultrasonic Lenses and Transmission Plates, *Journal of Scientific Instruments*, 22, Dec. 1945, 238-242
77. P. J. Ernst, Ultrasonic Lenses and Prisms, *Journal of Scientific Instruments*, 23, March 1946, 63

78. P. J. Ernst, Measurement and Specification of Ultrasonic Lenses, *Journal of the Acoustical Society of America*, 19, 1947, 474
79. P. J. Ernst, Ultrasonography, *Journal of the Acoustical Society of America*, 23, 1951, 80
80. O. Mattiat, Transducers for Producing Ultrasonic Waves, *Journal of the Acoustical Society of America*, 25, 1953, 291
81. L. D. Rosenberg, *Ultrasonic Focusing Radiators, Sources of High-Intensity Ultrasound*, Springer, ISBN 978-1-4757-6455-0, 1969, 223-309
82. MG Silk, Ultrasonic techniques for inspecting austenitic welds, *Research techniques in NDT*, 4, 1980
83. Ph. Dombert, Methodology for ultrasonic testing of austenitic stainless steel, SMIRT-10 Post Conference Seminar No. 3, NDE in relation to structural integrity, 1989, 1-11
84. JA Ogilvy, Use of focused beams in austenitic welds, *British Journal of Non-Destructive Testing* 29, 4, July 1987, 238-246
85. P. Dombret, M. Delaide, G. Maes, Ultrasonic in-service inspection of main coolant pump bowl welds, Part 1. Examination technique, *Proc. of Main coolant pump workshop*, EPRI, 1991
86. S. Crutzen, M. Certo, Ph. Dombret and R. Murgatroyd, Results of the PISC parametric studies on the effect of defect characteristics, *Proc. of 9th Int. Conf. on NDE in nuclear industry*, Tokyo 1988
87. H. Kawai, Piezoelectricity of Poly (vinylidene Flouride), *Japan Journal of Applied Physics*, 8, 1969, 975
88. D.P. Skinner, R.E. Newnham and L.E. Cross, Flexible Composite Transducer, *Material Research Bulletin*, 13, 1978, 599-607
89. R.E. Newnham, L.J. Bowen, K.A. Klicker and L.E. Cross, Composite Piezoelectric Transducers, *Materials in Engineering*, 2, 1980, 92-106
90. Gin-Shin Chen, Hsin-Chih Liu, Yu-Cheng Lin, and Yu-Li Lin, Experimental Analysis of 1-3 Piezocomposites for High-Intensity Focused Ultrasound Transducer Applications, *IEEE Transactions on Biomedical Engineering*, 60, 2013, 128-134
91. P. Dumas, J. Poguët, G. Fleury, Piezocomposite technology, An innovative approach to the improvement of NDT performance using ultrasounds, *Proc. of 8th ECNDT*, Barcelona, June 2002
92. J. Poguët, G. Fleury, O. Burat, G. Moreau, Circular phased array probes for inspection of Superphoenix steam generator tubes, *Proc. of EPRI Phased Array inspection seminar*, 1998
93. C. W. Sherwin, J. P. Ruina and R. D. Radcliffe, Some Early Developments in Synthetic Aperture Radar Systems, *IRE Transactions on Military Electronics*, 6, 1962, 111-115
94. J. Kovaly, G. S. Newell, W. C. Prothe and C. W. Sherwin, The Observations of Snorkels and Sea Clutter Using Coherent Airborne Radar, *Control Systems Lab., University of Illinois, Urbana, Ill., Rept. R-27*; November 20, 1952

95. B. L. Hicks, N. Knable, G. S. Newell, J. P. Ruina and C. W. Sherwin, The spectrum of x-band radiation backscattered from the sea surface, *Journal of Geophysical Research*, 65, 1960, 825-837
96. L.J. Cutrona, W. E. Vivian, E. N. Leith, and G. O. Hall, A High Resolution Radar Combat Surveillance System, *IRE Transactions on Military Electronics*, 5, April 1961, 127-130
97. L. J. Cutrona and G. O. Hall, A Comparison of Techniques for Achieving Fine Azimuth Resolution, *IRE Transactions on Military Electronics*, 6, April 1962, 119-121
98. J. R. Frederick, J. A. Seydel, and R. C. Fairchild, Improved ultrasonic non-destructive testing of pressure vessels, Progress Report, NUREG-0007-1, NRC-5, University of Michigan, Aug. 1974-July 1975
99. G. S. Kino, M. Grant, P. D. Corl, and C. S. De Silets, A Digital synthetic aperture acoustic imaging for NDE, *IEEE Ultrasonics Symposium Proceedings*, 1979, 459-467
100. S.R. Doctor, L.J. Busse and H.D. Collins: The SAFT-UT Technology Evolution, Proc. 6th International Conference on NDE in the Nuclear Industry, Zurich, 1983, ISBN: 0-87170-192-8
101. Tadeusz Stepinski, Synthetic Aperture Focusing Technique in Ultrasonic Inspection of Coarse Grained Materials, *SKI Report 2008:06*, ISSN 1104-1374
102. A.W. Elbern and L. Guimarães, Synthetic Aperture Focusing Technique for Image Restoration, Proc. of International Symposium on NDT Contribution to the Infrastructure Safety Systems, Nov. 1999, Brazil
103. Tadeusz Stepinski and Fredrik Lingvall, Synthetic aperture focusing techniques for ultrasonic imaging of solid objects, *EUSAR 2010*, 438-441
104. Martin H. Skjelvareid, Yngve Birkelund and Yngvar Larsen, Internal pipeline inspection using virtual source synthetic aperture ultrasound imaging, *NDT & E International*, 54, 2013, 151-158
105. Abhijit Ganguli, Carey M. Rappaport, David Abramo and Sara Wadia-Fascetti, Synthetic aperture imaging for flaw detection in a concrete medium, *NDT & E International*, 45, 2012, 79-90
106. J. Seydel, Ultrasonic Synthetic Aperture Focusing Techniques in NDT, *Research Techniques in Non-destructive Testing*, Ed. R.S. Sharpe, Academic Press, London, 1982, 6, 1-47.
107. J. Johnson, Parameter Study of Synthetic Aperture Focusing in Ultrasonics, *Review of Progress in QNDE*, Ed. D.O. Thompson, D.E. Chimenti Plenum Press, New York, 1, 1982, 735-752
108. S.F. Burch, J.T. Burton, Ultrasonic synthetic aperture focusing using planar pulse-echo transducers, *Ultrasonics*, 22, 1984, 275-281
109. S.R. Doctor, T.E. Hall, L.D. Reid, SAFT—the evolution of a signal processing technology for ultrasonic testing, *NDT International*, 19, 1986, 163-167

110. S. Kramer, Ultrasonic Weld Defect Sizing Using the Synthetic Aperture Focusing Technique, Review of Progress in QNDE, Ed. D.O. Thompson, D.E. Chimenti, Plenum Press, New York, 8, 1989, 1995-2002
111. Martin Spies and Winfried Jager, Synthetic aperture focusing for defect reconstruction in anisotropic media, Ultrasonics, 41, 2003, 125–131.
112. <http://www.olympus-ims.com/en/ndt-tutorials/intro/breif-history/>
113. https://en.wikipedia.org/wiki/Phased_array
114. Joseph Woo, A short history of the development of ultrasound in obstetrics and gynaecology, <http://www.ob-ultrasound.net/history1.html>
115. Ian Donald, J Macvicar and TG Brown, Investigation of abdominal masses by pulsed ultrasound, Lancet, 1958, <http://www.ob-ultrasound.net/lancet.html>
116. J. C. Somer, Electronic sector scanning for ultrasonic diagnosis, Ultrasonics, July 1969, 153-159
117. Olaf T Von Ramm and FL Thurstone, Cardiac imaging using a phased-ray ultrasound system, I: system design Circulation, 53, 1976, 258-262
118. Carlisle L. Morgan, William S. Trought, William M. Clark, Olaf T. Von Ramm and Frederick L. Thurstone, Principles and applications of a dynamically focused phased array real time ultrasound system, Journal of clinical ultrasound, 6, December 1978, 385-391
119. <http://www.livescience.com/32071-history-of-fetal-ultrasound.html>
120. A. McNab, M.J. Campbell, Ultrasonic phased arrays for non-destructive testing, NDT International, 20, 1987, 333-337
121. I. Komura, S. Nagai, H. Kashiwaya, T. Mori, M. Aarii, Improved ultrasonic testing by phased array technique and its application, Nuclear Engineering and Design, 87, 1985, 185-191
122. W. Gebhardt, Improvement of ultrasonic testing by phased arrays, Nuclear Engineering and Design, 76, 1983, 275-283
123. X.E. Gros, N.B. Cameron and M. King, Current applications and future trends in phased array technology, Insight, 44 (11), Nov 2002, 673-678
124. L. Azar, Y. Shi, S.C. Wooh, Beam focusing behaviour of linear phased arrays, NDT & E International, 33, 2000, 189-198
125. Andreas Gommlich and Frank Schubert, Determination of Focal Laws for Linear Phased Array Probes as to the Active and Passive Element Size, Proc. of 19th World Conference on NDT, Germany, 2016
126. Olaf T Von Ramm and Stephan W Smith, Beam steering with linear arrays, IEEE transactions on biomedical engineering, BME-30, Aug 1983, 438-452
127. Shi Chang Wooh, Yijun Shi, Influence of phased array element size on beam steering behaviour, Ultrasonics, 36, 1998, 737-749

128. Shi Chang Wooh, Yijun Shi, Optimum beam steering of linear phased arrays, *Wave Motion*, 29, 1999, 245-265
129. Shi Chang Wooh and Yijun Shi, A Simulation Study of the Beam Steering Characteristics for Linear Phased Arrays, *Journal of Non-destructive Evaluation*, 18, 1999, 39-57
130. Elfgard Kuhnicke, Plane arrays - Fundamental investigations for correct steering by means of sound field calculations, *Wave Motion*, 44, 2007, 248-261
131. F. Pompei, S.C. Wooh, Phased array element shapes for suppressing grating lobes, *Journal of Acoustic Society of America*, 111, 2002, 2040–2048
132. Sung Jin Song, Hyeon Jae Shin, You Hyun Jang, Development of an ultrasonic phased array system for non-destructive tests of nuclear power plant components, *Nuclear Engineering and Design*, 214, 2002, 151-161
133. A. Lamarre, M. Moles, V. Lupien, Phased array ultrasonic inspection of friction stir weldments, *Review of Progress in Quantitative Non-destructive Evaluation*, Ed. D.O. Thompson, D.E. Chimenti, 19B, 1999, 1333-1348
134. G. Brekow, H. Wustenberg, W. Mohrle, E. Schulz, Phased array concept for the ultrasonic in-service inspection of the spherical bottom of BWR pressure vessels, *Nuclear Engineering and Design*, 112, 1989, 105-114
135. A. Erhard, G. Schenk, T. Hauser, U. Volz, New applications using phased array techniques, *Nuclear Engineering and Design*, 206, 2001, 325-336
136. Samuel Hill and Steve Dixon, Localisation of defects with time and frequency measurements using pulsed arrays, *NDT & E International*, 67, 2014, 24-30
137. S.J. Song, H.J. Shin, Y.H. Jang, Ultrasonic phased array transducers for non-destructive evaluation of steel structures, *Review of Progress in Quantitative Non-destructive Evaluation*, Ed. D.O. Thompson, D.E. Chimenti, 19A, 1999, 1079-1086.
138. S Chatillon, G Cattiaux, M Serre, O Roy, Ultrasonic non-destructive testing of pieces of complex geometry with a flexible array transducer, *Ultrasonics*, 38, 2000, 131-134
139. S Mahaut, O Roy, C Beroni, B Rotter, Development of phased array techniques to improve characterisation of defect located in a component of complex geometry, *Ultrasonics*, 40, 2002, 165-169
140. Steve Mahaut, Jean-Louis Godefroit, Olivier Roy, Gerard Cattiaux, Application of phased array techniques to coarse grain components inspection, *Ultrasonics*, 42, 2004, 791-796
141. S. Yang, B. Yoon, Y. Kim, Using phased array ultrasonic technique for the inspection of straddle mount-type low-pressure turbine disc, *NDT & E International*, 42, 2009, 128-132
142. CJ Brotherhood, BW Drinkwater, RJ Freemantle, An ultrasonic wheel-array sensor and its application to aerospace structures, *Insight*, 45, 2003, 729-734

143. L. Satyanarayan, Anish Kumar, T. Jayakumar, CV Krishnamurthy, Krishnan Balasubramaniam, Baldev Raj, Sizing Cracks in Power Plant Components Using Array Based Ultrasonic Techniques, *Journal of Non-destructive Evaluation*, 28, 2009, 111-124
144. PP Nanekar, N Jothilakshmi and T Jayakumar, Simulation studies for optimization of phased array parameters for examination of roll-joints in pressurized heavy water reactor coolant channels, *Insight: Non-Destructive Testing and Condition Monitoring*, 55 (6), June 2013, 316-322
145. Jing Ye, Hak Joon Kim, Sung Jin Song, Sung Sik Kang, Kyungcho Kim, Mung Ho Song, Model-based simulation of focused beam fields produced by a phased array ultrasonic transducer in dissimilar metal welds, *NDT & E International*, 44, 2011, 290-296
146. Hun Hee Kim, Hak Joon Kim, Sung-Jin Song, Kyung-Cho Kim, and Yong-Buem Kim, Simulation Based Investigation of Focusing Phased Array Ultrasound in Dissimilar Metal Welds, *Nuclear Engineering and Technology*, 48, 2016, 228-235
147. Steve Mahaut, Christian Gondard, Mostapha El Amrani, Philippe Benoist, Gerard Cattiaux, Ultrasonic defect characterization with a dynamic adaptive focusing system, *Ultrasonics*, 34, 1996, 121-124
148. Patrick Tremblay and Daniel Richard, Development and validation of full matrix capture solution, 9th International Conference on NDE in Relation to Structural Integrity for Nuclear and Pressurized Components, May 22-24, 2012, Seattle, Washington, USA, 457-466
149. Caroline Holmes, Bruce W. Drinkwater, Paul D. Wilcox, Advanced post-processing for scanned ultrasonic arrays: Application to defect detection and classification in non-destructive evaluation, *Ultrasonics*, 48, 2008, 636-642
150. Jie Zhang, Bruce W. Drinkwater and Paul D. Wilcox, Effects of array transducer inconsistencies on total focusing method imaging performance, *NDT & E International*, 44, 2011, 361-368
151. Chengguang Fan, Mihai Caleap, Mengchun Pan, Bruce W. Drinkwater, A comparison between ultrasonic array beam forming and super resolution imaging algorithms for non-destructive evaluation, *Ultrasonics*, 54, 2014, 1842-1850
152. Nicolas Quaegebeur, Patrice Masson, Correlation-based imaging technique using ultrasonic transmit–receive array for Non-Destructive Evaluation, *Ultrasonics*, 52, 2012, 1056-1064
153. Alan J. Hunter, Bruce W. Drinkwater, and Paul D. Wilcox, The wavenumber algorithm for Full-Matrix Imaging Using an Ultrasonic Array, *IEEE Transactions on Ultrasonics, Ferroelectrics, and Frequency Control*, 55, November 2008, 2450-2462
154. Jie Zhang, Bruce W. Drinkwater, Paul D. Wilcox and Alan J. Hunter, Defect detection using ultrasonic arrays: The multi-mode total focusing method, *NDT & E International*, 43, 2010, 123-133

155. Mark Sutcliffe, Miles Weston, Ben Dutton and Ian Cooper, Real-time full matrix capture with auto-focussing of known geometry through dual layered media, www.bindt.org/downloads/ndt2012_3a1.pdf
156. Mark Sutcliffe, Miles Weston, Ben Dutton, Peter Charlton, Kelvin Donne, Real-time full matrix capture for ultrasonic non-destructive testing with acceleration of post-processing through graphic hardware, *NDT & E International*, 51, 2012, 16-23
157. David I A Lines, J Wharrie and J Hottenroth, Real-time Full Matrix Capture + Total Focusing and other novel imaging options using general purpose PC-based array instrumentation, *Insight: Non-Destructive Testing and Condition Monitoring*, 54, 2012, 86-90
158. Mickael Njiki, Abdelhafid Elouardi, Samir Bouaziz, Olivier Casula, Olivier Roy, Total Focusing Method for Non Destructive Evaluation: Toward Real-Time Imaging Systems, *IEEE 56th International Midwest Symposium on Circuits and Systems (MWSCAS)*, Columbus, OH, 2013
159. Ewen Carcreff and Gavin Dao, Fast total focusing method for ultrasonic imaging, *IEEE International Ultrasonics Symposium Proceedings*, 2015
160. J Verkooijen and A Boulavinov, Sampling phased array – a new technique for ultrasonic signal processing and imaging, *Insight*, 50, March 2008, 153-157
161. Ludwig von Bernus, Andrey Bulavinov, Michael Dalichov and Krishna Mohan Reddy, Sampling Phased Array: A New Technique for Signal Processing and Ultrasonic Imaging, *Proc. of ECNDT*, 2006
162. A. Bulavinov, R. Pinchuk, S. Pudovikov, K. M. Reddy, F. Walte, Industrial Application of Real-Time 3D Imaging by Sampling Phased Array, *European Conference for Non-destructive Testing*, Moscow, June 2010
163. Catherine H. Frazier and William D. O'Brien, Synthetic Aperture Techniques with a Virtual Source Element, *IEEE transactions on ultrasonics, ferroelectrics and frequency control*, 45, January 1998, 196-207
164. A. Morcira, Real-time synthetic aperture radar (SAR) processing with a new sub-aperture approach, *IEEE Transaction on Geoscience and Remote Sensing*, 30, 1992, 714–722
165. M. Karaman, P. C. Li, and M. O'Donnell, Synthetic aperture imaging for small scale systems, *IEEE transactions on ultrasonics ferroelectrics and frequency control*, 42, 1995, 429–442
166. Mo o-Ho Bae and Mok-Kun Jeong, A Study of Synthetic Aperture Imaging with Virtual Source Elements in B-Mode Ultrasound Imaging Systems, *IEEE transactions on ultrasonics, ferroelectrics, and frequency control*, 47(6), November 2000, 1510-1519
167. L. Le Jeune, S. Robert, E. Lopez Villaverde and C. Prada, Plane Wave imaging for ultrasonic non-destructive testing: Generalization to multimodal imaging, *Ultrasonics*, 64, 2016, 128-138

168. Charles R. Morin, Roch J. Shipley, John A. Wilkinson, Fractography, NDE, and fracture mechanics applications in failure analysis studies, *Materials Characterization*, 33, October 1994, 255-274
169. Baldev Raj, M. Thavasimuthu, and T. Jayakumar, *Practical Non-Destructive Testing*, Third Ed., India, Narosa Publishing House, ISBN 81-7319-072-0
170. ASM handbook Volume 17: Non-destructive evaluation and quality control, ASM International, ISBN 978-0-87170-023-0, 1989
171. P.P. Nanekar and B.K. Shah, Non-Destructive Testing, An Overview, Proc. of INS National workshop on corrosion and condition monitoring, Indian Nuclear Society, 2013, Paper No. 12, 1-12
172. Rohit Rastogi, Fitness for service assessment using API 579 Code, Proc. of INS National workshop on corrosion and condition monitoring, Indian Nuclear Society, 2013, Paper No. 19, 1-31
173. British Standard 7910:2005, Guide to methods for assessing the acceptability of flaws in metallic structures, ISBN 0 580 45965 9, 2005, 15-23
174. Ward D. Rummel, Non-destructive Evaluation – A Critical Part of Structural Integrity, *Procedia Engineering* 86, 2014, 375-383
175. J.K. Sharples, R.A. Ainsworth and A.R. Dowling and P.J. Budden, Developments in UK defect assessment procedures R6 Revision 4 and BS 7910, Proc. of 3rd International Conference on strength, durability and stability of materials and structures, 2002, 280-296
176. Ted Lynn Anderson, Recent advances in fitness for service assessment, www.ndt.net/article/mendt2007/papers/anderson.pdf
177. Baldev Raj, T Jayakumar and BPC Rao, Non-destructive testing and evaluation for structural integrity, *Sadhana*, 20, 1995, 5-38
178. Development of protocols for corrosion and deposits evaluation in pipes by radiography, IAEA-TECDOC-1445, International Atomic Energy Agency, Vienna, Austria, ISBN:92-0-102105-4, 2005
179. *Practical Eddy Current Testing*, BPC Rao, Indian Society for Non-Destructive Testing National Certification Board Series, Alpha Science International Limited, ISBN 1842652990, 2007
180. Hiroyuki Fukutomi, Haoyu Huang, Toshiyuki Takagi and Junji Tani, Identification of Crack Depths from Eddy Current Testing Signal, *IEEE transactions on magnetics*, 34, September 1998, 2893-2896
181. Kozo Shiraishi, Masanori Izumida, Kenji Murakami, Estimation of depth and volume for defects by eddy current testing, *Electrical Engineering in Japan*, 127, June 1999, 29-38
182. T.R. Schmidt, The Remote Field Eddy Current Inspection Technique, *Materials Evaluation*, 42, February 1984, 225-230

183. M.D. MacLean, Defect Characterization by the Remote-Field Eddy Current Technique in Small-Diameter Tubing, *Materials Evaluation*, 47, January 1989, 24-28
184. K. Krzywosz, G. Dau, Comparison of Electromagnetic Techniques for Non-destructive Inspection of Ferromagnetic Tubing, *Materials Evaluation*, 48, January 1990, 42-45
185. *Non-Destructive Testing Handbook*, 3rd Edition, Vol. 7, Ultrasonic Testing, American Society for Non-Destructive Testing, ISBN: 978-1-57117-105-4
186. Fredrik Lingvall and Tadeusz Stepinski, Ultrasonic Characterization of Defects, Study of Realistic Flaws in Welded Carbon Steel, *SKI Report 99:25*, ISSN 1104-1374, 1989, 1-34
187. J. Krautkramer, Determination of the size of defects by the ultrasonic impulse method, *British Journal of Applied Physics*, 10, 1959, 240
188. J.F. Gubernatis, E. Domany, M. Huberman, J.A. Krumhansl, Theory of the scattering of ultrasound by flaws, *Ultrasonics, Symposium Proceedings*, IEEE New York, 1975, 107-110
189. A. Brown, Materials testing by ultrasonic spectroscopy, *Ultrasonics*, 11, 1973, 202-210
190. P.A. Doyle and C.M. Scala, Crack depth measurement by ultrasonics: A review, *Ultrasonics*, 16, July 1978, 164-170
191. H. Wüstenberg, A. Erhard, Matching of ultrasonic flaw sizing methods to the defect type and location, *Nuclear Engineering and Design*, 81, September 1984, 315-323
192. Gordon E. Smith and Uwe Aschemeier, Back to Basics: A Guide to AWS, Ultrasonic Weld Inspection, How to do weld UT according to the AWS D1.1, <https://app.aws.org/itrends/2005/01/021/>
193. RV Murphy, Ultrasonic defect sizing using decibel drop methods, Vol. I, Project no. 85.1.9, Atomic Energy Control Board, Ottawa, Canada
194. Best Practice for The Procurement and Conduct of Non-Destructive Testing. Part 1: Manual Ultrasonic Inspection, HSE Gas and Process Safety Technology Division, November 2000
195. P. G. Heasler, T. T. Taylor, J. C. Spanner, S. R. Doctor, J.D. Deffenbaugh, Ultrasonic inspection reliability for intergranular stress corrosion cracks, NUREG/CR-4908, PNL-6196
196. Alok Prakash, N Jothilakshmi, PP Nanekar, Ultrasonic Simulation Studies for Sizing of Planar Flaws in Thick Carbon Steel Welds, National Conference NDE 2015, Hyderabad, India 2015
197. M.G. Silk, B.H. Lidington, The potential of scattered or diffracted ultrasound in the determination of crack depths, *Non-destructive Testing*, 8, 1975, 146-151
198. M. G. Silk, Shear-wave time of flight diffraction (S-TOFD) technique, *NDT&E International*, 39, 2006, 458-467
199. J. A. Ogilvy and J. A. G. Temple, Diffraction of elastic waves by cracks: application to time-of-flight inspection. *Ultrasonics*, 21, November 1983, 259-269

200. TOFD technique covered by British standard, NDT & E International, 27, Issue 2, April 1994, 117
201. J. P. Charlesworth, J. A. G. Temple, Engineering Applications of Ultrasonic Time-of-Flight Diffraction, Second Edition, Research Studies Press LTD, 2001, ISBN 0-86380-239-7
202. BS 7706-1993: Guide to calibration and setting-up of the ultrasonic time of flight diffraction (TOFD) technique for defect detection
203. Ultrasonic time-of-flight-diffraction (TOFD) examination of butt-fusion joints of high-density polyethylene (HDPE), Application Notes, Olympus, <http://www.olympus-ims.com/en/applications/ultrasonic-tofd-butt-fusion>
204. Time of Flight Diffraction Inspection for Weld Flaw Detection and Sizing, [http://www.vsonomatic.com/downloads/managed/496/Time of Flight Diffraction Inspection for Weld Flaw Detection and Sizing.pdf](http://www.vsonomatic.com/downloads/managed/496/Time_of_Flight_Diffraction_Inspection_for_Weld_Flaw_Detection_and_Sizing.pdf)
205. S.K. Nath, Krishnan Balasubramaniam, C.V. Krishnamurthy, B.H. Narayana, Reliability assessment of manual ultrasonic time of flight diffraction (TOFD) inspection for complex geometry components, NDT & E International, 43, March 2010, 152-162
206. A. Hecht, Time of Flight Diffraction Technique (TOFD) - An Ultrasonic Testing Method for all Applications? NDTnet, 2, 1997, <http://www.ndt.net/article/tofd/hecht/hecht.htm>
207. G Baskaran, K Balasubramaniam, CV Krishnamurthy, C. Lakshmana Rao, Ultrasonic TOFD flaw sizing and imaging in thin plates using embedded signal identification technique (ESIT), Insight, 46, 2004, 1-6
208. S Baby, T Balasubramanian, RJ Pardikar, Time-of-flight diffraction(TOFD) technique for accurate sizing of surface-breaking cracks, Insight, 45, 2003, 426-430
209. S Baby, T Balasubramanian, RJ Pardikar, Time-of-flight diffraction(TOFD) technique for accurate sizing of cracks embedded in sub-cladding, Insight, 45, 2003, 600-604
210. API-UT-10, Defined procedure for advanced ultrasonic crack sizing, 2012, 1-24, www.api.org/~media/Files/.../QUSE-TestProcedure-API-UT-10_Rev1-2012.pdf
211. G.J. Gruber, Defect identification and sizing by the ultrasonic satellite-pulse technique, Journal of Non-destructive Evaluation, 1, 1980, 263-276
212. L. Satyanarayan, C. Sridhar, C.V. Krishnamurthy, Krishnan Balasubramaniam, Simulation of ultrasonic phased array technique for imaging and sizing of defects using longitudinal waves, International Journal of Pressure Vessels and Piping, 84, 2007, 716-729
213. P. Calmon, S. Mahaut, S. Chatillon, R. Raillon, CIVA: An Expertise Platform for Simulation and Processing NDT Data, Ultrasonics, 44, September 2006, 975-979
214. N. Gengembre, Pencil Method for Ultrasonic Beam Computation, Proceedings of World Congress on Ultrasonics, Paris, 2003, 1533-1536
215. P. Calmon, A. Lhemery, I. Lecœur-Taibi, R. Raillon, L. Paradis, Models for the Computation of Ultrasonic fields and their Interaction with Defects in Realistic NDT Configurations, Nuclear Engineering and Design, 180, 1998, 271-283.

216. P. Calmon, A. Lhemery, L. Paradis, Modeling of Ultrasonic Fields and their Interaction with Defects, IEEE Ultrasonics symposium, 1998, 779-783
217. LJ Cutrona, Comparison of sonar system performance achievable using synthetic-aperture techniques with the performance achievable by more conventional means, Journal of Acoustic Society of America, 58, August 1975, 336-348
218. M. Silk, Transfer of ultrasonic energy in the diffraction technique for crack sizing, Ultrasonics, 17, 1979, 113
219. J. A. G. Temple, Time-of-flight inspection with compression waves: cracks and slag-lines, AERE TP Report 932, 1981
220. Information for the Procurement and Conduct of NDT, Part 4: Ultrasonic Sizing Errors and their Implication for Defect Assessment, HSE Document, April 2008, 1-32 www.hse.gov.uk/comah/sragtech/ndt4.pdf
221. Measurement uncertainty in Non-destructive Testing, NATA Document, Technical Note 35 - June 2014, www.nata.com.au/nata/phocadownload/publications/Guidance_information/tech-notes-information-papers/technical_note_35.pdf.
222. SC Katiyar, SS Bajaj, Tarapur Atomic Power Station Units-1 and 2, Design Features, Operating Experience and License Renewal, Nuclear Engineering and Design, 236, 2006, 881-893
223. IAEA, Assessment and Management of Ageing of Major Nuclear Power Plant Components Important to Safety, BWR Pressure Vessel Internals, Vienna, Austria, 2005
224. ER Dykes, An advanced ultrasonic system for BWR vessel weld inspection, Nuclear Engineering and Design, 148, 1994, 101-108
225. H Chatterjee, JP Singh, R Ranjon, MP Kulkarni, RJ Patel, Design & Development of Weld Inspection Manipulator for Reactor Pressure Vessel of TAPS-1, BARC Newsletter, Issue No. 330, 2013
226. S. Ganapathy and B. Schmult, Design of a real-time inspection system for NDE of reactor vessels and piping components, International Journal of Pressure Vessels and Piping, 20, 1985, 17-41
227. Mato Cvitanovic, Elido Oreb, Vedran Mudronja, Vladimir Zado, Hrvoje Bezljaj, Miladin Petkov, Jonko Gledatchev, Stefan Radomirski, Teodara Ribarska, Bert Kroes, Boat sampling and in-service inspections of the reactor pressure vessel weld No. 4 at Kozloduy NPP, Unit 1, Nuclear Engineering and Design, 191, August 1999, 293-312